

Klimis Ntalianis
Anca Croitoru *Editors*

Applied Physics, System Science and Computers

Proceedings of the 1st International
Conference on Applied Physics, System
Science and Computers (APSAC2016),
September 28–30, Dubrovnik, Croatia

Lecture Notes in Electrical Engineering

Volume 428

Board of Series editors

- Leopoldo Angrisani, Napoli, Italy
Marco Arteaga, Coyoacán, México
Samarjit Chakraborty, München, Germany
Jiming Chen, Hangzhou, P.R. China
Tan Kay Chen, Singapore, Singapore
Rüdiger Dillmann, Karlsruhe, Germany
Haibin Duan, Beijing, China
Gianluigi Ferrari, Parma, Italy
Manuel Ferre, Madrid, Spain
Sandra Hirche, München, Germany
Faryar Jabbari, Irvine, USA
Janusz Kacprzyk, Warsaw, Poland
Alaa Khamis, New Cairo City, Egypt
Torsten Kroeger, Stanford, USA
Tan Cher Ming, Singapore, Singapore
Wolfgang Minker, Ulm, Germany
Pradeep Misra, Dayton, USA
Sebastian Möller, Berlin, Germany
Subhas Mukhopadhyay, Palmerston, New Zealand
Cun-Zheng Ning, Tempe, USA
Toyoaki Nishida, Sakyo-ku, Japan
Bijaya Ketan Panigrahi, New Delhi, India
Federica Pascucci, Roma, Italy
Tariq Samad, Minneapolis, USA
Gan Woon Seng, Nanyang Avenue, Singapore
Germano Veiga, Porto, Portugal
Haitao Wu, Beijing, China
Junjie James Zhang, Charlotte, USA

About this Series

“Lecture Notes in Electrical Engineering (LNEE)” is a book series which reports the latest research and developments in Electrical Engineering, namely:

- Communication, Networks, and Information Theory
- Computer Engineering
- Signal, Image, Speech and Information Processing
- Circuits and Systems
- Bioengineering

LNEE publishes authored monographs and contributed volumes which present cutting edge research information as well as new perspectives on classical fields, while maintaining Springer’s high standards of academic excellence. Also considered for publication are lecture materials, proceedings, and other related materials of exceptionally high quality and interest. The subject matter should be original and timely, reporting the latest research and developments in all areas of electrical engineering.

The audience for the books in LNEE consists of advanced level students, researchers, and industry professionals working at the forefront of their fields. Much like Springer’s other Lecture Notes series, LNEE will be distributed through Springer’s print and electronic publishing channels.

More information about this series at <http://www.springer.com/series/7818>

Klimis Ntalianis · Anca Croitoru
Editors

Applied Physics, System Science and Computers

Proceedings of the 1st International
Conference on Applied Physics, System
Science and Computers (APSAC2016),
September 28–30, Dubrovnik, Croatia



Springer

Editors

Klimis Ntalianis
University of Applied Sciences
Athens
Greece

Anca Croitoru
Faculty of Mathematics
Alexandru Ioan Cuza University
Iași
Romania

ISSN 1876-1100

ISSN 1876-1119 (electronic)

Lecture Notes in Electrical Engineering

ISBN 978-3-319-53933-1

ISBN 978-3-319-53934-8 (eBook)

DOI 10.1007/978-3-319-53934-8

Library of Congress Control Number: 2017939605

© Springer International Publishing AG 2018

This work is subject to copyright. All rights are reserved by the Publisher, whether the whole or part of the material is concerned, specifically the rights of translation, reprinting, reuse of illustrations, recitation, broadcasting, reproduction on microfilms or in any other physical way, and transmission or information storage and retrieval, electronic adaptation, computer software, or by similar or dissimilar methodology now known or hereafter developed.

The use of general descriptive names, registered names, trademarks, service marks, etc. in this publication does not imply, even in the absence of a specific statement, that such names are exempt from the relevant protective laws and regulations and therefore free for general use.

The publisher, the authors and the editors are safe to assume that the advice and information in this book are believed to be true and accurate at the date of publication. Neither the publisher nor the authors or the editors give a warranty, express or implied, with respect to the material contained herein or for any errors or omissions that may have been made. The publisher remains neutral with regard to jurisdictional claims in published maps and institutional affiliations.

Printed on acid-free paper

This Springer imprint is published by Springer Nature

The registered company is Springer International Publishing AG

The registered company address is: Gewerbestrasse 11, 6330 Cham, Switzerland

Contents

Part I Applied Physics

Quantum Thermodynamics and Coherence in Ion Channels	3
Samyadeb Bhattacharya and Sisir Roy	
Micro-pulse Stimulation	13
Marie Nedvedova, Milan Chmelar, Ivo Provaznik and Zdenek Reznicek	
Exploring the Therapeutic Effects of Micro-pulse Stimulation	21
Marie Nedvedova, Milan Chmelar, Ivo Provaznik and Kristina Zuffova	
Application of BaTiO₃ Perovskite Material for Piezoelectric Multilayer Actuators	29
Magdalena Gromada, Mojtaba Biglar, Tomasz Trzepiecinski and Feliks Stachowicz	
Modeling of the Waterflooding Process in the Presence of Discontinuities in the Oil Reservoirs	37
Vladimir Astafev, Elena Andriyanova and Andrey Kasatkin	
Terahertz Spectroscopy Applications in Medicament Analysis	45
Kateřina Sulovská	
Stability of Capillary Waves of Finite Amplitude	51
Alexander Petrov, Mariana Lopushanski and Vladimir Vanovskiy	
High Temperature Behavior of Two Titanium Aluminides for Blade Engine Applications. Preliminary Study	59
Alexandra Banu, Alexandru Paraschiv, Luminita Georgescu and Cristina Juganaru	
The Numerical Scheme for the Basset Type Integro-Differential Equation in Hydrodynamics	69
Vladimir Vanovskiy and Alexander Petrov	

On the Issue of Choosing the Measuring Zones in a Faraday Balance When Studying Magnetic Susceptibility of Small Samples	77
Alexander Sandulyak, Anna Sandulyak, Maria Polismakova, Vera Ershova, Darya Sandulyak and Dmitriy Kiselev	
 Part II System Science and Computers	
Energy Aware Autonomous Deployment for Mobile Wireless Sensor Networks: Cellular Automata Approach	87
Shahinaz M. Al-Tabbakh and Eman Shaaban	
An Optimal Process for Average Value-at-Risk Portfolios in Financial Management	101
Yuji Yoshida	
On Quantification of the Hidden Distributed Generation Capacity and Its Effects	109
Vladislav Samoylenko, Stanislav Eroshenko and Andrew Pazderin	
Modeling the Operating Costs for Production of the Hydrolyzate	117
Hana Vaskova and Karel Kolomaznik	
The Problems of Data Security in Cloud Computing and Its Solution Using Petri Nets	123
Zoltán Balogh and Martin Magdin	
Designing of the Pseudorandom Number Generators on the Basis of Two-Dimensional Cellular Automata	137
Stepan Bilan, Mykola Bilan, Ruslan Motornyuk, Andrii Bilan and Sergii Bilan	
A Mixed Fixed Point and Floating Point Graphics Pipeline	145
Ovidiu Sicoe and Mircea Popa	
Functional Verification of AMS-SoC Models Using Hardware Emulation Platforms	153
Hanan Tawfik, Mohamed AbdElSalam, Mona Safar and Ashraf Salem	
Influence of the Antenna's Height to the Standing Waves Ratio When Performing the Electromagnetic Susceptibility Tests in Anechoic Chambers	161
Martin Pospisilik, Milan Adamek and Petr Neumann	
Carstairs-McCarthy's Morphological Rules of English Language in RDFCFL Graphs	169
Alena Lukasová, Martin Žáček and Marek Vajgl	

Mathematical Modeling and Computer Simulation of Simple Permutation Brainteaser in MS Excel	175
Michal Musilek, Stepan Hubalovsky and Marie Hubalovska	
Research of Methods of Learning of Programming Objects-First and Object-Later	183
Ondrej Korinek and Stepan Hubalovsky	
Multichannel Queueing Systems and Their Simulation	191
Miloš Šeda, Jindřiška Šedová and Miroslav Horký	
On Computational Evaluation of Stress Concentration Using Micropolar Elasticity	199
Victor A. Eremeyev, Andrzej Skrzat and Feliks Stachowicz	
An Algorithm for Edge Detection of the Image for Application in WSN	207
Adrian Shehu, Astrit Hulaj and Xhevahir Bajrami	
A Mathematical Model of the Behavior of SIP Signaling and Media Messages	215
Naser K.A. Alajmi, Hadeel Saleh Haj Aliwi, Kamal Alieyan and Muhammad-Imran Sarwar	
Blood Vessel Segmentation from Color Retinal Images Using K-Means Clustering and 2D Gabor Wavelet	221
Aziah Ali, Wan Mimi Diyana Wan Zaki and Aini Hussain	
Training Samples Construction for Energy Utilities Operational Assets Management	229
Alexandra Khalyasmaa and Stanislav Eroshenko	
A Host Program Implementation for Linux File System Tracing Method Using the Kprobes Linux Dynamic Instrumentation System	237
Sang-Young Cho	
Simulation VANET Networks on a Random and Realistic Spatial Scenario	245
Suad Kasapovic and Lejla Banjanovic-Mehmedovic	
Sensor Module for Monitoring Wine Fermentation Process	253
Dimitrija Angelkov and Cveta Martinovska Bande	
Study the Transmittance Properties of Light Sources Under Simulated Hazy Condition	263
Haibo Yuan, Xiaoli Zhou, Zheqian Zhang and Fanghui Xu	

Numerical Study on the Thermal Fatigue of Cryogenic Vacuum Insulated Pipe.....	273
Jae-Hoon Lee, Si-Pom Kim, Rock-Won Jeon and Geun-Ho Lee	
Unconventional Usage of Entropy in the Field of Web Usage Data Preprocessing and Machine Translation Evaluation	281
Michal Munk and Ľubomír Benko	
Advantages of Intelligent Multimedia Application	287
Eva Milkova and Abdel-Badeeh M. Salem	
FFLD-Based Modeling of Fractional-Order State Space LTI MIMO Systems	293
Krzysztof J. Latawiec, Rafał Stanisławski, Marian Łukaniszyn, Marek Rydel and Bogusław R. Szkuta	
A Dispatching Policy for the Dynamic and Stochastic Pickup and Delivery Problem	303
Gianpaolo Ghiani, Emanuele Manni and Alessandro Romano	

Part I

Applied Physics

Quantum Thermodynamics and Coherence in Ion Channels

Samyadeb Bhattacharya and Sisir Roy

Abstract We showed that quantum mechanical superposition can sustain in the process of ion transfer in protein membrane for a substantial period in spite of the presence of the interactions with environmental modes of molecular vibration. The spectral temperature, as defined in quantum thermodynamical framework plays a significant role in maintaining the coherence. The ratio of decoherence time and dwell time has been calculated, which can be directly related to the degree of coherence. The results shed new light to build quantum information system of entangled ionic states in the voltage gated biological channels.

Keywords Ion channels • Decoherence time • Dwell time • Spectral temperature

1 Introduction

The approaches towards dynamics of ion transport in protein membranes (ion channels) are generally considered to be classical and based on molecular dynamics or Brownian dynamics. Recently, one of the present authors showed that [1] the dynamics of K-ion channel can be explained using nonlinear Schrodinger equation which is compatible with the results of MacKinnon's experimental observation [2]. Here, the two K-ions may form an entangled state within selectivity filter during a finite period of time. The temperature within the channel is generally considered to be high enough to destroy the coherence within very short period. Moreover, molecular modes of the protein environment induce dynamical decoherence, which destroys the quantum mechanical superposition of states in a very short period of time. So quan-

S. Bhattacharya
Harish-Chandra Research Institute, Allahabad, India
e-mail: sbh.phys@gmail.com

S. Roy (✉)
National Institute of Advanced Studies, IISc Campus, Bangalore, India
e-mail: sisir.sisirroy@gmail.com
URL: <http://www.springer.com/lncs>

tum mechanical approach in these area of research was mostly speculative and far from experimental realization. But in recent times, some experimental demonstration of the presence of quantum coherence in the process of photosynthetic energy transfer [3, 4] lead us to reconsider the theoretical approach and understanding. Here we are concerned with the question that whether and under what condition a sustainable quantum superposition is achievable in the process of transfer of ions through biological channels. Now it is quite a practical argument that the quantum state of the traversing ion is strongly coupled with the molecular vibrational modes of the protein environment and hence fast decoherence is almost absolutely unavoidable. But it is to be noted that the traversal time of the ion through the membrane is also quite small and it is the ratio of the time scale of decoherence with this traversal time that plays an important role in understanding the maintenance of coherence. If the decoherence time is larger than the traversal time of the ion, then the quantum superposition of the ionic states is sustainable enough for the traversing entity within the period of ionic transfer. Here we also need to consider the effect of temperature in estimating the decoherence time. With the recent developments of quantum thermodynamics [5], a new concept of temperature (known as spectral temperature) for micro-states at non-equilibrium condition has been proposed, instead of the usual concept of thermodynamic temperature. Since ion transport through protein membrane is essentially a non-equilibrium phenomena, we propose that the spectral temperature plays important role in understanding the coherence in the channel dynamics.

2 Decoherence Time and Dwell Time

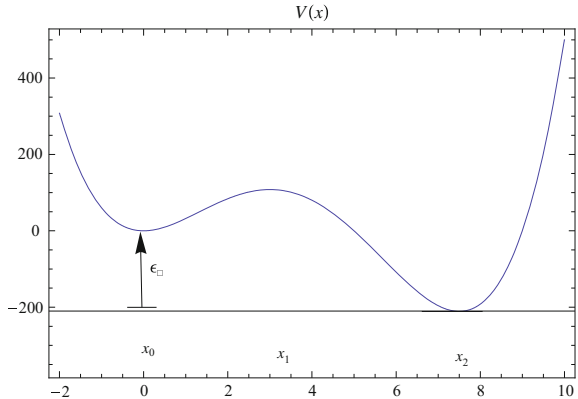
Considering the master equation of the density operator for a certain quantum system, the decoherence time [6] can be written as

$$\tau_{dec} = \frac{\hbar^2}{2m\gamma K_B T(x - x')^2} \quad (1)$$

where γ is the relaxation (dissipation) parameter, T is the thermodynamic temperature and $\Delta x = x - x'$ is the spatial shift of the particle. Now there are numerous definition of traversal time, among which phase time and dwell time are generally accepted by the community [7]. Phase time is equated to dwell time with an additive self-interference term and argued to be the time interval between the energy storage and release in the barrier region [8–11]. So for non-dispersive barrier, where the self-interference term vanishes, the dwell time can be readily interpreted as the life time of energy storage and release in the barrier region. In a previous work [12], we have calculated the weak value of dwell time as

$$\tau_D = \frac{1}{\gamma} \coth \left(\frac{\gamma \tau_M}{2} \right) \quad (2)$$

Fig. 1 $V(x)$ versus x with parameters $A = 14$ and $B = 45$



where τ_M is the measurement time.

The protein membrane can be assumed as an array of molecules with certain modes of vibration. We have mentioned earlier that the quantum states of the traversing entity is interactively coupled to the molecular vibration modes of the protein membrane. The traversing quantum entity loses energy to the vibrational modes, due to the presence of this environmental coupling. So the protein membrane can be interpreted as sort of capacitive system, which can store and release energy with the dwell time as its lifetime of energy storage. In this case the time interval between the opening and closing of the channel gates can be taken as the measurement time (τ_M). Now we consider a double well potential of the form [13]

$$V(x) = \frac{1}{2}m\omega^2x^2 \left[\left(\frac{x}{a}\right)^2 - A \left(\frac{x}{a}\right) + B \right] \quad (3)$$

where A and B are dimensionless constants. For the particular case of asymmetric double well, $A = 14$ and $B = 45$. The bistable nature of the potential is useful in practical situation, since the ionic transfer in the channel can be interpreted as tunneling between the two stability regions situated at x_0 and x_2 (see Fig. 1).

3 Spectral Temperature and the Ratio of Decoherence Time and Dwell Time

It is also very important to reconsider the concept of temperature in this aspect. Temperature, as we know from the context of thermodynamics, is a property of equilibrium. The ensemble mean of the kinetic energy equals to Boltzmann constant times the temperature. So assuming ergodicity, temperature is defined as the time averaged kinetic energy. But the process of ion transfer through channels is a dynamical process interactive to the protein environment and subject to energy exchange with

the environment. This is certainly not a situation for thermodynamic equilibrium and hence the usual concept of thermodynamic temperature may not be suitable. Here we introduce the concept of spectral temperature, originally formulated by Gemmer et al. [5]. It is defined as a function of the microstates, to include the non-equilibrium properties of the system. It is formulated as a function of energy occupation probability of the different states of a certain quantum system. This temperature evolves with the evolution of the probability of occurrence. The inverse of the spectral temperature is defined as [5]

$$\frac{1}{K_B T_{spec}} = - \left(1 - \frac{P_0 + P_N}{2} \right)^{-1} \sum_{i=1}^N \left(\frac{P_i + P_{i-1}}{2} \right) \times \left[\frac{\ln\left(\frac{P_i}{P_{i-1}}\right) - \ln\left(\frac{\phi_i}{\phi_{i-1}}\right)}{E_i - E_{i-1}} \right] \quad (4)$$

where P_i is the probability of finding the particle within an energy compartment with mean energy E_i , having the degree of degeneracy ϕ_i . This definition depends on the energy probability distribution and of course, the spectrum of the concerning system. So it cannot change in time for an isolated system and defined independent of the fact that whether the system is in equilibrium or not. In this definition, the association of quantum probability, which evolves in time, gives temperature a evolving feature representing the dynamical situation between two successive equilibrium. Now here we are approximating the bistable potential as a two-state system having only the ground states of the asymmetric wells. So for our case of non-degenerate two-state system, the expression of the spectral temperature reduces to

$$\frac{1}{K_B T_{spec}} = - \left(1 - \frac{P_0 + P_1}{2} \right)^{-1} \left(\frac{P_0 + P_1}{2} \right) \left[\frac{\ln\left(\frac{P_0}{P_1}\right)}{E_0 - E_1} \right] \quad (5)$$

where P_0 and P_1 are the probabilities corresponding to the ground states of the lower and higher well respectively. Since P_0 is the probability corresponding to the lowest state, it should not decay. Now using the decay probability of the higher state ($P_1 \sim e^{-\gamma t}$) within the time interval equal to the dwell time, we find

$$\frac{1}{K_B T_{spec}} = \frac{1}{E_1 - E_0} \coth\left(\frac{\gamma \tau_M}{2}\right) \coth\left[\frac{1}{2} \coth\left(\frac{\gamma \tau_M}{2}\right)\right] \quad (6)$$

Now if we consider the energy loss by the particle traversing from the higher barrier to the lower one in terms of the usual kinetic temperature (T_k) as $E_1 - E_0 = \frac{1}{2} K_B T_k$, we get

$$\frac{T_{spec}}{T_k} = 2 \tanh\left(\frac{\gamma \tau_M}{2}\right) \tanh\left[\frac{1}{2} \coth\left(\frac{\gamma \tau_M}{2}\right)\right] \quad (7)$$

Fig. 2 T_{spec}/T_k versus $\gamma\tau_M$. Here we keep γ as a constant and basically study the variation with increasing τ_M

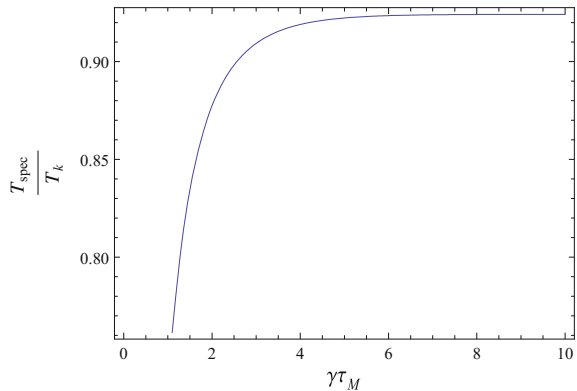
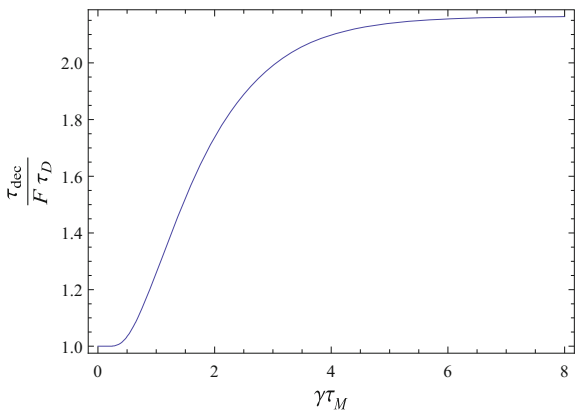


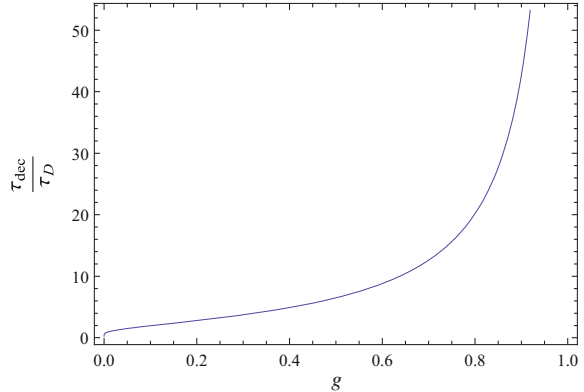
Fig. 3 τ_{dec}/τ_D versus $\gamma\tau_M$. Here also we keep γ as a constant and basically study the variation with increasing τ_M . Here $F = \frac{2\hbar}{w} \sqrt{\frac{2}{me_0}}$. As with increment of τ_M , the process becomes quasi-static, we see that the ratio of the two timescales also reach a stable value



From Eq. (7), under the condition $\tau_M \gg \frac{1}{\gamma}$, we find that $T_{spec} \simeq T_k$. i.e. the spectral temperature is almost equal to the usual kinetic temperature, if the time interval of gate opening and closing is very greater than the dissipation time scale. If the gate opening and closing mechanism is slow enough to be considered as a quasi-static process, the spectral temperature remains very close to its kinetic counterpart. Now it should also be noted that though the process is sort of quasi-static one, it should not be considered as a reversible process, because the coupling to the molecular vibrational modes of the protein environment ensures some generation of dissipative entropy (Figs. 2, 3, and 4).

In case of a double well potential given by (3), using (1), (2) and (7) we get

$$\frac{\tau_{dec}}{\tau_D} = \frac{2\hbar}{w} \sqrt{\frac{2}{me_0}} \coth \left[\frac{1}{2} \coth \left(\frac{\gamma\tau_M}{2} \right) \right] \quad (8)$$

Fig. 4 τ_{dec}/τ_D versus $g^{(1)}$ 

where $\epsilon_0 = E_1 - E_0$ is the asymmetry energy of the potential and $w = \frac{15a}{2}$ is the separation length between the wells. For the quasi-static condition $\tau_M \gg \frac{1}{\gamma}$

$$\frac{\tau_{dec}}{\tau_D} \simeq \frac{4.5\hbar}{w} \sqrt{\frac{2}{me_0}} \quad (9)$$

So we find that in the quasi-static region, whether the decoherence time scale is larger than the dwell time depends on the mass of the traversing particle, the length scale of the channel and the asymmetry energy which is basically the energy lost by the particle during the process of traversal. The ratio of the time scales is inversely proportional to all the mentioned parameters. i.e. greater the inertia of the traversing particle, stronger the interaction (hence greater energy loss) and larger the traversal length, faster shall be the decoherence and hence the situation will be more and more classical. But if the parameter can be chosen in such a way in which the process of decoherence is slower than the process of ionic transfer (i.e. $\tau_{dec}/\tau_D > 1$), then quantum superposition will be sustainable enough within the time period of ionic transfer.

4 Relation Between Degree of Coherence and Decoherence Time-Dwell Time Ratio

Now we turn our attention to the “degree of coherence” for such cases of ionic transfer through protein membranes and try to establish a relation of the afore mentioned ratio of decoherence-dwell time scales with it. Convenient way to discuss coherence in quantitative terms can be done through the introduction of normalized form of correlation functions such as “degree of coherence” [14]

$$g^{(n)}(\xi_1 \dots \xi_{2n}, t_1 \dots t_{2n}) = \frac{G^{(n)}(\xi_1 \dots \xi_{2n}, t_1 \dots t_{2n})}{\prod_{j=1}^{2n} [G^{(1)}(\xi_j, \xi_j, t_1)]^{1/2}} \quad (10)$$

where $\xi = x/a$. For our case of double well system approximated as two-state system, (10) is reduced to

$$g^{(1)} = \frac{G_{12}^{(1)}(\tau)}{\sqrt{G_{11}^{(1)}(0)G_{22}^{(1)}(0)}} \quad (11)$$

where

$$\begin{aligned} G_{12}^{(1)}(\tau) &= \langle \psi_1(\xi, t)\psi_2(\xi, t + \tau) \rangle \\ &= e^{-\gamma\tau} \int_{-\infty}^{\infty} \psi(\xi - \xi_1)\psi^*(\xi)d\xi \end{aligned} \quad (12)$$

and

$$0 \leq g^{(1)} \leq 1 \quad (13)$$

For completely coherent situation, the degree of coherence is 1 and for completely decohered case it is 0. Generally the value should lie in between. If we approximate the potential around the left well at $\xi = 0$ as a harmonic potential, we find that the wavefunction can be estimated as [13]

$$\psi(\xi) = \left(\frac{\nu}{\pi}\right)^{1/2} \exp\left[-\frac{1}{2}\nu\xi^2\right] \quad (14)$$

where $\nu = \sqrt{B \frac{m\omega^2}{\hbar}}$. Expressing the asymmetry energy as

$$\epsilon_0 = V(x_0) - V(x_2) \quad (15)$$

we find that for a double well potential ($A = 14$ and $B = 45$)

$$\omega = \frac{4}{15a} \sqrt{\frac{2\epsilon_0}{15m}} = \frac{2}{w} \sqrt{\frac{2\epsilon_0}{15m}} \quad (16)$$

So for the interval of dwell time given by Eq. (2), we find that the degree of coherence

$$g^{(1)} = \exp\left[-\sqrt{\frac{m\epsilon_0}{2}} \frac{w}{\hbar}\right] \exp\left[-\coth\left(\frac{\gamma\tau_M}{2}\right)\right] \quad (17)$$

For the quasi-static condition $\tau_M \gg 1/\gamma$

$$g^{(1)} \approx \exp\left[-\sqrt{\frac{m\epsilon_0}{2}} \frac{w}{\hbar}\right] \quad (18)$$

From Eqs. (9) and (18), we can also establish a relation

$$\frac{\tau_{dec}}{\tau_D} = \frac{4.5}{\ln \left[\frac{1}{g^{(l)}} \right]} \quad (19)$$

From this relation we see that for completely coherent and decoherent situation, the decoherence-dwell time ratio is infinity and zero respectively and in general situation it lies in between. So this time-scale ratio gives us a certain measure of coherence. As the value of this ratio gets bigger, the “quantumness” of the traversing entity increases.

5 Conclusion

Depending on the above analysis, we suggest that the ion selectivity filter may exhibit quantum coherence which can play crucial role in the process of selectivity and conduction of specific ions in biological membranes. For the time scales shorter than that of decoherence time, quantum coherence can be expected to sustain and have vital importance in the dynamics, despite the presence of interactive protein environment. Our analysis shows that for a sort of quasi-static situation, where the gate opening and closing mechanism is slower than the relaxation (dissipation) time scale, the decoherence-dwell time ratio reaches a static value and can also be greater than unity depending on the mass, energy and length parameters. In such situations, coherent phenomena like entanglement can be of vital importance in understanding the mechanism of selectivity and transport. In case of K^+ filter, there exists two energetically almost degenerate binding states, commonly referred as (1, 3) and (2, 4) states [15–17]. Presence of quantum superposition may lead us to explain the transport phenomena in terms of quantum mechanical tunneling between these two states. The interplay between quantum coherence and environmental noise induced dephasing may also be of fundamental importance. Progress in the atomic spectroscopy of membrane proteins indicate that protein membrane organization may carry a certain coding potency, implying quantum entanglement within ion channels [15–18]. Increasing number of studies are indicating towards the probabilistic nature of ion channel gating mechanism [2, 19]. In the light of these researches, we conclude that it may be relevant to build certain model of quantum information system driven by the entangled ionic states in the voltage gated selectivity filters, which can provide necessary inferences into the biological ion channel dynamics.

References

1. Roy, S., Llinás, R.: C.R. Biologies **332**, 517 (2009)
2. Doyle, D., MacKinnon, R., et al.: Science **280**, 69 (1998)

3. Engel, G.S., et al.: *Nature* **446**, 782 (2007)
4. Mercer, I.P., et al.: *Phys. Rev. Lett.* **102**, 057402 (2009)
5. Gemmer, J., Michel, M., Mahler, G.: *Quantum Thermodynamics*, vol. LNP657. Springer, Heidelberg, Berlin (2004)
6. Zurek, W.H.: *Prog. Math. Phys.* **48**(1) (2007)
7. Hauge, E.H., Stoveng, J.A.: *Rev. Mod. Phys.* **61**(917) (1989)
8. Winful, H.G.: *New J. Phys.* **8**, 101 (2006)
9. Winful, H.G.: *Opt. Express* **10**, 1491 (2002)
10. Winful, H.G.: *Phys. Rev. E* **68**, 016615 (2003)
11. Winful, H.G.: *Phys. Rep.* **436**, 1 (2006)
12. Bhattacharya, S., Roy, S.: *Phys. Rev. A* **85**, 062119 (2012)
13. Mohsen, R.: *Quantum Theory of Tunneling*, p. 255. World Scientific Publishing (2003)
14. Glauber, R.J.: *Quantum Theory of Optical Coherence*. WILEY-VCH Verlag GmbH and Co, KGaA (2007)
15. Bernroider, G., Roy, S.: *SPIE* **5841**, 205 (2005)
16. Summhammer, J., Salari, V., Bernroider, G.: *J. Integr. Nanosci.* **11**, 123 (2012)
17. Salari, V., Tuszyński, J., Rahnama, M., Bernroider, G.: *JPCS* **306**, 012075 (2011)
18. Hans, J.B., Popescu, S.: [arXiv:0806.4552v2](https://arxiv.org/abs/0806.4552v2) (2009)
19. Zhou, Y., Morais-Cabral, A., Kaufman, A., MacKinnon, R.: *Nature* **414**, 43 (2001)

Micro-pulse Stimulation

Marie Nedvedova, Milan Chmelar, Ivo Provaznik
and Zdenek Reznicek

Abstract This paper deals with a new electrotherapeutic method for use in physiatric treatment. The micro-pulse stimulation is based on the combination of three electrotherapeutic methods: burst therapy, high-voltage pulsed current therapy, and microelectrostimulation. Micro-pulse stimulation is special for its unusual configuration of pulse parameters; high-voltage electric pulses are safely used as a result of a cumulative effect of the subthreshold monophasic pulses with a very short duration. This combination of parameters should connect the advantages of used methods. This includes an analgesic effect without any obvious adaptation of the stimulated tissue and making the tissue penetration easier. As the micro-pulse stimulation was designed especially for the treatment of swelling and pain in animal therapy, the device is small, portable, battery-operated and easy to use.

Keywords Burst therapy • High-voltage pulsed current therapy • Micro-pulse stimulation • Subthreshold stimulation

1 Introduction

The role of electrotherapy and electrostimulation is quite extraordinary in comparison to other methods of physical therapy. Their usage is limited not only for rehabilitation as a standard application but it has a great significance for the

M. Nedvedova (✉) · M. Chmelar · I. Provazník

Faculty of Electrical Engineering and Communication, Department of Biomedical Engineering, Brno University of Technology, Technická 3082/12, 61600 Brno,
Czech Republic
e-mail: tobolova@fai.utb.cz

M. Nedvedova

Faculty of Applied Informatics, Department of Electronics and Measurements,
Tomas Bata University in Zlín, Nad Stranemi 4511, 76005 Zlín, Czech Republic

Z. Reznicek

Hybrid Integrated Technologies, Ltd., Nedachlebice 233, 68715 Nedachlebice,
Czech Republic

diagnostics, treatment and for research. Instead of the classical electrostimulation methods with single pulses of the specified frequency, shape, duration and period, there were found new alternatives that seem to be more effective in some applications. We can mention various types of modulation (amplitude, frequency) or burst therapy [1–3]. Micro-pulse stimulation was designed as a type of electrotherapy which could combine the advantages of the three chosen methods, especially microelectro stimulation, high-voltage pulsed current and burst therapy.

MicroElectroStimulation (MES) is also known as MicrocurrentElectroTherapy (MET) or MicroElectroNeuroStimulation (MENS). The prefix “micro” is common for all modalities because of using extremely low values of electric current about the millionth of ampere. Similar microampere values can be measured both at humans and some animals because their bodies form the natural electromagnetic field [4]. That is why it can be also called Biostimulation. The current values for the MES are subthreshold and thousand times lower than for the Transcutaneous Electrical NeuroStimulation (TENS). There are described positive therapeutic effects of MES on all sorts of pain, it moderates inflammation and edema, evolves the moving potential, muscular strength and relaxation [5]. Furthermore, MES supports significantly the wound healing [6–8], treatment of patients with the diabetes mellitus, hypertension and chronic wounds [9], obesity reduction [10], reduction of inflammatory induced by ultraviolet irradiation [11]. But not all the studies are so optimistic [12]. Study [13] revealed that MES could enhance apoptosis, the adverse effect to the tissue healing. Despite it, MES is highly promising for very problematic tendon regeneration at horses.

High-Voltage Pulsed Current (HVPC) uses the pulsed current with relatively low intensity, short duration (usually 10–30 µs), but voltage much higher than it is usual in electrotherapy (up to 500 V) [1]. The device for HVPC must work in the regime of the constant voltage. The level of the stimulation intensity is usually threshold up to motor suprathreshold. The pulse frequency can be constant or modulated and it directly influences the myorelaxation and analgesic effect. HVPC causes vasodilatation supporting the edema reduction [14], tissue regeneration and wound healing, especially decubitis ulcers [15], venous crural ulceration [16] and diabetic foot ulcers [17].

The Burst Therapy is based on the theory of the subthreshold pulses summation [18]. The pulses of the burst come separately and gradually summate so that each of them brings the membrane closer to its threshold. The membrane threshold is reached when the pulse summation culminates in the sufficient depolarization leading to the formation of an action potential (AP). The total number of APs agrees with the number of bursts [19]. The summation effect requires that each pulse in the burst follows so fast that there is not enough time for the membrane relaxation after the subthreshold polarization. The depolarization caused by the summation of the subthreshold pulses is expected at the higher kilohertz frequencies [20]. According to available sources, the burst therapy has good results in the prevention of venous thrombosis at the orthopaedic patients and postoperative cases [21] and in treatment of the various types of arrhythmia, such as ventricular and atrial tachycardia [22]. Further, it has a noticeable analgesic effect and the great advantage lies in no

obvious adaptation of the tissues that is a common problem in all classic electrotherapeutic methods [1].

2 Device Working Principles

The goal was to construct the device combining the principles of high-voltage pulsed current, microelectrostimulation and burst therapy. Using voltage up to 1000 V makes the tissue penetration easier, but the high voltage must be compensated by the setting of other parameters to maximally keep the safety [23]:

- (a) An appropriate choice of the pulse duration and working frequency prevents inadequate load.
- (b) The electric circuit is closed between the concentric electrodes that precisely define the application area and prevent the current flow through other area.
- (c) The battery power itself disables the secondary circuit formation (e.g. through the heart); this is a prevention of the electric current injury.

Microstimulator generates high-voltage pulses (about hundreds volts) with a very short duration (microseconds). Considering the easier construction and therapeutic advantages, an accumulation of subthreshold pulses was used for formation of the final pulse with required characteristics. Several pulses are arranged in the burst coming with the working frequency many times lower than the repeating frequency of each pulse. The advantage of high carrier pulse frequency is an easier penetration into the body, again. In this case, the envelope of the whole burst can be understood as one therapeutic pulse in classic electrotherapy. This agrees also with the fact that the threshold voltage drops with the cumulative number of the pulses in one series (with the burst width) [19]. The burst can be formed by both biphasic and monophasic pulses. The experiments using the bursts in Functional ElectroStimulation advert to the better efficacy of the monophasic rectangular pulses for the lower threshold of the AP initiation [24]. In our case, we have used just the monophasic pulses.

3 Design of the Microstimulator

The design of the Microstimulator is protected by the patent no. 304960 published in the Bulletin No. 5/2015 by the Industrial Property Office of Czech Republic. An exact electrotechnical scheme of the device exceeds the range of this article; however, Fig. 1 shows a principal scheme of the Microstimulator.

The circuit consists of three 555 precision timers (marked A, B, C), two NAND gates (D, E), switch (F) and pulse transformer (G). Generator C generates the pulses with high frequency (about 100 kHz) that are arranged into the bursts with the

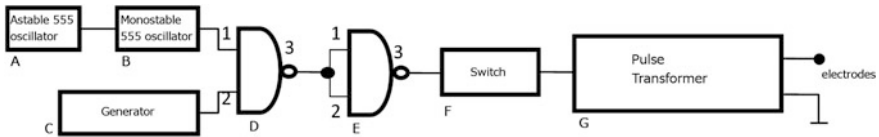


Fig. 1 Principal scheme of microstimulator

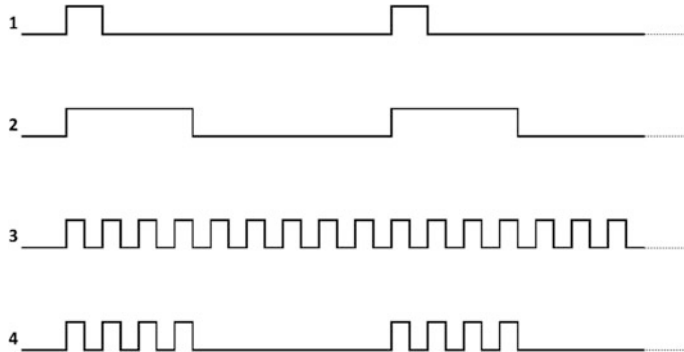


Fig. 2 Time diagram of the output signals from the astable 555 oscillator (1), monostable 555 oscillator (2), generator (3), and switch (4)

stimulation parameters (frequency and burst width) adjusted by the astable and monostable 555 oscillators. NAND gate D separates the burst of pulses according to the required parameters of stimulation. NAND gate E inverts the output of gate D. Switch F manages transfer of the pulses to the primary winding of pulse transformer G.

The time relation of the important output signals is demonstrated in Fig. 2. Signal no. 3 represents function of the generator C. Signal no. 1 demonstrates the output of the astable 555 oscillator A that activates the monostable 555 oscillator B to generation of the pulse with the required width, see signal no. 2. This way, the equivalent number of pulses is defined and transferred from the generator, see signal no. 4.

A final realization of the Microstimulator and measured signal output are shown in Fig. 3. Microstimulator was designed in such a way the device is suitable for human and also for animal electrotherapy, particularly for horses that were chosen as the target objects for the following micro-pulse stimulation effect testing [25].

The device is small, portable, battery-operated and easy to use. The horse is a typical skittish and restless animal with an unpredictable behaviour which could be the reason of some dangerous situations not only for themselves but also for their close surroundings. Therefore, a compliance with some requirements and conditions was in an effort to keep considering the safety and preventive precaution when an unpredictable situation occurs. Microstimulator is classified as a medical electrical device and strict requirements for the design and function must be kept

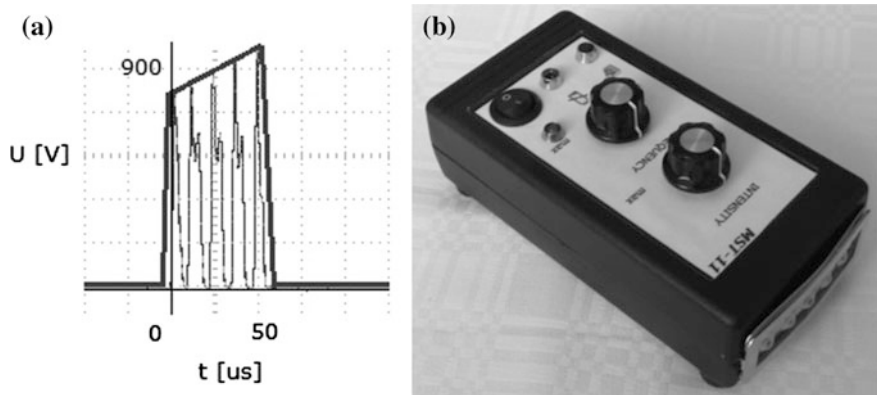


Fig. 3 The Microstimulator (**b**) and the shape of pulses on Microstimulator's output (**a**) [23]. The recording was made during the real measurement using oscilloscope. The therapeutic pulse is marked clearly as an envelope of the burst

according to the relevant standards. The device was tested by the accredited testing laboratory and got CE mark certification.

Two preliminary studies of the micro-pulse stimulation effects were carried out. First experiment explored the physiological effect of the micro-pulse stimulation in an objective way [25]. Two miniature thermodynamic sensors were applied on the skin of two limbs when one of them was stimulated and the other one was just considered as a reference. This type of sensor is able to detect even minor thermal changes. Based on the results, an increased thermal activity was detected in the stimulated limb compared to the reference. This should be caused by an increased blood perfusion and warming-up of the stimulated area. Parallel to this experiment, a pilot experiment investigating the therapeutic effect on the edema reduction of the horses' limbs was carried out with the promising result [26]. The edema treatment relates to the blood circulation support closely, therefore the results of both studies complement each other.

4 Conclusion

This paper presents a design of the Microstimulator; a new electrotherapeutic device for a micro-pulse stimulation. Its therapeutic effect is based on the connecting of the selected electrotherapeutic methods to take the therapeutic advantages of all of them; using high-voltage pulses coming with high frequency makes tissue penetration easier and causes no adaptation of stimulated tissue. The device is designed especially for animal electrotherapy, therefore there must be kept both the strict safety instructions and preventive precautions to manage also unpredictable reaction of animal. The therapeutic effects of the micro-pulse stimulation were successfully tested on horses.

Acknowledgements This work was supported by the Hybrid Integrated Technologies, Ltd., Brno University of Technology and European Regional Development Fund under the project CEBIA-Tech Instrumentation No. CZ.1.05/2.1.00/19.0376.

References

1. Podebradsky, J., Vareka, I.: Fyzikální terapie I. Grada Publishing, Praha (1998)
2. Podebradsky, J., Vareka, I.: Fyzikální terapie II. Grada Publishing, Praha (1998)
3. Capko, J.: Základy fyziatrické léčby. Grada Publishing, Praha (1998)
4. Plonsey, R., Barr, R.C.: Bioelectricity: a Quantitative Approach. Springer, New York (2007)
5. Mercola, J.M., Kirsch, D.L.: The basis for microcurrent electrical therapy in conventional medical practice. *J. Adv. Med.* **8**, 107–120 (1995)
6. Poltawski, L., Watson, T.: Bioelectricity and microcurrent therapy for tissue healing—a narrative review. *Phys. Ther. Rev.* **14**, 104–114 (2009)
7. Butcher, M.: How to use POSIFECT® bio-electric stimulation therapy in chronic wounds. *Wound Essentials* **2**, 186–193 (2007)
8. De Gaspi, F.O. et al.: Effects of the topical application of hydroalcoholic leaf extract of Oncidium flexuosum Sims. (Orchidaceae) and Microcurrent on the healing of wounds surgically induced in Wistar rats. *Evid. Based Complement. Altern. Med.* 1–9 (2011)
9. Lee, B.Y., et al.: Ultra-low microcurrent in the management of diabetes mellitus, hypertension and chronic wounds: Report of twelve cases and discussion of mechanism of action. *Int. J. Med. Sci.* **7**, 29–35 (2010)
10. Park, R., et al.: The effect of wearing shoes generating micro-currents on body composition and blood lipid concentrations of overweight females. *J. Phys. Ther. Sci.* **23**, 177–180 (2011)
11. Lee, J., et al.: The effects of microcurrents on inflammatory reaction induced by ultraviolet irradiation. *J. Phys. Ther. Sci.* **23**, 693–696 (2011)
12. Gossrau, G., et al.: Microcurrent transcutaneous electric nerve stimulation in painful diabetic neuropathy: A randomized placebo-controlled study. *Pain Med.* **12**, 953–960 (2011)
13. Lin, Y., Van Weeren, P.R., et al.: Effect of microcurrent electrical tissue stimulation on equine tenocytes in culture. *Am. J. Vet. Res.* **67**, 271–276 (2006)
14. Karnes, J., et al.: High-voltage pulsed current: Its influence on diameters of histamine-dilated arterioles in hamster cheek pouches. *Arch. Phys. Med. Rehabil.* **76**, 381–386 (1995)
15. Kloth, L.C., Feedar, J.A.: Acceleration of Wound Healing with High Voltage, Monophasic, Pulsed Current. *Phys. Ther.* **68**, 503–508 (1988)
16. Franek, A., Polak, A., Kucharzewski, M.: Modern application of high voltage stimulation for enhanced healing of venous crural ulceration. *Med. Eng. Phys.* **22**, 647–655 (2000)
17. Burdge, J.J., Hartman, J.F., Wright, M.L.: A retrospective study of highvoltage, pulsed current as an adjunctive therapy in limb salvage for chronic diabetic wounds of the lower extremity. *Ostomy Wound Manag.* **55**, 30–38 (2009)
18. Gildemeister, M.: Zur theorie des elektrischen Reizes. V. Polarisation durch Wechselströme. *Berichte über die Verhandlungen der Sachsischen Akademie der Wissenschaften zu Leipzig. Math. Phys. Kl.* **81**, 303–313 (1930)
19. Laufer, Y., Elboim, M.: Effect of burst frequency and duration of kilohertz-frequency alternating currents and of low-frequency pulsed currents on strength of contraction, muscle fatigue, and perceived discomfort. *Phys. Ther.* **88**, 1167–1176 (2008)
20. Ward, A.R., Robertson, V.J., Ioannou, H.: The effect of duty cycle and frequency on muscle torque production using kilohertz frequency range alternating current. *Med. Eng. Phys.* **26**, 569–579 (2004)
21. Powell, J.H. et al.: Parameter selection and electrode placement of neuromuscular electrical stimulation apparatus. United States Patent 5358513 (1994)

22. Salama, G., Kanai, A., Efimov, I.R.: Subthreshold stimulation of Purkinje fibers interrupts ventricular tachycardia in intact hearts. experimental study with voltage-sensitive dyes and imaging techniques. *Circ. Res.* **74**, 604–619 (1994)
23. Tobolova, M.: Microstimulator: Master's Thesis. Brno University of Technology, Brno (2012)
24. Kaczmarek, P., et al.: Investigation of the relationship between stimulus parameters and a human muscle contraction force during stimulation of the gastrocnemius muscle. *Artif. Organs* **34**, 126–135 (2009)
25. Tobolova, M., et al.: Testing the effects of micro-pulse stimulation on blood circulation using the thermodynamic sensors. *J. Biosens. Bioelectron.* **5**, 1–7 (2014)
26. Nedvedova, M., Chmelar, M., Provaznik, I., Zuffova, K.: Exploring the therapeutic effects of micro-pulse stimulation. In: 1st International Conference on: Applied Physics, System Science and Computers, Dubrovnik (2016)

Exploring the Therapeutic Effects of Micro-pulse Stimulation

Marie Nedvedova, Milan Chmelar, Ivo Provaznik
and Kristina Zuffova

Abstract Electrotherapy is not so commonly used in veterinary practice as in human. Microstimulator is a new electrotherapeutic device designed especially for the horses' patients. Its unusual configuration of pulse parameters makes this method appropriate for the swelling treatment and tissue regeneration after the minor injuries. Nine horses with swelling of the limb caused by minor injury such as tendinitis, sprains etc. were included in the study. Micro-pulse stimulation was applied once a day until the total regress of problems. The course of the experiment was documented in photographs and video recordings that were significant for evaluation of the effectiveness of micro-pulse stimulation in this application. Based on the results, it seems the micro-pulse stimulation really has positive effect on swelling reduction, and so the overall tissue regeneration, consisting probably in analgesic and anti-inflammatory effects.

Keywords Burst therapy • Swelling treatment • High-voltage pulsed current therapy • Subthreshold stimulation

M. Nedvedova (✉) · M. Chmelar · I. Provaznik

Faculty of Electrical Engineering and Communication, Department of Biomedical Engineering, Brno University of Technology, Technicka 3082/12, 61600 Brno, Czech Republic
e-mail: tobolova@fai.utb.cz

M. Nedvedova

Faculty of Applied Informatics, Department of Electronics and Measurements, Tomas Bata University in Zlin, Nad Stranemi 4511, 76005 Zlin, Czech Republic

K. Zuffova

Faculty of Veterinary Medicine, Equine Clinic, University of Veterinary and Pharmaceutical Sciences Brno, Palackeho 1/3, 61242 Brno, Czech Republic

1 Introduction

The positive effect of electrotherapy was found some tens of years ago and many companies started a successful business on manufacturing electrostimulators and one type of device was recommended as a universal therapeutic device for a number of problems. But this is a mistake, because even the change of one parameter of stimulation could have totally different effect. Therefore, the possible negative impact of the stimulation should be considered carefully as well and the task is a choice of the relevant pulse parameters according to the therapeutic application as well as the possible cytotoxicity [1–6]. Maybe this is one of the reasons of focusing on the subthreshold stimulation.

Micro-pulse stimulation was designed as a type of electrotherapy which could combine the advantages of the three chosen methods, especially microelectrostimulation, high voltage pulsed current and burst therapy [7]. Microelectrostimulation is known for its positive effect on pain [8], inflammation [9], swelling reduction [10] and tissue healing [11–14]. High voltage pulsed current is beneficial for the tissue regeneration, wound healing and also swelling reduction [15–18]. The burst therapy based on subthreshold pulses summation [19] is not so common in electrotherapy, yet. But some studies point out on its demonstrable analgesic effect without any obvious adaptation of the stimulated tissue [20]. The combination of these parameters seems to be efficient for the painful swelling treatment. From this point of view, a horse seems to be appropriate for testing the therapeutic effect of micro-pulse stimulation. The breeders face the problem of swollen horses' limbs quite frequently because just the limbs are the most vulnerable part at the horses considering their usage for sport and work in harness. Usually, the treatment is quite costly and also lengthy process because the appropriate quiescent regime is not possible to observe due to the constant loading of the limbs. The aim of the following experiment is to observe if the micro-pulse stimulation has any positive effect on the reduction of swelling of the horses' legs and if it could help to make the whole treatment faster and less costly.

2 Experimental Design

The Microstimulator, a device for micro-pulse stimulation, was used in this study. It generates very short (microseconds) high-voltage pulses (hundreds volts). The main advantage of using the high voltage (peak up to 1000 V) lies in making the tissue penetration easier. However, the high voltage must be compensated by the setting of other parameters to keep safety maximally. An accumulation of subthreshold pulses is used to form the final pulse of defined intensity and width [7]. The design of the Microstimulator is described more detailed in [21].

It seems that the micro-pulse stimulation would be better and easier to test on humans, but an important advantage of the testing on animals is at least partial

elimination of the placebo effect. We expect that testing on animals could bring more objective results. Especially in this application, the improvement is visible and the condition of the horse as a target animal can be well evaluated. The procedure of the whole experiment was approved by the ethics committee and all steps were carried out under the veterinary supervision. The informed consent form was prepared for each owner of participating horse. It documented his familiarization with the methods and aims of the experiment, possible problems and also conditions of the Privacy Policy. Using the handwritten signature, each owner agreed with the participation of his horse in the study, with the publication and usage of the results.

All measured data were further provided anonymously, it means that the alpha-numeric code Txx was assigned to each horse. There were no special limitations of the breed, sex or age. The adult horses between the ages of 5 and 22 participated. The common mark and also the assumption of the subject submission into the experiment was obvious presence of the acute swelling of some limb. Only the swelling caused by minor injuries (such as distortion, kicking by another horse and tendinitis) was considered. In many cases, the aching swelling is attended by the walking with the limp or total rejecting of the walking. The studied parameters were the swelling reduction, mobility and also soreness of the injured limb, or wound healing. The horses with swelling of an infectious origin did not participate in the study. In this case, the antibiotics are preferred type of medication; however, the micro-pulse stimulation could be used as an additional supporting therapy for the acceleration of the healing.

Altogether, nine subjects with swelling of the above-mentioned origin were documented. The documentation included probable cause of the injury, description of the affected area, localization and extent of the swelling, description of used parameters and time of stimulation, reaction of horse to the stimulation and progress of the treatment in the following days. The whole experiment was supported by photography and video recordings that ensure demonstrative material for effectiveness evaluation of the micro-pulse stimulation.

Before the stimulation, the affected limb was cleaned and gently washed with the pure water to reduce the electric resistance of the skin. Then, the electrodes of Microstimulator were applied on the swollen area. Microstimulator stayed in one position for several minutes. Then, the position was changed in the proximal direction from the affected part of the limb. This procedure was repeated once a day for maximally 30 min at each horse, until the total regress of the problems.

3 Results

For a better interpretation of the results, a case of the 7-year Moravian Warmblood gelding is described in detail. This horse was affected by a milder form of the mud fever which is the disease causing irritation and dermatitis in the lower limbs. First, only a small swelling formed in the pastern area of the left hind-limb and warmed. The limb was very painful to touch and the horse limped. Occasionally, the owner

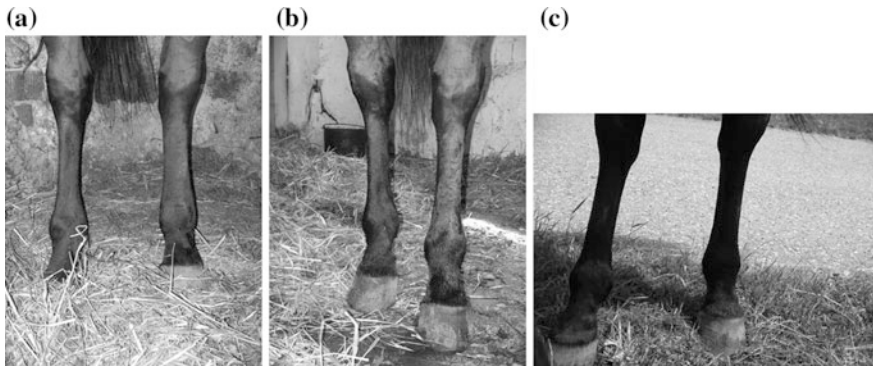


Fig. 1 Front view on the limbs before therapy (a), after the first (b) and second therapy (c) [7]

cared for the affected limb by washing with the iodine solution and packing into the wet wrap. After a week, the painful sores and scabs did not regress and the painful swelling extended from the pastern area up to the hock of the limb, see Fig. 1a. The first electrotherapy was carried out for 30 min and regarding the parameters of stimulation, the intensity was steadily set on the maximal value, while the frequency of the pulses was changed gradually from minimal to maximal level. After 2 days, before the second therapy, a significant swelling reduction was noticed, but the swollen pastern area remained, see Fig. 1b. The limb was less sensitive to touch and the horse was less nervous during the therapy. The procedure was repeated again. Next day, the swelling and pain disappeared completely and the scabs' healing was evident, see Fig. 1c.

The experimental results are summarized in Table 1. A progress of the treatment in time is presented at each horse using the description of four observed parameters —Limp (L), Swelling (S), Sensitivity and Pain (SP), and Warm (W). The values from the range 0 to 2 classify the actual state of the parameter in particular phase of the treatment (before therapy, after 1st and 2nd therapy). The evaluation scale has three levels expressing the strength of appropriate symptom: 2—intensive, 1—mild, 0—practically without symptom.

4 Discussion

The swelling is the typical epiphénoménon of the acute inflammation. The semipermeability of the blood vessels is damaged and normal penetration of water, salts and other low-molecule-weight substances into the tissues is affected and water retains inside bigger molecules, such as the proteins. When the tissue is affected by inflammation, the blood vessel wall becomes permeable also for proteins that get into the surrounding tissue and disrupt the osmotic pressure balance between the interstitium and plasma; therefore the fluid is collected in the tissue. In

Table 1 Evaluation of the observed parameters during the phases of the treatment at each horse marked with Txx code. Each parameter (L—Limp, S—Swelling, SP—Sensitivity and Pain, W—Warm) was evaluated according to its intensity (2—intensive, 1—mild, 0—practically without it)

Code	Before therapy				After 1st therapy				After 2nd therapy			
	L	S	SP	W	L	S	SP	W	L	S	SP	W
T01	2	1	1	1	1	1	0	0	0	0	0	0
T02	0	2	2	2	0	1	0	0	0	0	0	0
T03	0	2	2	2	0	1	1	1	0	0	0	0
T04	2	1	0	2	1	1	0	1	0	0	0	0
T05	2	2	2	2	1	1	2	1	0	0	0	0
T06	1	2	2	2	0	2	1	1	0	0	0	0
T07	2	2	2	2	1	0	0	0	0	0	0	0
T08	1	2	2	2	0	1	1	1	0	0	0	0
T09	2	2	2	2	1	1	1	1	0	1	0	0

addition, the function of the lymph system is also affected and the lymph flowing becomes sluggish [22].

Based on the results of this study, a significant improvement is obvious at all participated horses after two therapies with the micro-pulse stimulation. However, the course of treatment was very individual depending on the extent of injury. The longest therapy lasts 4 days; considerable improvement was registered most often in 2 days. The results of the study and complete documentation (photography and video recordings) of the experiment were reviewed by the independent veterinarian. The analgesic and anti-inflammatory effects were confirmed [7]. It seems that the principal reason of the shortened time of swelling treatment using electrostimulation is based just on the influencing the blood vessel permeability. The mobility of proteins, blood cells and lymph increases and this supports the fluid absorption in the swollen area.

The approximate mechanism of the micro-pulse stimulation can be deduced based on the results of the experiment [23] which was running parallel to this study. It studied the physical principle of the stimulation effect on the living tissue. The blood circulation in the stimulated area was monitored using the thermodynamic sensors. Just the swelling treatment is closely associated with the blood circulation support. Based on the results, an increased thermal activity connected with an increased blood perfusion was detected in the stimulated limb compared to the reference.

5 Conclusion

The presented pilot experiment explores the therapeutic effects of the micro-pulse stimulation. There were found positive effects on the swelling and pain reduction of the horses' limbs. The problem of swollen leg caused by minor injury is widespread among the horses because of their usage for sport and work in harness. Based on the

results, we can observe a significant shortening of the treatment time when the stimulation is applied. This preliminary study could be the first step leading to the realization of major research project.

Acknowledgements This work was supported by Brno University of Technology and the European Regional Development Fund under the project CEBIA-Tech Instrumentation No. CZ.1.05/2.1.00/19.0376.

References

1. Lin, Y., van Weeren, P.R., et al.: Effect of microcurrent electrical tissue stimulation on equine tenocytes in culture. *Am. J. Vet. Res.* **67**, 271–276 (2006)
2. Kaczmarek, P., et al.: Investigation of the relationship between stimulus parameters and a human muscle contraction force during stimulation of the gastrocnemius muscle. *Artif. Organs* **34**, 126–135 (2009)
3. Sooksood, K., Stieglitz, T., Ortmanns, M.: An active approach for charge balancing in functional electrical stimulation. *IEEE T. Biomed. Circ. S.* **4**, 162–170 (2010)
4. Pakhomov, A.G., et al.: Characterization of the cytotoxic effect of high-intensity, 10-ns duration electrical pulses. *IEEE T. Plasma Sci.* **32**, 1579–1586 (2004)
5. Nosaka, K., et al.: Muscle damage induced by electrical stimulation. *Eur. J. Appl. Physiol.* **111**, 2427–2437 (2011)
6. Mackey, A.L., et al.: Sequenced response of extracellular matrix deadhesion and fibrotic regulators after muscle damage involved in protection against future injury in human skeletal muscle. *FASEB J.* **25**, 1943–1959 (2011)
7. Tobolova, M.: Microstimulator: Master's Thesis. Brno University of Technology, Brno (2012)
8. Gossrau, G., et al.: Microcurrent transcutaneous electric nerve stimulation in painful diabetic neuropathy: a randomized placebo-controlled study. *Pain Med.* **12**, 953–960 (2011)
9. Lee, J., et al.: The effects of microcurrents on inflammatory reaction induced by ultraviolet irradiation. *J. Phys. Ther. Sci.* **23**, 693–696 (2011)
10. Mercola, J.M., Kirsch, D.L.: The basis for microcurrent electrical therapy in conventional medical practice. *J. Adv. Med.* **8**, 107–120 (1995)
11. Poltawski, L., Watson, T.: Bioelectricity and microcurrent therapy for tissue healing—a narrative review. *Phys. Ther. Rev.* **14**, 104–114 (2009)
12. Butcher, M.: How to use POSIFECT® bio-electric stimulation therapy in chronic wounds. *Wound Essentials* **2**, 186–193 (2007)
13. de Gaspi, F.O., et al.: Effects of the topical application of hydroalcoholic leaf extract of *Oncidium flexuosum* Sims. (Orchidaceae) and Microcurrent on the healing of wounds surgically induced in Wistar rats. *Evid. Based Complement. Alternat. Med.* **9**, art. ID 950347 (2011)
14. Lee, B.Y., et al.: Ultra-low microcurrent in the management of diabetes mellitus, hypertension and chronic wounds: report of twelve cases and discussion of mechanism of action. *Int. J. Med. Sci.* **7**, 29–35 (2010)
15. Karnes, J., et al.: High-voltage pulsed current: Its influence on diameters of histamine-dilated arterioles in hamster cheek pouches. *Arch. Phys. Med. Rehabil.* **76**, 381–386 (1995)
16. Kloth, L.C., Feedar, J.A.: Acceleration of wound healing with high voltage, monophasic. Pulsed Current. *Phys. Ther.* **68**, 503–508 (1988)
17. Franek, A., Polak, A., Kucharzewski, M.: Modern application of high voltage stimulation for enhanced healing of venous crural ulceration. *Med. Eng. Phys.* **22**, 647–655 (2000)

18. Burdge, J.J., Hartman, J.F., Wright, M.L.: A retrospective study of highvoltage, pulsed current as an adjunctive therapy in limb salvage for chronic diabetic wounds of the lower extremity. *Ostomy Wound Manage.* **55**, 30–38 (2009)
19. Gildemeister, M.: Zur theorie des elektrischen Reizes. V. Polarisation durch Wechselströme. Berichte über die Verhandlungen der Sachsischen Akademie der Wissenschaften zu Leipzig. Mathematisch–Physische Klasse **81**, 303–313 (1930)
20. Podebradsky, J., Vareka, I.: Fyzikální terapie I. Grada Publishing, Praha (1998)
21. Nedvedova, M., Chmelar, M., Provaznik, I., and Reznicek, Z.: Micro-pulse stimulation. In: 1st International Conference on: Applied Physics, System Science and Computers, Dubrovnik (2016)
22. Kankova, K., et al.: Patologická fyziologie pro bakalářské studijní programy. Masaryk University Publishing, Brno (2007)
23. Tobolova, M., et al.: Testing the effects of micro-pulse stimulation on blood circulation using the thermodynamic sensors. *J. Biosens. Bioelectron.* **5**, 1–7 (2014)

Application of BaTiO₃ Perovskite Material for Piezoelectric Multilayer Actuators

Magdalena Gromada, Mojtaba Biglar, Tomasz Trzepiecinski
and Feliks Stachowicz

Abstract In this paper, the results of the manufacturing of BaTiO₃ material destined for use in stacked-disk multilayer actuator production are presented. SEM microstructures and electric properties of the fabricated pellets are presented and discussed. The dilatometric curve was executed using the high temperature dilatometer in order to determine at which temperature barium titanate pellets and beams should be sintered to receive full dense sinters. Finally, the problem of metal layer deposition on barium titanate ceramics during actuator fabrication is considered.

Keywords Barium titanate • Piezoelectric properties • Multilayer actuator

1 Introduction

The dielectric properties of BaTiO₃ are controlled by purity and microstructure which are dependent on the methods of preparation [1]. Controlling the phase, composition homogeneity, particle size and monodispersity are other concerns in developing techniques for synthesizing barium titanate. The electrical properties of ceramic materials are a direct result of their microstructure [2], while it is well

M. Gromada
Ceramic Department CEREL, Institute of Power Engineering,
Research Institute, ul. Techniczna 1, 36-040 Boguchwała, Poland
e-mail: gromada@cerel.pl

M. Biglar · T. Trzepiecinski · F. Stachowicz (✉)
Department of Materials Forming and Processing, Rzeszow University
of Technology, al. Powstańców Warszawy 8, 35-959 Rzeszów, Poland
e-mail: stafel@prz.edu.pl

M. Biglar
e-mail: m_biglar@prz.edu.pl

T. Trzepiecinski
e-mail: tomtrz@prz.edu.pl

known that there is a connection between microstructure and type of porosity, grain size distribution and second-phase content [3]. Generally, the properties of BaTiO₃ depend on the synthesis method and sintering regime.

The traditional solid-state method used in our research for BaTiO₃ synthesis has strict criteria with regard to particle size and purity of the raw material, while it is also easy to produce non-homogeneous powders [4]. The advantages of the solid-state reaction used in mass production are its simplicity, precise stoichiometric control and low cost, with the main disadvantage being that the high calcining temperature results in very large and non-uniform grain sizes [5]. As a consequence, this method does not allow the production of materials with a high dielectric constant [5]. In order to eliminate the disadvantages of the solid-state reaction, a variety of novel wet chemical synthesis methods have been developed [6].

In this study, we analyse the manufacture of BaTiO₃ material destined for use in stacked-disk multilayer actuator production. SEM microstructures and electric properties of the fabricated pellets are also presented and discussed. The problem of metal layer deposition on barium titanate ceramics during actuator fabrication is considered.

2 Results and Discussion

The BaTiO₃ pellets were obtained in a mould of external diameter 11.5 mm, with home-made BaTiO₃ granulate of weight 0.6 g and uniaxial pressing under a pressure of 1 MPa. The beams were uniaxially pressed under a pressure of 5 MPa in a full mould filled for beam execution with barium titanate granulate. The green discs and beams obtained in this manner were then isostatically pressed under a pressure of 150 MPa.

The dilatometric curve was executed using the high temperature dilatometer from BÄHR-Gerätebau GmbH company in order to determine at which temperature barium titanate pellets and beams should be sintered to receive full dense sinters. On the basis of the obtained dilatometric curve (Fig. 1a), the maximal sintering temperatures were estimated as 1250 °C. Pellets and beams were sintered in the electric furnace with the rate of both heating and cooling equal to 100 °C/h and the dwell time—4 h. Sintered pellets and beams are hereafter denoted as BT_0.

The electrical properties of BT_0 pellets were determined, with pellet AC conductivity measured as a function of frequency at 150 °C as shown in Fig. 1b. It is well known that at room temperature, conductivity is almost independent of temperature and instead depends strongly on frequency. Analysis of AC conductivity versus frequency plot (Fig. 1b) reveals that BT_0 conductivity increases with increasing frequency. However, there is a little signature of a plateau in the curve at higher frequencies, beyond the measuring range. It is therefore evident that the linear (dispersion) region represents some sort of relaxation process. The dependence of AC conductivity on frequency may be influenced by carrier transport

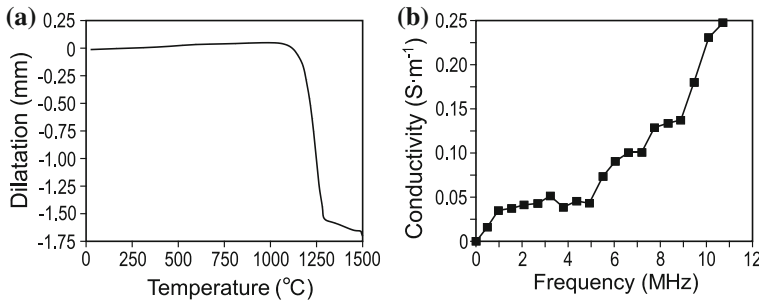


Fig. 1 The dilatometric curve of beam before sintering (a) and AC conductivity versus frequency (b)

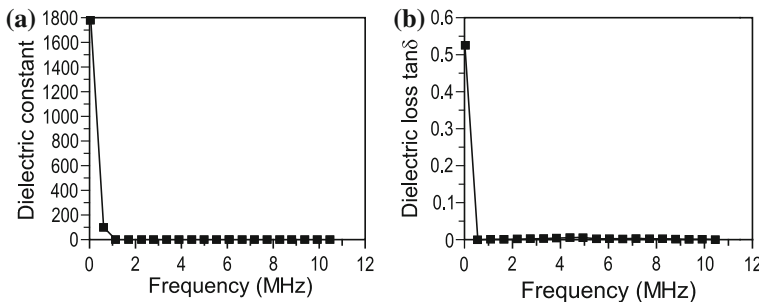


Fig. 2 Dielectric constant versus frequency (a) and dielectric loss versus frequency (b)

excited to localised states near the band edge, as well as hopping of the charge carriers through trap sites separated by energy barriers of various heights. In other words, AC conductivity contributes in the form of the hopping of localised and free charge carriers [7].

Particularly, at low temperature, AC conductivity can occur through the carrier motion over a shorter distance between sites in the potential well. In the present study, the AC conductivity for BT_0 was found to be of the order of 10^{-9} , which is close related with literature. It is considered that the AC conductivity is contributed by hopping of localized and free charges.

At room temperature, the dielectric constant value for BT_0 pellets was found to decrease with frequency (Fig. 2a). BT_0 thus exhibits normal dielectric dispersion because the dielectric constant (ϵ' and ϵ'') decreases with increasing frequency. The phenomenon of dielectric dispersion is attributed to Maxwell–Wagner type interfacial polarisation in accordance with Koop's phenomenological theory [8]. This theory states that the conductivity of grain boundaries contributes more to dielectric permittivity at lower frequencies and temperatures. The sintering of polycrystalline perovskite involves the formation of grains with high conductivity. These grains are separated by poorly conducting grain boundaries, as can be seen in SEM images,

and exhibit low conduction; BT_0 perovskite thus behaves as a heterogeneous dielectric material.

In addition Ti^{4+} is reduced to Ti^{3+} and formed a conduction electron ($\text{Ti}^{4+}\bullet\text{e}$) in order to keep charge neutrality. It can be found that dielectric permittivity measured at lower frequency is always greater than higher frequency. With the increasing frequency, dielectric constant decreases very fast up to 10^5 Hz and in frequency range from 10^6 to 10^7 Hz it is almost constant. The higher value of dielectric constant of 1700 may possibly also strongly depend on the density of the sample due to the sintering process of BaTiO_3 .

The dielectric loss represents a combined result of electrical conduction and orientational polarization of the matter. Figure 2b shows the variation of dielectric loss tangent δ ($\tan\delta$) with frequency for BT_0. The investigated material shows a normal dielectric behaviour. Dielectric loss tangent decreases with increasing frequency of the alternating field, and the maximum value of 0.5 was obtained at low frequencies. The permittivity loss curve at 30 °C shows two relaxation peaks which occurs when the frequency jumping of electrons $\text{Ti}^{4+} \leftrightarrow \text{Ti}^{3+}$ is equal to the frequency of the applied AC field [9]. Moreover, the values of $\tan\delta$ decrease at higher frequency in the range 0.007–0.001. Therefore, the energy losses were due to conductivity and dipole relaxation. The loss factor $\tan\delta$ of a dielectric material is a useful indicator of the energy loss as heat.

The first stage of actuator fabrication is frequently characterised by the problem of metal layer deposition on barium titanate ceramics. In order to ensure the most suitable adhesion of layers, pellets were polished using abrasive paper 320, which also enabled the production of the expected pellet thickness of 0.71 mm and diameter of 9.66 mm.

Two commercial products (Technicqll, Chester Molecular Metal Super) developed for metallic layer deposition were applied. Technicqll is a silver-based product, which allows the creation of adhesive layers that conduct an electric current, and is characterised by a low resistance equal to 0.01Ω . The second product—Chester Metal Super—is a two-element tixotropic epoxy-metallic composite. Both commercial products were utilised during trials of metallic layer deposition on BT_0 pellets. The treated samples are hereafter denoted as BT_0_S for Technicqll and BT_0_M for Chester Molecular Metal Super treatments.

Analysis of the top-most metallic layers deposited on the barium titanate pellets revealed their high quality at the macroscopic scale. However, in order to verify whether the bonding layers adhered well to the ceramic pellets, SEM images of fracture surfaces for BT_0_S (Fig. 3a, b) and BT_0_M (Fig. 3c, d) were obtained.

Considered fracture surfaces of BT_0_S and BT_0_M samples with indicated three areas under observation are presented in Fig. 4. In both samples, areas number 1 and 3 are placed on barium titanate ceramic and area number 2 is situated on bonding layers.

Results of weight % of chemical elements presented in these three indicated areas for BT_0_S and BT_0_M samples, were determined. As one can expected, on areas number 1 and 3, Ba and Ti elements are presented and the weight percent of these elements is very similar in all area, $56.9\% \pm 0.4$ and $23.5\% \pm 0.1$

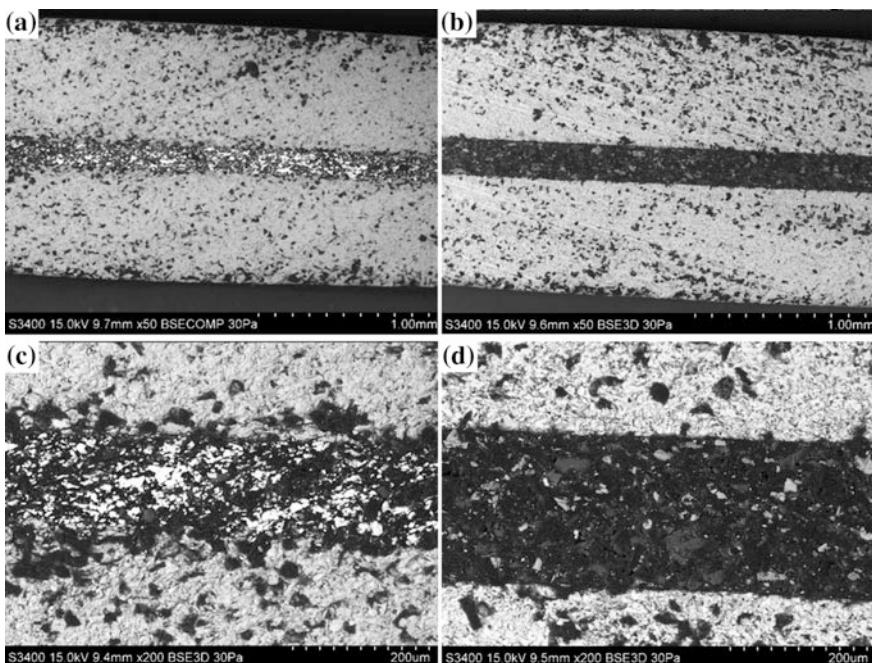


Fig. 3 SEM images of (a, b) BT_0_S and (c, d) BT_0_M fracture surfaces at two different magnifications: (a, c) $\times 50$ and (b, d) $\times 200$

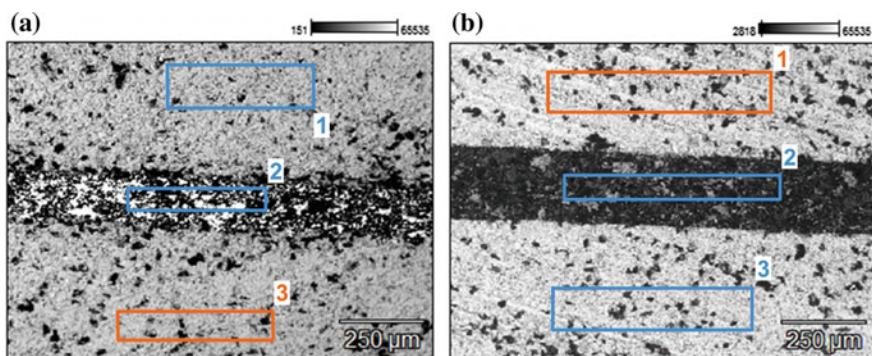


Fig. 4 SEM microstructure of fracture surface of BT_0_S (a) and BT_0_M (b) samples with identified three considered areas

respectively for Ba and Ti. In the case of BT_0_S sample, the metallic layer is mainly composed from silver (66.4%), which is also according to expectation. A small amount of Si (3.3%) in bonded layer comes probably from the applied product composition. The chemical composition of Chester Molecular Metal Super

Fig. 5 Photo of the actuator manufactured from barium titanate ceramic and three metallic layers



was not presented on the product datasheet but from obtained results follow that this product is composed from Fe (10.7%), Cr (25.4%), Ti (12.8%) and Si (22.3%). It should be underlined that at both metallic layers Ti element is present but it is not sure whether its appearance is connected with local migration from ceramic layers to bonding one.

The first short actuator presented in Fig. 5, was made from a piece of BT_0 beams with cutting three gaps by saw. Finally, these gaps are filled in using Technicql product to obtain metal layers.

3 Conclusions

The investigated material shows a normal dielectric behaviour. Dielectric loss tangent decreases with increasing frequency of the alternating field, and the maximum value of 0.5 was obtained at low frequencies. What is interesting, the sintering temperature did not increase considerably the size of grains. The obtained in this approach the sinter microstructure, is very similar to this presented in literature by other authors. In order to receive better result of the barium titanate dielectric constant, the microstructure of sinter must be improved in the direction of the smaller grains getting.

The SEM images of both BT_0_S and BT_0_M samples reveal high quality ceramic-metallic-ceramic bonding, with very good adhesion properties and without any fractures. In the case of BT_0_S, additional intermediate layers between the barium titanate and metallic material were created. These thin layers should ensure better adhesion of appropriate materials. Therefore, Technicql was selected for use in further investigations.

Acknowledgements. The research leading to these results has received funding from the People Programme (Marie Curie Actions) of the European Union's Seventh Framework Programme FP7/2007-2013/under REA grant agreement No. PITN-GA-2013-606878.

References

1. Zhao, Z., Buscaglia, V., Viviani, M., Buscaglia, M.T., Mitoseriu, L., Testino, A., Nygren, M., Johnsson, M., Nanni, P.: Grain-size effects on the ferroelectric behavior of dense nanocrystalline BaTiO₃ ceramics. *Phys. Rev. B.* **70**, 024107 (2004)
2. Hu, J., Shen, Z.: Intragrannular heterojunctions formed by ordered coalescence of strontium and barium titanate nanocrystals. *Scr. Mater.* **107**, 14–17 (2015)
3. Cai, W., Fu, C., Lin, Z., Deng, X.: Vanadium doping effects on microstructure and dielectric properties of barium titanate ceramics. *Ceram. Int.* **37**, 3643–3650 (2011)
4. Yu, P., Wang, X., Cui, B.: Preparation and characterization of BaTiO₃ powders and ceramics by the Sol-Gel process using organic monoacid as surfactant. *Scr. Mater.* **57**, 623–626 (2007)
5. Kao, C.F., Yang, W.D.: Preparation of barium strontium titanate powder from citrate precursor. *Appl. Organomet. Chem.* **13**, 383–397 (1999)
6. Chen, J.F., Shen, Z.G., Liu, F.T., Liu, X.L., Yun, J.: Preparation and properties of barium titanate nanopowder by conventional and high-gravity reactive precipitation methods. *Scr. Mater.* **49**, 509–514 (2003)
7. Park, J.H., Yoo, D.H., Kim, C.S., Yang, H.S., Moon, B.K., Jung, G.J., Jeong, E.D., Hong, K.S.: Synthesis, structure and dielectric properties of BaTiO₃ nanoparticles. *J. Korean Phys. Soc.* **49**, S680–S683 (2006)
8. Koops, C.G.: On the dispersion of resistivity and dielectric constant of some semiconductors at audiofrequencies. *Phys. Rev.* **83**, 121–124 (1951)
9. Batoo, K.M., Kumar, S., Lee, C.G., Alimuddin.: Influence of Al doping on electrical properties of Ni–Cd nano ferrites. *Curr. Appl. Phys.* **9**, 826–832 (2009)

Modeling of the Waterflooding Process in the Presence of Discontinuities in the Oil Reservoirs

Vladimir Astafev, Elena Andriyanova and Andrey Kasatkin

Abstract The knowledge of the nature of flooding allows us to optimize the system of oilfield development. The study of the filtration process in reservoirs with discontinuities, such as highly permeable cracks or impermeable barriers, has a great importance for the oilfield development. The steady-state flow process of incompressible fluid to the production well in a reservoir of constant height and permeability is considered. There is a thin area in the reservoir, which might be a highly permeable crack or impermeable barrier. The production and injection wells are placed inside the reservoir's external boundary. The characteristics of flooding process are studied for different locations of the discontinuity and a pair of wells. The flow lines of the fluid flow will be analyzed for every considered case.

Keywords Hydrodynamic model of waterflooding · Highly permeable cracks · Impermeable barriers

1 Introduction

As we know, the main part of fluid flow occurs through the more permeable zones, therefore any deviation in the reservoir homogeneity acts on the production [1]. A characteristic feature of the development process of such reservoirs has the deviation in the dependence well productivity and rock permeability, significant dependence of IPR curves (Inflow Performance Relationship) on the pressure, etc.

Oil filtration modelling in reservoirs with cracks is also interesting from the point of view of application for hydraulic fracturing. Hydraulic fracturing is currently one of the most effective methods to increase oil production [2], especially for tight sands and shale gas. Therefore these days it is especially important to study the

V. Astafev (✉) · E. Andriyanova · A. Kasatkin
Oil Field Development Department, Samara State Technical University,
Molodogvardeiskaya Str., 244, 443100 Samara, Russian Federation
e-mail: vladimir.astafev@mail.ru

filtration process in the reservoirs with tectonic faults, hydraulic fractures (HF) and impermeable boundaries.

The previous our papers [3–6] have discussed the fluid flow to the single production well in the reservoir with cracks of different permeability, and the skin effect equations were defined for every case. These articles show the impact of such inclusions in the reservoir on the waterflooding process. The problem is about the fact, that in some cases injected water appears in producing well too fast, so we need understand the mechanism of fluid flow and nature of water breakthrough time.

So, in this work modelling of the fluid flow process from an injection well to a production well in the presence of crack (discontinuity) with different permeability will be discussed, the impact of such discontinuities on the nature of the fluid flow process will be studied. The task is modified by the representation of crack in the section view of zero thickness but finite conductivity and by the difference of pressure above and below the section.

2 Problem Formulation

Let us consider a plane stationary flow of incompressible fluid to the vertical production well in an isotropic porous medium. This process in the plane (x, y) is described by the equation of incompressibility and the Darcy's law of filtration [1]:

$$\operatorname{div} \vec{V}(x, y) = 0, \vec{V} = -(k/\mu) \operatorname{grad} p, \quad (1)$$

where $V(x, y)$ is the velocity vector of fluid filtration, $p(x, y)$ is the pressure in the liquid, μ is the fluid viscosity and k is the reservoir permeability by the thickness h .

In early works of other authors the highly permeable area is usually represented by ellipse [7, 8]. In our works [3–6, 9] the discontinuity in the section view of zero thickness but finite conductivity.

Let us consider, that in the reservoir at the point $M_1(x_1, y_1)$ is placed the production well with a flow rate Q_1 and at the point $M_2(x_2, y_2)$ is placed the injection well with a flow rate Q_2 . Inside the external boundary there is a crack with length $2l$ and thickness 2δ ($\delta \ll l$) and permeability k_f . Let us consider that the crack is oriented along the axis x , and its center coincides with the origin plane (x, y) .

Then, as described in work [9], the flow potential, can be represented in the form:

$$\Phi(z) = q^{-1} \varphi(z) = \ln(z - z_0) + \sum_{n=0}^{\infty} c_n z^{-n}. \quad (2)$$

where $q = \mu Q/(2\pi kh)$ is the modified flow rate, and c_n are the unknown coefficients.

In the symmetrical case [9], when the well is located on the crack line, the fracture conductivity parameter $Fcd = \delta k_f/lk$ has been introduced and the flow potential has been written in the following form:

$$\Phi(v) = \ln(v, v_0) + \sum_{n=0}^{\infty} \frac{1}{n} \left[\frac{n \cdot F_{cd} - 1}{n \cdot F_{cd} + 1} (v\bar{v}_0)^{-n} \right] + C_0. \quad (3)$$

But if we consider nonsymmetrical case, when the well is located on the some distance from the discontinuity, or we have a couple of injection and production wells, we need to evaluate the inflow and the outflow from the crack. Thus we need to take into account the pressure difference above and below the section, and we use more complicated boundary conditions [5, 6]:

$$\begin{cases} \alpha_0 \sqrt{1 - \xi^2} \frac{d}{d\xi} \operatorname{Re}(\Phi^+ + \Phi^-) = \operatorname{Im}(\Phi^+ - \Phi^-), \\ \beta_0 \sqrt{1 - \xi^2} \frac{d}{d\xi} \operatorname{Im}(\Phi^+ + \Phi^-) = -\operatorname{Re}(\Phi^+ - \Phi^-); \end{cases} \quad (4)$$

where $-1 < \xi = x/l < 1$, $\Phi^+(\xi)$ and $\Phi^-(\xi)$ are the flow potentials above and below the section, coefficient $\alpha_0 = \delta k_f/lk$ is similar to Fcd for the hydraulic fractures and $\beta_0 = \delta k/lk_f$ is very important for the impermeable case.

3 Problem Solution

Now let us consider the case when we have a pair of wells. Flow potential can be expressed by this equation:

$$\varphi(z) = q_1 \ln(z - z_1) + q_2 \ln(z - z_2) + \sum_{n=0}^{\infty} c_n z^{-n}. \quad (5)$$

Further, we consider the case when $q_1 = 1$ and $q_2 = -1$ or the case of injection and production wells with equal injectivity and productivity. The solution the boundary-value problem (4) allows us to express the flow potential in the following form:

$$\varphi(v) = \ln \frac{(v, v_1)}{(v, v_2)} + \sum_{n=1}^{\infty} \left[\frac{n \cdot \alpha_0 - 1}{n \cdot \alpha_0 + 1} \left(\frac{\cos n\theta_1}{n\rho_1^n} - \frac{\cos n\theta_2}{n\rho_2^n} \right) - i \frac{n \cdot \beta_0 - 1}{n \cdot \beta_0 + 1} \left(\frac{\sin n\theta_1}{n\rho_1^n} - \frac{\sin n\theta_2}{n\rho_2^n} \right) \right] v^{-n} + C_0. \quad (6)$$

where $z = l(v + v^{-1})/2$, $v_1 = \rho_1 \cdot e^{i\theta_1}$, $v_2 = \rho_2 \cdot e^{i\theta_2}$.

For the case, when $\alpha_0 = \infty$ and $\beta_0 = 0$, the flow potential can be expressed as follows:

$$\varphi(v) = \ln \frac{(v, v_1)}{(v, v_2)} - \sum_{n=1}^{\infty} \frac{1}{n} ((v\bar{v}_1)^{-n} - (v\bar{v}_2)^{-n}) = \ln \frac{(v, v_1)}{(v, v_2)} \frac{\left(1 - \frac{1}{v\bar{v}_2}\right)}{\left(1 - \frac{1}{v\bar{v}_1}\right)}. \quad (7)$$

For the case, when $\alpha_0 = 0$ and $\beta_0 = \infty$, the flow potential can be expressed as follows:

$$\varphi(v) = \ln \frac{(v, v_1)}{(v, v_2)} - \sum_{n=1}^{\infty} \frac{1}{n} ((v\bar{v}_1)^{-n} - (v\bar{v}_2)^{-n}) = \ln \frac{(v, v_1)}{(v, v_2)} \frac{\left(1 - \frac{1}{v\bar{v}_1}\right)}{\left(1 - \frac{1}{v\bar{v}_2}\right)}. \quad (8)$$

Flow lines for this kind of potentials are shown on the Figs. 1 and 3 (left—for the case $\alpha_0 = \infty$ and $\beta_0 = 0$; right – for the case $\alpha_0 = 0$ and $\beta_0 = \infty$).

On the Figs. 2 and 4 we can see the water tracer lines along the flow lines. These results have been obtained by the use of method of calculations, published in [10]. Different colors in this pictures, shows the boundaries between the flooding stages, so we can predict the water front at any moment, and water breakthrough time.

As we can see, the obtained flow potential equation allows us to solve the problem for any wells and discontinuity location and for different fracture conductivity.

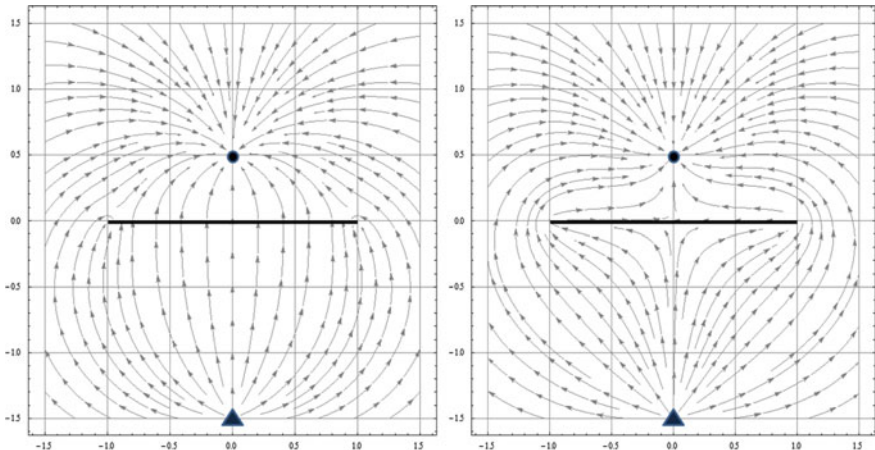


Fig. 1 Streamlines of the fluid, the injection well located at the point $(0, -1.5)$, the production well—at the point $(0, 0.5)$, for the values of $\alpha_0 = \infty$; $\beta_0 = 0$ (left) and $\alpha_0 = 0$; $\beta_0 = \infty$ (right)

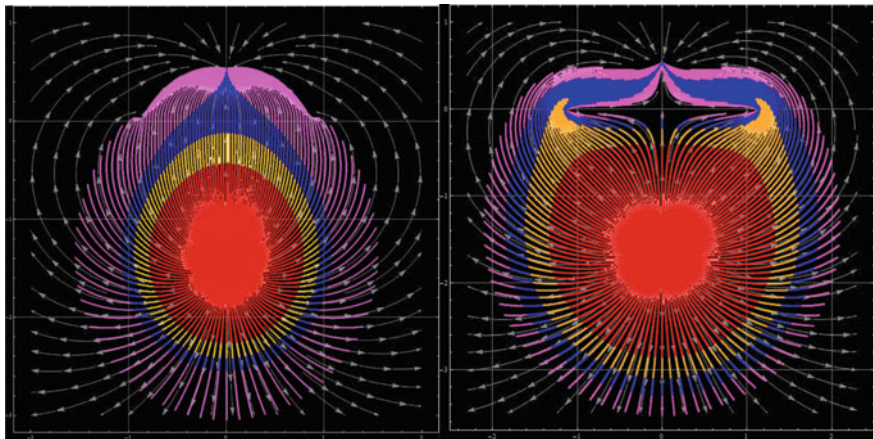


Fig. 2 Streamlines waterflooding process with tracer lines, the injection well located at the point $(0, -1.5)$, the production well—at the point $(0, 0.5)$, for the values of $\alpha_0 = \infty; \beta_0 = 0$ (*left*) and $\alpha_0 = 0; \beta_0 = \infty$ (*right*)

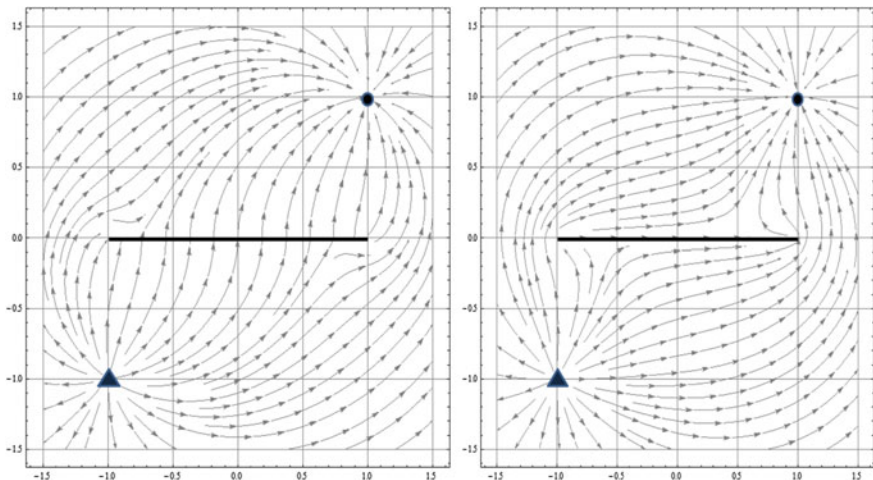


Fig. 3 Streamlines of the fluid, the injection well located at the point $(-1, -1)$, the production well—at the point $(1, 1)$, for the values of $\alpha_0 = \infty; \beta_0 = 0$ (*left*) and $\alpha_0 = 0; \beta_0 = \infty$ (*right*)

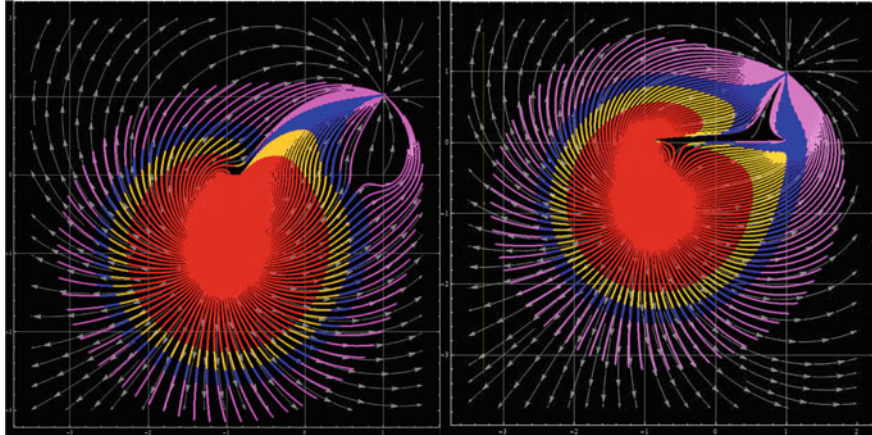


Fig. 4 Streamlines waterflooding process with tracer lines, the injection well located at the point $(-1, -1)$, the production well—at the point $(1, 1)$, for the values of $\alpha_0 = \infty$; $\beta_0 = 0$ (left) and $\alpha_0 = 0$; $\beta_0 = \infty$ (right)

4 Conclusions

In this work the formulation and solution of the problem of waterflooding process at the presence of a crack of different permeability has been done. The solution has been obtained under consideration the discontinuity like the crack zero thickness but finite conductivity. More general boundary conditions were considered taking into account the pressure difference above and below the section. This solution is suitable for any cases of various wells and discontinuity places and for different values of fracture permeability.

In the final part of the paper the nature of fluid flow was analyzed. The tracer lines for waterflooding process were calculated. As the result, we can predict the water front at any time of the process and define the water breakthrough time.

As we can see, the problem has enough interest from the petroleum engineers. Further development of the solutions is to present the flow potential through singular integral equations, which will greatly expand the applications.

Acknowledgements This work is performed on the grant of the Russian Science Foundation (Project № 15-17-00019).

References

1. Muskat, M.: The Flow of Homogeneous Fluids Through Porous Media. J. W. Edwards, Inc., Ann Arbor, Michigan (1946)
2. Economides, M., Oligney, R., Valko, P.: Unified Fracture Design. Bridging the Gap Between Theory and Practice. Alvin, TX, Orsa Press (2002)
3. Astafiev, V.I., Andriyanova, E.V.: Modeling of the Fluid Flow to the Production Well in the Presence of Discontinuities in the Reservoir. In: 11th International Conference on Fluid Mechanics, Budapest, Hungary, pp. 65–68 (2015)
4. Astafiev, V.I., Andriyanova, E.V.: Influence of reservoir's discontinuities on the process of oil filtration to the production Well. In: Fourth International Geoscience Conference, Deep Subsoil and Science Horizons, Tyumen, Russia, pp. 52–56 (2015). DOI:[10.3997/2214-4609.2014203420152015](https://doi.org/10.3997/2214-4609.2014203420152015)
5. Astafiev, V.I., Andriyanova, E.V.: The influence of the reservoir discontinuities on fluid filtration to the production well. WSEAS Trans. Fluid Mech. **11**(2), 10–17 (2016)
6. Andriyanova, E.V.: The influence of discontinuities in the reservoir on well productivity. In: 78th EAGE Conference and Exhibition 2016—Student Programme, Vienna, Austria, (2016). DOI:[10.3997/2214-4609.201601621](https://doi.org/10.3997/2214-4609.201601621)
7. Prats, M.: Effect of vertical fractures on reservoir behaviour—incompressible fluid case. SPE J. 103–118 (1961)
8. Kanevskaya, R.D.: Mathematical Modeling of the Development of Oil and Gas using Hydraulic Fracturing. Nedra Publishing, Moscow (1999) (in Russian)
9. Astafiev, V.I., Fedorchenko, G.D.: Simulation of fluid flow in the presence of a crack fracture. Vestnik of SamSTU, Ser. Phys. Math. Sci. **2**, 128–132 (2007) (in Russian)
10. Astafiev, V.I., Kasatkin, A.E.: Modeling and Numerical Calculation of Piston-like Oil Displacement for Doubly-periodic Systems of Oil Fields Development. In: VI International Conference on Coupled Problems in Science and Engineering, Venice, Italy, 734–743 (2015)

Terahertz Spectroscopy Applications in Medicament Analysis

Kateřina Sulovská

Abstract Terahertz spectroscopy came to the attention of the broader scientific community in the 90s of the 20th century with the development of science and technology in particular, enabling to work in terahertz spectral region. Terahertz spectroscopy has a wide possibilities of applications beginning in classical spectroscopy of gun powders, plastics, explosives, liquids, through terahertz imaging of medicaments, tissues, materials or layers, to remote observation/identification of hidden objects mainly for security purposes. The aim of this paper is to introduce possible applications in analysis of pharmaceuticals with different amount of active ingredient content. According to the results, the classical terahertz spectroscopy is not as suitable as other spectroscopic methods targeted on analyzing content of pharmaceuticals showing persistent inconveniences of this spectroscopy. All measurements were done using the TPS Spectra 3000 instrument.

Keywords Attenuated total reflection (ATR) terahertz time-domain spectroscopy • Terahertz imaging • Transmittance • Absorbance • Pharmaceutical analysis • Euthyrox

1 Introduction

Terahertz (THz) spectroscopy came to the attention of the broader scientific community in the 90s of the 20th century with the development of science and technology in particular, enabling to work in terahertz spectral region. Terahertz spectroscopy has a wide possibilities of applications beginning in classical spectroscopy of gun powders, plastics, explosives, liquids, through terahertz imaging of medicaments, tissues, materials or layers (including searching for cracks, air

K. Sulovská (✉)

Faculty of Applied Informatics, Department of Electronics and Measurement,
Tomas Bata University in Zlín, Nám. T. G. Masaryka 5555, 760 01 Zlín,
Czech Republic
e-mail: sulovska@fai.utb.cz

pockets, etc.), to remote observation/identification of hidden objects mainly for security purposes (see Fig. 1). Therefore, the area for potential employment of the THz spectroscopy is very wide [1–9].

The drug control is a pharmaceutical discipline theoretically and practically aimed at ensuring the quality, safety and drug efficacy, together with identification and quantity analysis of the medicament, with emphasis on detection of active ingredients, accompanying impurities and the stability of drugs. The chemical structure of the drug is the starting point for drug control and determination of appropriate procedure for analyses. The identification of pharmaceuticals can be made on ground of physical constants (melting point, distillation range, refractive index, optical rotation or density) with utilization of physico-chemical methods (spectral, separation and electrochemical), chemical reaction, etc.

This paper is dealing with a spectral method, which can in future serve as a useful tool to obtain sufficient information for handling and manufacturing drugs—the THz spectroscopy. One of the commonly used methods for examination of pharmaceuticals in terahertz spectral region is attenuated total reflection (ATR) THz time-domain spectroscopy [10, 11]. This method is very suitable for samples that can be measured in a whole, e.g. tablets, plastics. Together with THz imaging, one can get an information about the content behavior in the sample, i.e. wetting, stability, and decomposition of content [12, 13]. Such information may be crucial for further processes in not only developing the medicament but also for mechanisms, kinetics and potential effects on pre-clinical and clinical procedures. THz spectroscopy may be a good tool for these trials, as it stand between microwave and infrared spectral region gap and therefore can support other spectroscopic techniques.

The aim of this paper is therefore to demonstrate the possibility of detecting specific vibrations and rotations of medicament content by the THz spectroscopy with respect to the amount of active ingredient, and to evaluate the possibility of these technique as a stand-alone method.

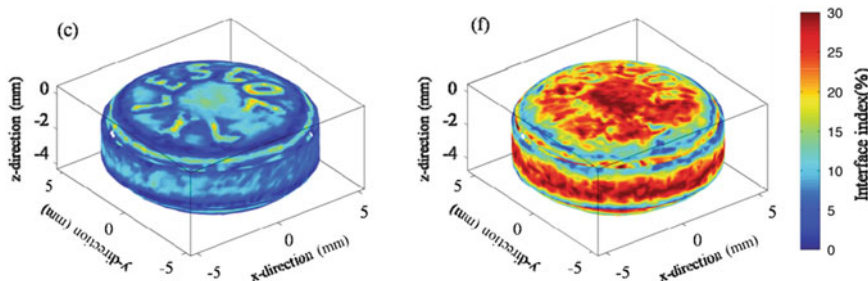
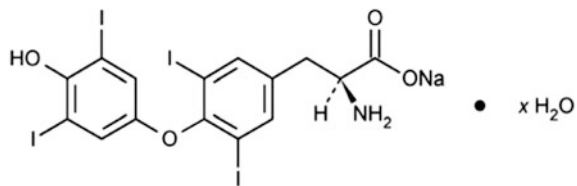


Fig. 1 Examples of practical applications of THz spectroscopy—THz imaging of pharmaceuticals [14]

Fig. 2 Levothyroxinum naticum (also known as levothyroxine sodium) [15]



2 Materials and Methods

As a testing medicament used in this paper was selected the Euthyrox tablets by Merck with 75, 88 or 100 µg of levothyroxinum naticum. These pills are used for patients with thyroid issues or as a prophylaxis as they supplement the thyroid hormone (Fig. 2).

Tablets were measured whole as manufactured using the ATR module of the TPS Spectra 3000 spectrometer, which measures spectra by direct contact of sample with the module inserted on the workplace of the device. Each measurement were done ten times, for three tablets of same dosage to obtain as accurate data as possible.

All experiments were done on the TPSTM Spectra 3000 by TeraView Ltd., using the ATR module with contact angle 35°. The measured data of prepared samples are processed via device software. The spectrometer was operating with resolution of 1.2 cm⁻¹ (32 GHz), scanning frequency of 1800 scans per second with 30 scans in each point. The instrument was operating in vacuum to lower the amount of atmospheric water vapours spectra. As a reference, a module without sample was chosen. Thickness of each sample was measured at ten different spots and averaged for proper spectra calculations in TeraView spectrometer's software and to get representative values of material for a total overview of selected behaviour in THz frequency. The measurements were done in ambient laboratory conditions. The frequency range of the experiment was set from 0 THz to 3 THz.

3 Results and Discussion

The whole experiment was focused on changes in behavior in THz spectral region of Euthyrox tablets with different content of active ingredients. As can be seen from following figure, some characteristic peaks are found throughout whole spectra between 0.5 and 2.1 THz for absorbance measurements. Aside this region, small changes in spectra occurs. All behaviors are in agreement with basic absorbance predicaments, supported by data obtained for the transmittance.

The main issue during assigning specific spectral peaks to rotation/vibration positions of known molecules in pharmaceuticals is the fact, that these medicaments always contain not only vibrations/rotations of smaller molecules, but also states of

more complex molecules, their structure, and their amount in the whole medicament resulting in intermolecular bonds overlaying monitored molecules (Fig. 3).

An example of this statement and presence of very similar compounds is the vibration of aromatic rings, which are present in majority of drugs, and can be found at 1.75 THz. The methyl torsion group vibration can be found in the spectral region of 0–0.2 THz and is connected with the compounds of the Euthyrox tablets. The peak at 1.15 THz belong to bond with hydrogen, while peaks between 1.45 and 1.55 THz belong to O–H vibrations, which are also contained in the Euthyrox tablets, and are probably caused by the lattice vibrations. A very small peak around 1.75 THz belonging to N–H vibration occurs, together with the C–C vibration small peak around 1.9 THz. Therefore, the behaviors in region from 1 to 2 THz are the most important ones for characterization of tablets, as the region beneath 2.5 THz may contain noise and interference, even when the vacuum was used for the measurements. Nevertheless, the region behind 2 THz contain peaks of CH₃ transition between torsional levels, nitrogen bonds, O–H vibrations and vibrations like NH₂ belonging not only to active ingredient of the medicament, but there can be also traits of compounds forming the filling.

Figure 4 depicts the information about average refractive indices of examined medicaments. As is visible from the plot, the behavior for all three samples is identical, with small changes in spectra at the beginning of observed spectral range at 0–0.3 THz, which can be caused by differences in amount of filling and active ingredient and also with noise produced by small vibrations in lattice. Such information can be a satisfactory one in case of drug identification.

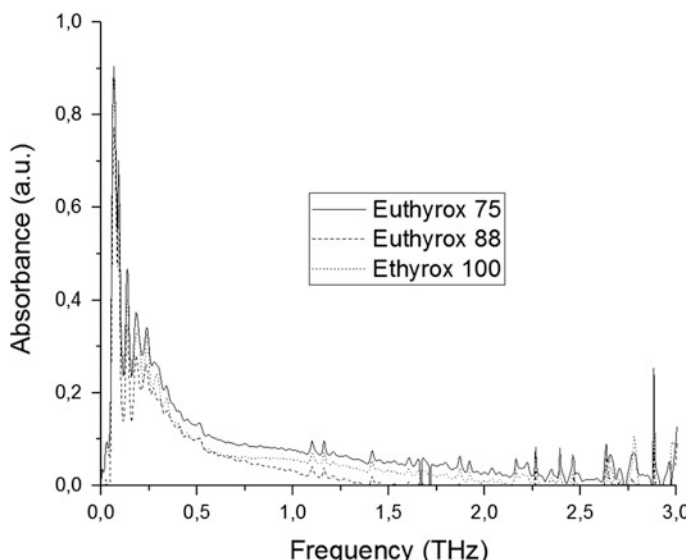


Fig. 3 Plot for averaged absorbance of particular medicaments

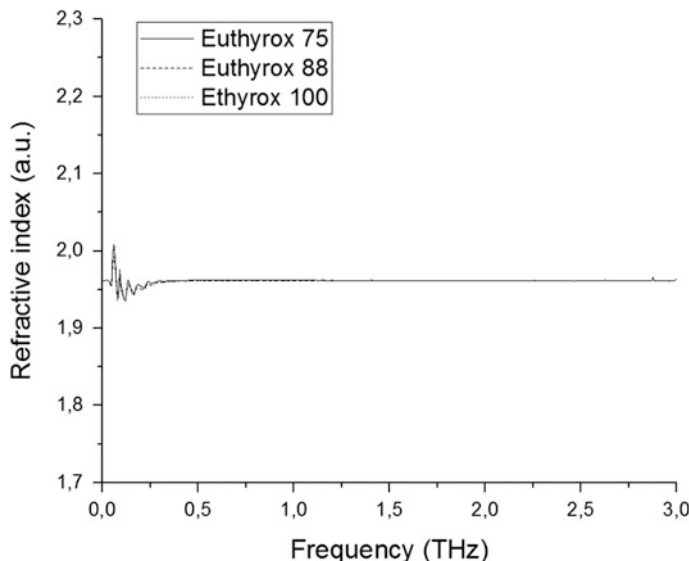


Fig. 4 Averaged refractive indices for Euthyrox tablets

4 Conclusion

This paper presents experiment focused on the solid pills with different amount of active ingredient (and also slightly different amount of fillings). Terahertz spectroscopy is said to be a potential method for distinguishing between various pharmaceuticals or compounds in different ratios, or for their identification during pharmaceutics study. The challenging issue of studying basic steps for identification and analysis of drugs is presented. Results of our experiments showed that this method has a potential for such analyses, but a more effective and accurate techniques/procedures must be found; currently the method remains only a supportive and highly experimental one. The main issue is to discover proper peak positions belonging to chosen active ingredient without any doubt as the terahertz spectroscopy may provide misleading data due to intermolecular vibrations of other compounds in medicament, and to study spectral changes over time. Therefore, further and discerning research in this sphere is necessary.

Acknowledgements This work was supported by the Ministry of Education, Youth and Sports of the Czech Republic within the National Sustainability Programme project No. LO1303 (MSMT-7778/2014) and the European Regional Development Fund under the project CEBIA-Tech (CZ.1.05/2.1.00/03.0089). The authors declare no competing financial interests.

References

1. Shen, Y.C., Taday, P.F., Newnham, D.A., Pepper, M.: Chemical mapping using reflection terahertz pulsed imaging. *Semicond. Sci. Technol.* **20**, S254–S257 (2005)
2. Soltani, A., Jahn, D., Duschek, L., Castro-Camus, E., Koch, M., Withayachumnankul, W.: Attenuated total reflection terahertz time-domain spectroscopy: uncertainty analysis and reduction scheme. *IEEE Trans. Terahertz Sci. Technol.* **6**, 1–8 (2015)
3. Banerjee, D., von Spiegel, W., Thomson, M.D., Schabel, S., Roskos, H.G.: Diagnosing water content in paper by terahertz radiation. *Opt. Express* **16**, 9060–9066 (2008)
4. Watanabe, Y., Kawase, K., Ikari, T., Ito, H., Ishikawa, Y., Minamide, H.: Component spatial pattern analysis of chemicals using terahertz spectroscopic imaging. *Appl. Phys. Lett.* **83**, 800–802 (2003)
5. Ajito, K., Ueno, Y., Song, H.-J.: Visualization of pharmaceutical drug molecules by Terahertz chemical imaging. *NTT Tech. Rev.* **10** (2012)
6. Giles, J.P., Raitt, B.J., Joseph, C.S., Hines, M.E., Giles, R.H.: Investigating the effects of terahertz radiation on *Bacillus subtilis*. In: Tuchin V.V., Duncan D.D., Larin K.V., Leahy M. J., Wang R.K. (eds.) *Proceedings SPIE 8222; Dynamics and Fluctuations in Biomedical Photonics IX*. p. 9. SPIE (2012)
7. Sun, Y., Fischer, M.B., MacPherson, E.P.: Effects of formalin fixing on the THz properties of biological tissues. *J. Biol. Opt.* **14**(6), 6401–6417 (2009)
8. Globus, T., Bykhovskaia, M., Woolard, D., Gelmont, B.: Sub-millimetre wave absorption spectra of artificial RNA molecules. *J. Phys. D Appl. Phys.* **36**, 1314–1322 (2003)
9. Jin, Y., Kim, G., Jeon, S.: Terahertz dielectric properties of polymers. *J. Korean Phys. Soc.* **49**, 513–517 (2006)
10. Suhandy, D., Suzuki, T., Ogawa, Y., Kondo, N., Ishihara, T., Takemoto, Y.: A quantitative study for determination of sugar concentration using attenuated total reflectance terahertz (ATR-THz) spectroscopy. *Proceedings SPIE*. 8027, 802705–802705-6 (2011)
11. Takebe, G., Kawada, Y., Akiyama, K., Takahashi, H., Takamoto, H., Hiramatsu, M.: Evaluation of drug crystallinity in aqueous suspension using terahertz time-domain attenuated total reflection spectroscopy. *J. Pharm. Sci.* **102**, 4065–4071 (2013)
12. Liu, G.F., Ma, S.H., Ji, T., Zhao, H.W., Wang, W.F.: Differentiation of illicit drugs with THz time-domain spectroscopy. *Nucl. Sci. Tech.* **21**, 209–213 (2010)
13. Williams, M.R.C., Aschaffenburg, D.J., Ofori-Okai, B.K., Schmuttenmaer, C.A.: Intermolecular vibrations in hydrophobic amino acid crystals: experiments and calculations. *J. Phys. Chem. B* **117**, 10444–10461 (2013)
14. Zhang, Q., Gladden, L.F., Avalle, P., Axel Zeitler, J., Mantle, M.D.: Terahertz pulsed imaging and magnetic resonance imaging as tools to probe formulation stability. *Pharmaceutics* **5**, 591–608 (2013)
15. Pharmacopeia, U.S.: Levothyroxine sodium. http://www.pharmacopeia.cn/v29240/usp29nf24s0_m45000.html. Accessed 09 July 2016

Stability of Capillary Waves of Finite Amplitude

Alexander Petrov, Mariana Lopushanski and Vladimir Vanovskiy

Abstract The direct Lyapunov method is used to prove the stability of the exact Crapper solution for capillary waves. The dynamic equations of the capillary wave are presented in the form of an infinite Euler-Lagrange chain of equations for the Stokes coefficients. The stationary solution found for these equations is the Crapper solution for capillary waves. With the help of energy and momentum conservation laws the Lyapunov function is constructed. It is shown that the Lyapunov function is positive definite with respect to any perturbations of waves surfaces, for waves with the period multiple of wavelength.

Keywords Direct Lyapunov method · Capillary waves · Lyapunov function

1 Introduction

In [1] the exact solution of the problem of the potential plane-parallel flow of an ideal fluid in the domain $-\infty < x < \infty$, $-\infty < y < \eta(kx)$ was constructed, where the function $\eta(kx)$ is periodic $\eta(kx) = \eta(kx + 2\pi)$, the wave number k is related to the wave length as follows $\lambda = 2\pi/k$. The Laplace condition $p - p_0 + \sigma/r = 0$ is satisfied on the wave surface $\eta(kx)$, where r is the curvature radius of the cylinder, p

A. Petrov · M. Lopushanski (✉) · V. Vanovskiy
Moscow Institute of Physics and Technology, Institutskiy per. 9,
141700 Dolgoprudny, Russia
e-mail: masha.alexandra@gmail.com

A. Petrov
e-mail: petrovipmech@gmail.com

V. Vanovskiy
e-mail: vovici@gmail.com

A. Petrov · M. Lopushanski · V. Vanovskiy
Institute for Problems in Mechanics RAS, Pr. Vernadskogo 101-1,
119526 Moscow, Russia

and p_0 are the fluid pressure inside and outside the cylinder, σ is the surface tension coefficient.

The Crapper wave stability was studied in [2]. The infinite chain of linear differential equations for perturbations was obtained and the eigenvalues of these equations were studied. Such a solution requires an excessively large number of computations. The Lagrange method of generalized coordinates may be proposed as an alternative. An analogic method was used in [3] to study the stability of the McLeod plane-parallel flow [4], which models the motion of a drop with surface tension.

The direct Lyapunov method reduces the stability problem to the efficient potential energy minimum condition. The potential energy minimum condition is used to prove the stability of the stationary motion of capillary waves in the frames of the weakened Lyapunov stability definition [5].

In this work we present the analytic solution for the capillary waves stability problem (earlier numerical methods were used). We use the second variation of the Lyapunov function to prove the stability of capillary waves with respect to symmetric and non-symmetric disturbances.

2 Lyapunov Function

To describe the dynamics of capillary waves, we use the wave parametrization, introduced by Stokes [6, 7]. We seek the conformal mapping of the disc $|\zeta| < 1$ of the complex plane ζ with a cut on the positive part of abscissa on the domain of one wave period on the complex plane $z = x + iy$ in the following form

$$z(\zeta) = \frac{\lambda}{2\pi} \left[i \ln \zeta + \sum_{n=1}^{\infty} z_n \zeta^n \right] . \quad (1)$$

The circle $\zeta = e^{i\gamma}$ corresponds to the surface of the wave $z = x_s + i\eta$. We consider the real and imaginary parts of the Laurent series coefficients $z_n = x_n + iy_n$, $n = 1, 2, \dots$ to be the generalized coordinates of the wave q_i , $i = 1, 2, \dots$.

The kinetic energy of the wave is the quadratic function of generalized velocities \dot{x}_0 , \dot{q}_i , $i = 1, 2, \dots$, where x_0 is the cyclic coordinate that determines the horizontal movement of the wave, \dot{x}_0 —the wave propagation velocity.

The summands in the kinetic energy may be separated into three groups: quadratic in \dot{x}_0 , linear in \dot{x}_0 and independent of \dot{x}_0

$$E_{\text{kin}} = \frac{1}{2} M \dot{x}_0^2 + M_1 \dot{x}_0 + M_2 = \frac{(M \dot{x}_0 + M_1)^2}{2M} + M_* , \quad M_* = M_2 - \frac{M_1^2}{2M} . \quad (2)$$

Here M is independent of velocities, M_1 and M_2 are the linear and quadratic function of velocities \dot{q}_i . As E_{kin} is positively definite, then M_* is also a positively definite quadratic form of \dot{q}_i .

Suppose that the system of Lagrange equations has a stationary solution, for which

$$\dot{x}_0 = u, \quad \dot{q}_i = 0, \quad i = 1, 2, \dots .$$

In this solution the surface of the wave moves with velocity u , without changing its form.

For stationary motion $M_* = 0$ and, thus, the energy value is

$$\frac{(M_0 u^2)}{2} + E_{\text{pot}}^0 = E_0 ,$$

where E_{pot}^0 is the value of potential energy at a stationary point. The function E is a Lyapunov function if it is positively definite. As M_* is positively definite, we consider only the functional t

$$U = \frac{(M_0 u)^2}{2M} + E_{\text{pot}} ,$$

If the stationary point is the minimum of U , the Lyapunov Theorem implies that the stationary motion is stable.

Consider the system of coordinates in which the fluid is at rest at infinity. The kinetic energy of one period of the stationary wave in this system is expressed through the Stokes coefficients y_n as follows [8]

$$E_{\text{kin}} = \frac{1}{2} M \dot{x}_0^2, \quad M = \frac{\rho \lambda^2}{2\pi} \frac{S}{2}, \quad S = \sum_{n=1}^{\infty} n(x_n^2 + y_n^2) . \quad (3)$$

The capillary potential energy is proportional to the arc length l of one wave period

$$E_{\text{pot}} = \sigma l,$$

where σ is the surface tension coefficient. On the complex plane ζ the arc length is calculated as follows

$$l = \oint ds = \oint \left| \frac{dz}{d\zeta} \right| \frac{d\zeta}{i\zeta} , \quad (4)$$

where the integral of the differential of the arc length ds is taken along the circle $|\zeta| = 1$.

The Stokes coefficients are not very suitable for arc length calculation l . So, an analytical function, expressed through parameters q_i , is introduced and, using the Residue Theorem we obtain that the Lyapunov function can be expressed in the dimensionless form as follows

$$U = \sigma \frac{\lambda}{2\pi} \bar{U}, \quad \bar{U} = \frac{S_0^2}{4S} c^2 + \bar{l}, \quad \bar{l} = \frac{l}{\lambda} = 1 + \sum_{k=1}^{\infty} |q_k|^2 , \quad (5)$$

where \bar{U} and \bar{l} is a dimensionless Lyapunov function and the arc length of one wave period and c is the dimensionless wave velocity.

The assertion that the first variation of \bar{U} equals zero allows us to find the parameters q_n of the wave and its propagation velocity c .

3 Stationary Capillary Waves

The solution of the variational equation $\delta\bar{U} = 0$ may be presented as follows

$$q_i = 2b^i , \quad (6)$$

where b is a parameter of a family of solutions. To prove this we consider small disturbances of coordinates with respect to stationary values

$$q_n = 2b^n + \epsilon(\xi_n + i\eta_n), \quad n = 1, 2, \dots . \quad (7)$$

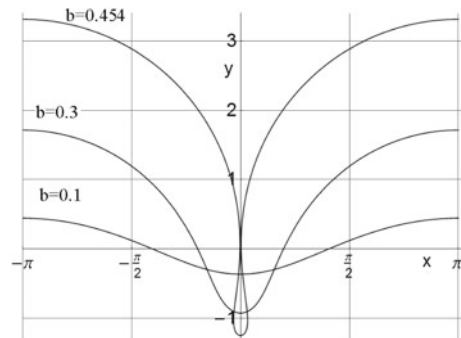
We substitute them into function \bar{l} (5) and expand by parameter ϵ . Then we will find the expansion for the Stokes coefficients x_n and y_n , for functional S and for function U :

$$\bar{l} = 1 + \sum_{k=1}^{\infty} ((2b^n + \epsilon\xi_n)^2 + \epsilon^2\eta_n^2) = 1 + \epsilon\delta\bar{l} + \epsilon^2\delta^2\bar{l} , \quad (8)$$

$$S = S_0 + \epsilon\delta S + \epsilon^2\delta^2 S , \quad \bar{U} = U_0 + \epsilon\delta U + \epsilon^2\delta^2 U ,$$

where δ and δ^2 denote the first and second variation accordingly. Then we calculate the first variation of U , considering (6). Then we obtain the same expressions for x and y as did Crapper. Therefore, a new deduction method for the known exact solution for the capillary wave [1] is presented. The values $b = b_0 = 0.454$, $a = 2.280$ corresponds to the maximum wave development. In Fig. 1 the graphs of waves with values $b := 0.1; 0.3$ and maximum wave development $b = 0.454$ are presented.

Fig. 1 Capillary waves at different values of parameter b



4 Second Variation

The second variation

$$\delta^2 \bar{U} = \frac{1}{2} \frac{d^2 \bar{U}}{d\epsilon^2} \Big|_{\epsilon=0}$$

is the quadratic form of variations $\xi_i, \eta_i, i = 1, 2, \dots$. It is expressed through the first and second variations of functionals S and \bar{l} . The variables ξ_n and η_n of the second variation $\delta^2 \bar{U}$ may be separated and the second variation $\delta^2 \bar{U}$ may be presented as the sum of two quadratic forms $\delta^2 \bar{U} = \delta^2 \bar{U}_1(\xi) + \delta^2 \bar{U}_2(\eta)$. The first $\delta^2 \bar{U}_1(\xi)$ depends only on ξ and is expressed through $\delta^2 S_1$ and $\delta^2 \bar{l}_1$, which depend only on ξ . The second is expressed through $\delta^2 S_2$ and $\delta^2 \bar{l}_2$, which depend only on η .

The first quadratic form defines the stability of the wave with respect to the symmetric disturbances ξ_n , the second one defines the stability with respect to the asymmetric disturbances η_n .

Let us first consider the quadratic forms of second variations for symmetric disturbances

$$\delta^2 \bar{U}_1 = \frac{c^2}{4} \left(\frac{(\delta S)^2}{S_0} - \delta^2 S_1 \right) + \delta^2 \bar{l}_1 .$$

For $\delta^2 U_1(\xi)$ the following inequality holds

$$\delta^2 \bar{U}_1 > \lambda_{\min} \sum_{n=1}^{\infty} (\xi_n)^2 , \quad (9)$$

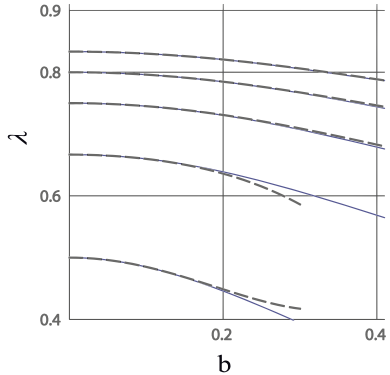
where λ_{\min} is the smallest eigenvalue of the quadratic form.

The matrix a_{mn} of the quadratic form $\delta^2 \bar{U}_1$ as $b = 0$ is diagonal and its diagonal elements are $a_{11} = 4$, $a_{nn} = (n-1)/n$, $n = 2, 3, \dots$. The eigenvalues that correspond to the adjoint linear operator are $\lambda_n = a_{nn}$. The smallest eigenvalue is equal to the second diagonal element $\lambda_{\min} = a_{22} = 1/2$. For eigenvalues the expansion in powers of b may be obtained. In Fig. 2 the dependences of the first five eigenvalues on b are presented. The solid lines stand for the results of numeric calculations, the dashed lines stand for the expansions in powers of b . From the graphs we see that the greater the index of the eigenvalue is, the better it is approximated by its expansion. In the second variation $N = 20$ independent variations $\delta q_i, i = 1, 2, \dots, 20$ are taken into consideration. The smallest eigenvalue $\lambda_1(b)$ decreases monotonously until it reaches the value $\lambda(b_0) = 0.03069$ and for $N > 15$ almost does not depend on N .

Thus, inequality (9) implies that the second variation $\delta^2 U > 0$ is strictly positive for all variations δq_i . By the Lyapunov Theorem the stationary motion of capillary wave is stable for all possible amplitude values.

The eigenvalues determine the main oscillation frequencies near stationary motion.

Fig. 2 Eigenvalues
(symmetric disturbances)



Consider now the quadratic form of the second variation for non-symmetric disturbances

$$dU_2 \delta^2 \bar{U}_2 = -\frac{c^2}{4} \delta^2 S_2 + \delta^2 \bar{l}_2 . \quad (10)$$

The matrix

$$b_{mn} = \frac{1}{2} \frac{\partial^2 (\delta^2 \bar{U}_2)}{\partial \eta_m \partial \eta_n}$$

for $b = 0$ is diagonal and $b_{nn} = (n - 1)/n$, $n = 2, 3, \dots$. The eigenvalues are $\lambda_n = b_{nn}$.

The matrix b_{mn} is singular, its determinant equals zero. This is due to the linear dependence of the generalized $\eta_1, \eta_2, \eta_3, \dots$, which is expressed as follows

$$r = \frac{1}{2} \sum_{k=1}^{\infty} k b^k \frac{\partial (\delta^2 U_2)}{\partial \eta_k} = 0 . \quad (11)$$

Equality (11) is equivalent to the fact that the linear combination of the matrix columns $b_{\cdot n}$ satisfies the equality

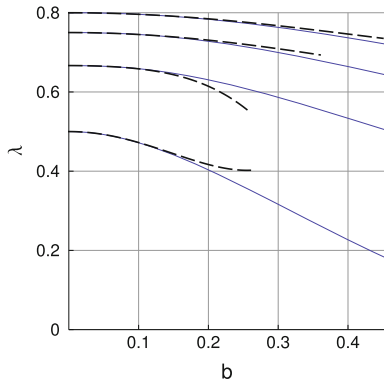
$$\sum_{k=1}^{\infty} k b^k b_{km} = 0$$

and, thus, the matrix (b_{mn}) is singular.

This can also be explained by the fact that the mapping (1) is multivalued. The mapping $\zeta' = e^{i\gamma_0}$ maps the circle $|\zeta| = 1$ into itself, therefore the form of the wave does not change. So, let us put the first coordinate η_1 equal to zero. Then all the other coordinates η_n , $n = 2, 3, \dots$ are independent.

Such choice of coordinates implies that the matrix (b_{mn}) as $b = 0$ is diagonal $b_{nn} = (n - 1)/n \delta_{nn}$, and the smallest eigenvalue equals the second diagonal element $\lambda_{\min} = b_{22} = 1/2$. For eigenvalues we may obtain expansion in powers of b . In Fig. 3

Fig. 3 Eigenvalues
(non-symmetric
disturbances)



the dependences of the first four eigenvalues on parameter b are presented. The solid lines stand for the numeric calculations, the dashed ones for the expansion in powers of b . The smallest eigenvalue $\lambda_1(b)$ monotonously decreases until $\lambda(b_0) = 0.181408$ and for the number of generalized coordinates $N > 15$ almost does not depend on N .

Acknowledgements The study has been supported by the Russian Science Foundation (project N 14-19-01633) in IPMech RAS.

References

1. Crapper, G.D.: An exact solution for progressive capillary waves of arbitrary amplitudes. *J. Fluid Mech.* **2**, 532–540 (1957)
2. Tiron, R., Choi, W.: Linear stability of finite-amplitude capillary waves on water of infinite depth. *J. Fluid Mech.* **696**, 402–422 (2012)
3. Petrov, A.G.: On the stability of a liquid cylinder in a plane-parallel flow of ideal fluid. *J. Appl. Math. Mech.* **3**, 366–374 (2016). [in Russian]
4. McLeod, E.B.: The explicit solution of a free boundary problem involving surface tension. *J. Ration. Mech. Anal.* **4**(4), 557–567 (1955)
5. Lyapunov, A.M.: On the stability of ellipsoidal equilibrium forms of a rotating fluid. Collected works, vol. 3, pp. 5–113. Izd. Akad. Nauk SSSR, Moscow (1959) [in Russian]
6. Sretenskii, L.N.: Theory of Wave Motion of Fluid. Nauka, Moscow (1977) [in Russian]
7. Petrov, A.G.: Analytical Hydrodynamics. Fizmatlit, Moscow (2009) [in Russian]
8. Maklakov, D.V., Petrov, A.G.: On stokes coefficients and wave resistance. *Dokl. RAN* **463**(2), 155–159 (2015)

High Temperature Behavior of Two Titanium Aluminides for Blade Engine Applications. Preliminary Study

Alexandra Banu, Alexandru Paraschiv, Luminita Georgescu
and Cristina Juganaru

Abstract The developmental tendencies in obtaining high performance of gas turbines are chiefly connected with an increase in the engine's capacity, its efficiency, lifetime, and reduce the deleterious emissions. One way to achieve these targets is the usage of lighter and stronger materials and enhancing the method of parts manufacture. The present work is a part of a national project whose main goal is to develop a new class of light alloys-coatings structures for aerospace, energy and the automotive industry, fated to reduce pollution and to contribute to a friendlier environment. One way to enhancing the high temperature response against the severe environmental conditions, is by development of titanium aluminides with increased niobium content and two different structures: $\alpha_2 + \gamma$ ($Ti_2Al + TiAl$), and Ortho $AlNbTi_2$. The paper present the preliminary results on mechanical properties modification because of niobium content increased from 10 at.% to 25% and on beneficial influence of Thermal barrier coating.

Keywords Titanium aluminide • Mechanical properties • Tensile test • Creep test

1 Introduction

Today there are increasing demands for the development of energy conversion systems with improved efficiency and ecological compatibility. In aerospace, energy and automotive industry, and advanced design concepts are based on higher service temperatures, lighter weight and higher operation speeds. The

A. Banu (✉) · L. Georgescu · C. Juganaru

Department of Manufacturing Engineering, Politehnica University from Bucharest,
Splaiul Independentei 313, Bucharest, Romania
e-mail: alexandrabanu14@yahoo.com

A. Paraschiv

Comoti, Romanian Research & Developmet Institute for Gas Turbines,
220 D Iuliu Maniu Bd, Bucharest, Romania

developmental tendencies in obtaining high performance of gas turbines are chiefly connected with an increase in the engine's capacity, its efficiency, lifetime, reliability, decrease in the fuel consumption and reduce the deleterious emissions. One way to achieve these targets is the usage of lighter and stronger materials and enhancing the method of parts manufacture. The main goal of our work is to develop a new class of light alloys-coatings structures and new technologies for aerospace, energy and the automotive industry, fated to reduce pollution and to contribute to a friendlier environment. In this context, 30 years ago, a new class of materials begins to develop: the Ti-Al intermetallics alloys. There has been a major effort aimed at developing TiAl-based alloys because they have a density about one half that of Ni-based alloys and they retain their strength up to about 750 °C. It has been argued that if these alloys could be manufactured so that an acceptable balance could be obtained between their high and low temperature properties they would be used widely in aerospace engineering (gas-turbine parts), heat power engineering (gas-turbine units), and car engine (internal combustion engine) parts [1]. The main aim of this work was to highlight the influence of niobium content on mechanical behavior of titanium aluminide at 850 °C. To minimize the temperature effect on materials properties and improve their behavior during heating service, the samples were covered with thermal barrier coating formed from two layers. The inner metallic layer and the outer ceramic layer were obtained by Air Plasma deposition technique. The main concern is the poor high temperature oxidability followed by embrittlement of titanium aluminide alloys and as consequence, premature fracture can occur in service. The present work is going to focus on studying the influence of alloying level on the structure and mechanical properties of titanium aluminides. In this context were studied two materials with two niobium alloying levels with two different microstructures, $\alpha_2 + \gamma$, and Ortho AlNbTi₂. In order to improve the oxidation behavior, at work temperature during mechanical tests, the samples were covered with modified thermal barrier coatings formed from inner bonding layer (NiCrMoY + Al₂O₃) and zirconia yttria outer layer.

2 Experimental Detail

The titanium aluminides whose chemical compositions are presented in the Table 1 are used in casting state. The experimental samples were machined by EDM at specific shapes and dimension samples for mechanical properties verification. As protective coating was studied a new system composed from a bonding layer type (NiCr MoAlY) and an outer layer with diffusion and thermal barrier function, Al₂O₃. The coatings were obtained from micro sized powders by Air Plasma Spraying procedure. The structure of base materials and coatings were performed by SEM + EDX techniques.

High temperatures mechanical properties were evaluated, according the ASTM E8, by tensile testing at temperature of 850 °C (processed specimens Fig. 2) on universal static and dynamic testing machine Instron 8802, equipped with high

Table 1 The chemical compositions of titanium aluminides (at.%)

Alloy	The structure of alloy	Ti	Al	Nb	Mo	V
1	$\alpha_2 + \gamma$	52.3	40.2	4.7	—	2.8
2	Ortho AlNbTi_2	50	22	25	3	—

temperature system, for maximum 1000 °C, and extensometer with a measuring basis of 40 mm. The creep tests were performed on creep testing machine SF50 Wolpert, with a maximum 50 KN force, a force measurement accuracy of $\pm 1\%$ and endowed with a system of automatic compensation of force. The tests were conducted in accordance with ASTM E 139 at a temperature of 850 °C.

3 Results and Discussions

3.1 Structural Evaluation

The structures of cast studied alloys presented in the Fig. 1 have been analyzed by SEM technique. The microstructure of alloy 1 is monophasic, with well-formed grains of α_2 phase. No secondary phases were observed in the grain boundaries and intergranular area. The grains are very fine for a cast material, the grains with sizes ranging between 10 and 30 μm . The increasing in niobium content (alloy 2) has, as a structural consequence, a high order level of lamellas arrangement, with transformation of AlTi_3 phase in AlNbTi_2 , a hard phase and relative uniform distribution of alloying elements in the matrix. The XRD analysis revealed that the alloy has a monophasic orthorhombic AlNbTi_2 structure Fig. 2, and the SEM analysis revealed a well-ordered slides aspect characterizing the Orto structure.

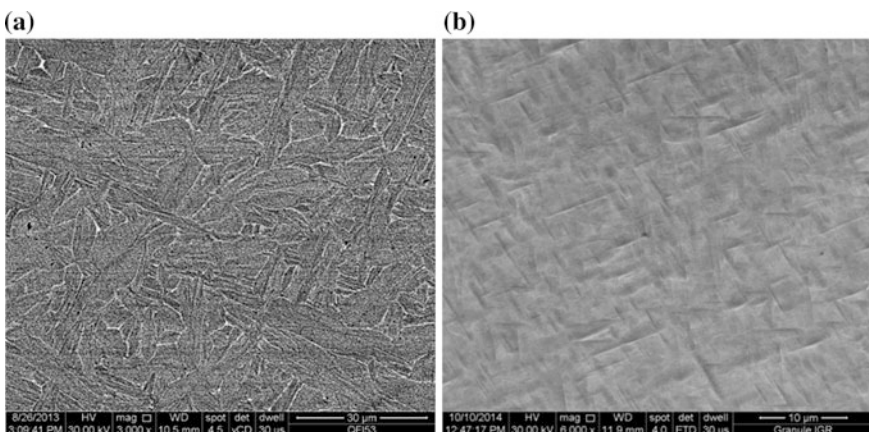


Fig. 1 SEM secondary electrons image of alloys **a** alloy 1($\alpha_2 + \gamma$) and **b** alloy 2 (Orto)



Fig. 2 The general view of tensile samples before mechanical test

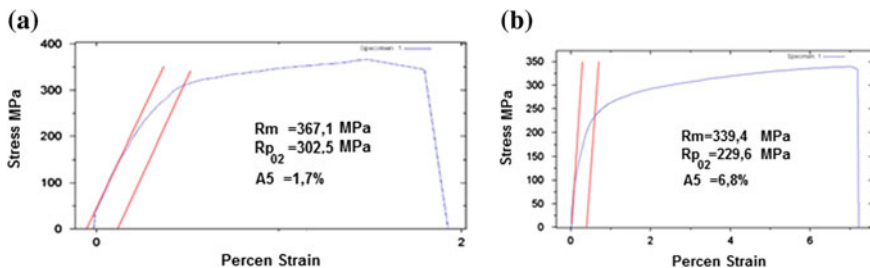


Fig. 3 The tensile curves at 850 °C for alloy 1 in two states: (a) noncovered sample and (b) covered with TBC

Knowing that the increasing in the hard alloying elements such molybdenum and niobium has as a consequence a deterioration of mechanical properties because of hardening effect, for improving the mechanical properties of alloy 2 were done the aging thermal treatments at 850 °C for 12 h followed by 990 °C for 2 h in order to stimulate the formation of B2 phase, see Fig. 3. The samples, in final thermal treatment state, were covered with metallo ceramic double layers using atmospheric plasma spray technique. The SEM evaluation of coating quality before mechanical tests showed a continuous and relative uniform layers.

3.2 High Temperature. Mechanical Properties Evaluation

3.2.1 The 850 °C Tensile Test Results

The samples prepared for tensile test are presented in the Fig. 2 (general view for shape and surface aspect).

In order to highlight the importance of protective coatings on mechanical properties of titanium aluminides, were performed tensile tests on alloy 1 in two surface states: with protected layers and no covered.

Comparing the tensile behaviour of low Nb content titanium aluminide (alloy 1) in these two surface states, can be summarized the following aspects (Fig. 3):

- the shape of deformation curve is similar for both states;
- was observed decreasing of conventional yield strength R_{p_02} at approx. 70 MPa and at approx. 30 MPa of tensile strength after applying protective coatings;

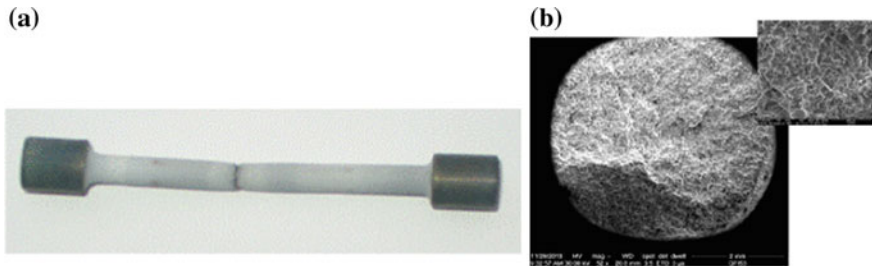


Fig. 4 The aspects after tensile test of alloy 1: (a) The tensile broken sample and (b) the SEM aspect of surface of rupture (fragile, intergranular fracture)

Table 2 The tensile test parameters values, for studied titanium alloys with TBC at 850°C

Alloy	R _m , MPa	R _{p0.2} , MPa	A ₅ , %
1	367.1	302.5	1.7
2	393.7	—	2.5

- was observed too increasing the value of elongation from 1.7 to 6.8% (four times higher) and increasing the flow range at approx. 100 MPa.

On the other hand, can be shown that on the protected sample the slight hardening trend of the material, after material is flowing, remains at comparable levels to that exhibited by the uncovered sample. So, the protection does not improve the hardening resistance of alloy 1. The broken specimen aspect is shown in Fig. 4a and the surface appearance of rupture observed microscopically (SEM) is shown in Fig. 4b. Because of benefic influence of thermal barrier coatings the alloy 2 samples have been tested only in protected state.

The 850 °C tensile test results—Table 2 show that although the alloy 2 show the more coarse appearance of surface breaking, indicating a fragile intergranular cracking and the breaking elongation at a lower temperature, is superior of alloy 1. That can be explained by the important volume fraction of B2 phase in microstructure.

3.2.2 The 850 °C Creep Resistance Results

The creep resistance test of covered samples from both titanium aluminide was performed at 850 °C with a load of 180 MPa. Both materials have a similar behavior with specific three stages of deformation. Both materials revealed a fragile behavior. The Extensometer used was one dedicated testing at high temperatures, with the base measuring 40 mm and an accuracy of $\pm 1\%$ (class B1 acc. To ASTM E83). Fixturing of specimens were machined from plastic deformed bar of nickel based superalloy. The value of efforts maintained during the tests was chosen from

the results of tensile tests at elevated temperatures presented above. The creep behaviour of $\alpha_2 + \gamma$ TiAl alloys (1) at 850 °C and 180 MPa (severe conditions) kept in good condition coverage, presented as a first creep stage in Fig. 5, even in the outer areas intensely deformed. In these areas, examined microscopically, micro-cracks were observed in the outer layer of alumina but the adhesion of the coating, in its entirety, was good. This will be followed by long term test of the experimental model.

The scanning electron microscopy of breaking surface revealed the presence of voids specific for high temperatures break, but also the character of the intergranular fracture (Fig. 6). Microscopic examination of broken specimen in the cross and longitudinal section showed the following: We're not observed phenomenon of recrystallization of grain, not even close to the breaking surface, where deformation

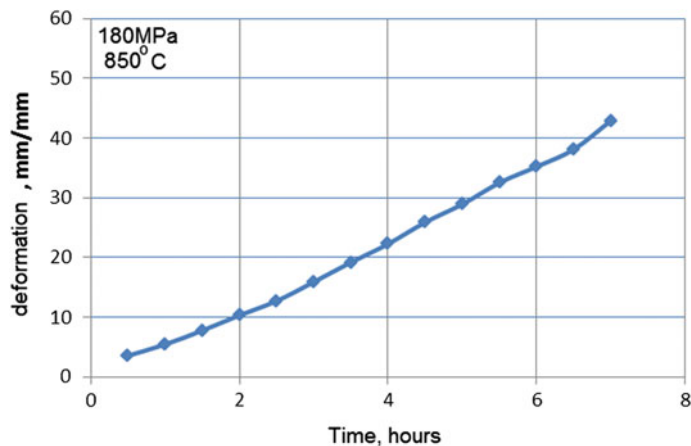
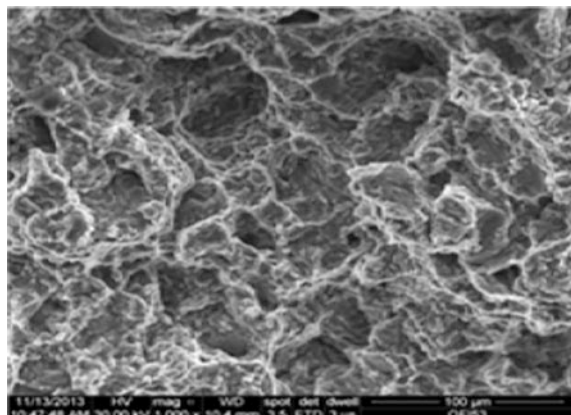


Fig. 5 The first creep stage of alloy 1. Effort: 180 MPa; 850 °C temperature

Fig. 6 The SEM aspect of creep surface After creep test (alloy 1)



is more pronounced; on the longitudinal sample, was observed, however, a rearrangement of the grains, with the formation of preferential orientation strip (see Fig. 7). The breaking was initiated by the appearance of intergranular cracks seen on the longitudinal sample. The coatings behaved well, proven adherent and compact, except in areas where deformation of the specimen is relatively high. It was observed on a cross section, a certain amount of diffusion of nickel and cobalt from the bonding alloy layer in the support, to form compounds rich in nickel and niobium Fig. 8 selected area 1. The TBC layer is compact and adherent. The high

Fig. 7 The SEM longitudinal aspect of creep samples alloy 1 (near creep surface) with rearrangement of the grains, the formation of preferential orientation strip and micro intergranular cracks

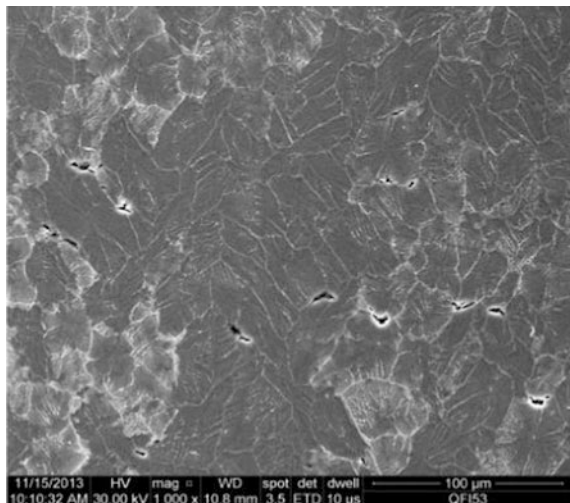


Fig. 8 The SEM image in transversal section on coated creep sample. (X 2500)

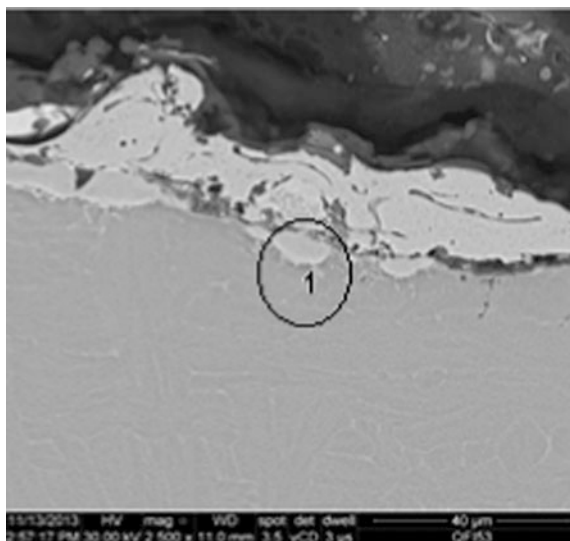
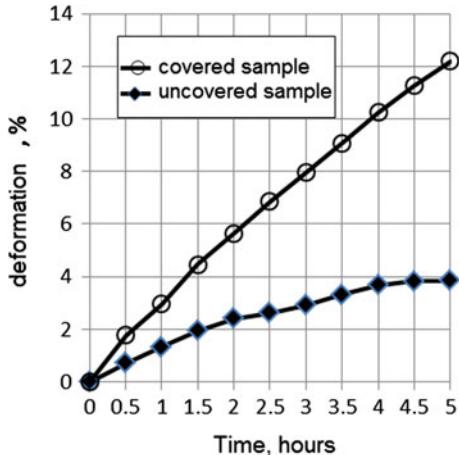


Fig. 9 The first creep stage of alloy 2 curves in two state of samples: with and without TBC



temperatures behavior of alloy (2) is determined, outside by the chemical composition or material state (molded, plastic deformation, etc.), by the mechanisms by which heat treatments favors structural changes that influence mechanical properties. Boehlert [2] showed, citing several authors, that the alloys with predominant orthorhombic structure are generally fragile and is therefore required such heat treatment to maintain an appropriate level of phase volume fraction of the bcc for improving ductility.

Smith and Porter [3] have investigated the influence of heat treatment on a titanium orthorhombic alloy Ti-22Al-23Nb and reveal that all heat treatments to temperatures below-transus led improve tensile strength, yield strength, elongation and creep resistance. It has also mentioned, as was observed after application of the coating diffusion barrier, an increase of plasticity of alloy but at this stage we cannot say that this is due to stopping uptake of oxygen and brittle superficial or structural changes induced by diffusion of elements Fig. 9.

4 Conclusion

The increasing of niobium content of titanium aluminides for high temperature oxidation increasing reasons has a consequence the deterioration of mechanical properties in terms of elongation and creep resistance. The mechanical properties of alloys with more than 10 at.% of niobium cannot be improved significantly by heat treatments. However, the thermal barrier coatings improve mechanical behavior of these alloys. The next studies will be going to focus on development of a new thermal barrier coating in order to improve the both oxidation resistance and mechanical properties of niobium titanium aluminides.

Acknowledgements This work was funded by National Project PCCA no. 65/2012.

References

1. Belyanchikov, L.N.: Special electrometallurgy of promising structural materials based on titanium aluminides. Russ. Metall. (Metally) **2008**(7), 567–576. © Pleiades Publishing, Ltd. (2008)
2. Boehlert, C.J.: Microstructure, creep, and tensile behavior of a Ti–12Al–38Nb (at.%) beta + orthorhombic alloy. Mat. Sci. Eng. **A267**, 82–98 (1999)
3. Smith, P.R., Porter, W.J.: The effect of heat treatment on the tensile and creep behaviour of “neat” matrix Ti–22Al–23Nb. J. Mater. Sci. **32**, 6215–6220 (1997)

The Numerical Scheme for the Basset Type Integro-Differential Equation in Hydrodynamics

Vladimir Vanovskiy and Alexander Petrov

Abstract A high-order precision numerical scheme was proposed for the Basset kernel integrals and the Basset type integro-differential equations that often arise in hydrodynamics. The scheme was tested on a model integral and on a real problem of particle focusing in a standing acoustic wave in liquid. The scheme showed around 2 orders higher speed of integral estimation compared with the existing analogs. The obtained results show that the integral can be approximated with high order of precision and the real problem is simulated well by the proposed scheme. A variable step technique was used to increase the precision of integro-differential equation simulation even more by eliminating the discrepancy at the very start of the simulation. The proposed numerical scheme may found its applications in many biological and medical problems related to acoustophoresis or in particle sedimentation simulations.

Keywords Basset force • Basset kernel • Fractional derivative • Integro-differential equation • Acoustophoresis • BBO equation

1 Introduction

The numerical simulation of the integro-differential equations describing “history” forces or physical systems with memory is complicated because at any step of the numerical integration all the previous steps should be considered and the time of execution may become quadratic in the number of simulation steps. In case of the integrals with the singular kernels the situation may become even worse as the usual numerical integration schemes of the Newton-Cotes family are useless.

V. Vanovskiy (✉) · A. Petrov
Moscow Institute of Physics and Technology, Institutskiy per. 9,
141700 Dolgoprudny, Russia
e-mail: vladimir.vanovsky@gmail.com

V. Vanovskiy · A. Petrov
Institute for Problems in Mechanics of the Russian Academy of Sciences,
Pr. Vernadskogo 101-1, 119526 Moscow, Russia

The example of such an integral is the Basset kernel integral described by the integral operator

$$\hat{I}(f) = \int_{\tau=0}^t \frac{f(\tau)d\tau}{\sqrt{\pi(t-\tau)}} . \quad (1)$$

The kernel is singular at $\tau \rightarrow t$ and its fast computation is a big challenge in all the problems where such a kernel appears such as Basset force consideration in hydrodynamics or fractional derivative calculation. Many approaches of such an integral approximation were developed in the last years. A comprehensive review that contains most of them was recently published [1]. We try to focus on the exact integral estimation without changing the kernel as it was done in [2]. However the proposed here approach is much simpler and the integral is calculated more than 100 times quicker. Also the proposed approach gives the possibility for the exact estimation of the obtained error of integration for the functions with limited corresponding order derivative value.

2 The Numerical Scheme

The integrand function in (1) is assumed to be $k - 1$ times continuously differentiable over the closed interval $[0, t]$ and to have the k th derivative in the opened interval $(0, t)$ limited by some constant. The integral is assumed to be taken over the uniform mesh containing n points with step h , $t = nh$. It will be shown that under such an assumptions there exists a numerical scheme providing the integration error limited by $Mh^n\sqrt{t}$ where M stays for some constant. The numerical scheme coefficients will be calculated for $k = 3$.

The integral may be rewritten as follows

$$I = \hat{I}(f) = -2\sqrt{\frac{h}{\pi}} \sum_{i=1}^N \int_{i-1}^i f(hx) d\sqrt{n-x} = 2\sqrt{\frac{h}{\pi}} \sum_{i=1}^n I_i, \quad (2)$$

$$I_i = -\int_{i-1}^i f(hx) d\sqrt{n-x} .$$

The function f on the interval $((i-1)h, ih)$ may be represented by the Taylor polynomial with the remainder in the Lagrange form

$$f(\tau) = f_{i-1} + f'_{i-1}(\tau - t_{i-1}) + f''_{i-1}(\tau - t_{i-1})^2/2 + \dots$$

$$\dots + f_{i-1}^{(k-1)}(\tau - t_{i-1})^{k-1}/(k-1)! + f^{(k)}(\xi)(\tau - t_{i-1})^k/k!, \quad (3)$$

$$(i-1)h \leq \xi \leq \tau \leq ih, \quad t_{i-1} = (i-1)h, \quad f_i = f(t_i) = f(ih) .$$

One may substitute (3) in (2) up to the needed order of precision and after integrating and approximating the result by the function values in the grid points the scheme coefficients will be obtained. The following integral is obtained for $k = 3$

$$I_i = - \int_{i-1}^i \left\{ f_{i-1} + hf'_{i-1}(x-i+1) + (h^2/2)f''_{i-1}(x-i+1)^2 + (h^3/6)f'''(\xi)(x-i+1)^3 \right\} d\sqrt{n-x}, \quad \xi \in ((i-1)h, ih) \quad (4)$$

and approximated by the weighted sum of function values in the points $(i-2)h$, $(i-1)h$, ih

$$\tilde{I}_i \approx \left(\sqrt{n-i+1} - \sqrt{n-i} \right) \left(\alpha_i f_{i-2} + \beta_i f_{i-1} + \gamma_i f_i \right). \quad (5)$$

Three points are used for approximation because it is the minimal amount that can provide the difference between the exact value of the integral and the approximation value to be smaller or proportional to h^3 . After calculating the integral and making an important substitution

$$\varepsilon_i = \left(\sqrt{n-i+1} - \sqrt{n-i} \right)^2,$$

the following expansion in powers of h is obtained

$$\begin{aligned} I_i / \sqrt{\varepsilon_i} &= f_{i-1} + hf'_{i-1} \left(\frac{1}{2} + \frac{\varepsilon_i}{6} \right) + \frac{h^2}{2} f''_{i-1} \left(\frac{1}{3} + \frac{\varepsilon_i}{6} + \frac{\varepsilon_i^2}{30} \right) + \\ &+ \frac{h^3}{6} f'''(\xi) \left(\frac{1}{4} + \frac{3\varepsilon_i}{20} + \frac{\varepsilon_i^2}{20} + \frac{\varepsilon_i^3}{140} \right), \quad \xi \in ((i-1)h, ih). \end{aligned} \quad (6)$$

After the expansion of (5) in a Taylor series and equating it with (6) up to the second power of h the following linear system of equations together with the error estimation is obtained

$$\begin{aligned} \alpha_i + \beta_i + \gamma_i &= 1 & \alpha_i &= -1/12 + \varepsilon_i^2/60 \\ \gamma_i - \alpha_i &= 1/2 + \varepsilon_i/6 & \beta_i &= 2/3 - \varepsilon_i/6 - \varepsilon_i^2/30 \\ \alpha_i + \gamma_i &= 1/3 + \varepsilon_i/6 + \varepsilon_i^2/30 & \gamma_i &= 5/12 + \varepsilon_i/6 + \varepsilon_i^2/60 \\ \frac{I_i}{\sqrt{\varepsilon_i}} + \frac{h^3}{6} f'''(\xi) \left(\frac{1}{4} + O(\frac{1}{n-i}) \right) &= \Leftrightarrow \frac{|I_i - \tilde{I}_i|}{\sqrt{\varepsilon_i}} < \frac{h^3}{6} f'''_{i\max} \left(\frac{11}{12} + O(\frac{1}{n-i}) \right) & (7) \\ = \frac{\tilde{I}_i}{\sqrt{\varepsilon_i}} + \frac{h^3}{6} (\gamma_i f'''(\xi') - \alpha_i f'''(\xi'')) & & f'''_{i\max} &= \max(f'''(\xi)), \\ \xi, \xi' \in ((i-1)h, ih) & & \xi &\in ((i-2)h, ih) \\ \xi'' \in ((i-2)h, (i-1)h) & & & . \end{aligned}$$

The proposed scheme estimates the integral I_i using function values in three grid points $(i-2)h$, $(i-1)h$ and ih . For $i = 1$ it means that the integrand should also possess all the good properties on the interval $(-h, 0)$. Speaking about higher degrees of approximation this interval will be extended even more. A selection of asymmetric interval $((i-k+1)h, ih)$ for every I_i estimation is recommended because the use of the grid points bigger than ih for I_i estimation leads to the implicit numerical schemes for the problems where such integrals enter some integro-differential equation and increases vastly the overall simulation time.

Using (7) the whole integral (2) value and the approximation error can be estimated

$$I \approx \tilde{I} = 2\sqrt{\frac{h}{\pi}} \sum_{i=1}^n \tilde{I}_i = 2\sqrt{\frac{h}{\pi}} \sum_{i=1}^n \sqrt{\epsilon_i} (\alpha_i f_{i-2} + \beta_i f_{i-1} + \gamma_i f_i),$$

$$\text{err} = |I - \tilde{I}| < \frac{11}{36\sqrt{\pi}} h^3 \sqrt{tf''_{\max}} \left(1 + O(\frac{1}{\sqrt{n}})\right), \quad n \rightarrow \infty.$$
(8)

The same way the numerical scheme may be obtained for every k value but for high k values it becomes less stable. Following [2] we will say that the scheme has k th order of precision as the error is majorized by $O(h^k \sqrt{f})$ (strictly speaking the order of precision is $k - 1$ —the highest order of polynomial which will be integrated precisely). The scheme may be summarized as

$$I \approx 2\sqrt{\frac{h}{\pi}} \sum_{i=1}^n \sqrt{\epsilon_i} ((-1/12 + \epsilon_i^2/60)f_{i-2} + (2/3 - \epsilon_i/6 - \epsilon_i^2/30)f_{i-1} + (5/12 + \epsilon_i/6 + \epsilon_i^2/60)f_i).$$
(9)

The numerical schemes of the orders 1–3 are evaluated on a model function $f(\tau) = \cos \tau$ integrated over interval $[0, 50\pi]$. The answer can be expressed analytically in terms of Fresnel integral as $\sqrt{2}C(10) \approx 0.70696351315804088$. The function and interval were chosen the same as in [1] in order to compare the obtained results. All the calculations were made in Matlab environment with a modern i7 CPU. Matlab is considered to be far from the fastest computing environment and some speed increase from 3 to 5 times may appear if the simulations were done using Fortran as in [1].

However in (Fig. 1) one may observe that the precision of the schemes corresponds to declared and calculation speed is more than two orders higher than of the third order Daitche scheme and much better than any other scheme investigated

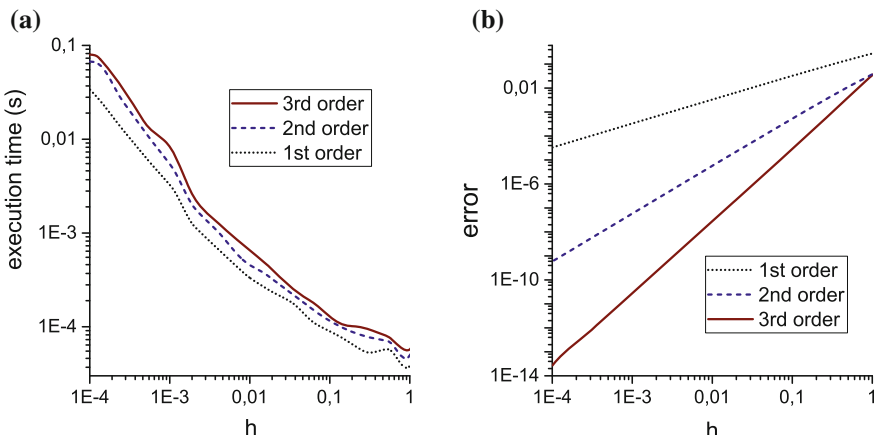


Fig. 1 The time and error values versus step size plotted for the different order of accuracy methods. *Dotted, dashed and solid lines* stay for the 1st–3rd order numerical schemes correspondingly

in [1]. Furthermore, the coefficients in the scheme depend only on $n - i$ and may be calculated in advance once for all the n in order to boost the simulation of the integro-differential equation when the integral is calculated on every step.

3 The Basset Type Integro-Differential Equation Solution

The Basset-Boussinesq-Oseen equation (BBO equation) is used to describe the motion of a small spherical particle in unsteady flow with velocity field $v(x, t)$ at low Reynolds numbers

$$\begin{aligned}
 (m_{\text{particle}} + m_{\text{added}})\ddot{x} &= F_{\text{inertial}} + F_{\text{Stokes}} + F_{\text{Basset}} + F_{\text{Faxen}} + F_g, \\
 m_{\text{particle}} &= \frac{4}{3}\pi\rho_p a^3, \quad m_{\text{added}} = \frac{2}{3}\pi\rho a^3, \\
 F_{\text{inertial}} &= \frac{4}{3}\pi\rho a^3 \left(w + \frac{W}{2} \right), \quad w = \frac{\partial v}{\partial t} + v \frac{\partial v}{\partial x}, \quad W = \frac{\partial v}{\partial t} + \dot{x} \frac{\partial v}{\partial x}, \\
 F_{\text{Stokes}} &= -6\pi\mu a(\dot{x} - v), \\
 F_{\text{Basset}} &= -6\pi\mu a t_\mu^{1/2} \left(\frac{d}{dt} \right)^{1/2} (\dot{x} - v), \quad t_\mu = \frac{\rho a^2}{\mu}, \\
 \left(\frac{d}{dt} \right)^{1/2} (\dot{x} - v) &= \int_{t'=0}^t \left(\frac{d^2 x}{dt'^2} - W(t') \right) \frac{dt'}{\sqrt{\pi(t-t')}} + \frac{\dot{x}(0)-v(0)}{\sqrt{\pi t}}, \\
 F_{\text{Faxen}} &\sim \mu a^3 \nabla^2 v \sim \mu a v (a/\lambda)^2, \\
 F_g &= \frac{4}{3}\pi a^3 (\rho_p - \rho) g .
 \end{aligned} \tag{10}$$

Here ρ_p and ρ stand for particle and fluid densities, a stands for particle radius, μ stands for fluid viscosity which we consider not to depend on density. By w and W are denoted fluid acceleration along fluid and along the particle trajectory. The Basset force is used in the form proposed by [3] which contains the corrections for nonzero initial particle relative velocity with the fluid. The inertial force is used in the Maxey-Riley form [4].

The last two forces are neglected because of their smallness and (10) is divided by $(2/3)\pi a^3$

$$\begin{aligned}
 (\rho + 2\rho_p)\ddot{x} &= 2\rho w + \rho W - \frac{9\mu}{a^2} \left(\frac{dx}{dt} - v \right) + F_B, \\
 F_B &= -\frac{9\sqrt{\rho\mu}}{a} \left(\int_{t'=0}^t \left(\frac{d^2 x}{dt'^2} - W(t') \right) \frac{dt'}{\sqrt{\pi(t-t')}} + \frac{\dot{x}(0)-v(0)}{\sqrt{\pi t}} \right) .
 \end{aligned} \tag{11}$$

The dimensionless acoustic wave amplitude is denoted by $b \ll 1$. It is defined as the ratio of maximal fluid velocity in the wave to the sound speed in the fluid. The dimensionless variables $q = (\omega/c)x$, $\tau = \omega t$ and the dimensionless viscosity parameter $K = \frac{3\mu}{\omega\rho a^2 b} \sim 1$ are introduced, ω stands for the wave angular frequency. The asymptotic averaged equation for $b \rightarrow 0$ is obtained using the Krylov-Bogoliubov averaging technique as described in [5].

The initial and the averaged equations were modeled using a proposed numerical scheme (9) for the Basset integral calculation. As the integrand contains second order

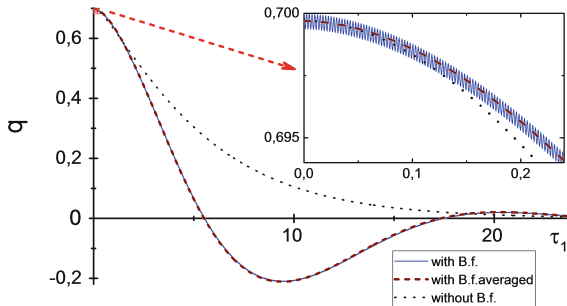


Fig. 2 The asymptotic and the exact numerical solutions of the integro-differential BBO equation (light solid line and dashed line) and the numerical solution of the same equation without the Bassett force (dotted line). The inset shows the magnified part of the dependence. $\tau_1 = 3b\tau/4$ stands for the “slow” dimensionless time

derivatives the 5-point grid was used in order to estimate the integrand with the needed precision. As the initial conditions are not defined very well a step variation technique was used [2]. The first 400 steps were calculated with a small step $h/100$ and than the numerical scheme step size was reset to h .

In the (Fig. 2) the trajectories of heavy particle $\rho_p/\rho = 1.5$ are modeled for $b = 16/3 \cdot 10^{-4}$. The trajectory for small b practically coincides with the asymptotic solution at $b \rightarrow 0$. The initial equation simulation took about 8 h of one core CPU time and the averaged integro-differential equation simulation took only 170 ms using the same numerical scheme. The ability to compare the results for these two approaches up to such a big time ($\tau_{\max} = 60000$, $h = 0.05$, 1.2M steps) shows the advantage of our scheme over the one used in [5] where only the small part of the particle trajectory was calculated.

4 Conclusion

The proposed numerical scheme for the Bassett integral approximation proves to be much simpler and faster than the analogs. It also allows some optimizations such as the precomputed coefficients for the integro-differential equation solution and the smaller step size in the beginning of the grid. The work of the scheme with the 3rd order of the integral approximation was demonstrated on the example of the model integral and in a model problem of particle focusing in the standing acoustic wave. The proposed scheme allows the solution to be extended to much bigger interval than in the previous works on this problem up to the moment of the particle focusing in a standing wave pressure node.

Acknowledgements The work was supported by the Russian Science Foundation (project 14-19-01633) in IPMech RAS.

References

1. Moreno-Casas, P.A., Bombardelli, F.A.: Computation of the Basset force: recent advances and environmental flow applications. *Environ. Fluid Mech.* **16**(1), 193–208 (2016)
2. Daitche, A.: Advection of inertial particles in the presence of the history force: Higher order numerical schemes. *J. Comput. Phys.* **254**, 93–106 (2013)
3. Michaelides, E.E.: A novel way of computing the Basset term in unsteady multiphase flow computations. *Phys. Fluids A Fluid Dyn.* **4**(7), 1579–1582 (1992)
4. Maxey, M.R., Riley, J.J.: Equation of motion for a small rigid sphere in a nonuniform flow. *Phys. Fluids* **26**(4), 883–889 (1983)
5. Aksenov, A.V., Petrov, A.G., Shunderyuk, M.M.: Motion of solid particles in fluid in a nonlinear standing ultrasonic wave. *Dokl. Phys.* **439**(1), 37–41 (2011)

On the Issue of Choosing the Measuring Zones in a Faraday Balance When Studying Magnetic Susceptibility of Small Samples

Alexander Sandulyak, Anna Sandulyak, Maria Polismakova,
Vera Ershova, Darya Sandulyak and Dmitriy Kiselev

Abstract By the example of polar pieces of spherical, conical and truncated conical shape, we substantiate and implement the approach to identifying a local, spatially limited, working zone (to position and examine magnetic susceptibility of ‘microsamples’) for the Faraday balance, viz. the zone with stable inhomogeneity of the field. It involves obligatory obtaining and analyzing coordinate characteristics of induction (intensity) in the interpolar area, at this, sinuous characteristics, i.e. the ones with an inflection, should be give preference to out of the traditional nonlinear characteristics. Then, the well-linearized zone near the inflection point (the corresponding derivative here demonstrates an extremum) most fully satisfies the requirement (to a working zone) for preserving the field inhomogeneity constancy. It is established that in comparison with the spherical polar pieces, the conical ones provide a working zone that is closer to the axial line, whereas the truncated conical polar pieces ensure the zone farther from their axial line.

Keywords Faraday balance • Measurement working zone • Coordinate characteristic of intensity (induction) • Sinuosity characteristic • Gradient extremum

1 Introduction the Framework of the Approach

A Faraday balance is usually used to obtain information on magnetic susceptibility χ for samples of low volume V , both solid and dispersed ones (e.g. samples of ferro- or ferrimagnetic powders which represent disperse phase of many technological media subjected to magnetophoresis and magnetic control [1–6]). When we create a field with intensity H (induction $B = \mu_0 H$) and inhomogeneity $\text{grad}H$ ($\text{grad}B$) between the polar pieces, the magnetic (ponderomotive) force F affecting the studied ‘microsample’ becomes the main measured quantity. Then if we employ the

A. Sandulyak · A. Sandulyak (✉) · M. Polismakova · V. Ershova · D. Sandulyak ·
D. Kiselev

Moscow Technological University, Stromynka 20, 107076 Moscow, Russian Federation
e-mail: anna.sandulyak@mail.ru

known functional expression $F = \mu_0 \cdot \chi \cdot V \cdot H \text{grad}H = \chi \cdot V \cdot B \text{grad}B / \mu_0$ (where $\mu_0 = 4\pi \cdot 10^{-7}$ H/m is a magnetic constant) with some values of the constituent variables, it becomes possible to define values χ by back calculating (for ferro- and ferrimagnetics—the values χ of its nonlinear field dependence).

The key requirements to implementing the Faraday ponderomotive method usually include the demand for rigorous positioning of the sample studied, i.e. in the zone of interpolar area (working zone) where the constant field inhomogeneity condition is observed. However, the issue of ensuring the zone with stable field inhomogeneity (the choice of polar pieces shape) and the diagnostics of this zone is sadly not given due consideration. The features necessary to define these conditions are virtually absent; the available recommendations are quite vague and hardly suitable for specific practical application.

To give an unbiased estimation on the acceptability of the polar pieces choice and to have the data on the inhomogeneity (gradient) characteristic of some direction x , permeating the interpolar area, e.g. in the line of ponderomotive force, we must initially have the coordinate characteristic, i.e. the dependence of parameter H or B on x . Such a characteristic, specifically, parameter B , obtained e.g. by small stepwise movement of the Hall sensor represented in graphic and/or analytical form, allows us to find the coordinate characteristic of the gradient, i.e. parameter $\text{grad}B = dB/dx$. Judging by it, we can define, firstly, whether there is (or is not) the zone in question in some given interpolar area, i.e. the zone with stable values $\text{grad}B$, and secondly, we can estimate the coordinates of its location, which means, the coordinates of positioning the studied sample.

Thus, it is suffice to pose a question on identifying a linear (or near-linear) segment, even a short one (commensurable with the sample dimensions), of dependence B on x . The presence of such a segment will mean that this is the place where $\text{grad}B = dB/dx = \text{Const}$, and its coordinates will definitely point at the location of the working zone.

Here we must specially bespeak that for the polar pieces of traditional and specific shapes dependences B (or H) on x in general are usually objectively non-linear, and this somewhat contradicts to the whole concept of detecting their linear segment. However, this inconsistency can be eliminated by an approach which essentially stipulates the choice of polar pieces of the shape (not obligatory something special) that would ensure the key characteristic B (or H) is sinuous, i.e. it has a bend (inflection). Then its segment (short in relation to all expanded non-linear characteristic) near the inflection point can be considered close to the desired linear one, and value $\text{grad}B$ ($\text{grad}H$) almost stable. This argument can be additionally (and quite illustratively) supported by the corresponding derivative of the obtained dependence B (or H) on x , i.e. a coordinate characteristic $\text{grad}B$ ($\text{grad}H$) which will have an extremum (conforming to the defined inflection) in the vicinity of which values $\text{grad}B$ ($\text{grad}H$) are practically stable.

The research into magnetization (by the field with intensity H_0) of the ball chain [7, 8] also points to the acceptable (for a Faraday balance) shape of the polar pieces. It is these nonlinear characteristics with a noticeable inflection for the field with

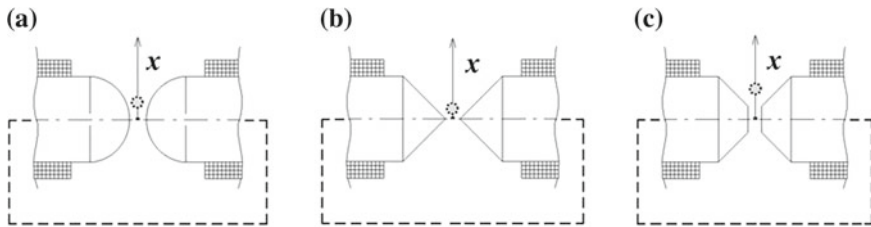
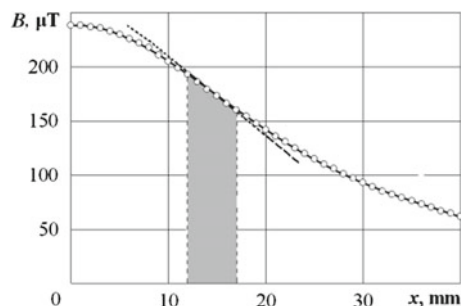


Fig. 1 Options of creating local (located near the abscissa of the inflexion point of the coordinate characteristic of intensity or induction and, respectively, the abscissa of the gradient extremum) working zones between spherical **a**, conical **b** and truncated conical **c** poles; the working zones are conditionally highlighted according to results in Figs. 2, 3, 4, and 5

Fig. 2 Coordinate characteristic of the field induction between polar pieces of spherical shape: dots—experiment, lines—calculation

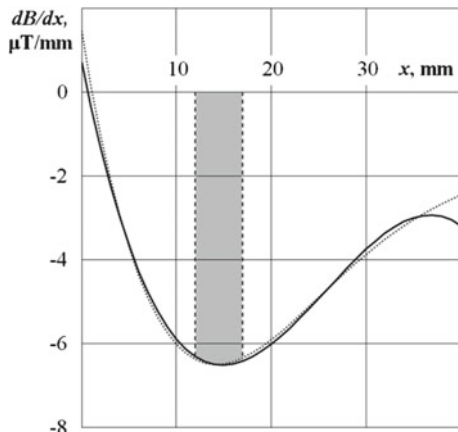


intensity H ($H \gg H_0$), that are inherent to the gap areas between opposing spherical surfaces in the normal direction from centre-to-centre line of balls. In the inflection point of characteristic H , there is a pronounced extremum of characteristic dH/dx [7, 8]. It means, that from the perspective of creating the required working zone, the use of spherical polar pieces (Fig. 1a) is one of the satisfactory solutions for choosing the polar pieces for a Faraday balance (clearly, as non-contacting semi-spherical bodies).

2 Research Outcomes and Their Discussion

Figure 2 (points) exhibits the results of measuring induction B in the symmetry plane of the area between polar spherical pieces (diameter is 100 mm, mutual distancing is 10 mm) located at different x distances from the axial line (coil feeding current is 16A). The inflection of the obtained coordinate characteristic B is clearly observed, which tells about a possible linear approximation of the data in the vicinity of the inflection point (shown by dashed lines), thus proving the stability of value $\text{grad}B$ here.

Fig. 3 Coordinate characteristic of induction gradient (by data in Fig. 2); dashed and solid lines—calculation by expressions obtained by polynomial differentiation according to the 5th and 4th degree for coordinate characteristic of induction



The extreme view of characteristic $\text{grad}B$ in Fig. 3 illustratively proves the same: near the extremum value $\text{grad}B$ is actually virtually stable. To obtain characteristic $\text{grad}B$, we should resort to analytical (phenomenological) approximation of characteristic B (Fig. 2, dots) with its further differentiation. It is reasonable in this context to use, for example, an approximating function in the form of a polynomial of the 4th, or 5th degree at the most (in Fig. 2 this is practically one unified line which describes the original feed experimental data well).

Characteristics $\text{grad}B = dB/dx$ obtained for 5th and 4th degree polynomials are pronounced extreme ones and correlate between each other (Fig. 3 the dashed and solid lines respectively). Their mutual separation is noticeable only at relatively high and low values x , here even with the sign reversal (Fig. 3). However, taking into the account that these data are of no interest for solving the given task, the preference in this case should be given to the 4th degree polynomial, even more so that it provides an opportunity to get a formula for calculating the extremum abscissa $x = x_{\text{extr}}$ of characteristic $\text{grad}B$ in the analytical form. We should only make double differentiation of this polynomial, zero out and solve the deduced quadratic equation.

The results of calculating abscises x_{extr} conform exactly to the results which are provided by software (to name a few: Advanced Grapher, Excel). At that, the obtained value $x_{\text{extr}} = 14.8 \text{ mm}$ is close to values $x_{\text{extr}} = 14.1 \text{ mm}$ when using the 5th degree polynomial.

As to the size of the working zone itself (the area between the given spherical pieces), i.e. the zone of practically stable value $\text{grad}B$ it ranges (by x) from 12 to 17 mm, the corresponding interval of x in Figs. 2 and 3 is specially highlighted. At that, the proper size of this zone, i.e. the size of the sample studied, should not exceed here 5 mm.

The same approach to identifying the working zone and based on deriving and analyzing a coordinate characteristic of induction B (intensity H) of the field in interpolar area is applicable to other shapes of polar pieces, including traditional

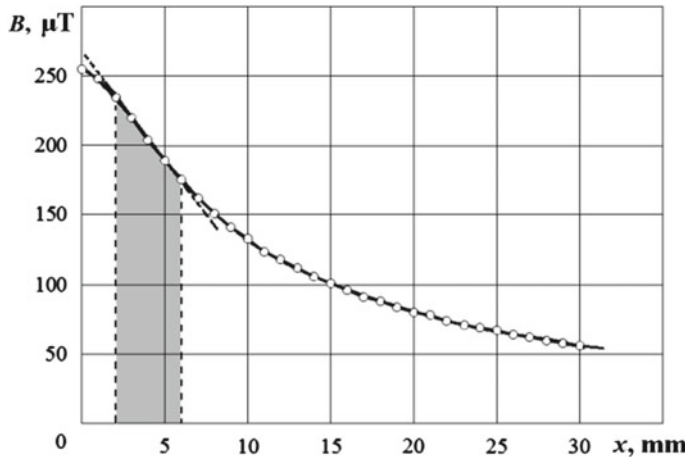


Fig. 4 Coordinate characteristic of field induction between polar pieces of conical shape (Fig. 1b)

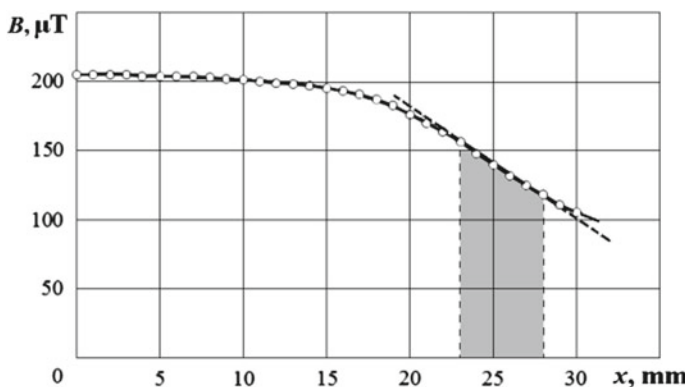


Fig. 5 Coordinate characteristic of field induction between polar pieces of truncated conical shape (Fig. 1c)

ones. Figures 4 and 5 feature coordinate nonlinear characteristics B in the area between same-size and mutually distanced polar pieces but of conical shape (Fig. 1b, the vertex angle of 90°) and truncated conical shape (Fig. 1c, diameters 100/40 mm).

We can clearly see in Figs. 4 and 5 that each of these characteristics is sinuous which allows us to speak about the applicability (as a matter of principle) of these pieces for a Faraday balance. Near the inflection point the corresponding segment of characteristic B yields to artificial linearization (it is illustrated by straight dashed lines in Figs. 4 and 5), which indicates practically stable values of parameter $\text{grad}B$ here (in other words—near the extremum of the corresponding characteristic $\text{grad}B$).

It is worth mentioning that in comparison with the spherical pieces (Figs. 1a, 2 and 3), the location of the working zone between the conical (Fig. 1b) and truncated conical ones (Fig. 1c) differs greatly. Thus, in these cases (see Figs. 4 and 5, individual intervals of x are shadowed) the working zones are limited by x values, i.e. by the distances to the poles axial lines from 2 to 6 mm respectively (i.e. closer to the axial line) and from 23 to 28 mm (i.e. farther from the axial line).

3 Conclusion

The paper considers the issue covered rather poorly in modern literature, it concerns identifying a working zone with spatial constraints, zones in the inter-polar area of Faraday balance—the zones for positioning the small-sized samples studied when examining their magnetic susceptibility. We observed that such identification can be productive when the specially obtained coordinate characteristic of induction (intensity) of the field between the polar pieces (it is usually nonlinear and defying the desired, even partial, linear approximation—in order to ascertain the induction gradient values that are stable here, which corresponds to the accepted condition of the sample positioning) is sinuous, i.e. it has an inflection. In this case, there is an opportunity to objectively perform linear approximation of a relatively short segment of this characteristic, i.e. in the vicinity of the inflection point, with additional illustration of the corresponding extreme form of the induction gradient characteristic, near the extremum of which the values of the gradient are relatively stable. The research is conducted on defining the location of the working zones between the polar pieces of spherical, conical and truncated conical shape (diameter of 100 mm, mutual distancing of 10 mm). It has been established that the working zones in them are localized within the following ranges: from 12 to 17 mm, from 2 to 6 mm, and from 23 to 28 mm respectively.

Acknowledgements The reported study was funded by RFBR according to the research projects № 16-38-60034 mol_a_dk, №16-58-10049 KO_a.

References

1. Nandy, K., Chaudhuri, S., Ganguly, R., Puri, I.K.: Analytical model for the magnetophoretic capture of magnetic microspheres in microfluidic devices. *J. Magn. Magn. Mater.* **320**, 1398–1405 (2008)
2. Kawano, M., Watarai H.: Two-dimensional flow magnetophoresis of microparticles. *Anal. Bioanal. Chem.* **403**(9), 2645–2653 (2012)
3. Murariu, V., Svoboda, J.: The applicability of Davis tube tests to ore separation by drum magnetic separators. *Phys. Sep. Sci. Eng.* **12**(1), 1–11 (2003)
4. Das, S., Chakraborty, S., Mitra, S.K.: Magnetohydrodynamics in narrow fluidic channels in presence of spatially non-uniform magnetic fields: framework for combined magnetohydrodynamic and magnetophoretic particle transport. *Microfluid. Nanofluid.* **13**(5), 799–807 (2012)

5. Sandulyak, A.A., Sandulyak, A.V., Belgacem, F.B.M., Kiselev, D.O.: Special solutions for magnetic separation problems using force and energy conditions for ferro-particles capture. *J. Magn. Magn. Mater.* **401**, 902–905 (2016)
6. Sandulyak, A.V., Garaschenko, V.I., Korkhov, O.J.: Method of determining the quantity of solid fraction of ferromagnetic matter in a fluid. Patent USA No 4492921
7. Sandulyak, A.V., Sandulyak, A.A., Ershova, V.A.: Magnetization curve of a granulated medium in terms of the channel-by-channel magnetization model (New approach). *Dokl. Phys.* **52**(4), 179 (2007)
8. Sandulyak, A.V., Sandulyak, A.A., Ershova, V.A.: On the model of channel-by-channel magnetization of a granular medium (with a radial permeability profile of a quasi-continuous channel). *Techn. Phys.* **54**(5), 743 (2009)

Part II

System Science and Computers

Energy Aware Autonomous Deployment for Mobile Wireless Sensor Networks: Cellular Automata Approach

Shahinaz M. Al-Tabbakh and Eman Shaaban

Abstract Wireless sensor networks are formed of thousands of nodes that need to be deployed to maintain good sensing coverage area. Deployment of a wireless sensor network in a hostile or hazardous environment is a challenging problem. To address this problem, a bundle of sensors to be deployed is initially placed in a definite region within the area of the network. Then the sensor nodes are diffused cooperatively and gradually to increase coverage area. This paper proposes a self-deployment heuristic approach for WSN based on the Four Quadrants Deployment Model (FQDM). It studies the effect of applying a realistic energy model to FQDM, and proposes an extended version of FQDM to enhance the coverage at border areas. The proposed approach relocates the sensors in a way that maximizes the coverage while minimizing energy consumption. Results show that it gives a good coverage for definite region while conserving energy of sensors.

Keywords Sensor networks • IOT • Sensor deployment • Sensor coverage • Cellular automata

1 Introduction

Wireless Sensor Network (WSN) is a promising technology as it is the basis of future “Internet Of Things”. In WSNs, the sensors are capable of communicating with each other and in a multi-hop way propagating sensing information to data sinks and operations centers. In the last few years, wireless sensor networking has

S.M. Al-Tabbakh

Faculty of Girls for Arts, Sciences and Education, Ain Shams University,
Cairo, Egypt

e-mail: Shahinaz.altabbakh@women.asu.edu.eg

E. Shaaban (✉)

Faculty of Computer and Information Science, Ain Shams University,
Cairo, Egypt

e-mail: eman.shaaban@cis.asu.edu.eg

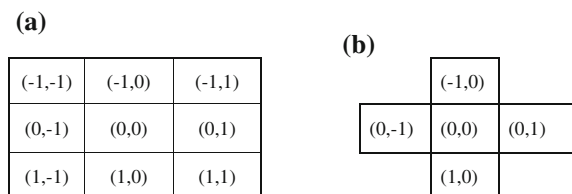
been a very active research area in both academia and industry with a wide variety of applications such as area monitoring, environmental sensing, industry automation, structural monitoring, water and wastewater monitoring, surveillance, health monitoring, tracking of materials, and many others. Recently, numerous researches are conducted regarding diverse challenges in wireless sensor networks. These challenges include coverage and connectivity issues, MAC protocol design, routing protocol design, power saving, and data gathering and fusion. However, the performance of the proposed solutions strongly depends on the way sensors are deployed in the sensed area. Sensors deployment is still an active research area in WSN, where the main objective of these researches is maximizing the area coverage while preserving connectivity and minimizing energy consumption.

Cellular automata CA is a discrete mathematical model for systems consisting of large number of simple identical components with local interactions in which space and time are discrete. A cellular automaton works on a grid of cells, and each cell can assume a state from a finite set of states. The cells update their states synchronously on discrete steps according to a local rule. The new state of each cell depends on the previous states of a set of cells, including the cell itself, and constitutes its neighborhood. The state of all cells in the lattice is described by a configuration. The rule and the initial configuration of the CA specify the evolution of CA that tells how each configuration is changed in one step. Cellular automata perform complex computations with a high degree of efficiency and robustness [1].

The neighbourhood of a cell might be defined as the set of cells located at equal distance from the cell. Two commonly used neighborhoods include Moore and Von Neumann neighbourhood. Figure 1a shows the eight Moore neighborhoods cells of cell(0, 0): cell(1, 0), cell(-1, 0), cell(0, 1), cell(0, -1), cell(1, 1), cell(1, -1), cell(-1, 1), cell(-1, -1). Figure 1b shows the four Von Neumann neighborhood cells of cell(0, 0): cell(1, 0), cell(-1, 0), cell(0, 1), cell(0, -1).

Given that sensors of WSNs have limited bandwidth and processing capability that communicates only with its neighbour's processors, proposed solutions for WSN have distributed processing nature to ensure efficiency and scalability. This is similar to CA where the communication between constituent cells is limited to local interaction. Each individual cell in CA is in a specific state which changes over time depending on the states of its local neighbours.

Fig. 1 CA neighborhood:
a Moore. b Von Neumann



This paper proposes a feasible self-deployment heuristic approach for WSN based on the Four Quadrants Deployment Model (FQDM) proposed by Choudhury in [2]. FQDM is a cellular automata model that divides the neighborhood of a cell into four quadrants (North West, North East, South West and South East), and sensors try to find out the directions where they can move to increase the coverage. However FQDM is an ideal deployment approach as it assumes unlimited energy source for sensor nodes, and does not take into account the real energy consumption rates for movement and communication of the sensors nor their residual energy during deployment. Also FQDM reaches a saturated state where no coverage improvement is obtained. Hence FQDM does not give a good coverage especially at border areas. The objective of this paper is to study the effect of applying a realistic energy model to FQDM, and propose an extended version of FQDM to enhance the coverage at border area. The goal of the proposed approach is to relocate the sensors in a way that maximizes the coverage while minimizing energy consumption.

The rest of paper is organized as follows: Sect. 2 surveys researches related to coverage problem. Section 3 presents network model and assumptions. Section 4 describes the energy-aware realistic version of the Four Quadrant Deployment Model (FQDM). Section 5 presents the proposed Drift Towards Corners Algorithm (DTCA). The performance of FQDM and DTCA is evaluated and compared through conducting a simulation study presented in Sect. 6. Section 7 concludes the paper.

2 Related Work

The deployment of sensors to achieve the maximum coverage of grid area with minimum number of mobile sensors is proven to be NP-hard problem [3]. Many researches have targeted the area coverage problem, and proposed several heuristics to find sub-optimal solutions. In this section we briefly discuss some of the related works.

Authors in [4] proposed an autonomous sensor deployment algorithm to optimize energy consumption and solve energy holes problem for unattended mobile sensor networks. It divides the target area into multiple equal width rings, and solves a mathematical problem that models sensor nodes layout and energy-aware transmission mechanism to maximize network coverage and reduce communication cost. The simulation results demonstrate its effectiveness in terms of coverage and network lifetime.

Another optimal placement algorithm based on a “mosaicked technology” such that different types of mobile sensors organize themselves forming a mosaicked pattern to achieve efficient coverage with minimum cost is proposed in [5]. To converge to the optimal state, a swarm intelligence (SI)-based sensor movement algorithm is developed to drive the randomly deployed sensors self-organizing themselves and reach the optimal placement state. Simulation results are presented

to demonstrate the effectiveness of the mosaic placement and the SI-based movement. Other solutions of this problem in some class of work [6–8] are inspired from physics where the sensor node determines its movement direction based on the force received from its neighbours. Other strategies are the grid-based [9, 10] which provide a deterministic deployment where the position of the sensor nodes is fixed according to a special grid pattern such as a triangular lattice, a square grid or a hexagonal grid.

Quite number of researches in coverage for wireless sensor networks is presented in the last decade using cellular automata by deterministic algorithm and probabilistic algorithm [2, 11–13]. In [11] proposes a cellular learning automata-based deployment strategy which guides the movements of unaware location sensor nodes within the area of the network. The learning automaton in each node in cooperation with the learning automata in the neighbouring nodes controls the movements of the node in order to attain high coverage. The work in [12] focuses on a subset of topology control algorithms (duty cycling and scheduling while maintaining connectivity and coverage) and use the cellular automata simulation approach to experimentally investigate which type of neighborhood should be preferred. The algorithm in [13] determines the movement direction of a sensor based on the weighted number of its neighbours in the positive and in the negative direction.

Choudhury in [2] proposes a cellular automata based Four Quadrants Deployment Model (FQDM) that divides the neighbourhood of a cell into four quadrants (North West, North East, South West and South East), and sensors try to find out the directions where they can move to increase the coverage. However FQDM is an ideal deployment approach as it assumes unlimited energy source for sensor nodes, and does not take into account the real energy consumption rates for movement and communication of the sensors nor their residual energy during deployment. Moreover FQDM does not give a good coverage at border areas. Hence the objective of this paper is to study the effect of applying a realistic energy model to FQDM, and propose an extended version of FQDM to enhance the coverage at border area. The goal of the proposed heuristic approach is to relocate the sensors in a way that maximizes the coverage while minimizing energy consumption.

3 Network Model and Assumptions

The monitored area is assumed to be a grid of cells where the state of the cell indicates the existence or the absence of a mobile sensor. We consider a mobile WSN with a set of sensors initially accumulated on a center of two dimensional area. Sensor nodes are homogenous in terms of the communication range, sensing range, power consumption rate, and initial energy values. The sensing radius R_s and communication range R_c of mobile sensors are Moore's neighbourhood, and are taken up to two and four layers respectively. When $R_c \leq 2R_s$ sensor deployments that maximize coverage of WSNs maintaining the connectivity of its nodes [3]. In each time epoch, a sensor can move a maximum of one cell in any direction. Each

sensor tracks its energy reserve. Obstacle free terrain is assumed in the deployment. The sensors are allowed to spread gradually according to CA rules as we discuss in the following section.

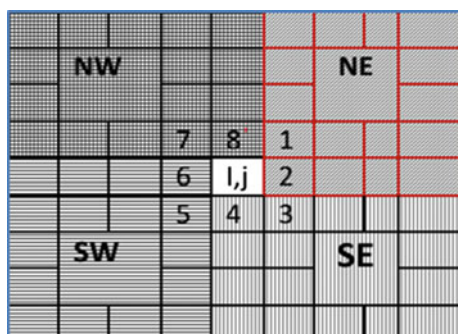
4 Energy Aware Four Quadrant Deployment Model

Energy aware FQDM is a feasible self-deployment heuristic approach for WSN based on FQDM. FQDM is a cellular automata model that divides the neighborhood of a cell into four quadrants (North West NW, North East NE, South West SW and South East SE), and sensors follow CA rules to find out the quadrant where they can move to increase the coverage. However FQDM is an ideal deployment approach as it assumes unlimited energy source for sensor nodes, and does not take into account the real energy consumption rates for movement and communication of the sensors nor their residual energy during deployment. Each time epoch of FQDM is divided into two phases: In the first phase, each sensor determines whether it should move or not, and direction of movement, and the weight value according to following equation:

$$W_x = 4 * N1 + 3 * N2 + 2 * N3 + 1 * N4 \quad (1)$$

where N_i is the number of sensors in quadrant x at distance exactly i from the current cell [2]. A higher weight is given for sensors that are closer to the current sensor. Each sensor determines the maximum and the minimum weight values for its four quadrants. If the minimum value is less than k_1 and the maximum value is more than k_2 , then the sensor chooses the quadrant with the minimum weight value to direct to. Where k_1, k_2 are two chosen adjusted positive integers. For each quadrant, there are two nearest position where the sensor node can move to. As shown in Fig. 2, sensor i, j can move to cell 1 or 2 in NE, for SE it can move to cell

Fig. 2 FQDM deployment model



3 or 4, for SW it can move to cell 5 or 6, and cell 7 or 8 for NW. In the second phase, the sensor moves to previously chosen cell if that cell is empty.

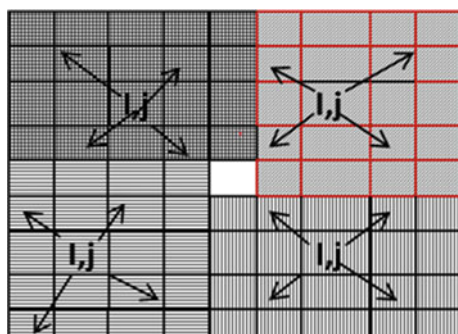
For each time epoch of energy aware FQDM, sensor node in the field exchanges a status packet with its neighbors up to radius four (communication range) that inform each other about its grid position.

The energy status of each node is updated by calculating the energy cost for communication (transmit and receiving), and motion taking into consideration the residual energy of each node. Each sensor iterates the procedures of the two phases for each time epoch until it reaches a steady state where its residual energy reaches a previously set threshold value E_{th} , or a final configuration is obtained. At this state, the sensor node remains still to save energy, however it shares its status with its neighbors. For each quadrant a negative weight -1 is assigned to a steady state node.

5 Proposed Drifting Towards Corners Algorithm (DTCA)

To enhance the coverage of the monitored area specially at corners, we proposed a Drifting Towards Corners Algorithm (DTCA). Energy aware FQDM is initially applied until we reach an epoch where no significant coverage improvement is observed. Then DTCA changes the transition rules of a subset of sensor nodes whose residual energy reaches a previously set threshold value in order to improve the obtained coverage. DTCA assumed that the whole monitored area is divided into four equivalent adjacent partitions: North East (NE), North West (NW), South East (SE) and South West (SW). It also assumes that the sensors are aware of which partition they belong to in each epoch. Sensors that reach their steady state (residual energy reached a threshold value) start a timer of T epochs to save energy. After elapsing the period T , the sensor opts randomly to migrate to one corner of its partition with different probabilities, and updates its energy status as illustrated in Fig. 3. The impact of variation of these probability settings was heuristically

Fig. 3 DTCA deployment model



investigated to distribute the sensors as evenly as possible while conserving their energy as much as this is possible. Different probability settings are assigned as follows.

The sensor node in the North West partition of the area is assigned a highest probability 60% to move to north west neighborhood positions $\text{cell}(i - 1, j - 1)$ or $\text{cell}(i - 1, j)$ to maximize the coverage of border area, and 10% to move back to opposite corner SW $\text{cell}(i + 1, j + 1)$ or $\text{cell}(i + 1, j)$ to prevent hole creation. It is also assigned a probability 15% to move to $\text{cell}(i, j - 1)$ or $\text{cell}(i + 1, j - 1)$ in SW and 15% move to $\text{cell}(i - 1, j + 1)$ or $\text{cell}(i, j + 1)$ in NE to distribute the sensors as evenly as possible.

The sensor node in the North East partition of the area is assigned a highest probability 60% to move to north east neighborhood positions $\text{cell}(i - 1, j + 1)$ or $\text{cell}(i, j + 1)$ to maximize the coverage of border area, and 10% to move back to opposite corner $\text{cell}(i, j - 1)$ or $\text{cell}(i + 1, j - 1)$ to prevent hole creation. It is also assigned probability 15% to move to $\text{cell}(i - 1, j)$ or $\text{cell}(i - 1, j - 1)$ in NW and 15% move to $\text{cell}(i + 1, j + 1)$ or $\text{cell}(i + 1, j)$ in SW to distribute the sensors as evenly as possible.

The sensor node in the South West partition of the area is assigned a highest probability 60% to move to south west neighborhood positions $\text{cell}(i, j - 1)$ or $\text{cell}(i + 1, j - 1)$ to maximize the coverage of border area, and 10% to move back to opposite corner $\text{cell}(i - 1, j + 1)$ or $\text{cell}(i, j + 1)$ to prevent hole creation. It is also assigned probability 15% to move to $\text{cell}(i + 1, j)$ or $\text{cell}(i + 1, j + 1)$ in SE and 15% to move to $\text{cell}(i - 1, j - 1)$ or $\text{cell}(i - 1, j)$ in NW to distribute the sensors as evenly as possible.

The sensor node in the South East partition of the area is assigned a highest probability 60% to move to south east neighborhood positions $\text{cell}(i + 1, j)$ or $\text{cell}(i + 1, j + 1)$ to maximize the coverage of border area, and 10% to move back to opposite corner $\text{cell}(i - 1, j - 1)$ or $\text{cell}(i - 1, j)$ to prevent hole creation. It is also assigned a probability 15% to move to $\text{cell}(i, j - 1)$ or $\text{cell}(i + 1, j - 1)$ in SW, and 15% to move to $\text{cell}(i - 1, j + 1)$ or $\text{cell}(i, j + 1)$ in NE to distribute the sensors as evenly as possible. DTCA algorithm is listed in Fig. 4.

6 Performance Evaluation

We evaluated the coverage of FQDM deployment model in a bounded area with realistic energy model and compare its performance with DTCA deployment model through conducting an extensive simulation study. To save WSN energy during deployment in FQDM, sensors opt to stop moving when their energy reserves reach a given threshold value E_{th} specified by the designer. Setting a proper value for energy threshold highly affects the network lifetime. Our goal is to study and compare the effect of different energy thresholds on the deployment performance for both FQDM and DTCA. This section describes the simulation environment, performance metrics, and analyses of the obtained results.

6.1 Simulation Environment and Performance Metrics

To evaluate the performance of the energy aware FQDM, we simulated an environment of two dimension 100×100 grid in Matlab. We applied the Energy model in [14] that simulate the well-known IEEE 802.15.4 Mica2 wireless sensor

```

Set energy threshold to  $E_{th}$ ;
Do while coverage is improving
    Each sensor in WSN applies Energy-aware FQDM;
End Do
Repeat
    Select steady state nodes  $\{S_{th}\}$  with residual energy  $\leq E_{th}$ 
    For each sensor S in  $\{S_{th}\}$ 
    {
        Wait for T epochs
        If S is located in NW Then
            Assign 60% probability to move to cell(i-1, j-1) or cell(i-1, j) // to maximize coverage
            Assign 10% probability to move to cell(i+1, j+1) or cell(i+1, j) // to prevent hole creation
            Assign 15% probability to move to cell(i, j-1) or cell(i+1, j-1) // for even distribution
            Assign 15% probability to move to cell(i-1, j+1) or cell(i, j+1) // for even distribution
        ElseIf S is located in NE Then
            Assign 60% probability to move to cell(i-1, j+1) or cell(i, j+1) // to maximize coverage
            Assign 10% probability to move to cell(i, j-1) or cell(i+1, j-1) // to prevent hole creation
            Assign 15% probability to move to cell(i-1, j-1) or cell(i-1, j-1) // for even distribution
            Assign 15% probability to move to cell(i+1, j+1) or cell(i+1, j) // for even distribution
        ElseIf S is located in SW Then
            Assign 60% probability to move to cell(i, j-1) or cell(i+1, j-1) // to maximize coverage
            Assign 10% probability to move to cell(i-1, j+1) or cell(i, j+1) // to prevent hole creation
            Assign 15% probability to move to cell(i+1, j) or cell(i+1, j+1) // for even distribution
            Assign 15% probability to move to cell(i-1, j-1) or cell(i-1, j) // for even distribution
        ElseIf S is located in SE Then
            Assign 60% probability to move to cell(i+1, j) or cell(i+1, j+1) // to maximize coverage
            Assign 10% probability to move to cell(i-1, j-1) or cell(i-1, j) // to prevent hole creation
            Assign 15% probability to move to cell(i, j-1) or cell(i+1, j-1) // for even distribution
            Assign 15% probability to move to cell(i-1, j+1) or cell(i, j+1) // for even distribution
        EndIf
        Relocate sensor S and update its energy status;
    }
    For each sensor S not in  $\{S_{th}\}$ 
        Apply Energy-aware FQDM;
    Until maximum coverage is achieved

```

Fig. 4 DTCA algorithm

mote. Energy Tx = 3.12 μ J/bit. Energy Rx = 2.34 μ J/bit. Energy motion = 90 mJ/m. Each sensor is assigned an initial energy of 500 J. Different experiments are carried out to deploy a bundle of sensors N in bounded square field of dimension 100 * 100. We set N equal to 1225 after conducting many simulation experiments to get the best value. The sensors N are initially placed in the center of a two dimensions 100 \times 100 grid. Each cell has two states: state 1 (white) to indicate that the cell has a sensor node, while empty cell is set to state 0 (black).

The performance is evaluated using the following metrics:

- Area coverage percentage: the percentage of total grids covered by at least one sensor node.
- Deployment time: the required time epochs to get the final configuration.
- Residual energy percentage: the ratio of total energy reserved on sensor nodes to the total initial energy when the final configuration is reached.
- Number of relocations: total number of movement done by sensor nodes of the network while they are deployed.
- Steady state nodes: the ratio of nodes that reached Eth to the total deployed nodes while they are deployed.
- k-coverage: a sensor deployment pattern where each cell in the area is covered by at least k deployed sensor nodes.

6.2 Results Analysis

Figure 5a shows the initial position of sensor nodes on the field while Fig. 5b, c indicate the deployment pattern of 1225 sensors at 400 time epoch for FQDM and DTCA. Figure 6 shows the area coverage percentage for FQDM and DTCA with residual energy threshold Eth adjusted to 200J and 300J respectively. Figure 7 shows how the total residual energy is affected.

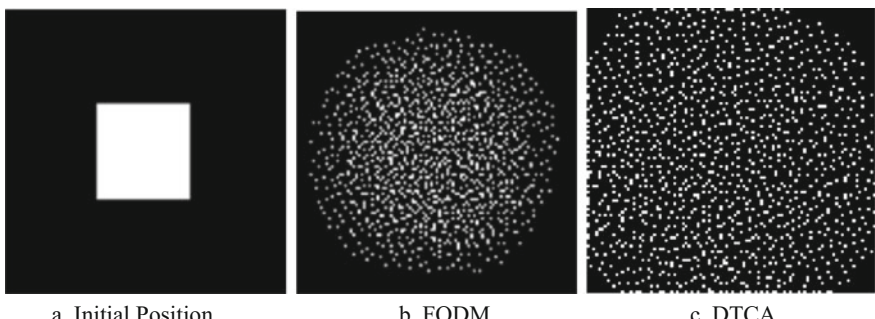


Fig. 5 Deployment pattern of 1225 sensors at 400 time epoch for FQDM and DTCA

Fig. 6 Area coverage percentage for FQDM and DTCA with different Eth

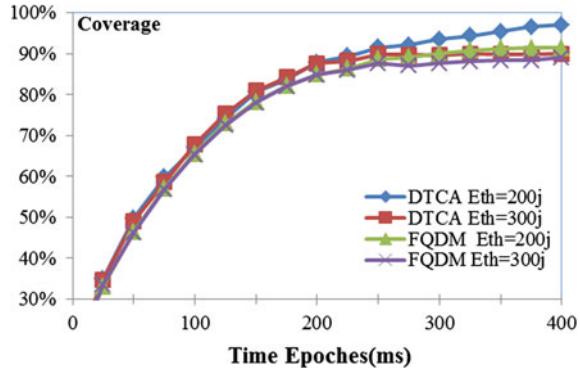
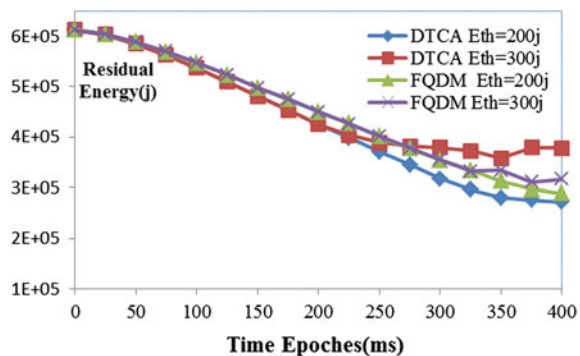


Fig. 7 Residual energy for FQDM and DTCA with different Eth



Results show that with increasing time epochs, DTCA achieves the highest area coverage during the deployment for Eth = 200j. The deployment pattern obtained by DTCA achieves a maximum coverage of 97% with saving 45% residual energy percentage at time epoch 375, while FQDM achieves 91% with almost the same residual energy saving 46% at the same time epoch and energy threshold.

With FQDM, varying Eth has no significant effect on the coverage percentage though it consumes a considerable higher amount of energy. It achieves a maximum coverage of 91% with 46% residual energy percentage for Eth = 200j, and 89% coverage with 52% residual energy percentage for Eth = 300j. However varying Eth highly affects the coverage percentage and residual energy for DTCA, it achieves a maximum coverage of 97% with 45% residual energy percentage for Eth = 200j, and 89% coverage with 52% residual energy percentage for 300j. From the simulation results we can deduce that with a given node density and adjusted energy threshold our proposed algorithm DTCA to enhance FQDM can converge to a global optimal distribution.

Figure 8 shows the total number of relocations during deployment for FQDM and DTCA with Eth equals to 200j and 300j respectively.

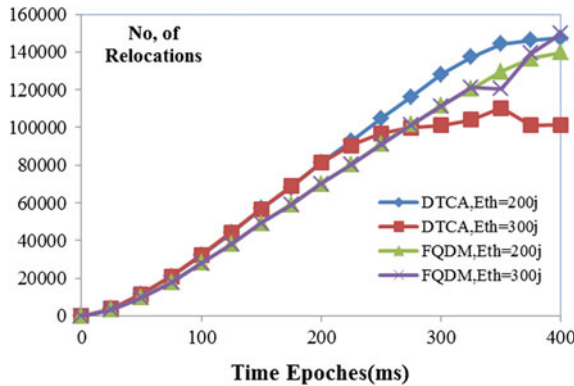


Fig. 8 Total relocations for FQDM and DTCA with different Eth

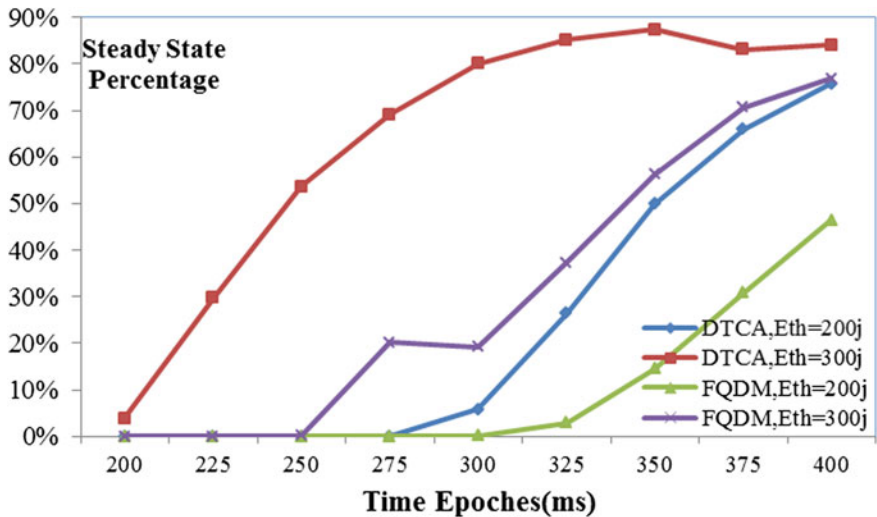


Fig. 9 Steady state nodes for FQDM and DTCA with different Eth

Results show that with increasing epochs, the number of relocations is increased constantly. Intuitively, steady state sensors growth with increasing number of relocations results in hindering further relocation and coverage improving. However it extends the lifetime of the network. Figure 9 shows the percentage of steady state nodes during deployment for both FQDM and DTCA with Eth equals to 200j and 300j respectively.

Interestingly we also observe that in DTCA deployment, the minimum residual energy gets close to the average residual energy (the total residual energy divided by the number of sensors) when reaching the final configuration. This demonstrates

Table 1 k-coverage for DTCA and FQDM

k/coverage	DTCA		FQDM	
	200j (%)	300j (%)	200j (%)	300j (%)
k >= 1	97	91	89	88
k >= 3	67	66	64	66
k >= 5	10	19	14	18
k >= 7	1	0.53	2	2

that DTCA has the ability to balance the energy consumption of WSN sensors and avoid overburdening some of the nodes.

It should be mentioned that although energy aware FQDM and DTCA are not designed for k-coverage requirement where each cell is covered by at least k sensors, they provide a good results for applications with k-coverage requirements. Table 1 shows k-coverage results at 375 epoch for DTCA and FQDM with different Eth. We noticed that 67% of the monitored area is covered by at least 3 sensors for DTCA with Eth = 200j, and 66% of the area for DTCA with Eth = 300j. For energy aware FQDM, 64% of the monitored area is covered by at least 3 sensors with Eth = 200j, and 66% of the area with Eth = 300j.

7 Conclusion

This paper proposes an energy aware autonomous deployment heuristic approach for mobile WSNs based on Four Quadrants Deployment Model (FQDM). The objective of the paper is to study the effect of applying a realistic energy model to FQDM, and propose an extended version DTCA to enhance the coverage at border areas by relocating the sensors in a way that maximizes the coverage as much as possible while minimizing energy consumption. We evaluate the coverage of FQDM in a bounded square area and compare its performance with DTCA. Simulation results demonstrate that DTCA can converge to a global optimal distribution. It gives a significant higher coverage while conserving energy of sensors.

References

- Chopard, B., Droz, M.: Cellular Automata Modelling of Physical Systems. Cambridge University Press (2005). ISBN 0521461685
- Choudury, S.: Cellular Automaton Based Algorithms for Wireless Sensor Networks. PhD thesis, School of Computing, Queen's University, Canada (2011)
- Wang, Y., Zhang, Y., Liu, J., Bhandari.: Coverage, connectivity, and deployment in wireless sensor networks. In: Recent Development in Wireless Sensor and Ad-hoc Networks, pp. 25–44. Springer, India (2015)
- Chen, J., Jie, J., Wen, Y., Zhao, D.: Towards an optimal energy consumption for unattended mobile sensor networks through autonomous sensor redeployment. Sci. World J. (2014)

5. Miao, L., Qi, H., Wang, F.: Biologically-inspired self-deployable heterogeneous mobile sensor networks. In: IEEE/RSJ International Conference on Intelligent Robots and Systems, 2005, (IROS 2005). IEEE (2005)
6. Zou, Y., Chakrabarty, K.: Sensor Deployment and Target Localization Based on Virtual Forces. IEEE INFOCOM (2003)
7. Li, J., Zhang, B., Cui, L., Chai, S.: An extended virtual force-based approach to distributed self-deployment in mobile sensor networks. *Int. J. Distrib. Sens. Netw.* (2012)
8. Chen, J., Li, S., Yuxian, S.: Novel deployment schemes for mobile sensor networks. *Sensors* **7** (11), 2907–2919 (2007)
9. Park, P., Min, S.G., Han, Y.H.: A grid-based self-deployment schemes in mobile sensor networks. In: Ubiquitous Information Technologies and Applications (CUTE), IEEE Explore, pp. 1–5 (2010)
10. Fletcher, G., Li, X., Nayak, A., Stojmenovic, I.: Back-tracking based sensor deployment by a robot team. In: 2010 7th Annual IEEE Communications Society Conference on Sensor, Mesh and Ad Hoc Communications and Networks (SECON), pp. 1–9. IEEE (2010)
11. Esnaashari, M., Meybodi, M.: A cellular learning automata-based deployment strategy for mobile wireless sensor networks. *J. Parallel Distrib. Comput.* 988–1001 (2011)
12. Athanassopoulos, S., Athanassopoulos, S., Kaklamanis, C., Kalfountzos, G., Papaioannou, E.: Cellular automata for topology control in wireless sensor networks using Matlab. In: Future Information Technology, Applications and Services. Springer, pp. 13–20 (2012)
13. Choudhury, S., Salomaa, K., Akl, S.G.: Cellular automaton based motion planning algorithms for mobile sensor networks. In: Theory and Practice of Natural Computing, pp. 108–120. Springer, Berlin (2012)
14. Calle, M.: Energy consumption in wireless sensor networks using gsp. Master's Thesis, School of Information Sciences, University of Pittsburgh (2006)

An Optimal Process for Average Value-at-Risk Portfolios in Financial Management

Yuji Yoshida

Abstract A dynamic average value-at-risk portfolio model under uncertainty is discussed. At each period analytical solutions for the problem are obtained. By dynamic programming, an optimality equation for optimal average value-at-risks is derived. It is shown that the optimal average value-at-risk portfolios are solutions of the optimality equation.

Keywords Average value-at-risk · Optimal portfolio · Dynamic risk allocation · Risk probability · Bankruptcy · Dynamic programming

1 Introduction

In financial asset management, portfolio technique is important for hedging the risk and it is used to make asset management stable. As a classical portfolio theory, *Markowitz's mean-variance model* is studied by many researchers and fruitful results have been achieved, and the variance-minimizing is also important to minimize the risk in portfolio [5, 7–9]. Recently, *value-at-risk (VaR)* is used widely in finance to estimate the risk of worst-scenarios. VaR is a risk-sensitive criterion based on percentiles, and it is one of the standard criteria in asset management [3, 6, 12–14]. VaR is a kind of risk values of the asset prices at a specified risk-level probability and it is for selecting portfolios to get rid of bad scenarios in investment. An extension of VaR is *average value-at-risk (AVaR)*, and it is known that AVaR is a *coherent risk measure* but VaR is not coherent [1]. Markowitz's mean-variance criterion and variance-minimizing criterion are represented by quadratic programming, and AVaR criterion is analyzed based on the results regarding Markowitz's criterion. In this paper dynamic AVaR portfolio selection problem is proposed in order to maximize both of AVaR and the expected rates of return, and owing to AVaR we can

Y. Yoshida (✉)

Faculty of Economics and Business Administration, University of Kitakyushu,
4-2-1 Kitagata, Kokuraminami, Kitakyushu 802-8577, Japan
e-mail: yoshida@kitakyu-u.ac.jp

maximize the expected rate of return after due consideration of the worst-scenarios. This paper derives analytical solutions for the AVaR portfolio problem at each step, which is strongly related to the bankruptcy and the falling in the asset prices [4]. Introducing AVaR based on conditional probability, we discuss a dynamic optimization problem and we derive the optimality equation and the optimal solution for the model by dynamic programming.

2 A Dynamic Portfolio Model

First we explain a portfolio model with n stocks, where n is a positive integer. Let $\{0, 1, 2, \dots, T\}$ be the time space with an expiration date T , and \mathbb{R} denotes the set of all real numbers. Let (Ω, \mathcal{M}, P) be a probability space, where \mathcal{M} is a σ -field and P is a non-atomic probability on a sample space Ω . For an asset $i = 1, 2, \dots, n$, a stock price process $\{S_t^i\}_{t=0}^T$ is given by *rates of return* R_t^i [10, 11]:

$$S_t^i = S_{t-1}^i(1 + R_t^i) \quad (1)$$

for $t = 1, 2, \dots, T$, where $\{R_t^i\}_{t=1}^T$ is an integrable sequence of independent real-valued random variables. Hence $(w_t^1, w_t^2, \dots, w_t^n)$ is called a *portfolio weight vector* if it satisfies $\sum_{i=1}^n w_t^i = 1$, and further the portfolio is said to *allow for short selling* if $w_t^i \geq 0$ for all $i = 1, 2, \dots, n$. Then the rate of return with a portfolio $(w_t^1, w_t^2, \dots, w_t^n)$ is given by

$$R_t = w_t^1 R_t^1 + w_t^2 R_t^2 + \dots + w_t^n R_t^n. \quad (2)$$

Therefore, the reward at time $t (= 1, 2, \dots, T)$ follows

$$S_t = S_{t-1} \sum_{i=1}^n w_t^i (1 + R_t^i) = S_{t-1} (1 + R_t). \quad (3)$$

This paper deals with a dynamic portfolio model for stock price processes $\{S_t^i\}_{t=0}^T$. The falling of asset prices is one of the most important risks in stock markets. The theoretical *bankruptcy* at time t occurs on scenarios ω satisfying $S_t(\omega) \leq 0$, i.e. it follows $1 + R_t(\omega) \leq 0$ from (3). Similarly, for a constant $\delta \in [0, 1]$, a set of sample paths $\{\omega \in \Omega \mid 1 + R_t(\omega) \leq 1 - \delta\} = \{\omega \in \Omega \mid R_t(\omega) \leq -\delta\}$ is the event of scenarios where the asset price S_t will fall from the current price S_{t-1} to a lower level than $100(1 - \delta)\%$ of the current price S_{t-1} , i.e. the rate of falling is $100\delta\%$. The parameter δ is called *the rate of falling*. Then the probability of falling is also given by

$$p_\delta = P(R_t \leq -\delta). \quad (4)$$

For example, p_δ denotes the probability of the falling below par value if ‘ $\delta = 0$ ’ and it indicates the probability of the bankruptcy if ‘ $\delta = 1$ ’. In this paper, we discuss dynamic portfolio optimization regarding the rate of falling δ .

For a positive probability p , VaR regarding the rate of return R_t is given by a real number v satisfying

$$P(R_t \leq v) = p \quad (5)$$

since P is non-atomic. VaR v is the upper bound of the rate of return R_t at the worst scenarios under a given risk probability p , and then VaR v in (5) is denoted by $\text{VaR}_p(R_t)$. From (4) and (5), for a risk probability $p = p_\delta$, the rate of falling is

$$\delta = -\text{VaR}_p(R_t). \quad (6)$$

In next section we discuss the minimization of the rate of falling (6). In this paper, we deal with a case where VaR v in (5) has the following representation.

$$(\text{VaR } v) = (\text{the mean}) - (\text{a positive constant } \kappa_p) \times (\text{the standard deviation}), \quad (7)$$

where the positive constant κ_p is given corresponding to the probability p . Equation (7) holds if the distribution of the rate of return R_t is Gaussian [2, 6].

3 A Dynamic AVaR Portfolio Model

First we introduce mathematical notations of average value-at-risk [12, 13]. Let \mathcal{X} be the set of all integrable \mathcal{M} -adapted real-valued random variables X on Ω with a continuous distribution function $x \mapsto F_X(x) = P(X < x)$ for which there exists a non-empty open interval I such that $F_X(\cdot) : I \rightarrow (0, 1)$ is strictly increasing and onto. Then there exists a strictly increasing and continuous inverse function $F_X^{-1} : (0, 1) \rightarrow I$. We note that $F_X(\cdot) : I \rightarrow (0, 1)$ and $F_X^{-1} : (0, 1) \rightarrow I$ are one-to-one and onto. The *value-at-risk (VaR)* at a probability $p \in (0, 1)$ is given by the percentile of the distribution function F_X , i.e. $\text{VaR}_p(X) = \sup\{x \in I \mid F_X(x) \leq p\}$. Then we have $F_X(\text{VaR}_p(X)) = p$ and $\text{VaR}_p(X) = F_X^{-1}(p)$. The *average value-at-risk (AVaR)* at a probability p is given by

$$\text{AVaR}_p(X) = \frac{1}{p} \int_0^p \text{VaR}_q(X) dq \quad (8)$$

for $p \in (0, 1)$. It is known that AVaR is a *coherent risk measure* [1] but VaR is not coherent. From (3), AVaR for the reward S_t at time t is given by $\text{AVaR}_p(S_t) = \text{AVaR}_p(S_{t-1}(1 + R_t))$. To discuss the dynamics, we introduce VaR based on conditional expectations. Let \mathcal{G} be a sub- σ -field of \mathcal{M} . Define a map $x \mapsto F_X(x \mid \mathcal{G}) = P(X < x \mid \mathcal{G}) = E(1_{\{X < x\}} \mid \mathcal{G})$. We introduce VaR of $X \in \mathcal{X}$ under a condition \mathcal{G} at a

probability p by $\text{VaR}_p(X \mid \mathcal{G}) = \sup\{x \in I \mid F_X(x \mid \mathcal{G}) \leq p\}$. Then *AVaR under a condition \mathcal{G}* is given by $\text{AVaR}_p(X \mid \mathcal{G}) = \frac{1}{p} \int_0^p \text{VaR}_q(X \mid \mathcal{G}) dq$ for $p \in (0, 1)$, and we note $\text{AVaR}_p(X \mid \mathcal{G})$ is a \mathcal{G} -measurable random variable and $F_X(\text{AVaR}_p(X \mid \mathcal{G}) \mid \mathcal{G}) \leq p$ for $p \in (0, 1)$. From (3), portfolio weights $(w_t^1, w_t^2, \dots, w_t^n)$ are decided sequentially and predictably. We note that S_t is estimated under information \mathcal{M}_{t-1} up to time $t-1$. Then VaR of S_t under information \mathcal{M}_{t-1} at a probability p is $\text{AVaR}_p(S_t \mid \mathcal{M}_{t-1}) = \text{AVaR}_p(S_{t-1}(1 + R_t) \mid \mathcal{M}_{t-1})$. This term means the risk of worst scenarios which occur on the transition from time $t-1$ to time t . Therefore, taking the sum of these risks which occur at each time, we demonstrate the following dynamic portfolio problem regarding the total AVaR under information $\{\mathcal{M}_{t-1}\}_{t=1}^T$. Let a discount rate β be a positive constant and take $S_0 = 1$ for simplicity. Define the set of portfolios by $\mathcal{W} = \{(w^1, w^2, \dots, w^n) \in \mathbb{R}^n \mid \sum_{i=1}^n w^i = 1 \text{ and } w^i \geq 0 (i = 1, 2, \dots, n)\}$.

Dynamic problem for AVaR: Maximize the total AVaR

$$E \left(\sum_{t=1}^T \beta^{t-1} \text{AVaR}_p(S_t \mid \mathcal{M}_{t-1}) \right) = \sum_{t=1}^T \beta^{t-1} \prod_{s=1}^{t-1} (1 + E(R_s)) \cdot (1 + \text{AVaR}_p(R_t)) \quad (9)$$

with portfolio weights $(w_t^1, w_t^2, \dots, w_t^n) \in \mathcal{W} (t = 1, 2, \dots, T)$.

By dynamic programming, we obtain the following equations.

Theorem 1 *The optimal AVaR in Dynamic problem for AVaR is given by v_1 which is defined inductively by the sequence $\{v_t\}$ of sub-total AVaR after time $t-1$ satisfying the following backward optimality equations:*

$$v_{t-1} = \max_{(w^1, \dots, w^n) \in \mathcal{W}} \left\{ 1 + \text{AVaR}_p \left(\sum_{i=1}^n w^i R_{t-1}^i \right) + \beta \left(1 + \sum_{i=1}^n w^i E(R_{t-1}^i) \right) v_t \right\} \quad (10)$$

for $t = 2, 3, \dots, T$, and

$$v_T = \max_{(w^1, \dots, w^n) \in \mathcal{W}} \left\{ 1 + \text{AVaR}_p \left(\sum_{i=1}^n w^i R_T^i \right) \right\}. \quad (11)$$

4 An Optimal Portfolio for AVaR

First we estimate the rate of return with a portfolio [12, 13]. Let the mean, the variance and the covariance of the rate of return R_t^i , which is given in (1), respectively by $\mu_t^i = E(R_t^i)$, $(\sigma_t^i)^2 = E((R_t^i - \mu_t^i)^2)$ and $\sigma_t^{ij} = E((R_t^i - \mu_t^i)(R_t^j - \mu_t^j))$ for $i, j = 1, 2, \dots, n$. Hence we assume that the determinant of the variance-covariance matrix $\Sigma_t = [\sigma_t^{ij}]$ is not zero and there exists its inverse matrix Σ_t^{-1} . This assumption is natural and

it can be realized easily by taking care of the combinations of assets. For a portfolio $(w^1, w^2, \dots, w^n) \in \mathcal{W}$, we calculate the expectation and the variance regarding $R_t = \sum_{i=1}^n w^i R_t^i$. The expectation μ_t of the rate of return R_t with the portfolio is $\mu_t = E(R_t) = \sum_{i=1}^n w^i E(R_t^i) = \sum_{i=1}^n w^i \mu_t^i$. On the other hand, the variance $(\sigma_t)^2$ of the rate of return R_t with the portfolio is $(\sigma_t)^2 = E((R_t - \mu_t)^2) = \sum_{i=1}^n \sum_{j=1}^n w^i w^j \sigma_t^{ij}$ for $i = 1, 2, \dots, n$. Therefore, for a positive probability p , AVaR of the rate of return R_t is evaluated as $\text{AVaR}_p(R_t) = \sum_{i=1}^n w^i \mu_t^i - \kappa \sqrt{\sum_{i=1}^n \sum_{j=1}^n w^i w^j \sigma_t^{ij}}$ with a positive constant $\kappa = \frac{1}{p} \int_0^p \kappa_q dq$ with κ_p in (7). Let $\mathbf{1}$ be a unit vector and let $\mu_t = [\mu_t^i]$, $\Sigma_t = [\sigma_t^{ij}]$, $A_t = \mathbf{1}^\top \Sigma_t^{-1} \mathbf{1}$, $B_t = \mathbf{1}^\top \Sigma_t^{-1} \mu_t$, $C_t = \mu_t^\top \Sigma_t^{-1} \mu_t$ and $\Delta_t = A_t C_t - B_t^2$, where \top denotes the transpose of a vector. Now step by step we discuss a portfolio problem to minimize the rate of falling. First, we deal with a variance-minimizing problem. For a given constant γ , which is the total expected rate of return to be guaranteed for portfolios, we consider the following quadratic programming with respect to portfolios.

Variance-minimizing (P1): Minimize the variance $\sum_{i=1}^n \sum_{j=1}^n w^i w^j \sigma_t^{ij}$ with respect to portfolios (w^1, w^2, \dots, w^n) satisfying $\sum_{i=1}^n w^i = 1$ under a condition $\sum_{i=1}^n w^i \mu_t^i = \gamma$.

Lemma 1 [12, 13]. *The solution of the variance-minimizing (P1) is given by $w = \xi \Sigma^{-1} \mathbf{1} + \eta \Sigma^{-1} \mu$ and then the corresponding variance is $\rho = \frac{A\gamma^2 - 2B\gamma + C}{\Delta}$.*

Solution w in Lemma 1 is called a *minimal risk portfolio*, and a set $\mathcal{E} = \{(\rho, \mu) \mid \rho = \frac{A(\mu)^2 - 2B\mu + C}{\Delta}$ and $\mu \geq \frac{B}{A}\}$ is also called the *efficient frontier* [7, 8], where ρ is a variance and μ is an expected rate of return for acceptable minimal risk portfolios. Next we consider a risk-sensitive model in order to deal with a portfolio problem to minimize the rate of falling in the third step. For a constant γ , we discuss the following risk-sensitive portfolio problem.

Risk-sensitive problem (P2): Maximize risk-sensitive expected rate of return

$$\sum_{i=1}^n w^i \mu_t^i - \kappa \sqrt{\sum_{i=1}^n \sum_{j=1}^n w^i w^j \sigma_t^{ij}} \quad (12)$$

with respect to portfolios (w^1, w^2, \dots, w^n) ($\sum_{i=1}^n w^i = 1$) under the condition $\sum_{i=1}^n w^i \mu_t^i = \gamma$.

Lemma 2 *Let A and Δ be positive. If κ satisfies $\kappa^2 > \Delta/A$, then a function $v : \mathbb{R} \rightarrow \mathbb{R}$ given by $v(\gamma) = \gamma - \kappa \sqrt{\frac{A\gamma^2 - 2B\gamma + C}{\Delta}}$ ($\gamma \in \mathbb{R}$) is concave and it has the maximum $v(\gamma^*) = \frac{B - \sqrt{Ak^2 - \Delta}}{A}$ at $\gamma^* = \frac{B}{A} + \frac{\Delta}{A\sqrt{Ak^2 - \Delta}}$.*

Now we discuss the following portfolio problem to minimize the rate of falling (6) without allowance for short selling. The rate of falling (6) is given by the following (13).

Portfolio minimizing the risk of falling (P3): Minimize the risk of falling

$$\delta = -\text{AVaR}_p(R_t) = - \sum_{i=1}^n w^i \mu_t^i + \kappa \sqrt{\sum_{i=1}^n \sum_{j=1}^n w^i w^j \sigma_t^{ij}} \quad (13)$$

with portfolio weights $(w^1, w^2, \dots, w^n) \in \mathcal{W}$.

Hence since we have $\inf_w (13) = \inf_\gamma (\inf_{w: \sum_{i=1}^n w^i \mu_i^\gamma = \gamma} (13)) = -\sup_\gamma (12)$, by Lemma 2 we arrive at the following analytical solutions for (P3).

Lemma 3 Let A and Δ be positive, and let κ satisfy $\kappa^2 > C$. Then an optimal solution for (P3) is given by $w^* = \xi \Sigma^{-1} \mathbf{1} + \eta \Sigma^{-1} \mu$, and then the corresponding rate of falling is $\delta(\gamma^*) = -\frac{B - \sqrt{A\kappa^2 - \Delta}}{A}$ at the expected rate of return $\gamma^* = \frac{B}{A} + \frac{\Delta}{A\sqrt{A\kappa^2 - \Delta}}$, where $\xi = \frac{C - B\gamma^*}{\Delta}$ and $\eta = \frac{A\gamma^* - B}{\Delta}$.

Condition (V). $v_t > 0$ for all $t = 1, 2, \dots, T$.

Condition (V) is a natural one because if Condition (V) is not satisfied at some time t , it has already gone bankrupt. Under Condition (V), from Theorem 1 and Lemma 3, we obtain the following results. We can calculate numerical optimal solutions by the optimality equation in Theorem 2 and numerical optimal solutions at each time given in Lemma 3.

Theorem 2 Suppose Condition (V) is satisfied. The optimal AVaR v_1 in Theorem 1 is given by the sequence $\{v_t\}$ of sub-total AVaR after time $t - 1$ satisfying the following backward optimality equations:

$$v_{t-1} = \max_{(w^1, \dots, w^n) \in \mathcal{W}} (1 + \beta v_t) \left(1 + \sum_{i=1}^n w^i \mu_{t-1}^i - \frac{\kappa}{1 + \beta v_t} \sqrt{\sum_{i=1}^n \sum_{j=1}^n w^i w^j \sigma_{t-1}^{ij}} \right) \quad (14)$$

for $t = 2, 3, \dots, T$, and

$$v_T = \max_{(w^1, \dots, w^n) \in \mathcal{W}} \left(1 + \sum_{i=1}^n w^i \mu_T^i - \kappa \sqrt{\sum_{i=1}^n \sum_{j=1}^n w^i w^j \sigma_T^{ij}} \right). \quad (15)$$

Acknowledgements This research is supported from JSPS KAKENHI Grant Number JP 16K05282.

References

1. Artzner, P., Delbaen, F., Eber, J.-M., Heath, D.: Coherent measures of risk. *Math. Finance* **9**, 203–228 (1999)
2. Chaoui, L.El., Oks, M., Oustry, F.: Worst-case value at risk and robust portfolio optimization: a conic programming approach. *Oper. Res.* **51**, 543–556 (2003)
3. Jorion, P.: *Value at Risk: The New Benchmark for Managing Financial Risk*. McGraw-Hill, New York (2006)
4. Kumar, P.R., Ravi, V.: Bankruptcy prediction in banks and firms via statistical and intelligent techniques—a review. *Eur. J. Oper. Res.* **180**, 1–28 (2007)
5. Markowitz, H.: *Mean-Variance Analysis in Portfolio Choice and Capital Markets*. Blackwell, Oxford (1990)
6. Meucci, A.: *Risk and Asset Allocation*. Springer, Heidelberg (2005)
7. Pliska, S.R.: *Introduction to Mathematical Finance: Discrete-Time Models*. Blackwell Publishers, New York (1997)
8. Ross, S.M.: *An Introduction to Mathematical Finance*. Cambridge University Press, Cambridge (1999)
9. Steinbach, M.C.: Markowitz revisited: mean-variance model in financial portfolio analysis. *SIAM Rev.* **43**, 31–85 (2001)
10. Yoshida, Y.: The valuation of European options in uncertain environment. *Eur. J. Oper. Res.* **145**, 221–229 (2003)
11. Yoshida, Y.: A discrete-time model of American put option in an uncertain environment. *Eur. J. Oper. Res.* **151**, 153–166 (2003)
12. Yoshida, Y.: A dynamic value-at-risk portfolio model In: Torra, V., et al. (eds.) *Modeling Decisions for Artificial Intelligence 2011*. LNAI, vol. 6820, pp. 43–54. Springer (2011)
13. Yoshida, Y.: A dynamic risk allocation of value-at-risks with portfolios. *J. Adv. Comput. Intell. Intell. Inform.* **16**, 800–806 (2012)
14. Yoshida, Y.: A decision process with portfolios for value-at-risks. *Int. Conf. Numer. Anal. Appl. Math.* **1648**(070008), 1–5 (2015). American Institute of Physics Publishing

On Quantification of the Hidden Distributed Generation Capacity and Its Effects

Vladislav Samoylenko, Stanislav Eroshenko and Andrew Pazderin

Abstract The energy efficiency starts from energy accounting. At the level of strategic planning, that means the formation energy balances. In terms of distributed generation (DG), the problem at hand is how to ensure a correct estimation of the installed capacity of DG in cases when it operates standalone. This “hidden” DG may sufficiently influence the power system operation. The paper presents the results of investigations devoted to DG penetration assessment. A novel approach to existing and prospective DG assessment is proposed, which combines statistical, economic and geographical methods. The approach provides DG power ranging according to the sphere of its application. It is suitable to predict the centers of DG interconnection.

Keywords DG • CHP • Energy efficiency • Installed capacity • Development plans

1 Introduction

Currently, in many documents that describe perspectives of the energy sector, the reference is made to the necessity for distributed generation (DG) development [1, 2]. DG is usually defined as a set of modular installations of about several MW (Gcal/h) installed capacity, producing electricity and heat at the point of consumption and not using an electrical grid to transmit it [3, 4]. At the areas of severe climatic conditions and the areas where the cogeneration is essential (both include the Russian Federation), preference is usually given to hydrocarbon-fueled DG.

V. Samoylenko · S. Eroshenko (✉) · A. Pazderin
Ural Federal University, Mira Str. 19, 620002 Yekaterinburg, Russia
e-mail: s.a.eroshonko@urfu.ru

V. Samoylenko
e-mail: v.o.samoylenko@urfu.ru

A. Pazderin
e-mail: trenina_katerina@mail.ru

However, the documents or their sections devoted to DG are often declarative: they promote the necessity for DG development, but do not take into account and do not clarify the mechanism of development. In other words, they do not respond fully to the questions as to where and why DG emerges, who are the main stakeholders, what benefits the region gain from DG implementation.

Furthermore, at the level of strategic planning, every power system needs the formation of generation and consumption balances. In terms of DG, the problem at hand is how to ensure a correct estimation of the installed capacity and the power available from DG, which is not scheduled, in cases when it operates standalone or just doesn't participate in the market. This "hidden" DG may sufficiently influence the power system operation as well as the region energy infrastructure development. For this reason, it should be taken into account in energy development plans.

The work presented includes compiled statistics of the DG success in Russia for different types of business entities; the active types of economic entities being potential DG stakeholders are considered; existing and prospective DG assessment is proposed, which combines statistical, economic and geographical methods [5, 6].

2 DG Penetration Level

The initial data sources for the quantification of DG are provided by:

- DG Interconnection Acts (for existing and prospective objects);
- Energy Development Plans (for existing objects);
- Opensource Data (for existing objects).

Interconnection acts make available the quantification of the interconnected DG according to the whole complex of the official requirements. Interconnection acts database is shared by authorities, such as the System Operator and Interregional Grid Company. Energy development plans enable to account existing and prospective objects in different areas of the region. The open source data is mostly lists of projects implemented by different design companies and corresponding analytical reviews.

The data collected show the level of DG at about 500 MW that is 4.9% of the region generation installed capacity (Fig. 1). It is much more than 1.2–2.0%

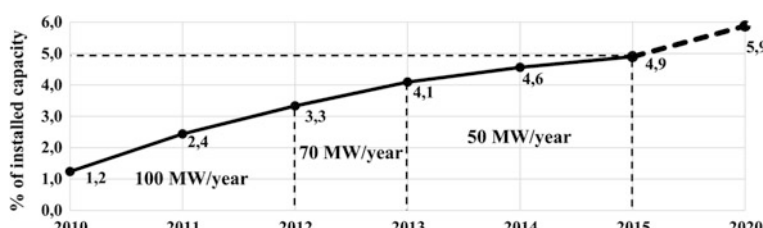


Fig. 1 The initial data sources

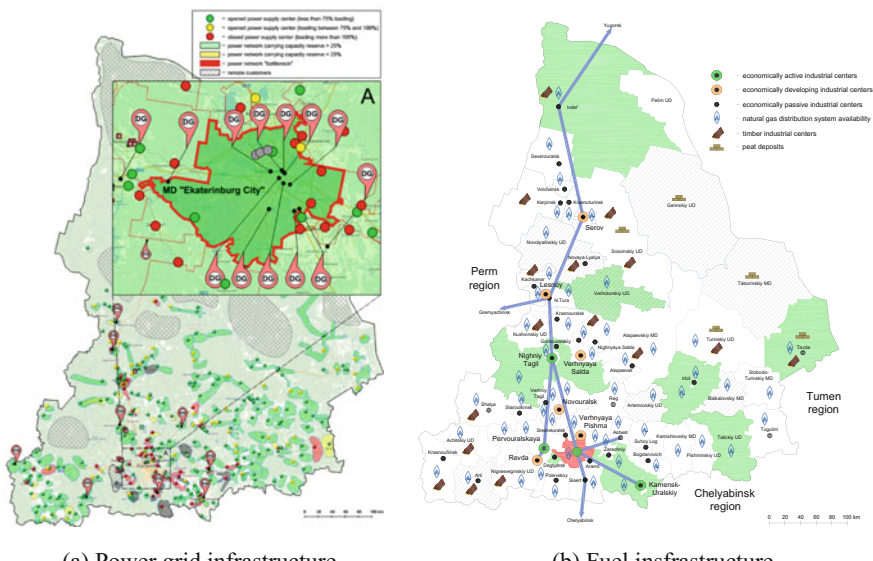
declared by the authorities. Also, the dynamics of the installed capacity is available, which makes it possible to make forecasts up to 2020. Currently, the share of DG does not exceed 4.9% of the installed capacity. The slowdown is due to general energy consumption reduction and the development of all types of civil engineering infrastructures. It is unlikely that the percentage of the DG installed capacity in the region energy system will exceed 6% up to 2020.

Then, it is necessary to consider the DG features possessed by the particular districts of the region.

3 DG Development Forecasting

First of all, the economic aspect is considered. It provides for the economic development of the region due to the profit gained by certain companies by reducing energy costs in case of DG utilization. Nevertheless, the reduction of region energy prices as a result of the market competition is unlikely to occur in the short-term perspective for a number of technological and organizational reasons.

The main technological background of the DG development (Fig. 2) is related to:



(a) Power grid infrastructure

(b) Fuel infrastructure

Fig. 2 The main technological background of the DG development **a** the availability of power grid infrastructure in the region; distant rural areas and villages without the grid interconnection; **b** cogeneration centers and main gas consumption centers

- the availability of the power grid infrastructure, including load of 35–110 kV power substations, the need for the electrification of distant rural areas and villages (Fig. 2a); DG capacity is also specified;
- the availability of external heat supply systems and the account of the possible consumption of low- and medium-grade heat for industrial purposes (green areas); the extent of development of gas distribution networks as the main fuel infrastructure; the use of local fuels as an alternative fuel infrastructure (these are given in Fig. 2b).

According to the research methods of economic and geographical zoning, a DG forecast map for the Sverdlovsk region of Russia has been obtained. It points out the specific groups of consumers that use energy produced by DG and marks it with corresponding numbers. Two-digit numbering allows dividing the groups into subgroups by the DG power which is directly proportional to the second digit. Hereinafter the numbers are given in italics.

The groups of typical DG-owners are listed in Table 1. The most high-powered DG projects are in mining {1} and construction industries {6.3} (16–25 MW), ferrous and non-ferrous metallurgy {2.2} (14–22 MW), as well as heavy engineering {3.3} (10–20 MW). Medium-power DG is used for the production of construction and decoration materials {6.2} (4–12 MW), metalworking companies {2.1} and integrated engineering {3.2} (4.5–6 MW).

Also, it is used to supply auxiliary needs of gas industry as well as for pipeline transportation of oil gas {5.1, 5.2} (1.7–10 MW). DG of capacity ranging from 6 to 18 MW is used for modern residential and office buildings energy supply {4}.

Low-power DG supplies the instrument-making industry {3.1}, chemical and production of innovative materials {6.1} (1–2 MW). DG is popular for power supply of transport and logistics centers and bases {7}, light industry {11} (0.5–1.5 MW). There is a potential for DG in the region to generate energy by waste processing {10}.

DG in the Sverdlovsk region is concentrated mostly in densely populated areas, especially in the industrial urban areas with a lot of companies, like Yekaterinburg city (the region center) and satellite towns. The positive dynamics can be expected from districts close to Yekaterinburg due to the suburbanization of economic activity.

In terms of technology, agriculture is convenient for DG application because of the smooth load curve and the inertia of the main production processes. DG is required by livestock farms, poultry farms, dairy, meat and bread factories {9.1} (1–4 MW), greenhouse farms {9.2} (4.5–9 MW). In this regard, a positive DG trend can be expected in agro-industrial areas.

The development of DG, using local fuels is possible due to the availability of an integrated production cycle, such as waste or by-products of primary production suitable as a fuel (sawdust, peat) and the use of a gasifier for syngas {8.1, 8.2} (0.5–1 MW). The payback period is acceptable for such social projects for the development of rural areas. In addition, unlike the grid to be serviced and the plants to be supplied with diesel power, such DG is almost autonomous.

The map is presented in Fig. 3. The boundaries of the DG and consumer groups are painted in accordance with Table 1.

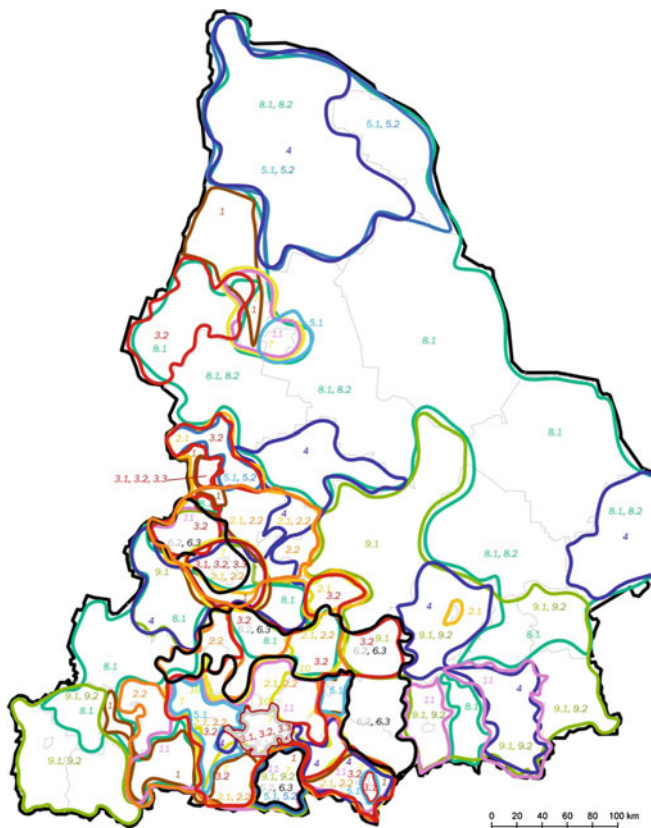


Fig. 3 A forecast DG map for Sverdlovsk region

Table 1 The groups of consumers using DG

Mark		DG power (MW)		DG purpose
Nº	Color	Electricity	Heat	
<i>1. Mining industry</i>				
1		16–25	16–50	Minerals mining
<i>2. Metallurgy</i>				
2.1		4.5–6	4.5–10	Metal working
2.2		14–22	14–45	Ferrous and non-ferrous metallurgy
<i>3. Machinery construction</i>				
3.1		1–2	1–2	Machinery, instrument-making industry
3.2		4.5–6	4.5–12	Complex engineering industry
3.3		10–20	10–30	Heavy engineering industry
<i>4. Power industry</i>				
4		6–18	6–36	Residential and office energy supply
<i>5. Gas industry</i>				
5.1		1.7–4	1.7–5	Gas industry auxiliary
5.2		4–10	4–15	Gas compressors
<i>6. Materials production and construction industry</i>				
6.1		0.5–1	0.5–1	Chemical materials
6.2		4–12	4–24	Decoration materials
6.3		16–25	16–50	Building materials
<i>7. Transport and logistics</i>				
7		0.5–2.5	1–15	Transport and logistics hubs and bases
<i>8. Dendrochemistry</i>				
8.1		0.5–1*	0.5–1*	Woodworking
8.2		1–2	1–4	Resin industry
<i>9. Agrarian industry</i>				
9.1		1–4	1–8	Poultry, meat, dairy, bread-baking plants
9.2		4.5–9	4.5–18	Greenhouses
<i>10. Waste utilization</i>				
10		0.5–1	0.5–1	Waste processing and utilization
<i>11. Light industry</i>				
11		0.5–2	1–2	Light industry

4 Conclusions

Geographical mapping is known to be an effective tool for decision making in power industry, especially regarding power generation siting and sizing tasks. Provided methodology provides more precise DG installed capacity assessment and

gives the possibility to perform approximate perspective DG forecasting. As far as DG development is influenced by different factors simultaneously, technical and economic criteria are to be taken into account. DG business-success statistical analysis gave us the possibility to obtain typical ranges of DG installed capacities according to the sphere of its application.

For a given case study, the share of distributed generation in 2020 perspective planning is expected to be about 6% of total power generation capacities. DG covers 4.9% of power balance against 1.2–2.0% estimated for earlier periods. About 80% of DG is used by small and medium-sized business companies, 20%—large companies. The most expected spheres of DG development and the corresponding expected DG installed capacities are directly correlated to economic performance of the district under consideration. In terms of Sverdlovsk region, which was taken as a case study, the leading spheres of industry are metallurgy and transport with DG capacity ranges 4.0–45.0 and 1.0–2.0, correspondingly. Almost all the DGs use gas as a fuel. This is due to a wide range of power generation based on gas, easy-to-use gas fuel infrastructure. However, provided methodology can be expanded for renewable energy source application in case energy source potential is adequately assessed.

Acknowledgements The work was supported by Act 211 Government of the Russian Federation, contract № 02.A03.21.0006 and the Ministry of Education and Science of the Russian Federation (in the framework of state assignment, №13.1928.2014/K (project №1928)).

References

1. Heating schemes of Yekaterinburg City municipality up to 2030. Management of housing and public utilities. Yekaterinburg City informational portal (2015) [in Russian]
2. The scheme of Yekaterinburg City municipality power supply up to 2025. Yekaterinburg City informational portal (2015) [in Russian]
3. Chicco, G., Mancarella, P.: Environmental sustainability of distributed cogeneration systems. In: Proceedings of the 14th IEEE Mediterranean Electrotechnical Conference, 2008. MELECON 2008, pp. 514–519. IEEE, Ajaccio (2008)
4. Schellong, W., Schmidla, T.: Optimization of distributed cogeneration systems. In: Proceedings of the 2013 IEEE International Conference on Industrial Technology (ICIT), pp. 879–884. IEEE, Cape Town (2013)
5. Samoylenko, V.O., Eroshenko, S.A.: The forecast of DG development features by methods of economic and geographical zoning on the example of Sverdlovsk region. The materials of public periodic seminar. The issues of distributed generation interconnection and operation. Russian National Committee of CIGRE (2014) [in Russian]. http://cigre.ru/activity/conference/seminar_c6/materials/
6. Khalyasmaa, A.I., Dmitriev, S.A. Expert system for engineering assets' management of utility companies. In: Proceedings—SDEMPED 2015: IEEE 10th International Symposium on Diagnostics for Electrical Machines, Power Electronics and Drives, pp. 421–427 (2015)

Modeling the Operating Costs for Production of the Hydrolyzate

Hana Vaskova and Karel Kolomaznik

Abstract Nowadays, the waste management is an important issue. In this paper a mathematic modeling of the main operating costs for production of collagen hydrolyzate from leather shavings is presented. The model is based on physical and chemical ongoing processes in the reactor and other parts of the production system, such as kinetics of the hydrolysis, mass and dry matter balances and protein balance in equilibrium. The aim is to determine optimal time of hydrolysis reaction, optimal mass fraction of decomposed protein and hence the main operating costs. The modeling is performed for a batch reactor and pilot plant conditions.

Keywords Collagen hydrolyzate • Modeling • Operating costs • Protein • Waste

1 Introduction

Leather industry contributes significantly to the production of several types of waste and pollutes the environment in the long-term. In the production of leather the utilization of a feedstock, the raw hides, is only about 20%. The rest consists of solid wastes and waste water containing in particular chromium, since the chrome tanning is still the most common method of tanning globally. Only in tanneries million tons of waste is generated annually [1].

Processes based on hydrolysis reaction offer a reasonable solution for the processing of certain part of these wastes. The ways for reduction of the amount of waste are needful, otherwise, waste end up in landfills or incinerators, what brings a risk of leakage into the soil and groundwater or pollution of the air [2]. However, necessary condition for implementation of new technologies for waste treatment is their economic aspect. In terms of processing a waste generated from the leather

H. Vaskova (✉) · K. Kolomaznik

Faculty of Applied Informatics, Tomas Bata University in Zlín,
Nad Stranemi 4511, 76005 Zlín, Czech Republic
e-mail: vaskova@fai.utb.cz

industry, one option consists in separating collagen protein (or its processed form) and its further utilization.

Mathematical modeling has gained a great importance recently for the analysis and prediction of behavior of processes and phenomena in various areas. Modeling enables to penetrate through the analysis into a nature of a problem and to obtain useful information, deeper, more thorough understanding, to influence real processes and to prepare the way for better, optimized design or control of the modeled system.

2 Treatment of Leather Waste

Hydrolysis, as a decomposition reaction is significantly used in technological processes for the purpose of fermentation of matrices (e.g. leather wastes) for subsequent analysis of the studied material. Hydrolysis of collagen material in alkaline or acidic medium is used also in a complex dechromatation process of leather industry wastes, such as shavings. One component—chromium or protein is subjected to liquefaction. In this study, the protein is liquified and after further treatment can be effectively utilized in forms of gelatin or protein hydrolysates.

2.1 *The Dechromatation Process*

The complex processing of leather shavings can be, in simplified way, divided into three stages as follows.

Collagen protein is liquefied and separated from the chromium sludge in the first stage. Chromium sludge is subjected to revitalization for obtaining chromium in a form of salts for further leather tanning [3]. One part of resulting gelatinous protein, a high-quality gelatin, finds cost-effective usage and applications in pharmacy, food industry or cosmetics. The rest of gelatinous protein is further processed. Enzyme activity leads in alkaline conditions to molar mass decrease of gelatinous hydrolysate. Further splitting of protein chain can continue by the act of acid. The hydrolysate with lower molar mass is acquired subsequently and can find application as biostimulator in agriculture [4].

2.2 *The Production System*

The production system for producing of the hydrolysate is composed of three fundamental elements: the reactor, the filter and the vacuum evaporator. The simplified diagram is shown in Fig. 1 [5]. Feedstocks in the reactor are leather waste, water and an alkali. Together they create a reaction mixture. When the desired

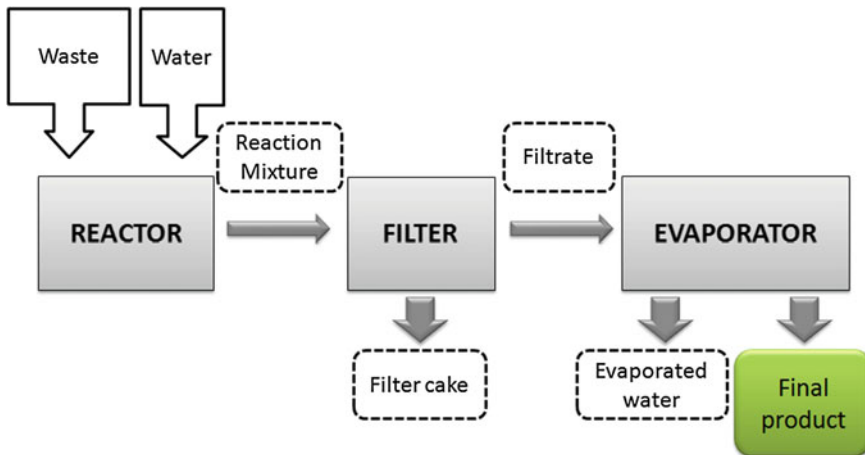


Fig. 1 Diagram of the production system for a production of gelatinous hydrolyzate

degree of hydrolysis is reached, hot heterogeneous mixture is filtered and the resulting filtrate is transferred to an evaporator, where the concentration of hydrolysed substance is increased.

3 Mathematical Model

The main operating costs for production of the hydrolyzate are expressed as a function of N , see Eq. (1). The function of N is considered for a batch reactor.

$$N = PtK_E + m_WHK_P + \dot{Q}_ZtK_P, \quad (1)$$

where first term represents the cost of power consumption to drive the stirrer, the second term describes the cost of the desired product concentration and the third term is heat loss. Physical quantities and constants occurring in the mathematical model are listed in Table 1.

A function of n is considered as a target function. The function corresponds to the operating costs for production of hydrolyzate relating to 1 kg of product containing 30% of dry matter. The function of n is

$$n = \frac{N}{m_D} = \frac{PtK_E + m_WHK_P + \dot{Q}_ZtK_P}{m_D}, \quad (2)$$

where m_D is a mass of the product—the hydrolyzate of collagen protein. The value of m_D is calculated from mass balances and dry matter balances of the reactor,

Table 1 Physical quantities and assignments for the mathematical model

Symbol	Physical quantity	Value [Unit]
P	Electric power of stirrer of hydrolysis reactor	10^4 [W]
t	Time	– [s]
K_E	Price of electricity	$1.25 \cdot 10^{-6}$ [CZK/Ws] ($\sim 4.62 \times 10^{-8}$ EUR/Ws)
m_W	Mass of evaporated water	– [kg]
H	Specific latent heat of vaporization	2.3×10^6 [J/kg]
K_P	Prize of steam	$0.6 \cdot 10^{-6}$ [CZK/Ws] ($\sim 2.2 \times 10^{-8}$ EUR/Ws)
\dot{Q}_Z	Loss of heat flow through a heat transfer area of the reactor	2.4×10^5 [W]
m_D	Mass of hydrolyzate	2×10^3 [kg]
a_E	Mass fraction of decomposed proteins in hydrolyzate	– [l]
k	Velocity constant of hydrolysis reaction	1.7×10^{-4} [s ⁻¹]
a_R	Mass fraction of protein in filtrate at equilibrium	– [l]
a_D	Final mass fraction of hydrolyzate	0.3 [l]

the filter and the evaporator. The balances describe the physicochemical processes occurring in reactor and other parts of the production system.

The specific expression of function of n is based on the kinetics of hydrolysis in the reactor to determine the optimal time of reaction, on the mass balance of protein in a steady state and on the balance of the evaporator. Assuming, the hydrolysis in the reactor proceeds according to first-order kinetics, i.e. the reaction rate depends on the concentration of the unreacted protein, the reaction is described by differential equation

$$\frac{da_E}{dt} = k(a_R - a_E). \quad (3)$$

A solution of the Eq. (3) gives the information about time t of the reaction

$$t = -\frac{1}{k} \ln\left(\frac{a_R - a_E}{a_R}\right). \quad (4)$$

Considering the balance of the evaporator to determine the mass of evaporated water and assuming that the mass fraction of dry matter in the filtrate corresponds to the proportion of decomposed protein, the function of n is

$$n = -\frac{PK_E + \dot{Q}_Z K_P}{km_D} \ln\left(1 - \frac{a_E}{a_R}\right) + HK_P \left(\frac{a_D}{a_E} - 1\right). \quad (5)$$

For minimizing operating costs, it is necessary to determine the extreme of the function of n . The concentration a_E is then given by the expression (6)

$$a_E = \frac{\sqrt{\beta a_D} \sqrt{\beta a_D + 4\alpha a_R} - \beta a_D}{2\alpha}, \quad (6)$$

where the coefficients α and β are given by (7) and (8)

$$\alpha = \frac{PK_E + \dot{Q}_Z K_P}{km_D}, \quad (7)$$

$$\beta = HK_P. \quad (8)$$

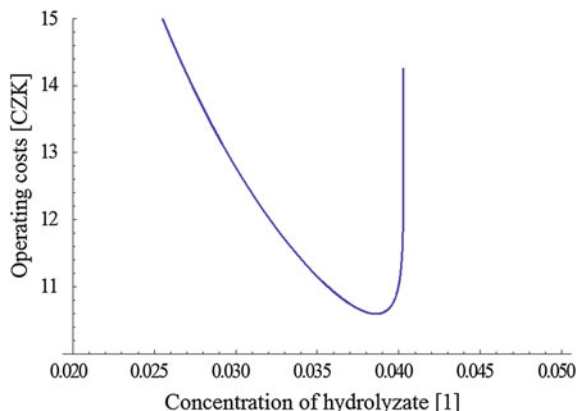
Substituting (6) into the Eq. (4) we obtain the expression for the optimal time

$$t = -\frac{1}{k} \ln\left(1 - \frac{\sqrt{\beta a_D} \sqrt{\beta a_D + 4\alpha a_R} - \beta a_D}{2\alpha a_R}\right). \quad (9)$$

3.1 Optimum Values of Variables

Modeling is performed for a batch reactor usable for pilot plant experiments, i.e. when processing materials on the order of tons. The optimal values of the search parameters t , a_E and a_R are obtained after substituting the known parameters from Table 1. Optimal time for the reaction based on the calculation is 5 h and 10 min, the optimal mass fraction of decomposed protein is 0.0386 with the mass fraction of protein in filtrate in equilibrium 0.0403. The target function of n was modeled in Wolfram Mathematica software. The dependence of the operating costs on the concentration a_E is shown in Fig. 2.

Fig. 2 The dependence of the operating costs on the concentration of collagen hydrolyzate a_E



The current price related to 1 kg of collagen hydrolyzate with optimal mass fraction a_E is calculated on 10.60 CZK (~0.39 EUR). Currently, a number of products for nutrition and joints support (a collagen hydrolyzate) available on markets, are sold from about 250–300 CZK/kg (~9.2–11 EUR/kg).

The steep decline to an optimum value of a_E and even sharper rise of the dependence clearly demonstrate sense of mathematical-physical modeling and contribution to the economic evaluation of the collagen hydrolyzate production process.

4 Conclusion

Mathematical model of main operating costs for the collagen hydrolyzate acquired from leather waste was presented in this paper. Hydrolysis reaction seems to be reasonable solution for safe and environmentally friendly method for reduction of waste gained from leather manufacturing sector. This method offers also economically effective way of waste reduction as the waste (e.g. shavings) still contains material usable in a form of gelatin or collagen hydrolyzate. Both of these forms are economically interesting. Reaching the optimal time of the reaction evaluated from the presented model brings another savings especially in energy required to operate the production system.

Acknowledgements This work was supported by the Ministry of Education, Youth and Sports of the Czech Republic within the National Sustainability Program project No. LO1303 (MSMT-7778/2014).

References

1. World Statistical Compendium for raw hides and skins, leather and leather footwear 1993-2012. http://www.fao.org/fileadmin/templates/est/MARKETS_MONITORING/HidesSkins/documents/COMPENDIUM2013.pdf
2. Janacova, D., Vasek, V., Kolomaznik, K.: Optimalizace recyklačních technologií. In: Automatizace, regulace a procesy, pp. 55–66 (2010)
3. Kolomaznik, K., Mladek, M., Langmaier, F., Janacova, D., Taylor, M.M.: Experience in industrial practice of enzymatic de-chromation of chrome shavings. J. Am. Leather Chem. Assoc. **94**, 55–63 (2000)
4. Pecha, J., Fürst, T., Kolomazník, K., Friebrová, V., Svoboda, P.: Protein biostimulant foliar uptake modeling: the impact of climatic conditions. AIChE J. **58**, 2010–2019 (2012)
5. Vaskova, H.: Modelovani chemickeho reaktoru pro dechromaci kozedelnych odpadu. Dissertation, Tomas Bata Univerzity in Zlin (2015)

The Problems of Data Security in Cloud Computing and Its Solution Using Petri Nets

Zoltán Balogh and Martin Magdin

Abstract Cloud is understood as a storage which provides space for data storage. The concept of Cloud and Cloud computing has a wider range. It can be characterized as providing services and various applications which are saved on servers while there is access to them through Internet. It is possible to work with data in cloud not only online mode but also in offline—it means to use the state of short-term connection and thus save data in mobile connection. Provided that the service is paid, the advantage of it is that the users do not pay for their software but for its use. Scientific publications state that the most often flaw of the service is its vulnerability in the form of data security. It is the reason why nowadays, all the attention is paid to this problematic field. In the report a data security design in Cloud computing will be described and also all the results will be stated that have been acquired through experiments to verify the overall security of a chosen cloud storage. According to measurements of chosen parameters of a basic and an extended cloud storage model, it has been found out that the security increase of data stored in cloud storage brings also worsening of other parameters of the storage. This is particularly the case of the access speed to data that (if they are automatically encrypted) can be influenced by the computing power of a particular PC hardware.

Keywords Petri nets • Cloud computing • Security • Cloud storage security

Z. Balogh (✉) · M. Magdin

Faculty of Natural Sciences, Department of Computer Science, Constantine the Philosopher University in Nitra, Tr. A. Hlinku 1, 949 74 Nitra, Slovakia
e-mail: zbalogh@ukf.sk

M. Magdin
e-mail: mmagdin@ukf.sk

1 Introduction

The concept of cloud is now a highly inflected term. Some experts explain this concept as a dominant computing model in IT infrastructures, enabling flexible, ubiquitous, on-demand and cost-effective access to a wide pool of shared resources [4].

Cloud Computing has emerged from the most promising business concept to new fast growing business trend. Cloud Computing provides the ability to utilize resources from distributed computing environments via Internet. Cloud Computing is the promising hosting platform that allows the resources and collection of applications usage in the shared infrastructure with pools of computers and storage resources [17]. The proliferation of the cloud paradigm has created a strong trend to transfer traditional services and applications to the cloud [18]. With the ubiquitous nature of social networks and cloud computing, we are starting to explore a new way to interact with and exploit these developing paradigms [11]. The gradual development of the Internet infrastructure and improving the various providers of services allow to accept the cloud paradigm and enjoying the following two key offerings [1, 6]:

- (a) low costs from the point of view of invest on hardware or software,
- (b) reduction of costs from the point of management of complex IT systems.

These two economic factors they are economy of scale enables additional decrease in total costs, as numerous small-scale and typically underutilized data centers are replaced by larger infrastructures that target higher resource efficiency [5].

With the rapid shift to the cloud computing paradigm, one of the most critical issues faced by system administrators is the construction and management of systems in a manner that eliminates or hides their complexity from the end users, and, at the same time, maintain their control, flexibility, dependability, and security [9]. Next generation cloud systems will require a paradigm shift in how they are constructed and managed. Conventional control and management platforms are facing considerable challenges regarding flexibility, dependability and security that next generation systems must handle [10].

Security, trust, and privacy always remain challenges for organizations that adopt cloud computing and big data. Although there are demands for businesses to move their data to the cloud and centralize management for data centers, services and applications are designed to reduce cost and increase operational efficiency. System design and deployment based on current security practices should be simultaneously enforced to ensure compliance of all data and services with up-to-date patches and policies. A risk-based approach to the development of a security program that recognizes (and funds) appropriate controls will ensure protection of all users and confidentiality, integrity, and availability of data [7].

Security is one of the main attributes of information technology. By access to cloud services and data through the Internet, the importance of security is increased because data is at bigger amount of security risk. Within various cloud service models, data responsibility is shared by more groups. Data is the most important for

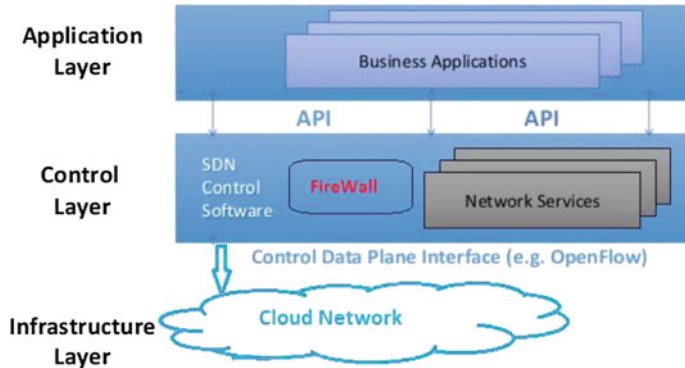


Fig. 1 Security SDN architecture with firewall in cloud networks [15]

the organization which owns them and uses the cloud services for storage. That is the reason why the organization should be aware of all risks which exist for data stored in cloud.

From the year 2013 was created many architectures that directly support data security in cloud repositories. Most often we meet with the protection on the basis of software solution.

By Mukundha [15] we can observed the fast change in the cloud network by the Software Defined Networking (SDN) paradigm that differentiate the control plane from the data plane to give the flexibility for programmability and centralized control of the cloud networks, SDN networks not only provide simplification of cloud network management it also provides more security with SDN by implementing firewalls with in the SDNs (Fig. 1).

The security of cloud repositories deserves our special attention for the challenges it brings and also the opportunities to enhance the network security. In the paper Modeling of Data Security in Cloud Computing (Balogh and Turčáni [3]; paper was published in 10th Annual IEEE International Systems Conference; <http://2016.ieeesyscon.org/>) we have designed the way of modeling of data security in cloud repositories. In the next section is short explanation of our proposal.

2 Data Security Modeling in Cloud Computing

Data in cloud computing is stored, transmitted and there is access to it through various layers of cloud computing in order to all data security attributes to be guaranteed such as confidentiality, integrity and availability. It is necessary to deal with data security in all layers of cloud computing. Therefore we designed expanded fourth-level model of data security in cloud computing (standard cloud storage uses three-level data security model) (Fig. 2).



Fig. 2 Expanded data security model in cloud computing (our creation)

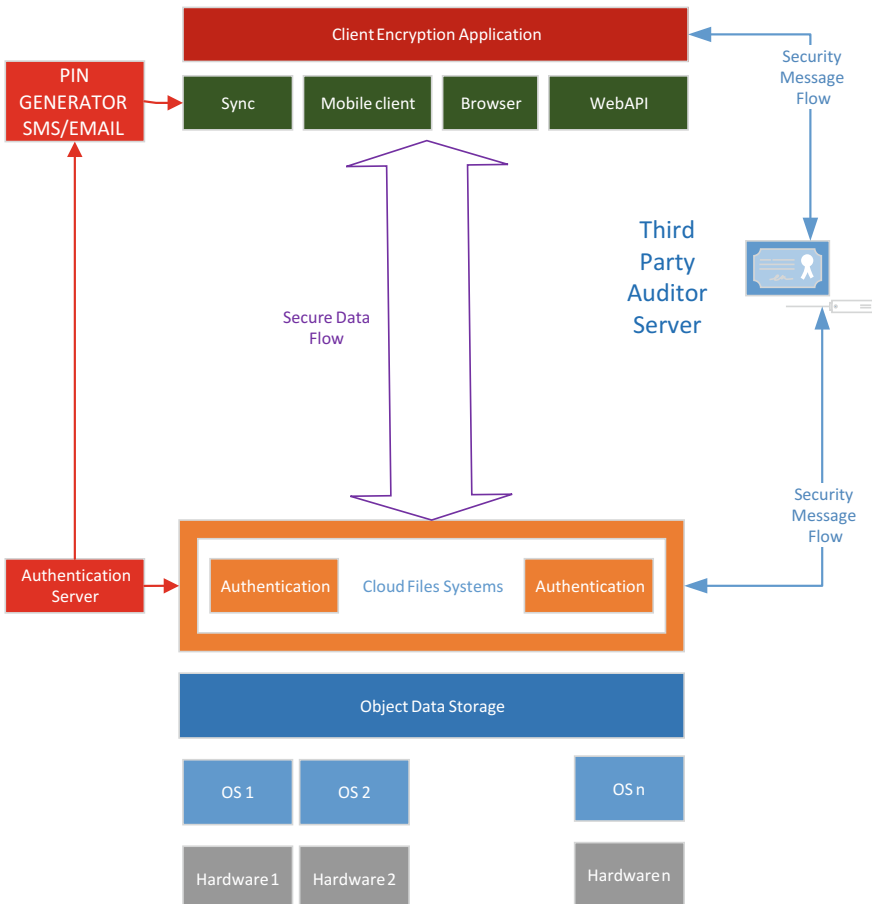


Fig. 3 Cloud storage model design with expanded security (our creation)

Data security model in cloud computing was designed as an expansion of the current standard use of data storage model in cloud computing. The standard model is used for example in Dropbox, Seafile or in other services to store or to work with. The base is an object data storage which was built on a server cluster creating n servers. Above the object storage there was the cloud file system which was provided by the application server (Dropbox, Seafile). In the following figure is an architecture model design of a secure data storage in cloud computing (Fig. 3).

To demonstrate architecture model operation of cloud storage with expanded security, Petri nets have been created, shown in Fig. 4. Petri nets are a mathematical means appropriate to model system, composing of parallel components in mutual interaction. By the use of Petri nets, it would be easier to discreetly simulate and also to understand how the security model operates. Then each step that has been made while securing data in cloud storage would be easily described. The definition of Petri nets according to [2]:

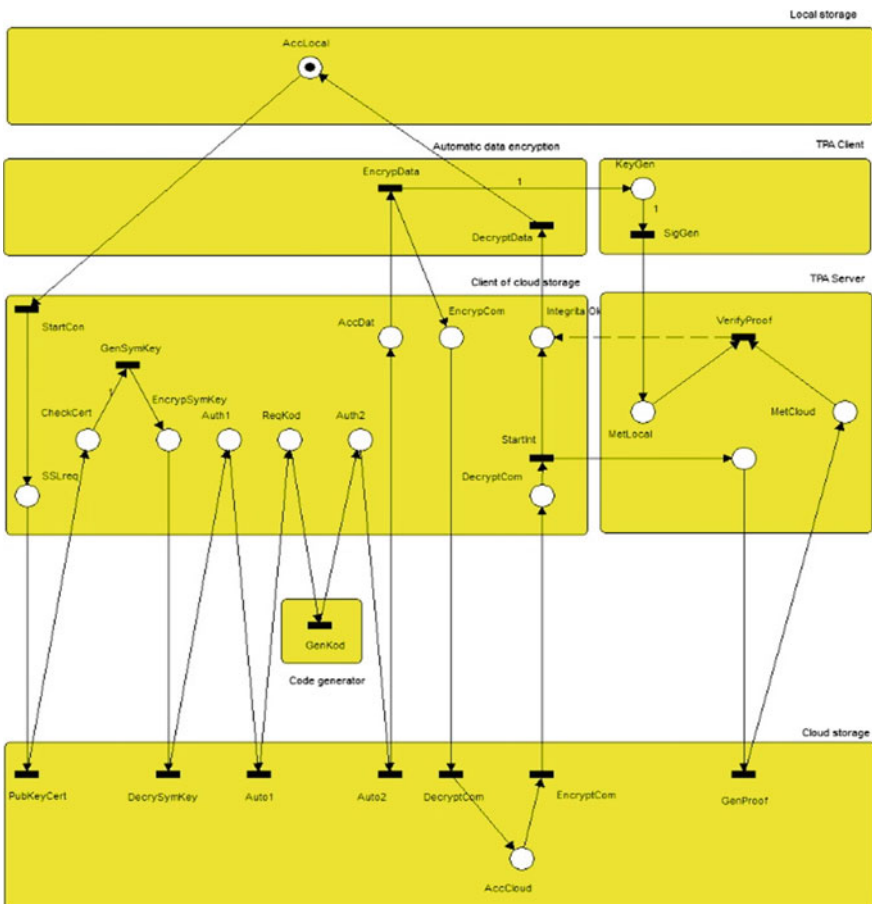


Fig. 4 Petri nets model for data security in cloud computing (our creation)

Petri nets is a trio $N = (P, T, F)$ where $P \neq \emptyset$ is a finite set of places, $T \neq \emptyset$ is a finite set of transitions and F is transition float.

$$F: (P \times T)U(T \times P) \rightarrow N_0$$

With this designed model of a complex data security in cloud computing has adequately increased data security in all three attributes of data security which are confidentiality, integrity and availability. In the next section is analysis of the likelihood of overcoming the security of cloud repositories and experiment describing the creation of cloud repositories and increasing its security.

3 An Experiment of Creating a Cloud Storage and Increasing Its Security

In the previous part, there was a designed and described model of extended data security in cloud storage. In this section, with an experiment the standard model would be compared with a model of extended security, a two-level authentication and data encryption in peace. The parameters for comparing the two models were gained based on experience of 7 years from the company LAN Systems Ltd. Those have been chosen which are considered to be the most important for the majority of users:

- the speed of setting up the data cloud storage,
- the speed of data synchronization between the client and cloud storage,
- costs of data storage.

For the experiment we have chosen a hardware and a software of the cloud storage provider which belong to the most spread among the cloud storage users according to the experiences of the company LAN Systems Ltd.

The cloud storage has been chosen from the company Dropbox (<https://www.dropbox.com>) because it is the most spread. For data deciphering in peace, the application Boxcryptor (<https://boxcryptor.com>) has been chosen because it is possible to implement it relatively quickly.

3.1 The Basic Parameters of the Hardware and Software for the Experiment

Hardware of the computer on which the Dropbox client has been installed:

CPU: Intel Core i3-2100 3,1 Ghz, RAM: 8 GB, HDD: SSD HDD, OS: Microsoft Windows 7 Professional Service Pack 1 64 bit, The speed of Internet connection: 100 Mbps, Cloud storage: Dropbox with a size of 50 GB.

3.2 Standard Security Model Description of Dropbox Cloud Storage

Authentication: one-level with name and password [8].

Data protection while transfer: SSL a AES-256 bit [8].

Data protection in peace: ciphering on Dropbox server with encryption method AES-256 bit with the access permission of the chosen workers of the company Dropbox. The data owner does not have access to the list of the third persons who have access to his data. The cipher key was saved on Dropbox servers and the data owner does not have access to them [8].

Quick data restore: Dropbox cloud storage saves all edits and deletions up to 30 days. Thus, it is possible to restore all the files up to 30 days that have been deleted. It is also possible to restore the previous versions of files which are not older than 30 days [8]

Data integrity check: is not implemented.

3.3 Extended Security Model Description of Dropbox Cloud Storage

Authentication: a two-step authentication is turned on:

1. Step: name and password
2. Step: A safe code from the phone, sent as a message or generated by a phone application [8]

Data protection while transfer: SSL a AES-256 bit [8]

Data protection in peace:

1. Level: ciphering on Dropbox server with encryption method AES-256 bit with the access permission of the chosen workers of the company Dropbox. The data owner does not have access to the list of the third persons who have access to his data. The cipher key was saved on Dropbox servers and the data owner does not have access to them [8].
2. Level: encryption on a client's device with the application Boxcryptor that uses encryption AES and RSA. The cipher key is saved on the client's device and the provider of Dropbox cloud service has no access [16].

Quick data restore: Dropbox cloud storage saves all edits and deletions up to 30 days. Thus, it is possible to restore all the files up to 30 days that have been deleted. It is also possible to restore the previous versions of files which are not older than 30 days [8].

3.4 Measurement Description of the Chosen Cloud Storage Parameters

The first step was to create a cloud storage with a standard security that had four operations: the creation of Dropbox account, download and installation the clients Dropbox into the client's device, authentication of the clients Dropbox on the client's device and finally, its configuration on the device.

The next step was a creation of a cloud storage with an extended security but which contained 10 following operations:

1. Creation of Dropbox account.
2. Turning on the second step of authentication.
3. Downloading and installation of client's Dropbox into the client's device.
4. The first step of authentication of client's Dropbox on a cloud storage.
5. The second step of authentication.
6. Configuration of client's Dropbox on the client's device.
7. Registration of Boxcryptor account.
8. Downloading and installation of client's Boxcryptor on a client's device.
9. Authentication of client's Boxcryptor into the Boxcryptor server.
10. Configuration of the client's Boxcryptor on a client's device.

The third step was to measure the synchronization time of testing data for both variants of cloud storage security. Within this measurement testing data synchronization speed were measured in sizes of 100, 200, 300, 400, 500, 1000, 1500, 2000, 3000 and 4000 MB. The data were created from the shared data of the LAN Systems Ltd. in which there were various types of files pdf, doc, png, txt, rar. The production data were used in order to get closer to the environment within the experiment in which the cloud storage is used in production [14].

The last step was calculation of monthly expenses on one user for both variants of cloud storage security.

4 The Results of the Experiment

4.1 Time Measurement of the Account in Cloud Storage

Creating an account in the Dropbox cloud storage with account registration, installation and setting the client in the standard security model lasted 6 min and 30 s. After the extended security model (that has been designed by us) with two-level authentication and data encryption in peace, the time of installation has increased to 13 min and 15 s because an account was needed to be created, and the encryption application Boxcryptor was needed to be installed t set. In the following

Fig. 5 The installation time of one account for one user

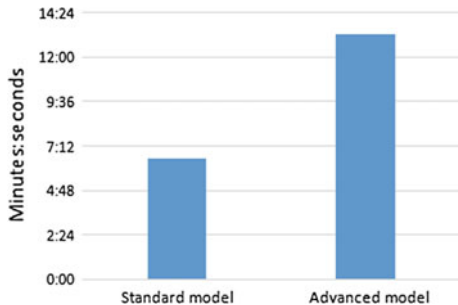


Table 1 Time measurement of account for one user in cloud storage

	Time of installation (minutes: seconds)
Standard model	6:30
Extended model	13:15

chart, the measured values were stated and there is the graphical difference of times in Fig. 5 (Table 1).

4.2 Time Measurement of Testing Data Synchronization

When measuring time of synchronization of various testing data sizes between the cloud storage and its client it has been found out that there are significant differences between the synchronization time of the standard data security model and the extended one. In data encryption in peace, the data synchronization time increases several times between the cloud storage and its client.

After the measurements in the experiment, it has been found out that synchronized data were saved more slowly into the cloud file of the client and consequently, they synchronize more slowly with the cloud storage. The slow storage of testing data into the file was caused by the fact that data were encrypted before storing them into this file. Since the encryption is power consuming for the CPU, additional measurements were completed within the experiment in order to find out in what extent the CPU influences the synchronization time of testing data with cloud storage (Table 2).

Table 2 Time measurements of testing data synchronization (Mb/s)

Model	100 MB	200 MB	300 MB	400 MB	500 MB	1000 MB	1500 MB	2000 MB	3000 MB	4000 MB
Standard model (s)	31	48	72	85	105	120	218	260	356	413
Extended model (s)	252	622	840	1170	1436	1848	3348	4154	5850	7080

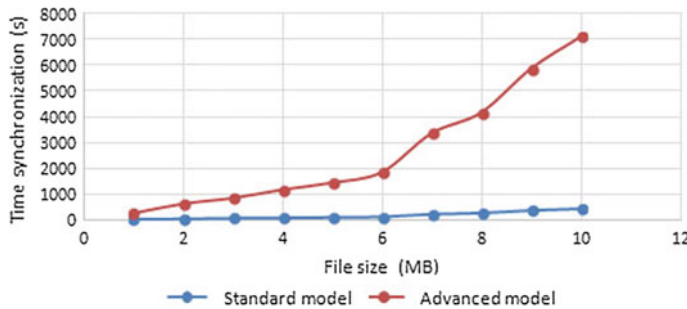


Fig. 6 Synchronization time of client's cloud with cloud storage

Table 3 Hardware of each testing computers

	PC1	PC2	PC3	PC4
CPU	Intel Pentium Dual Core T4300 2,1 Ghz	Intel Pentium 3558 1,7 Ghz	Intel Core i3-2100 3,1 Ghz	AMD Phenom 2 X4 965 3,4 Ghz
RAM	3 GB	4 GB	8 GB	8 GB
HDD	2,5" HDD 5400 rpm	SSD OCZ ARC 100	RAID10 HDD 7200 rpm SATA	SSD Intel 720
CPU power PassMark	1246	1765	3612	4267

While measuring the speed of data synchronization encrypted in peace it has been observed that the synchronization of testing data (of already encrypted data) itself took significantly longer. The synchronization increase of encrypted data in peace with cloud storage has been caused by low effectiveness of encrypted data compression for data transfer by computer network [13] (Fig. 6).

4.3 Additional Measurements of Sequential Read and Write on PC with Various Computing Power

To find out how a PC hardware power influences the speed of synchronization and the work with testing data in cloud storage, speed measurements of sequential read and write into cloud file on a PC with various computing power have been completed.

The measurements were completed into cloud file in the standard data security model where there were no data encryptions in peace completed, and in the extended data security model where the data encryption in peace took place by the application Boxcryptor (Table 3).

The power of CPU of each PC is according to source PASSMARK 2015.

Table 4 Measurements of sequential read (Mb/s) on various PC

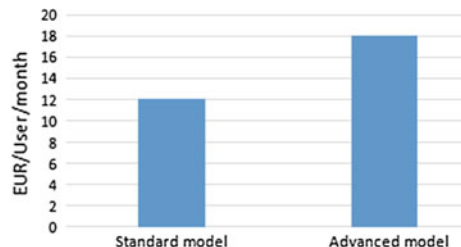
	PC1 (Mb/s)	PC2 (Mb/s)	PC3 (Mb/s)	PC4 (Mb/s)
Standard model	53,35	418	216,51	249,25
Extended model	19,66	26,57	46,45	47,15

Table 5 Measurements of sequential write (Mb/s) on various PC

	PC1 (Mb/s)	PC2 (Mb/s)	PC3 (Mb/s)	PC4 (Mb/s)
Standard model	24,59	364,2	132,7	132,04
Extended model	19,5	27,33	38	47,4

Table 6 Monthly costs on one user of cloud storage (EUR)

	EUR
Standard model	12
Extended model	18

Fig. 7 Monthly costs on one user

In Table 4, measurement results of sequential read on a PC with various computing power are stated. Then in Table 5, measurement results of sequential data write on a PC with various computing power.

4.4 Calculation of Monthly Cost for One User of Cloud Storage

In Table 6 there are monthly costs of one user on standard and extended security model. The differences on monthly costs on one user have been presented in a diagram on Fig. 7.

5 Conclusion

According to measurements of chosen parameters of a standard and an extended cloud storage model, it has been found out that the security increase of data stored in cloud storage brings also worsening of other parameters of the storage. The time of account creation for one user has increased twice on average and the monthly costs have increased by one third on average. In absolute numbers and small number of users, it is not big increase of costs and time, but in a bigger number of users, there is a bigger increase and it needs to be taken into account when designing the security of a cloud storage. The most significant difference between the standard and the extended model of data storage in cloud computing is the data synchronization time with cloud storage. With an additional measurement access speed to data, it can be observed that there was a considerable difference in access speed to data that have not been encrypted in peace and to data that have been encrypted in peace. The speed of access to data is influenced by the computing power of the PC's hardware in automatically encrypted data in peace. The access deceleration to data when encrypting in peace was caused by the fact that the data are decrypted and consequently encrypted while accessing them. Then deceleration of data synchronization with cloud storage when encrypting data in peace was caused by a low effectiveness for encrypted data when transferring them through a computer network. Data storage with the possibility of encryption in data storage is currently a trend that is justified. A typical example of the use of encrypted data storage is storing large amounts of data (example: Comparing individual facial features—see Magdin, Turciani, Hudec), which is achieved by datamining [12].

According to this experiment it can be stated that when designing the cloud storage model, it is recommended for cloud storage users to determine before designing what requirements they do have for securing their own data. Alternatively, they can divide data into groups with different level of required security.

Acknowledgements This publication is supported thanks to the project with a name “Pilot project with UKF Nitra university: Modelling the behaviour of users based on data mining with support of IBM Bluemix”.

References

1. Armbrust, M., Fox, A., Griffith, R., Joseph, A.D., Katz, R., Konwinski, A., Zaharia, M.: A view of cloud computing. *Commun. ACM* **53**(4), 50–58 (2010). doi:[10.1145/1721654.1721672](https://doi.org/10.1145/1721654.1721672)
2. Balogh, Z., Turčáni, M., Magdin, M.: Design and creation of a universal model of educational process with the support of petri nets. *Lecture Notes in Electrical Engineering*, vol. 269, pp. 1049–1060 (2014). doi:[10.1007/978-94-007-7618-0_103](https://doi.org/10.1007/978-94-007-7618-0_103)
3. Balogh, Z., Turčáni, M.: Modeling of data security in cloud computing. In: 10th Annual International Systems Conference, SysCon 2016. Institute of Electrical and Electronics Engineers Inc., pp. 940–946 (2016)

4. Barroso, L.A., Clidaras, J., Hölzle, U.: The datacenter as a computer: an introduction to the design of warehouse-scale machines. *Synth. Lect. Comput. Archit.* **2013**(24), 1–156 (2013)
5. Beloglazov, A., Abawajy, J., Buyya, R.: Energy-aware resource allocation heuristics for efficient management of data centers for cloud computing. *Future Gener. Comput. Syst.* **28**(5), 755–768 (2012). doi:[10.1016/j.future.2011.04.017](https://doi.org/10.1016/j.future.2011.04.017)
6. Buyya, R., Yeo, C.S., Venugopal, S., Broberg, J., Brandic, I.: Cloud computing and emerging IT platforms: vision, hype, and reality for delivering computing as the 5th utility. *Future Gener. Comput. Syst.* **25**(6), 599–616 (2009). doi:[10.1016/j.future.2008.12.001](https://doi.org/10.1016/j.future.2008.12.001)
7. Chang, V., Kuo, Y., Ramachandran, M.: Cloud computing adoption framework: a security framework for business clouds. *Future Gener. Comput. Syst.* **57**, 24–41 (2016). doi:[10.1016/j.future.2015.09.031](https://doi.org/10.1016/j.future.2015.09.031)
8. Dropbox Inc.: How secure is Dropbox? (2015). <https://www.dropbox.com/help/27>
9. Harirri, S., Khargharia, B., Chen, H., Yang, J., Zhang, Y., Parashar, M., Liu, H.: The autonomic computing paradigm. *Cluster Comput.* **9**(1), 5–17 (2006). doi:[10.1007/s10586-006-4893-0](https://doi.org/10.1007/s10586-006-4893-0)
10. Jararweh, Y., Al-Ayyoub, M., Darabseh, A., Benkhelifa, E., Vouk, M., Rindos, A.: Software defined cloud: survey, system and evaluation. *Future Gener. Comput. Syst.* **58**, 56–74 (2016). doi:[10.1016/j.future.2015.10.015](https://doi.org/10.1016/j.future.2015.10.015)
11. Kim, S.: Dynamic social cloud management scheme based on transformable stackelberg game. *Eurasip J. Wirel. Commun. Networking* **2016**(1), 1–9 (2016)
12. Magdin, M., Turčáni, M., Hudec, M.: Evaluating the emotional state of a user using a webcam. *Int. J. Interact. Multimedia Artif. Intell.* **4**(1), 61–68 (2016)
13. Mcgregor, J.P., Lee, R.B.: Performance Impact od Data Compression on Virtual Private Network Transactions (2000). <http://citeserx.ist.psu.edu/viewdoc/download?doi=10.1.1.92.7667&rep=rep1&type=pdf>
14. Munk, M., Kapusta, J., Švec, P.: Data preprocessing evaluation for web log mining: reconstruction of activities of a web visitor. In: 10th International Conference on Computational Science 2010, ICCS 2010, pp. 2273–2280, Amsterdam (2010)
15. Mukundha, C., Prabha, I., Sreenu, K.: Providing security in cloud based networks through software defined networks. *J. Theor. Appl. Inf. Technol.* **84**(2), 287–293 (2016)
16. Secomba GmbH: AES and RSA Encryption (2015). <https://www.boxcryptor.com/en/encryption/>
17. Sreedhar Acharya, B., Siddappa, M.: Novel method of designing and implementation of security challenges in data transmission and storage in cloud computing. *Int. J. Appl. Eng. Res.* **11**(4), 2283–2286 (2016)
18. Wu, J., Liang, Q., Bertino, E.: Improving scalability of software cloud for composite web services. Paper presented at the CLOUD 2009, 2009 IEEE International Conference on Cloud Computing, pp. 143–146 (2009). doi:[10.1109/CLOUD.2009.75](https://doi.org/10.1109/CLOUD.2009.75)

Designing of the Pseudorandom Number Generators on the Basis of Two-Dimensional Cellular Automata

Stepan Bilan, Mykola Bilan, Ruslan Motornyuk, Andrii Bilan and Sergii Bilan

Abstract In this paper three pseudorandom number generators are considered which are built on cellular automata. Structures and generator models, and the organization of a cellular automaton for each generator are studied. Two pseudorandom number generators are built on the asynchronous cellular automata, and the third generator is implemented on the synchronous cellular automata. The structure of cell that realizes the first two pseudorandom number generators is described. There is the analysis of the proposed pseudorandom number generators uses NIST test and also describes their main characteristics.

Keywords Cellular automata • Pseudorandom number generator • Tests

S. Bilan (✉)

State Economy and Technology University of Transport,
Lukeshevicha, str., 19, Kiev 03049, Ukraine
e-mail: bstepan@ukr.net

M. Bilan

The Municipal Educational Institution Mayakskaya Secondary School,
Mayak, Moldova
e-mail: nickni@mail.ru

R. Motornyuk

Data Processing Center of Southwestern Railways, Kiev, Ukraine
e-mail: hehap0@gmail.com

A. Bilan

Business Soft Ltd., Tiraspol, Moldova
e-mail: hl181582@gmail.com

S. Bilan

Win-Interactive LLC, Vinnytsia, Ukraine
e-mail: belan@svitonline.com

1 Introduction

Formation and obtaining pseudorandom numbers is a necessary operation that is widely used in different fields. Today, the need for the pseudorandom number generators (PRNG) has significantly increased. At the same time there is a need in the PRNG with the certain properties for each problem. These properties satisfy its positive solution [1, 2]. PRNG are implemented on the basis of the different mathematical, hardware and software approaches. The PRNG got the widespread popularity and development, which are implemented on the basis of cellular automata (CA). The first generator that was implemented on the one-dimensional CA has been proposed by S. Wolfram [3]. PRNGs, which are implemented on the hybrid CAs were considered in later works [4, 5]. The combination of rules for different CA cells are used in such generators. There were proposed some developed PRNGs, which are based on CA, that are implemented with usage of few CAs and additional generator. Additional generator is built on the linear feedback shift register (LFSR) [6, 7]. Different approaches are used to analyze the properties of the PRNG. They are implemented as software products that are available in the Internet in appropriate sites [8–10]. They include such software as: ENT, DIEHARD, NIST and etc.

The paper analyzes three PRNGs based on the CA and there are the results of using NIST tests for analysis presented here.

2 PRNG Based on the CA that the Additional Bits Using

The first PRNG is implemented on CA in which only one cell (the active cell) changes its own state at each timestep. In such a CA the neighborhood of cells are constitute in such a way so that the one active cell could be selected out of the whole neighborhood of active cell. This cell will be set in active state. Each active cell has one informational output and N informational inputs, N active inputs and N active outputs. Behavior of CA can be described by the following model.

$$b_i(t+1) = \begin{cases} f[b_{N_j}^i(t)], & \text{if } \exists b_{N_j}^{i,act}(t) = 1 \\ b_i(t), & \text{in other case} \end{cases}, \quad (1)$$

where $b_{N_j}^i(t)$ —signals on the information outputs of the cells that constitute the cell neighborhood of i -th cell at time t ; $b_{N_j}^{i,act}(t)$ —signal at the j -th activation input of i -th cell and this signal comes from activation output of the cell that belongs to the cell neighborhood of i -th cell at time t ($j = \overline{1, N}$); N —the amount of neighbor cells, that makes the neighborhood of the i -th cell.

The model shows the process of selecting of the active cell in the next timestep. The activating signal can be transmitted only to one cell of this

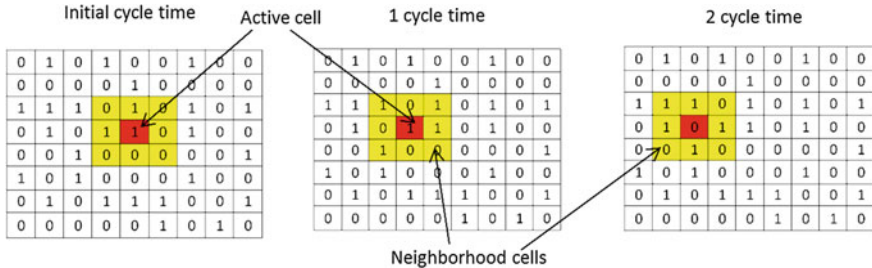


Fig. 1 The example of active signal transmission and the information state changes

neighborhood. At the same time the state of the active cell changes according to the function $f[]$. Each cell can hold the main (informational) and additional (active) states. The pictorial representation of the active signal transmission and the information state changes are represented on the Fig. 1.

Bits of the pseudorandom binary sequences are composed from the bits that come out from activated cells outputs in each timestep. For elimination of the cycles an additional bit is used which is also taken out of one of the CA cells. The information state of a cell is formed around the Moore's neighborhood by the following model.

$$b_j(t+1) = b_{j,1}(t) \oplus b_{j,2}(t) \oplus \dots \oplus b_{j,8}(t) \oplus b_{add}(t) \oplus b_j(t), \quad (2)$$

where $b_{j,1}(t), \dots, b_{j,8}(t)$ —the main informational state of cells, that make the Moore neighborhood for the cells with active state at time t ; $b_{add}(t)$ —informational state of the cell, the value of which is added according to XOR function to the state of the active cell at time t (additional bit value).

Each cell is connected with neighborhood cells by circuits of activation. The activating signal is transmitted by these circuits. The active cell analyzes the information state of neighborhood cells, forms the “1” signal on one of the active outputs, which is defined by a function of being activated and by the signals of neighborhood cells.

The cell of neighborhood is selected on the odd timesteps of the generator that is at the state of logic “1” and has bigger code of numbering among the neighborhood cells, which have the state of the log. “1”. In the even-numbered timestep the neighborhood cell of the active cell is selected, it has a state of logic “0” and has bigger value of numbering among the rest neighborhood cells in the zero state.

PRNG consists of two CA: the basic and additional (KA_{add}) one. There is the initial state of CA stored in CA_{add} . This state is stored during $N \times M$ timesteps in the CA_{add} (where $N \times M$ —the size of two-dimensional CA). Additional bits in each timestep are selected from CA_{add} cells. A signal of “1” on the active output of cell allows to connect its data-output to the output of the generator with the help of switching system (SC). The example of generator operation is represented on Fig. 2.

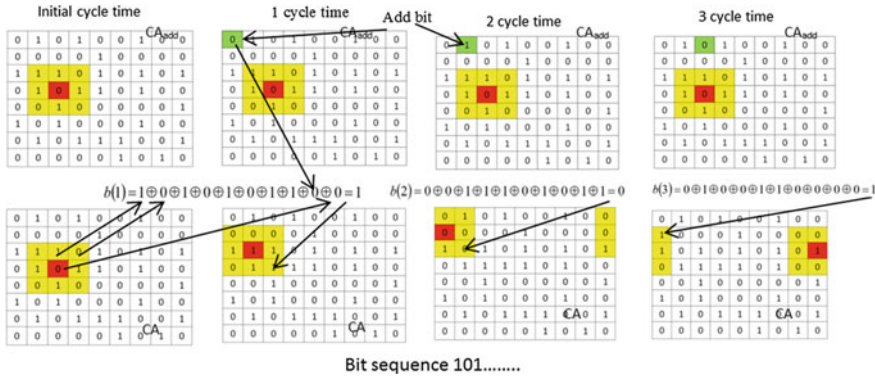


Fig. 2 An example of the first generator functioning

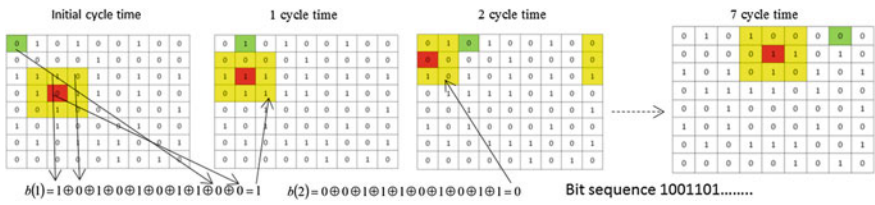


Fig. 3 Example of the PRNG with the inner CA scanning

The second PRNG constructed on the basis of a single CA. The scanning process of the current state of the cells CA is implemented in it. It allows reducing the time wasted for generating pseudorandom sequence. In such a PRNG the cells functioning in the same way. An example of the PRNG functioning is represented on Fig. 3.

3 PRNG Based on the CA with Heterogeneous Cells

The generators that are suggested above have a set of structural disadvantages. These generators uses a complicated switching circuitry for the constant switching the generator output to the data-output of active cells CA. Both generators have a large amount of connections, which deteriorate the reliability of functioning.

PRNG that contains the CA with homogeneous and heterogeneous cells is proposed in this work. Homogeneous cells are called all CA cells, which perform the same functions, and heterogeneous cells—are the cells that perform functions different from homogeneous cell function.

At the initial time all the CA cells are set in the state of the logical “1” and “0”, and all of them perform the same function. They are homogeneous cells. There is a

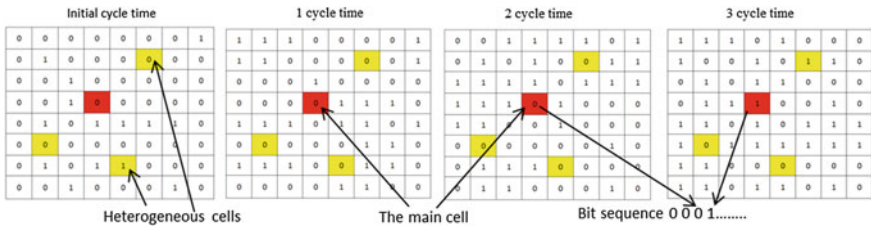


Fig. 4 An example of PRNG operation is based on the CA with heterogeneous cells

chosen cell, which date-output is connected to the output of the PRNG. Then, the few cells are selected among all the cells of CA. These cells will perform another function. These cells are heterogeneous ones. The XOR function is chosen for homogeneous cells, which perform this function above the signals of the neighborhood cells and the signal of its own state. Heterogeneous cells perform the majoritarian function of the signals from neighborhood cells and its own state.

At each timestep the CA state is recorded to the memory unit (MU), and it is also being compared with all the previous states, which are recorded in the MU. If the MU meaning does not equal the current state of CA, the comparison unit (CU) produces a signal to the control input MU and allows recording the current state of the CA inside of it. If the state of CA equals one of the MU code, CU resets the MU down to zero and CA changes the coordinates of the heterogeneous cells. In the next timesteps PRNG works in a similar way. The function of calculating new coordinates of heterogeneous cells is selected in advance. Figure 4 depicts the example of PRNG work.

The Fig. 4 shows the work of third PRNG. Formed bits are read from the data-output of the main cell at each timestep. This PRNG allows to increase significantly the repeating period, however, it has a low speed.

4 Analysis of the Quality of the PRNG Work Based on CA

Currently the quality of PRNG is evaluated by means of specially designed tests. These tests make it possible to determine the generator behavior and to determine the optimum range of the initial settings. Among all the tests the DIEHARD and NIST tests have the greatest authority. To use them, you have to create the files of appropriate format that store the generated bit sequence. ENT and NIST tests were used in this paper for the analysis of the proposed PRNG. These tests were used for the series of bit sequences from each PRNG. They gave positive results for sequences of different length [11].

There were NIST tests used for the analyses of these generators. And each of the tests was implemented in a separate program. Each program allows selecting the necessary parameters to perform the comprehensive analysis of the PRNG

Table 1 Results of the analysis of the first and second PRNGs (Only the Moore neighborhood) and third PRNG (Only the Neumann neighborhood)

Name of test	The length of the bit sequence	Test result		Test results for given number of heterogeneous cells			
		PRNG1	PRNG2	PRNG3			
				1	2	3	4
The Frequency (Monobit) Test	$10^4, 10^6$	+	+	±	+	+	+
Frequency Test within a Block	$10^4, 10^6$	+	+	±	+	+	+
The Runs Test	10^6	-	+	±	+	+	+
Tests for the Longest-Run-of-Ones in a Block	750000 128, 6272	+	+	±	+	+	+
The Binary Matrix Rank Test	10^4-10^6	-	-	-	-	-	-
The Discrete Fourier Transform Test	$10^3, 10^4-10^6$	+	+	±	+	+	+
The Non-overlapping Template Matching Test	10^3-10^6	+	+	±	±	+	+
The Overlapping Template Matching Test	10^6	-	-	-	-	-	-
Maurer's "Universal Statistical" Test	904960	+	+	±	±	+	+
The Lempel-Ziv Compression Test	10^6	+	+	±	±	+	+
The Linear Complexity Test	10^6	+	+	±	+	+	+
The Serial Test	$128, 10^3$	+	+	±	±	+	+
The Approximate Entropy Test	$10^4, 10^5$	+	+	±	±	+	+
The Cumulative Sums (Cusums) Test	$10^4, 10^3-10^6$	+	+	+	+	+	+
The Random Excursions Test	10^6	+	+	±	±	+	+
The Random Excursions Variant Test	10^6	+	+	-	±	+	+

behavior. The results of the analyzing the behavior of all three PRNGs are shown in Table 1. The symbol “+” indicates the positive result, and “−”—the negative one. If “±” is present in the table cell, this means that there were negative results among positive ones but these negative results do not exceed the permissible limits.

The second PRNG has the significantly greater operating speed because it spends the least time on the formation of a single bit of sequence. The third PRNG has poor operating speed performance. However, the third PRNG has the greatest length of the repeating period. The experiment showed that if the number of heterogeneous cells is more than 3, then there are not any coincidences of the CA states. In this case the third PRNG will have the highest speed operation.

5 Conclusion

The made PRNG analysis showed that the application of CA allows us to construct the PRNG that can compete with existing generators according to the main characteristics. The test application has shown that the PRNG based on CA has good characteristics, as they have positive results for the majority of tests. Research shows that the initial number of single cells and the size of the CA has the main influence on the quality of the PRNG. PRNGs showed the most effective work when the cells were in the logic state “1” and their amount was variable from 35 to 70%. The best CA size is determined from 17×17 to 30×30 of cells. The additional bit was formed by cells of CA itself, which excluded the applying of the external source of random numbers. Experimental research of PRNG based on the CA with heterogeneous cells allowed determining the amount of the initial CA cells with “1” state and size of CA, which give a positive result. Also results allowed to determine the number of heterogeneous cells (more than 3), in which there are almost no repeats. It was found that there is no need in the intermediate comparing. PRNG on the CA has high speed of random sequence generating without intermediate comparison.

References

1. Schneier, B.: Applied Cryptography: Protocols, Algorithms, and Source Code in C, 2nd edn., p. 784. Wiley Computer Publishing, Wiley (1996)
2. Marsaglia, G.: Random number generators. *J. Modern Appl. Stat. Methods* **2**, 2–13 (2003)
3. Wolfram, S.: Cryptography with cellular automata. *Lect. Notes Comput. Sci.* **218**, 429–432 (1986)
4. Rubio, C.F., Encinas, L.H., White, S.H., del Rey, A.M., Sánchez, G.R.: The use of linear hybrid cellular automata as pseudorandom bit generators in cryptography. *Neural Parallel Sci. Comput.* **12**(2), 175–192 (2004)
5. Cattell, K., Muzio, J.C.: Synthesis of one-dimensional linear hybrid cellular automata. *IEEE Trans. Comput.-Aided Des. Integr. Circuits Syst.* **15**(3), 325–335 (1996)
6. Suhinin, B.M.: Development of generators of pseudorandom binary sequences based on cellular automata. *Sci. Educ.* **9**, 1–21 (2010)
7. Hoe, D.H., Comer, J.M., Cerda, J.C., Martinez, C.D., Shirvaikar, M.V.: Cellular automata-based parallel random number generators using FPGAs. *Int. J. Reconfig. Comput.* Volume 2012 (2012), 1–13, Article ID 219028
8. Walker, J.: ENT. A Pseudorandom Number Sequence Test Program, 28 Jan 2008. <http://www.fourmilab.ch/random>
9. NIST—National Institute of Standards and Technology. Computer Security Division. Computer Security Resource Center. Download Documentation and Software: http://csrc.nist.gov/groups/ST/toolkit/rng/documentation_software.html
10. Marsaglia, G.: The Marsaglia Random Number CDROM Including the Diehard Battery of Tests of Randomness. Department of Statistics and Supercomputer Computations and Research Institute. <http://www.stat.fsu.edu/pub/diehard>
11. Bilan, S., Bilan, M., Bilan, S.: Novel pseudorandom sequence of numbers generator based cellular automata. *Inf. Technol. Secur.* **3**(1), 38–50 (2015)

A Mixed Fixed Point and Floating Point Graphics Pipeline

Ovidiu Sicoe and Mircea Popa

Abstract The current paper presents the results obtained by modifying a graphics pipeline implementation so that it partially operates with fixed-point numbers and partially with floating-point numbers. This was achieved by instrumenting a software implementation of the OpenGL ES 1.1 specification so that it uses the desired format for representing real numbers. The targeted outcome was to find a balance between the areas of the pipeline where the two different number formats were used so that the obtained output was similar. A variation in the format and precision of the fixed point number was also implemented and its impact on the output was studied.

Keywords Fixed-point • Floating-point • Graphics pipeline • Instrumentation

1 Introduction

Modern graphics processing units (GPUs) used in personal computers provide huge data throughput [1]. They are general purpose GPUs, designed to perform in all cases. Improvements can be made by specialized GPUs, designed to perform for particular applications. Such GPUs could be implemented using FPGAs [2]. We propose a study for optimizing the graphics pipeline of such an FPGA implemented GPU by analyzing the impact of using different formats for representing real numbers along the stages of the pipeline.

O. Sicoe (✉) · M. Popa
Computer Engineering Department, Politehnica University of Timisoara,
Timisoara, Romania
e-mail: ovidiu.sicoe@gmail.com

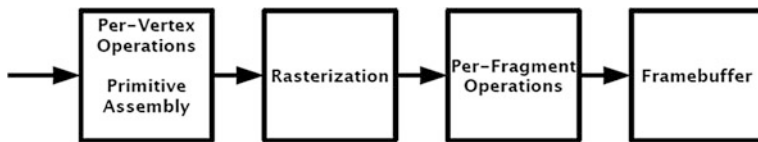


Fig. 1 OpenGL ES 1.1 pipeline [4]

2 Graphics Pipeline

Most of the graphics hardware works based on a multistage pipeline in which each step is specialized in doing a certain operation. Initial graphics pipelines were fixed [3], meaning that the user could use a limited set of standard transformations that could be applied to the processed data. Nowadays, the trend is to make the pipeline more and more flexible [3], allowing more complex effects to be applied during the data flow.

In order to use and control the graphics pipeline, certain application programming interfaces (APIs) were conceived. Two of the most known and used are OpenGL [4] and DirectX [5]. Those APIs are the interface to the graphic hardware and come as an abstraction of its capabilities. They are implemented in the driver, thus having little differences between each vendor.

Being an open specification, OpenGL was quickly adopted by different platforms and operating systems, allowing for easy, cross-platform graphics content deployment. We have chosen to instrument our own software implementation of the OpenGL ES 1.1 specification due to the simplicity of the concept and because it targets embedded systems.

Figure 1 presents the main stages of the abstraction of a graphics pipeline described by the OpenGL ES 1.1 specification.

In a fixed pipeline, like the one described by OpenGL ES 1.1 specification, most of the heavy real number computations happen in the Per-Vertex Operations stage, mainly implying matrix to matrix or matrix to vector computations [6], followed by the Rasterization stage.

3 Real Numbers Representations

Accurate real numbers cannot be represented in binary computers, so approximations are used. For this, there are several formats that suite different needs. Two of the most known and used are floating-point format and fixed-point format.

Fig. 2 Fixed-point format

sign	exponent	mantissa
------	----------	----------

Fig. 3 Floating-point format

3.1 Fixed-Point Numbers

The fixed-point number format always has a given number of bits for both the fractional part and the integer part. For example, the number 2.5 can be represented on a 16:16 format (16 bits for integer part and 16 bits for the fractional part) as 0000000000000010:1000000000000000.

The general rule is that the integer bits have ratios starting from 2^0 to 2^{i-1} , where i is the number of integer bits. On the other hand, the fractional bits have ratios from 2^{-1} to 2^{-f} , where f is the number of fractional bits. This can be better observed in Fig. 2.

It can be easily observed that the precision of a fixed-point number is 2^f . The main advantage of fixed-point representation is that the operations can be executed using the integer arithmetic and logic unit (ALU), so they are faster than the floating-point operations.

3.2 Floating-Point Numbers

For floating point, the point doesn't have a stationary position, thus the name floating. The general form of such a number is depicted in Fig. 3.

The mathematical interpretation of those bits according to the IEEE 754 specification [7] is $x = -1^{\text{sign}} \cdot 1 \cdot \text{mantissa} \cdot b^{\text{exponent}-\text{bias}}$, where b is the numeration base of the representation and bias is $2^{\text{size(exponent)}} - 1$. Following this, 2.5 is represented as 0.01111111.01000000000000000000000000 as a single precision floating-point number.

4 Graphics Pipeline Instrumentation

We have conceived a software implementation of the OpenGL ES 1.1 specification so that we could easily change the number representation across the logical stages of the pipeline. For this, we have provided hooks that are executed at the beginning and at the end of each stage, respectively.

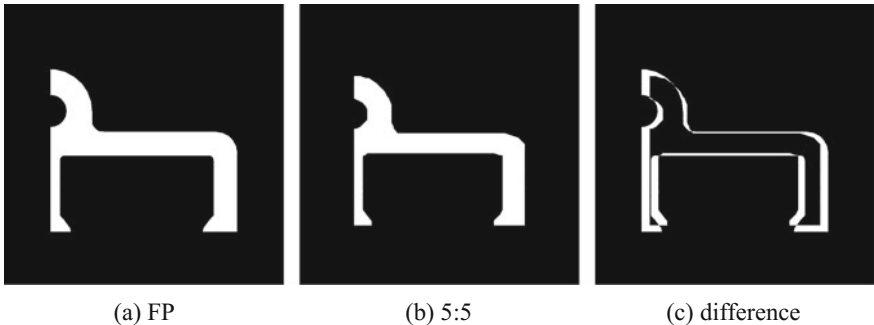


Fig. 4 Frame 0 images

We have also implemented an abstraction for real numbers and provided two concrete implementations, one for fixed point numbers and one for floating point numbers. This way, we could easily exchange the two different representations at any point of the execution, even at runtime.

For the fixed point representation, we have used 5:5, 10:10, 15:15, 16:16, 20:20 and 30:30 formats, while for the floating point representation, we have only used the IEEE 754 single precision format, with the exponent represented on 8 bits and the mantissa on 23 bits.

We have chosen the following instrumentation points, according to Fig. 1, taking into consideration the operations that were involved in between them:

- the start of the pipeline, before the Per-Vertex Operations stage
- after the Per-Vertex Operations stage and before the Rasterization

The Per-Vertex Operations stage is the most computation intensive, so we tried to see how a loss in precision during this stage would influence the final output. For this, we have considered that the reference images would be the ones that result from using the floating point representation across the whole pipeline. The next steps have been to replace the floating point number format during the Per-Vertex Operations stage with the fixed point format, taking into consideration different precisions. Here are the resulting combinations that we have used:

For each such combination we have generated 100 images, with the drawn object rotated by 2° around the vector $(-1; -1; -1)$ each frame. For example, Fig. 4a shows the first reference image by using floating point representation along the complete pipeline. Additionally, we have created difference images for each fixed point image, relative to the floating point counterpart, as briefly depicted in Fig. 4.

5 Results

The results we have obtained had shown that a full use of fixed point numbers across the complete pipeline would need a rather big increase in the size of the format, the 30:30 format being the only one that provided results almost identical to the original full FP rendering, as depicted in Fig. 5. Although the Fig. 5c seems black not highlighting any difference, there are actually 8 pixels different.

As depicted in Fig. 4, the differences are quite significant, so we tried to find a tradeoff between the output accuracy and the used formats, as depicted in Table 1. The output difference images pointed out that the formats presented at line 9 in the same Table 1 would yield outputs pretty close to the original floating point images.

Figure 6 presents the biggest difference between the outputs of the original full FP pipeline and the hybrid one using 16:16 fixed point combined with floating point numbers. A total of 161 pixels are different, out of the whole 640,000 pixels contained by the image.

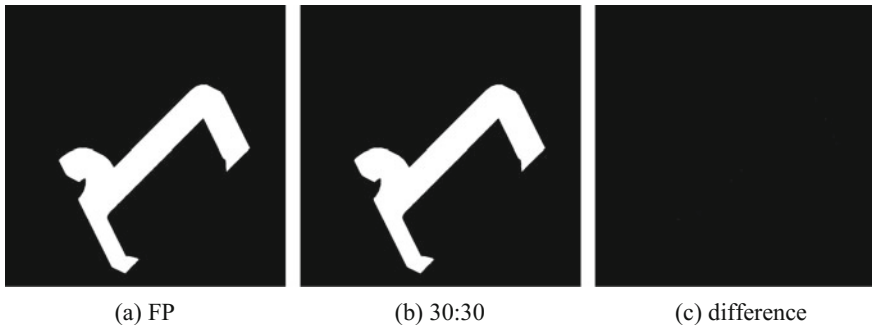


Fig. 5 Frame 30 images

Table 1 Precision combinations

	Per-Vertex operations	Rasterization
1	FP ^a	FP
2	5:5 ^b	5:5
3	10:10	10:10
4	15:15	15:15
5	20:20	20:20
6	30:30	30:30
7	10:10	FP
8	15:15	FP
9	16:16	FP
10	20:20	FP
11	30:30	FP

^aFloating point

^bFixed point format precision as integer size: fraction size

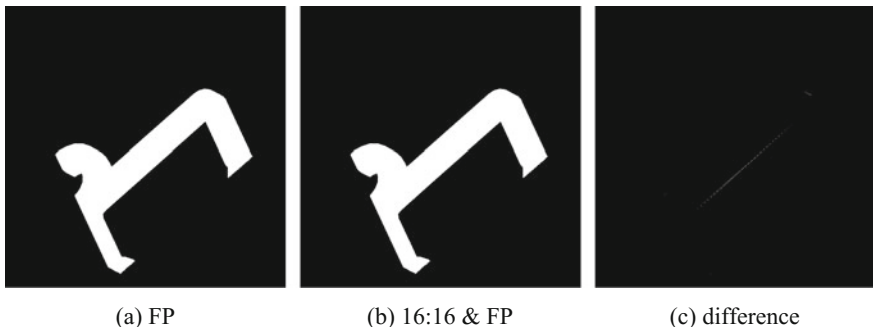


Fig. 6 Frame 28 images

6 Conclusions

We succeeded in comparing the outputs of a graphics pipeline that used different real number representations, either in a single format across the whole pipeline, either using mixed fixed and floating point representations along the stages.

We also drew the conclusion that the best mix of real number representations across the pipeline, without a significant increase in resources, but still preserving the original output, would be represented by a 16:16 fixed point representation being used in the Per-Vertex Operations stage and a floating point format being involved in the Rasterization and onward stages.

References

1. Lee, V.W., Kim, C., Chhugani, J., Deisher, M., Kim, D., Nguyen, A.D., Satish, N., Smelyanskiy, M., Chennupaty, S., Hammarlund, P., Singhal, R., Dubey, P.: Debunking the 100x GPU vs. CPU myth: an evaluation of throughput computing on CPU and GPU. In: Seznec, A., Weiser, U.C., Ronen, R. (eds.) 37th International Symposium on Computer Architecture (ISCA 2010), 19–23 June 2010, Saint-Malo, France, pp. 451–460. ACM (2010). doi:[10.1145/1815961.1816021](https://doi.org/10.1145/1815961.1816021)
2. Franchini, S., Gentile, A., Sorbello, F., Vassallo, G., Vitabile, S.: An embedded, FPGA-based computer graphics coprocessor with native geometric algebra support. Integration **42**(3), 346–355 (2009)
3. Luebke, D.P., Humphreys, G.: How GPUs work. IEEE Comput. **40**(2), 96–100 (2007). doi:[10.1109/MC.2007.59](https://doi.org/10.1109/MC.2007.59)
4. Inc, T.K.G.: Open GL ES Common/Common-Lite Profile Specification. <https://www.khronos.org/registry/gles/#specs11>
5. Microsoft: DirectX Graphics and Gaming. [https://msdn.microsoft.com/en-us/library/windows/desktop/ee63274\(v=vs.85\).aspx](https://msdn.microsoft.com/en-us/library/windows/desktop/ee63274(v=vs.85).aspx)
6. Hughes, J.F., van Dam, A., McGuire, M., Sklar, D.F., Foley, J.D., Feiner, S.K., Akeley, K.: Computer Graphics: Principles and Practice, 3rd edn. Addison-Wesley (2013)

7. Markstein, P.W.: The new IEEE-754 standard for floating point arithmetic. In: Cuyt, A.A.M., Kramer, W., Luther, W., Markstein, P.W. (eds.) Numerical Validation in Current Hardware Architectures, 6.1, 11 Jan 2008. Dagstuhl Seminar Proceedings, vol. 08021. Internationales Begegnungs- und Forschungszentrum für Informatik (IBFI), Schloss Dagstuhl, Germany. <http://drops.dagstuhl.de/opus/volltexte/2008/1448> (2008)

Functional Verification of AMS-SoC Models Using Hardware Emulation Platforms

Hanan Tawfik, Mohamed AbdElSalam, Mona Safar and Ashraf Salem

Abstract SystemC-AMS extensions to SystemC have been used in several applications to model the analog part of a heterogeneous SoC. The SoC is usually a pure simulation model where the digital part is modeled using SystemC. If an emulation verification environment is used, the digital part of the SoC would be running on the emulator while the analog part, modeled with SystemC-AMS, would be running on the co-model machine connected to emulator. In this paper, we propose an approach to interface SystemC-AMS models running on the emulator co-model machine with digital models running on the emulator. The verification challenge, addressed by this approach, lies in the fact that execution semantics of models running on the co-model machine connected to the emulator are inherently untimed, and SystemC-AMS is a timed environment with a time wheel completely independent from the emulation time wheel. Our approach presents execution dynamics to address this problem. We also describe a case study that demonstrates the validity of the proposed approach.

Keywords Functional verification • Hardware emulation • Dynamic TDF • SystemC-AMS

H. Tawfik · M. AbdElSalam · M. Safar · A. Salem (✉)
Mentor Graphics Egypt, Cairo 11361, Egypt
e-mail: ashraf_salem@mentor.com

H. Tawfik
e-mail: hanan_tawfik@mentor.com

M. AbdElSalam
e-mail: mohamed_abdelsalam@mentor.com

M. Safar
e-mail: mona_safar@mentor.com

1 Introduction

The main advantage of HW emulation in industry is full System-on-Chip (SoC) functional verification. SoC functional verification deals with protocols validation and correctness of functional behavior of each component in SoC design [1–3]. System-on-Chips (SoCs) nowadays, are heterogeneous in nature. They contain components from different domains such as digital, analog and RF components. This represents a big challenge when trying to functionally verify all components working together before final prototyping. In a system level pure simulation environment, digital components can already be modeled using SystemC [4]. To model analog/mixed signals behavior, defining a new extension to SystemC named SystemC-AMS, was necessary [5]. This extension allows SystemC and SystemC-AMS to co-exist in the same simulation environment and to communicate as well using the converter ports provided [6, 7].

There could be some cases where the digital part of a SoC is provided in RTL format running on a hardware emulator. In this case, the SystemC-AMS model running on an emulator host machine will have to exchange data with the digital part running on the hardware emulator. However according to [8], if the emulator environment implements the SCE-MI standard, then only untimed SystemC can be used for implementing models or testbenches running on the host machine. SystemC-AMS models are timed and although allowed to run with emulation, their simulation time is non-correlated to the emulation time.

In this paper, we present an approach to address this interface/co-verification challenge between SystemC-AMS models, running on a host machine, and the digital RTL logic running on the emulator. We have also implemented a proof of concept to demonstrate the validity of the proposed approach (Fig. 1).

The rest of this paper is organized as follows. Section 2 provides some background about SystemC-AMS extension and Direct Programming Interface (DPI). Section 3 goes through the previous related work. Section 4 proposes execution

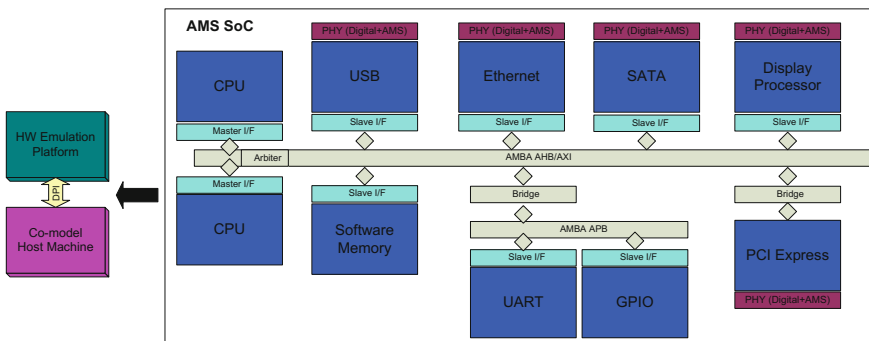


Fig. 1 Full SoC functional verification on HW emulation platforms

dynamics to solve the interface challenge between SystemC-AMS and any HDL design running on a hardware emulator using DPI. Section 5 describes the case study used to demonstrate our proof of concept. Section 6 concludes the paper.

2 Background

SystemC-AMS is an extension to SystemC. It allows the modeling of analog/mixed-signals systems at different level of abstractions. It can be used for different use cases: executable specification, virtual prototyping, architecture exploration and integration validation. SystemC-AMS provides three different models of computations [7, 9]:

Timed Data Flow. The system is modeled as a set of modules connected together where data samples flow from one module to another. The activation of a module depends upon the time step specified by the user. The port rate of the module is also specified by the user to determine the number of data samples, per activation, which is to be read or written by this specific module. A set of connected TDF modules is called a TDF cluster. To the SystemC scheduler, the TDF cluster is considered as a normal SystemC module, that will be scheduled similarly to the other pure SystemC modules. When the TDF cluster is selected to run, the SystemC-AMS scheduler blocks the SystemC scheduler and activates the modules inside the cluster. The activation occurs according to a static schedule that has been constructed based on the port rates and time steps previously defined by the user for each module in the cluster [7]. This static scheduling approach speeds up the simulation significantly [11].

Signal Flow (LSF). It allows the modeling of continuous-time non-conservative systems. The models are described using LSF pre-defined primitives like adders, integrators and differentiators. During elaboration phase, based on the description provided, SystemC-AMS composes a corresponding system of linear equations that can be solved by a dedicated solver that uses numerical methods to be applied at appropriate timesteps [7].

Electrical Linear Networks (ELN). It allows the modeling of continuous-time conservative systems. The models are described using ELN electrical network primitives like resistors, capacitors and inductor. During elaboration phase, the SystemC-AMS composes, based on the description provided, a corresponding system of equations that can be solved by a dedicated solver using numerical methods that are applied at appropriate timesteps [7].

In this paper, our focus is directed toward the TDF MoC and its interaction with a digital model running on an emulator. SystemC-AMS library is released in the form of proof of concept (PoC) releases. Latest stable release available is SystemC-AMS PoC 1.0.1. The work presented in this paper is based on SystemC-AMS PoC 2.0 Beta which is the latest release for this library. Although still in beta state, it has the advantage of supporting the set of dynamic TDF features, which mainly includes the TDF cluster activation based on events, and

dynamic time step assignment during simulation time [10]. The event-based TDF cluster activation is used in the approach proposed in this paper for proper interfacing with the hardware emulator.

The Direct Programming Interface (DPI) [12], defines the concept of import functions that will be used by the approach proposed in this paper. The import function is called from the transactor (usually written using a mix of System Verilog and Verilog) and is defined in the SystemC/C++ part in a layer usually called DPI proxy. An import function is used to transfer data from HDL to SystemC/C++ or vice versa. In [8], the concept of controlled and uncontrolled clock was also introduced. The uncontrolled clock is a free running clock that never gets interrupted. The controlled clock has the same time period as the uncontrolled clock but it can be freezed by the emulator in order for a transactor to complete an ongoing transaction and this to ensure correct operation of the DUT. When an import function is called, the controlled clock is usually stopped until the call returns.

3 Related Work

A large number of publications covers the use of SystemC-AMS (for analog mixed/signal components) coupled with SystemC (for digital components) to model heterogeneous SoC. In [13], wireless sensor network nodes have been modeled. In [14] the modeling of near-field communication transceiver has been explored. In [15], the model for a CMOS video sensor is implemented where SystemC-AMS interfaces with SystemC-TLM using the wrapper described in [11]. To our knowledge, the work in this paper is the first to establish a bridge between SystemC-AMS and the emulation technology.

4 Execution Dynamics

The execution semantics of models running on the co-model machine connected to the emulator are inherently untimed, and SystemC-AMS is a timed environment with a time wheel completely independent from the emulation time wheel.

The execution dynamics are composed of 2 phases: *Phase 1: Initialization*.

Initialization phase: should happen at the beginning of the emulation while no other import calls are running. During this phase, a clock calculator C++ object is used to calculate, approximately, the clock period of the uncontrolled clock of the emulator. This value is used later in any TDF modules in SystemC-AMS that calculates quantities that are a function of time. Figure 2a demonstrates the operation. An import call is called and the clock calculator entity records the current

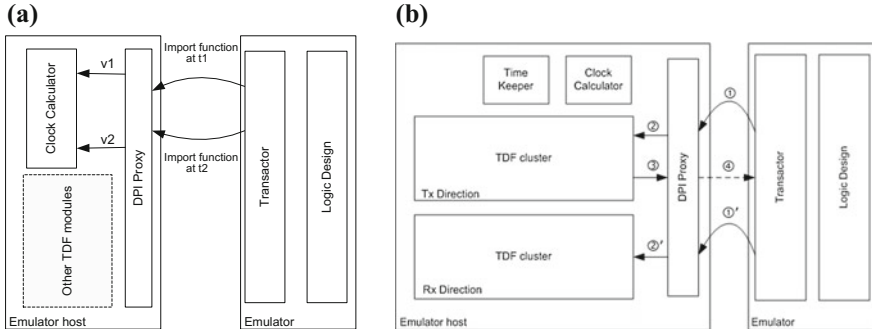


Fig. 2 a Initialization phase. b Data transfer phase

time t_1 . A second import function is called, one clock cycle later, and the clock calculator entity record the current time t_2 . It calculates the clock period by subtracting t_1 from t_2 and store the value.

Phase 2: Data transfer.

Time keeper update: During the data transfer operation, elapsed time is tracked using the time keeper entity which is basically a counter that gets updated each DPI call with the number of controlled clocks elapsed so far on the emulator side. Given the number of controlled clocks elapsed and the uncontrolled clock period obtained in the initialization phase, the approximate elapsed amount of time can be calculated (As mentioned the uncontrolled clock period is equal to the controlled clock period but the number of clock cycles elapsed is not the same given the controlled clock freezing time). This time being tracked by the time keeper can be used in TDF clusters that generate quantities that are function of time.

Data exchange: We assume that the testbench has two TDF clusters, one for each direction (directions are relative to the model running on the emulator host machine). The Tx direction cluster transfers data to the emulator and the Rx direction cluster receives data from the emulator. Data is transferred and received through two DPI import functions, one for each direction. In each of the import functions, corresponding TDF clusters are activated through events, using the new capabilities offered in SystemC-AMS 2.0 Beta [10]. Figure 2b demonstrates the operation described below:

Tx direction: ① Import function is called, from the transactor running on the emulator, with an empty output parameter to be filled with data generated from the testbench side. ② Import function activates the TDF cluster which was blocked on an event `event_tx_tdf`. The import function blocks on another event `event_tx_import` waiting for the response from the cluster. ③ Once the cluster is ready with the data, it unblocks the import function blocked on `event_tx_import` and wait for next cluster activation on the event `event_tx_tdf` during next DPI import call. ④ Import function returns with the data generated from the TDF cluster back to the transactor.

Rx direction: ①' Import function is called from the transactor running on the emulator with an input parameter filled with data generated from the testbench side. ②' Import function

activates the TDF cluster which was blocked on an event `event_rx_tdf`. The import function blocks on another event `event_rx_import` waiting for the cluster to consume the data.

5 Case Study

In order to verify the validity of our proposed interfacing approach, we have implemented a case study with a Tx TDF cluster composed of two TDF modules and an Rx cluster composed of a single TDF module. On the emulator side, a simple transactor module is implemented that receives the data from Tx direction and loop it back to the Rx direction (directions are relative to the model running on the host machine). Import functions for Tx and Rx direction are called every clock cycle Fig. 3 shows the case study's architecture.

The different TDF modules in the clusters are listed below under their respective directions:

Tx Direction:

Sine wave generator. The implementation has been reused from the example provided in [7]. This TDF module depends on time, so it will be using the time tracked by the time keeper to generate the values.

Flash ADC. An implementation of a 3 bit ADC with its circuit described [16].

Rx Direction:

Kelvin divider DAC (String DAC). An implementation of a 3 bit DAC with its circuit described in [17].

The operation is similar to the steps provided in the previous section. During the initialization phase, the clock period is determined. During data transfer phase, the time keeper is updated with each import function call and used for generating an analog value which is passed as an input to the ADC module, scheduled to run next. The ADC module converts the analog input value into a 3 bit value then unblocks the import function which returns the generated value to the transactor. In the Rx

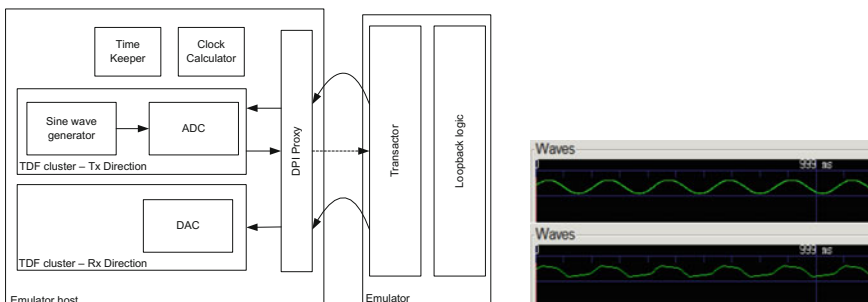


Fig. 3 Cast study architecture. Generated wave (*top*) versus Reconstructed wave (*bottom*)

Table 1 Import DPI statistics

Import DPI call	Total time consumed	Average time/call (μ s)	Number of time called
SendValue (One-way)	9 s, 999503 μ s	2	3,786,459
CalculateClockPeriod (One-way)	4 μ s	2	2
GetValue (Two-way)	88 s, 371095 μ s	23	3,786,459

direction, another import function is called to activate the cluster and then blocks until it executes. The DAC reads the value received from the transactor and converts it back into an analog value. Upon completion the cluster unblocks the import function in order to give it a chance to fetch another value from the transactor. Each cluster will be activated again whenever the import function, corresponding to the direction the cluster is used for, is called. The result expected is that the sine wave generated in Tx direction should be approximately reconstructed in the Rx direction. Figure 3 shows the generated waveform versus the reconstructed one. The amount of distortion shown in the reconstructed waveform is a factor of the accuracy of the ADC and DAC process.

Table 1 lists runtime statistics about the main import functions used in the case study. Those statistics include the total time consumed by each import function throughout the whole run, the average execution time for a single call and the number of times each import function has been called. SendValue is the import function used for the Rx direction and is labeled as one-way because it transfers data in one direction only, from RTL to software. GetValue is the import function used for the Tx direction and is labeled as two-way because it is called from RTL to software and returns back to RTL after fetching the required data from software. CalculateClockPeriod is a one-way import function that is used during the initialization phase to calculate the clock period. Those numbers have been collected while running the case study on a hardware emulator [3] with an operating frequency of 694 kHz.

6 Conclusion

In this paper we have demonstrated the execution dynamics to interface a SystemC-AMS model running on an emulator host machine with a digital design running on an emulator. Future work will be exploring the possibility of sending multiple analog values in a single import function in order to minimize context switching between emulation and System-C AMS simulation. In this case, controlled clock would need to freeze less frequently, leading to a better runtime performance.

References

1. Lin, Y.-S.: Essential Issues in SOC Design: Designing Complex Systems-on-Chip. Springer Science & Business Media, 31 May 2007
2. Nurmi, J., Tenhunen, H., Isoaho, J., Jantsch, A.: Interconnect-Centric Design for Advanced SoC and NoC. Kluwer Academic Publishers (2004)
3. Mentor Graphics Corporation, Veloce Emulation Platform. <http://www.mentor.com/products.fv.emulation-systems/>
4. SystemC. <http://www.systemc.org>
5. SystemC-AMS. <http://www.systemc-ams.org>
6. Vachoux, A., Grimm, C., Einwich, K.: Towards analog and mixed-signal SOC design with SystemC-AMS. In: Proceedings of Second IEEE International Workshop on Electronic Design, Test and Applications (DELTA), Perth, WA, Australia, pp. 97–102, Jan 2004
7. Accelera Systems Initiative: SystemC AMS Extensions User’s Guide, pp. 1–153 (2010)
8. Accelera Systems Initiative: Standard Co-Emulation Modeling Interface (SCE-MI) Reference Manual, v2.2, pp. 1–203, Jan 2014
9. Li, F., Dekneuvvel, E., Jacquemond, G., Quaglia, D., Lora, M., Pecheux, F., Butaud, R.: Multi-level modeling of wireless embedded systems. In: Proceedings of the Forum on Specification and Design Languages (FDL), Munich, Germany, pp. 1–8, Oct 2014
10. Accelera Systems Initiative: Standard SystemC AMS Extensions 2.0 Language Reference Manual, pp. 1–200 (2013)
11. Damm, M., Grimm, C., Haas, J., Herrholz, A., Nebel, W.: Connecting SystemC-AMS models with OSCI TLM 2.0 models using temporal decoupling. In: Proceedings of the Forum on Specification, Verification and Design Languages (FDL), Stuttgart, Germany, pp. 25–30, Sept 2008
12. Accelera: IEEE 1800-2012: SystemVerilog (SV), IEEE std 1800-2012, pp. 1–1275 (2012)
13. Vasilevski, M., Pecheux, F., Aboushady, H., De Lamarre, L.: Modeling heterogeneous systems using SystemC-AMS case study: a wireless sensor network node. In: Proceedings of the IEEE International Behavioral Modeling and Simulation Workshop (BMAS), San Jose, CA, USA, pp. 11–16, Sept 2007
14. Li, W., Zhou, D., Li, M., Nguyen, B.P., Zeng, X.: Near-field communication transceiver system modeling and analysis using SystemC/SystemC-AMS with the consideration of noise issues. *IEEE Trans. Very Large Scale Integr. Syst.* **21**, 2250–2261 (2013)
15. Cenni, F., Scotti, S., Simeu, E.: Behavioral modeling of a CMOS video sensor platform using SystemC-AMS/TLM. In: Forum on Specification and Design Languages (FDL), Oldenburg, Germany, pp. 1–6, Sept 2011
16. Kester, W.: MT-020 tutorial, ADC Architecture 1: The Flash Converter, Analog Devices. <http://www.analog.com>
17. Kester, W.: MT-014 tutorial, Basic DAC Architecture 1: String DAC and Thermometer (Fully Decoded) DACs, Analog Devices. <http://www.analog.com>

Influence of the Antenna's Height to the Standing Waves Ratio When Performing the Electromagnetic Susceptibility Tests in Anechoic Chambers

Martin Pospisilik, Milan Adamek and Petr Neumann

Abstract Immunity tests to radiated electromagnetic field are one of the most common tests performed within the framework of the electromagnetic compatibility. These tests are performed inside a shielded chamber provided the requirements given by the appropriate standards are kept. As the levels of the generated fields can be high and the output power of the transmitting amplifiers cannot be infinite, it is necessary to achieve a good performance of the transmitting antenna. By means of the real experiment the author of this paper shows how the height of the antenna placed above the conductive floor can affect the antenna's voltage standing waves ratio and how this phenomenon affects the parameters of the whole measurement system.

Keywords EMC • Susceptibility test • Semi anechoic chamber • Transmitting antenna • Voltage standing wave ratio • Transmitting power

1 Introduction

Testing of electromagnetic susceptibility became one of the important disciplines as the complexity of electrical systems that must operate together has increased. In 1968, H.M. Schilke, one of the founders of the field of science related to the electromagnetic compatibility, claimed: "The system itself may be perfectly reliable, but practically worthless in operation unless it is not electromagnetically compatible at the same time." [1]. Since that time constructers faced many problems

M. Pospisilik (✉) · M. Adamek · P. Neumann
Faculty of Applied Informatics, Tomas Bata University in Zlin,
Nad Stranemi 4511, 760 05 Zlin, Czech Republic
e-mail: pospisilik@fai.utb.cz

M. Adamek
e-mail: adamek@fai.utb.cz

P. Neumann
e-mail: neumann@fai.utb.cz

raising at the field of mutual electromagnetic compatibility of devices being in a concurrent operation. For example, as described in [2], in 1984 the NATO airplane "Tornado" crashed in Germany after its circuits interfered with a powerful transmitter in Holkirchen. In 1982, the British cruiser Sheffield was sunk by Argentine aircraft in the Falklands War, partly because its defence system abetting the enemy rockets was switched. Due to its electromagnetic incompatibility, it interfered with radio communication, crucial for the cruiser's crew. According to [3], there were several accidents reported in the Czech Republic.

Therefore, the electronic devices should be tested for their immunity to the radiated electromagnetic field.

1.1 Standardization

In Europe the current basic definition of the test of the electromagnetic susceptibility of common devices against the radiated electromagnetic field is provided by the standard EN 61000-4-3 [4]. It defines the frequency ranges, modulations and intensities that are to be developed in the area in which the tested device is placed. The field intensity levels specified by the standard [4] are enlisted usually between 1 and 10 V/m.

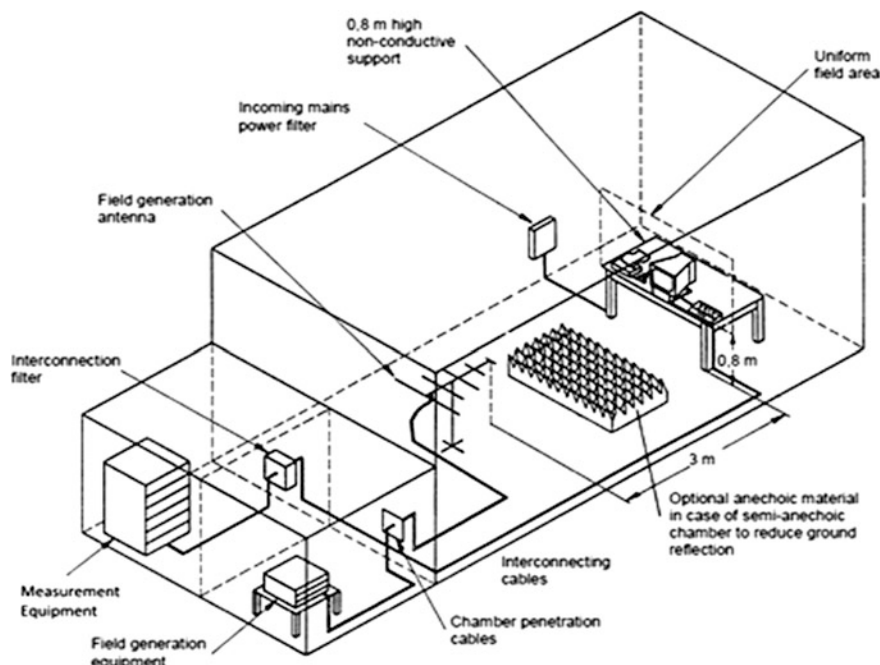


Fig. 1 Basic configuration of the immunity test [5]

1.2 Basic Configuration of the Test

The basic configuration of the test is depicted in Fig. 1. The tested device is placed in an anechoic chamber on a non-conductive table. It is irradiated by the modulated electromagnetic field generated by an antenna placed in the distance specified by the standards. The field intensity is checked inside the space called Uniform field area. Its dimensions as well as the tolerance for the intensity levels are specified in [4].

2 Problem Description

When the configuration as depicted in Fig. 1 is used, there exists a risk of interactions between the metal floor of the chamber and the transmitting antenna, resulting in changes in the antenna's impedance. This causes the impedance matching of the antenna to the amplifier is corrupted, resulting in the occurrence of standing waves on the cable between the antenna and the amplifier. The quantity of standing waves can generally be described as a voltage standing waves ratio (VSWR) by Eq. (1). It defines the ration between the maximum (V_{max}) and minimum (V_{min}) amplitude of the standing wave. Also the amplitudes of the incident (V_i) and the reflected (V_r) waves can be applied.

$$VSWR = \frac{V_{max}}{V_{min}} = \frac{V_i + V_r}{V_i - V_r} \quad (1)$$

The amount of energy reflected back from the point of impedance mismatch can be described by means of the reflection coefficient ρ .

$$\rho = \frac{V_r}{V_i} \quad (2)$$

Therefore the Eq. (3) can be applied.

$$VSWR = \frac{1 + \rho}{1 - \rho} \quad (3)$$

The efficiency of transmitting the energy to the space is then affected by mismatch losses that are caused by the reflections from the antenna. According to [6] the mismatch loss ratio (ML) is the ratio of incident power to the difference between incident and reflected power:

$$ML = 10 \log_{10} \frac{P_i}{P_i - P_r} = -10 \log_{10} (1 - \rho^2) [\text{dB}] \quad (4)$$

In (4), P_i stands for the incident power (generated by the amplifier) while P_r stands for the reflected power, that is not transmitted but loads the cable and the amplifier in the form of the standing waves.

In terms of the voltage standing wave ratio (VSWR) the following equation can be applied [6]:

$$ML = -10 \log_{10} \left(1 - \left(\frac{VSWR - 1}{VSWR + 1} \right)^2 \right) [\text{dB}] \quad (5)$$

3 Experiment Description

The experiment was held in the semi-anechoic chamber Frankonia SAC-3 Plus that is placed at the Faculty of Applied Informatics of Tomas Bata University in Zlin [7]. The signal was generated by the generator Rohde & Schwarz SMF 100 A and amplified by the amplifier Amplifier Research 150W1000. The signal was transmitted with the antenna Rohde&Schwarz HL046E. The frequencies and the modulation were set in accordance with the standard EN 61000-4-3, but the frequency range was limited to 250 MHz as the hereby described effects were observed in the frequency range from 80 to 150 MHz. The power of the amplifier was set by means of a feedback field probe ETS Lindgren HI-6005 that was located in the middle of the Uniform field area. The required level of the electromagnetic field was set to 10 V/m and the polarization of the antenna was angled to vertical. The instruments were driven by EMC 32 software. The configuration of the semi-anechoic chamber was as depicted in Fig. 1, using the absorbers placed on the floor.

During the experiment, the antenna's height above the floor was consequently changed from 90 to 135 cm with the step of 5 cm. For each of the heights the transmitting frequencies from 80 to 250 MHz were applied increasingly with the step of 1% and the response of the chamber (field level at the position of the probe) as well as the response of the transmitting system (output power of the amplifier and voltage standing waves ratio).

4 Results and Discussion

The results obtained by the experiment has shown that for vertical antenna's polarization the setting of its operating height can be critical in terms of VSWR and power losses, especially at the frequencies below approximately 200 MHz.

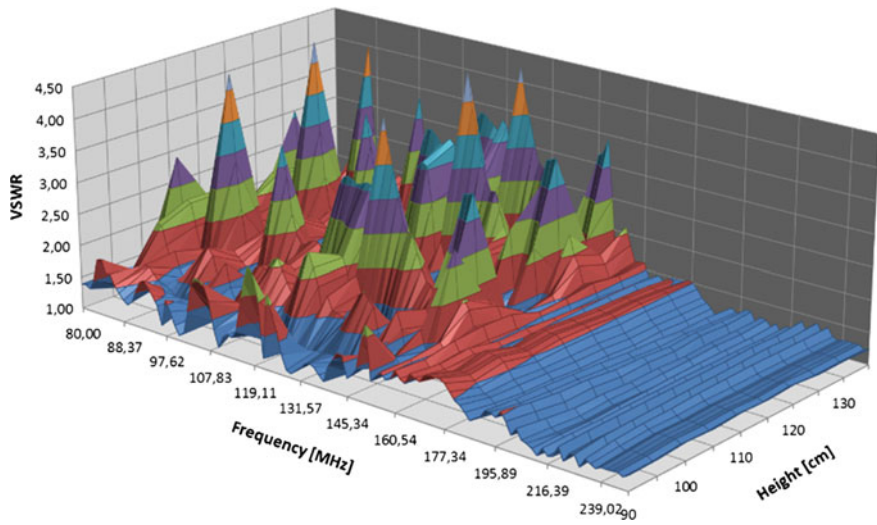


Fig. 2 VSWR versus antenna's height and carrier frequency

In Fig. 2 the VSWR dependence on frequency and the antenna's height above the conductive floor is depicted. In Fig. 3 there is depicted the dependence of the output power of the amplifiers needed to generate the required field intensity strength of 10 V/m at the point where the feedback sensor was placed on the antenna height and the frequency. Although the level of the power generated by the amplifier does not directly reflect the antenna's VSWR as there may be reflections inside the chamber that affect the level measured by the sensor, a certain correlation between the measured values of the amplifier's output power and the measured antenna's VSWR has been observed by means of the following method. For each of the antenna's height, the maximum of VSWR and of the output power has been registered regardless of the carrier frequency. From these values the graph depicted in Fig. 4 has been compiled.

In this graph, the dependencies of three different variables on the antenna's height are depicted in order to show the abovementioned correlation:

- Maximum VSWR observed in the range from 80 to 250 MHz,
- Maximum amplifier's power generated between 80 and 250 MHz,
- Hypothetical output power that would be needed to generate the required intensity provided VSWR was as low as 1 in the whole frequency range calculated according to Eq. (5).

According to Fig. 4, it can be stated that for antenna's heights above approximately 110 cm the need for transmitting power mostly depends on the antenna's VSWR that changes with the antenna's height. If the reflections on the antenna were cancelled, the transmitting power needed to achieve the required level 10 V/m in the distance of 3 m from the antenna would be from 40 to 55 W.

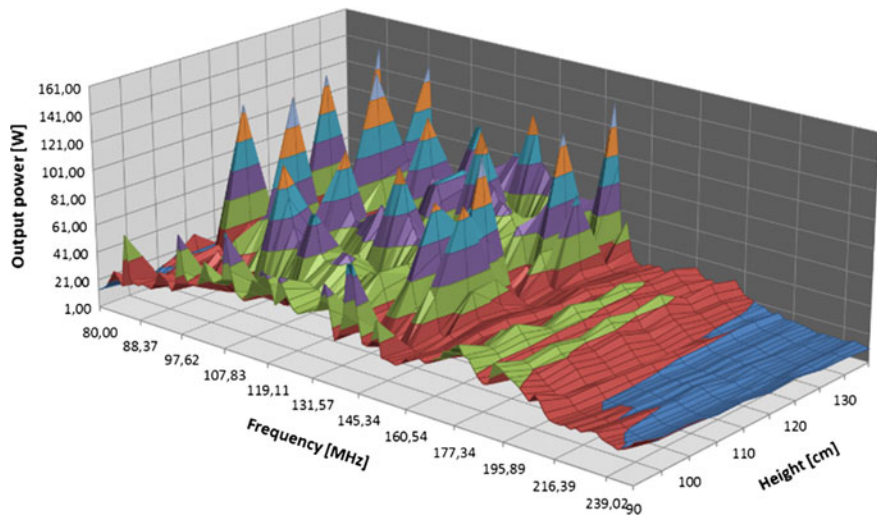


Fig. 3 VSWR versus antenna's height and carrier frequency

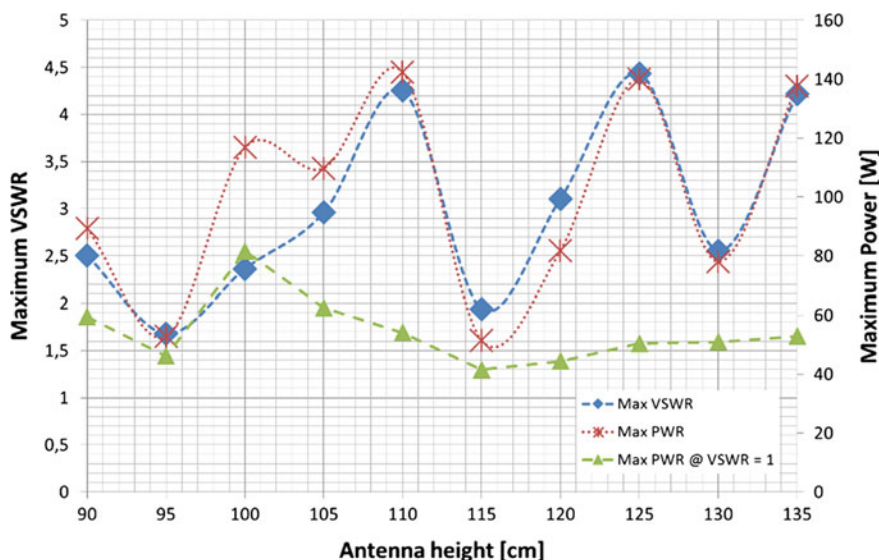


Fig. 4 VSWR, real output power and hypothetical output power at VSWR = 1 versus antenna's height

With the currently achieved VSWR the required output power varied from approximately 52 W at the antenna's height of 115 cm to approximately 142 W at 110 cm. For the antenna's heights below 110 cm the real output power needed to achieve the required field intensity has been even higher than expected.

A capacitive coupling between the floor and the antenna is suspected to cause this phenomenon.

Finally, this experiment shows how complex the issues on radiation of the EM field inside the semianechoic chambers are. In the past, the authors performed other types of experiments that could also be interesting for the audience, for example [8].

5 Conclusions

This paper describes the experiment in which the dependence of the transmitting antenna's VSWR was observed according to its height above the conductive floor. A typical situation of EMC susceptibility test in a semi anechoic chamber has been modeled. According to this experiment it can be generally stated that when vertically polarized, the coupling between the antenna and the chamber's floor affects the antenna's VSWR which results in increased requirements on the power of the transmitting amplifiers. Because the standard EN 61000-4-3 does not accurately specify the antenna's height, it is advisable to search for the optimal antenna's height prior to performing of the uniform field area calibration.

Acknowledgements This work was supported by the Ministry of Education, Youth and Sports of the Czech Republic within the National Sustainability Program project No. LO1303 (MSMT-7778/2014).

References

1. Svacina, J.: Electromagnetic compatibility [Elektromagneticka kompatibilita]. Brno University of Technology, Brno (2002)
2. Paul, C.R.: Introduction to Electromagnetic Compatibility. Wiley, New York (1992)
3. Vaculik, P.: Introduction to electromagnetic compatibility [Uvod do elektromagnetické kompatibility]. In: Proceedings of Radio-Komunikace '94, Pardubice (1994)
4. International Electrotechnical Commission: EN 61000-4-3
5. http://www.iec.ch/emc/basic_emc/basic_emc_immunity.htm
6. Eadie, A.: EMC Immunity Testing. <https://www.emcfastpass.com/emc-testing-beginners-guide/emc-immunity-testing/>
7. Lo, Y.T., Lee, S.W.: Antenna Handbook: Theory, Applications, and Design. Springer Science + Business Media, New York (1988)
8. Pospisil, M., Soldan, P.: Electromagnetic field distribution within a semi anechoic chamber. In: Proceedings of the 18th International Conference on Systems, Santorini Island (2014)

Carstairs-McCarthy's Morphological Rules of English Language in RDFCFL Graphs

Alena Lukasová, Martin Žáček and Marek Vajgl

Abstract The article presents an approach to express morphology and syntax rules or specifications of basic terminology of the English language in RDFCFL graphic metalanguage following the methodology of Andrew Carstairs-McCarthy's book. The formal modelling of English linguistics follows here two levels: syntactical (investigating lexical and functional categories of speech, in particular rules of their merging into larger units) and semantic-based morphology of the English language which covers the importance of language morphemes.

Keywords RDF model • Clausal form logic (CFL) • RDFCFL formal system

1 Motivation

An RDF modelling principle of real world and human activities has become more or less one of the leading approaches within artificial intelligence in the last decade. Databases of RDF-linked basic statements describe a lot of most important areas of real life. RDF modelling of a domain of real life has brought into knowledge representation a strong demand on precise specifications of concepts within their broader connections with other concepts of a modelled domain. From the point of view of precise concept formal representation, Linguistics generally belongs to the same category as exact sciences like Mathematics or Computer Science. No wonder

A. Lukasová · M. Žáček (✉) · M. Vajgl
Department of Computers and Informatics, University of Ostrava,
Ostrava, Czech Republic
e-mail: martin.zacek@osu.cz

A. Lukasová
e-mail: alena.lukasova@osu.cz

M. Vajgl
e-mail: marek.vajgl@osu.cz

that some specialists in formal modelling of human thinking did not miss a possibility to make an experiment with meta-language expressing basic linguistic concepts and to formulate linguistic research methodology by the RDF model formal tools.

2 Introduction

The authors of the paper completed the original RDF model by introducing general or existential statements (see [1]) as necessary conditions of formal deduction corresponding to the natural human mental activity. Moreover, they have extended the RDF model with “if – then” form of sentences following the Richard’s method known as “clausal form logics” (CFL [2]).

We present here an experiment to express ground terminology of the English language morphology and syntax on the base of first order logic’s graphic tools RDFCFL [3]. It seems that our meta-language representation of English grammatical rules taking into account predicate logic’s semantic principle with its high expressivity and easy-to-read graph-based form could generally bring new aspects into language theory.

The aim of this paper is modelling of linguistics at two levels

- syntactical: investigating lexical and functional categories of speech, in particular rules of their merging into higher units; here a graph-based tool of formal expressing became the RDFCFL metalanguage,
- semantical: semantic-based morphology of a particular language which covers the importance of language morphemes; here it is better to use simple semantic (associative) networks together with some explaining by example.

All the life people learn to form sentences according to certain rules. Any natural language has its own rules, e.g. the English language form sentences using a simple formula SVOMPT (**S**ubject, **V**erb, **O**bjects, **M**anner, **P**lace, **T**ime), while the Czech language has a structure that is much more complicated.

In order to model a natural language, it is necessary to find suitable means in the form of a formal system. As a default, the English language with its fairly simple morphology rules has been chosen for our experiment.

3 Drawing Sentences About English Linguistics by Means of RDFCFL Graph Language or Semantic Network

Richards [4] proposed the Clausal Form Logic (CFL) built on the base of the FOPL and well corresponding with common using of the conditional “if—then” statement. Generally, a conditional statement (clause) says that the consequent

composed as a disjunction of some predicate atoms follows from the antecedent composed as a conjunction of some predicate atoms.

The approach allows us to formulate clauses in the form

$$\langle \text{antecedent} \rangle \langle \text{implies} \rangle \langle \text{consequent} \rangle \quad (1)$$

Selecting a formal language for a knowledge representation is crucial. The formal basis should become here the first order predicate logic (FOPL) base for its high expressivity and a wide range of already developed formal deduction tools.

Knowledge Representation (originally those contained in Web resources), which are based on a domain ontology usually has been created in the framework of RDF (Resource Description Framework) model. An RDF model manipulates the semantic aspect of terms specified through URI references to resources in which their meanings are always elucidated by means of a certain position in a relevant ontology. The graphic RDF model in its form is easy and simple to understand even for the users who do not have experience with formal modelling. The idea is based on a simple statement concerning relations between items (resources) in the form of basic vector (Fig. 1).

The vector pattern corresponds with the SVO part of the general SVOMPT pattern of the English grammar.

The graph version of the vector representation uses notation of the Clausal Form Logic (CFL [5]).

Developments in the field of formal knowledge representation clearly show that the language of the FOPL and specifically its clausal form (in text or graph version) is an appropriate formal language that can virtually represent any assertion formulated in a natural language.

The graphic form of the CFL language [4] became the main idea of the RDFCFL graph language used here. Clauses use dashed lines in the cases of antecedent vectors and full lines for vectors of clause consequent.

By means of adding elements of Description logic [5] into the RDF model it has been possible to communicate with the web language OWL that also increases its expressiveness. Both languages in their text format are based on the XML syntax, making it easy for their machine processing.

Besides the RDFCFL representation of a clause we also use a simpler tool *semantic network* expressing interrelations of concepts in English linguistic known a long time before informatics ordered them among formal modelling tools. We use



Fig. 1 Basic vector

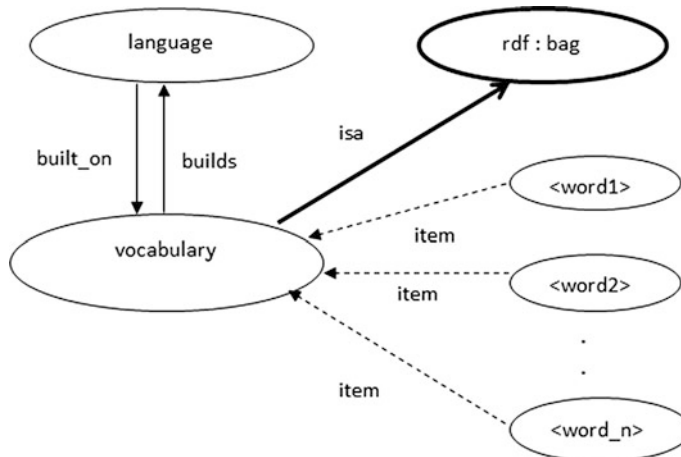


Fig. 2 Words are building blocks of a language

here the semantic network principle in the cases where the semantics of clauses is more important than syntax of their corresponding rules.

Example

The RDFCFL graphic clausal statement of the form (1) in the following figure expresses the fact (Fig. 2):

Words as building blocks of a language collected in its vocabulary expressed.

- by a collection of simple atomic statements of the form (1) like “word1 is item of a vocabulary”,
- by means of an advanced RDF constructor rdf: bag (thick full line).

To each name of the graph items RDF CFL orders a URI identifier within a chosen ontology (top-level or domain specified) conventional to the topic of linguistics.

In the book [6] Andrew Carstairs-McCarthy specifies the concept of word as follows:

“*Words* are units of language which are basic in two senses:

1. in that they have meanings that are unpredictable and so must be listed in dictionaries and
2. in that they are the building-blocks out of which phrases and sentences are formed.” (Figs. 3 and 4).

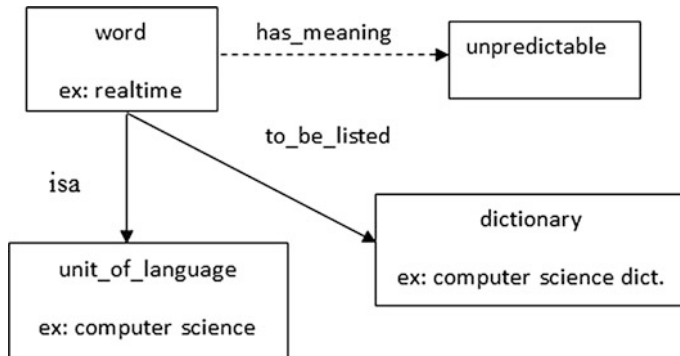


Fig. 3 Ad 1 semantic network expressing the role of dictionary to explain an unpredictable word

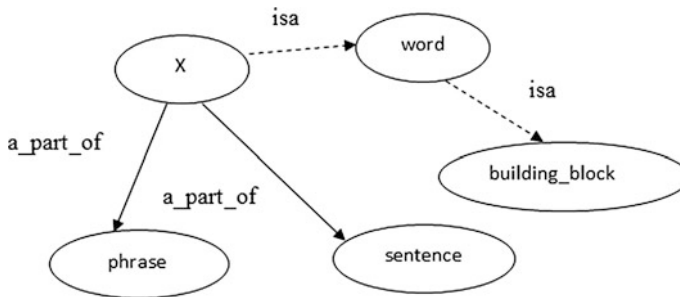


Fig. 4 Ad 2 pattern of the role of words as building blocks of phrases or sentences

4 Conclusion

We see a usability of our RDPCFL approach in two directions:

1. As an easy-to-understand tool of representation of language grammatical rules. It is possible to use only a simple semantic network.
2. The approach based on logical principles could push authors of definitions or specifications of rules to hold within special grammar categories to specify carefully what are items of clauses, antecedents—prerequisites and consequents—conclusions of clauses represented truth-full general sentences.
3. As a part of the knowledge base of general rules in domain ontology for concrete natural language because it gives a possibility of rewriting also into OWL language.
4. As a general part of the knowledge base together with further clauses describing the represented world gives a possibility to obtain new conclusions by means of the RDPCFL formal system.

Further work will be in this area: Creating words would inflexion and derivation, work with morphemes.

Acknowledgements The research described here has been financially supported by University of Ostrava grant SGS13/PŘF/16. Any opinions, findings and conclusions or recommendations expressed in this material are those of the authors and do not reflect the views of the sponsors.

References

1. Lukasová, A., Vajgl, M., Žáček, M.: Reasoning in RDF graphic formal system with quantifiers. In: Proceedings of the International Multiconference on Computer Science and Information Technology, 2010, pp. 67–72
2. Richards, T.: Clausal Form Logic. An Introduction to the Logic of Computer Reasoning. Addison Wesley (1989)
3. Lukasová, A., Žáček, M., Vajgl, M., Kotyrba, M.: Resolution reasoning by RDF clausal form logic. IJCSI Int. J. Comput. Sci. Issues **9**(3, No 1) (2012). ISSN (Online): 1694-0814. <http://www.IJCSI.org>
4. Lukasová, A., Žáček, M., Vajgl, M.: Reasoning in graph-based clausal form logic. IJCSI Int. J. Comput. Sci. Issues **9**(1, No 3), 37–43 (2012). ISSN (Online): 1694-0814
5. Baader, F., Calvanese, D., McGuinness, D., Nardi, D., Patel-Schneider, P.: The Description Logic Handbook. Cambridge University Press, United Kingdom (2004)
6. Carstairs-McCarthy, A.: An Introduction to English Morphology: Words and Their Structure. Edinburgh University Press 2002. ISBN 0748613269

Mathematical Modeling and Computer Simulation of Simple Permutation Brainteaser in MS Excel

Michal Musilek, Stepan Hubalovsky and Marie Hubalovska

Abstract Originally, the concept of the system and the system approach was used only in the natural sciences and technical disciplines. Currently, systems approach begins to be applied in other scientific disciplines such sociology, psychology and other social sciences, which deal with the behavior of the society. The system theory is closely related to modeling and computer simulation that are understand as one of the way of scientific research. Education has to reflect the application of scientific principles and therefore the principles of system approach, modeling and simulation should be applied even to pedagogical science and education. This new educational method should be implemented to learning of prospective teachers. The paper describes the implementation of principles of system approach, modeling and computer simulation to learning of prospective teacher of informatics in form of computer simulation of a simple permutation brainteaser.

Keywords Modeling • Computer simulation • Informatics • Education • Case study • Permutation brainteaser

1 Introduction

The education should reflect current trends of scientific knowledge. One of the approaches that are widely implement to scientific work are principles of system approach together with scientific modeling and computer simulation. Moreover computer simulation is now understand as “the third way” of the science [1]. System approach, modeling and simulation are implemented not only in the natural

M. Musilek · S. Hubalovsky (✉) · M. Hubalovska
University of Hradec Králové, Hradec Králové, Czech Republic
e-mail: stepan.hubalovsky@uhk.cz

M. Musilek
e-mail: michal.musilek@uhk.cz

M. Hubalovska
e-mail: marie.hubalovska@uhk.cz

sciences and technical disciplines, but also in economy, humanities, sociology and other social science. Many of universities has principles of system approach, modeling and simulation already implemented in their study programs.

The education has to reflect the application of scientific principles and therefore the principles of system approach, modeling and simulation should be applied to pedagogical science and education see e.g. [2, 3]. These principles should be successively applied in lower stages of the school education, in secondary schools. Implementation of system approach, modeling and simulation can support development of key competencies, particularly development of key competency for solving the problems, discovering and creativity [4, 5]. Development of the key competency by means of implementation of system approach, modeling and simulation requires from the teacher well knowledge of these principles, the teacher should be able to apply modeling and simulation in educational process.

The implementation of the method of modeling and computer simulation in education supports pupils and students discover and understand science's phenomenon and processes, it helps them understand technical equipment, it develops algorithmic as well as programming thinking and it develops computational, logical and mathematical thinking. Application of principles modeling and simulation develops student's intuition. Last but not least the method modeling and simulation helps to increase of ICT competency of pupils and students—see e.g. [4, 6]. Computer simulation together with visualization enable better understanding of the basic features of the real systems and develop their discovering. It is also essential that the teaching by means of simulation is much cheaper and faster than the teaching carried by real experiment. In some cases providing the real experiment cannot be feasible. Modeling and simulation can be and should be applied in all subjects of secondary school curricula thus it helps to complex development of children's personality.

The authors present in this paper the case study of implementation of principles of system theory, modeling and computer simulation to learning of prospective teacher of informatics within the study specialization Teaching of Informatics accredited by Department of Informatics, Faculty of Science, University of Hradec Kralove in their compulsory subject Modeling and Simulation. The paper illustrates problem analysis (system identification), creation of conceptual model and simulation program of solution and visualization of simple permutation brainteaser.

2 Case Study—Solution of Permutation Brainteaser in Programming Language Visual Basic for Application in MS Excel Spreadsheet

The students within the lectures of subject Modeling and simulation in study program Teaching of informatics are acquainted with the system theory, scientific modeling and simulation as well as with application of these principles in learning

at secondary schools. The seminar are focused to development of skills and knowledge in identification of real system and creation conceptual model and computer simulation program.

Within the subject the student has to create and pass the final project. The main requirement for students is to create computer simulation program of selected problem, phenomenon or process.

In the following text there is in the form of case study demonstrated example of final project created by students in the last academic year. The presented project represents the simulation of the permutation brainteaser programmed in Visual Basic for Application (VBA) implemented to MS Excel Spreadsheet.

2.1 Problem Analysis

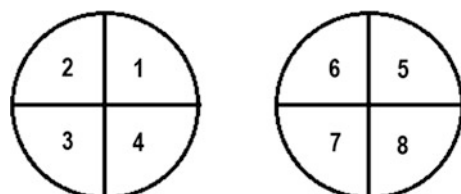
Although the puzzle can be solved intuitively (the permutation puzzle is very simple), the finding of automatic solution is not entirely elementary. Conversely, for a number of undergraduate students can be intuitive solution problem. Finally, those who are able to solve the puzzle intuitively are not sure that their solution is optimal (e.g. in terms of the number of steps used).

Before the algorithm as well as program of the solution of permutation puzzle will be described, it will be proved that mentioned puzzle is indeed permutation puzzle whose arbitrary mixing is permutations of basic positions and various possible moves also represent certain permutations and their chaining can be modeled by combining of the permutations.

Denote puzzle segments according to Fig. 1 by numbers 1, 2, 3, 4, 5, 6, 7 and 8. Then we the following four elementary strokes can be performed by counter-clockwise rotation of the circle segments:

1. Rotation of the left circle by angle 90° counterclockwise: the basic permutation $(1, 2, 3, 4, 5, 6, 7, 8)$ is permuted to $(4, 1, 2, 3, 5, 6, 7, 8)$. Let name of the move is “A”.
2. Rotation of the right circle by angle 90° counterclockwise: the basic permutation $(1, 2, 3, 4, 5, 6, 7, 8)$ is permuted to $(1, 2, 3, 4, 8, 5, 6, 7)$. Let name of the move is “B”.
3. Movement the upper half of both circles so that the upper right semicircle is exactly above the lower left semicircle followed by rotation thus created circle

Fig. 1 Numbering of the segments of permutation brainteaser



by angle 90° counterclockwise: the original permutation $(1, 2, 3, 4, 5, 6, 7, 8)$ we is permuted to $(1, 2, 6, 3, 4, 5, 7, 8)$. Finally the upper half of both circles are returned to the starting position. Let name of the move is “C”.

4. Movement the upper half of both circles so that the upper left semicircle is exactly above the lower right semicircle followed by rotation thus created circle by angle 90° counterclockwise: the original permutation $(1, 2, 6, 3, 4, 5, 7, 8)$ we is permuted to $(8, 1, 3, 4, 5, 6, 2, 7)$. Finally the upper half of both circles are returned to the starting position. Let name of the move is “D”.

Note that in each of these elementary strokes A, B, C, or D the positions of four segments of the puzzle are changed at once. This begs the question: How these elementary strokes can be combined (how the permutation can be composed), so the positions only two segments will be changed? If only the position of two segments is changed, the two segments are mutually replace, without changing the position of any of the remaining six segments.

The task can be extended as follows: Does exist the sequence of the elementary moves $\{A, B, C, D\}$ so that just two elements are in different positions than their original positions are and other six elements return to their original positions. Intuitive finding of such sequences of movements is difficult, so the solution can be created in any simulation software or programming language.

2.2 Design of Computer Simulation Program

Visual Basic for Application of MS Excel Spreadsheet can be understood as “appropriate tool” for solution of the permutation puzzle—see e.g. [7].

First, the function `Set()` will be created. The function defines the initial state of the puzzle (the variable `H` of type array contains the actual permutation of the segments of the puzzle):

```
Function Set() As Variant
    Dim H As Variant
    H = Array(0, 1, 2, 3, 4, 5, 6, 7, 8)
    Set = H
End Function
```

Another function `Move (H, i)` realizes the various elementary moves of the set $\{A, B, C, D\}$. The specific motion is defined by input of the second parameter `i`. The value of `i = 1` represents move A, `i = 2` represents the move B, `i = 3` represents move of C and finally `i = 4` represents move of D. Inside the functions are permuted only the elements that change their order within given permutation. The first argument represents the state of the puzzle before making the turn. The state of the puzzle after the turn is represented by the return value of the function (`Move = H`).

```

Function Move(H As Variant, i) As Variant
    If i = 1 Then
        p = H(4)
        H(4) = H(3)
        H(3) = H(2)
        H(2) = H(1)
    End If

```

... similar conditions are used for $i = 2$, $i = 3$ and $i = 4$...

```

        Move = H
    End Function

```

The last procedure Calculation () searches and writes (to Excel Active-sheet) the sequence of elementary strokes that have changed just two values of the elements, while the six element remains in original place. The procedure consist of nine nested cycles, because it was experimentally discovered that the shortest sequence satisfying the requirements consists nine elementary movements of the set {A, B, C, D}. The procedure consist of nine nested cycles of type For (see <http://musilek.eu/michal/>).

The procedure Calculation () can be run as macro in activesheet of Excel workbook. The macro will fill the first two columns of the excel table and lists a total of 96 different sequences and their corresponding resulting permutations. By inspection the listed sequence it is evident, that a quarter of the sequences represents three consecutive repetitive sequence of turns X, Y and Z, which can be labeled as XYZXYZXYZ, or short (XYZ)³. For such periodically repeated sequence (three repetitions of the same ordered strokes) there are three other sequences without any specified regularity. Thus the number of strokes is reduced to quarter, therefore from 96 to 24 sequences. The 24 sequences are shown in Table 1.

The strokes A and B or C and D are immediately carried in some sequences. The order A and B (C and D) doesn't affect each other, i.e. it does not depend on execution of order of strokes, $AB = BA$ and $CD = DC$. This allows exclude always one of the sequences leading to the same result—such redundant sequences are indicated in Table 1 by gray fill of the cells. The number of the sequence is reduced to 16. Generally, the commutative law cannot apply to the connection of the permutations.

Sequences shown in Table 1, solve 16 of the possible 28 two-element combinations of eight elements. There are total 28 combinations.

The remaining of given 12 combinations can be easily obtained by rotation of the given segment to suitable place, followed by performing some of the exchanges from Table 1 and finally returning the replaced segment back to the correct position.

The finding the sequence of commands solving the change of any two segments of a permutation puzzle show both, that any possible state of mixing of the segments can be solved as well as the algorithm of the solution was designed. For practical use it is not necessary to know all the sequences listed in Table 1, but

Table 1 Sequences of brainteaser solution

Element's exchange		Final permutation	Sequences
Adjacent by sides	1,4	42315678	DACDACD (DAC) ³
	2,3	13245678	CADCADCA (CAD) ³
	5,8	12348675	CBDCBDCBD (CBD) ³
	6,7	12345768	DBCDBCDBC (DBC) ³
Adjacent by vertex	1,3	32145678	CDACDACDA (CDA) ³
			DCADCADCA (DCA) ³
	2,4	14325678	ACDACDACP (ACD) ³
			ADCADCADC (ADC) ³
	5,7	12347658	CDBCBDCDB (CDB) ³
			DCBDCBDCB (DCB) ³
	6,8	12345876	BCDBCBDCD (BCD) ³
			BDCBDCBDC (BDC) ³
In different circles, after move, adjacent by sides	1,8	82345671	ADBDBADB (ADB) ³
	2,7	17345628	BDABDABDA (BDA) ³
	3,6	12645378	ACBACBACB (ACB) ³
	4,5	12354678	BCABCABC (BCA) ³
In different circles, after move, adjacent by vertex	1,7	72345618	ABDABDABD (ABD) ³
			BADBADBAD (BAD) ³
	2,8	18345672	DABDABDAB (DAB) ³
			DBADBADBA (DBA) ³
	3,5	12543678	ABCABCABC (ABC) ³
			BACBACBAC (BAC) ³
	4,6	12365478	CABCABCAB (CAB) ³
			CBACBACBA (CBA) ³

only four sequences can be selected, one from each group in Table 1, i.e. sequences for:

1. replacement of elements from one circle adjacent by sides;
2. replacement of elements from one circle adjacent by vertex;
3. replacement of elements from different circles, that after appropriate shift adjoin by side;
4. replacement of elements from different circles, that after appropriate shift adjoin by vertex.

Computer simulation written in form of program in Visual Basic for Applications helps us to find a set of sequences for easy solution of the permutation puzzle. The solution is not optimal in terms of the number of steps used. Finding the shortest solution excludes the scope of this paper.

3 Conclusion

The paper describes one of the possible way, how to provide the students of study program Teaching of informatics by the strategy of implementation the system approach, modeling and computer simulation to secondary school education. The case study present student's final projects in subject of Modeling and simulation. The paper presents the mathematical analysis of the permutation teaser. The model in form of computational algorithm is designed by process chart and process table. The simulation of the solution was programmed in Visual Basic for Application in MS Excel that easily enables transformation of the computational algorithm to simulation. The mathematic analysis of the permutation as well as simulation program are suitable for development of logical thinking of students. The simulation can be used as supporting tool in secondary stage of education.

Acknowledgements The paper has been supported by Specific Research Project of Faculty of Science, University of Hradec Kralove, 2016 and by Specific Research Project of Faculty of Education University of Hradec Kralove, 2016.

References

1. Sokolowski, J.A., Banks, C.M.: Principles of Modeling and Simulation: A Multidisciplinary Approach. Wiley, New Jersey (2009). ISBN 978-0-470-28943-3
2. Kollmansberger, S.: Helping students build a mental model of computation. In: Proceedings of the 15th Annual Conference on Innovation and Technology in Computer Science Education (2010)
3. Humphreys, P.: Extending Ourselves: Computational Science, Empiricism, and Scientific Method. Oxford University Press, Oxford (2004). ISBN 0-19-531329-1
4. Hubalovska, M., Hubalovsky, S.: Learning method for development of discovering and creativity of pupils and students in basic education. Int. J. Educ. Inf. Technol. **10**, 36–40 (2016). ISSN 2074-1316
5. National Educational Framework [online]. Praha, Institute for Educational Research in Prague (2007). http://www.nuv.cz/file/159_1_1/
6. Hubalovsky, S.: Modeling and computer simulation of real process—solution of mastermind board game. Int. J. Math. Comput. Simul. **6**(1), 107–118 (2012). ISSN 1998-0159
7. Musilek, M., Hubalovsky, S.: Principle and computer simulation model of variation of Delastell's Cipher BIFID. **9**, 86–194 (2015). ISSN 2074-1316

Research of Methods of Learning of Programming Objects-First and Object-Later

Ondrej Korinek and Stepan Hubalovsky

Abstract There are several ways to achieve the goals. Some ways are more direct and faster, and others are slower. Some ways lead to a goal, while others do not. It depends on the chosen way—procedure to achieve the chosen goals. A similar problem is experienced by teachers of programming. They often solves the fundamental problem of what programming style is best for introducing learning of programming. The goal of the learning of programming is to design and creation of object-oriented programming applications. Ways to reach the goals is several. Some teachers begin to teach the students by object-oriented design, which is followed by structured designs. Other teachers prefer completely opposite approach. They teach a structured design first followed by object-oriented constructs. These two methods of teaching of object-oriented programming are known Objects-First and Objects-Later techniques of learning of programming. These techniques are the most common practices of teaching programming. The paper presents results of research of application of above mentioned techniques to learning of object-oriented structures. The research was conducted among the students of study program Teaching of Education, Faculty of Science, University of Hradec Kralove in the academic years 2013/2014 and 2014/2015.

Keywords Programming methods • Objects-First • Objects-Later

1 Introduction

Object-oriented programming paradigm is currently the most common method of programs design. The main concepts are class, object instance, constructor, method, encapsulation, polymorphism, inheritance, interfaces and design patterns [1].

O. Korinek · S. Hubalovsky (✉)
University of Hradec Králové, Hradec Králové, Czech Republic
e-mail: stepan.hubalovsky@uhk.cz

O. Korinek
e-mail: ondrej.korinek@uhk.cz

Object-oriented programming can be taught in different ways. There are known large number of different learning methods for implementation concepts of object-oriented programming.

The well-known methods are Objects-First, Objects-Later, Model-First or Design Patterns First.

The most common methods of learning of programming are Objects-First, Objects and-Later, respectively. Although these methods are methodologically different they are complementary in programming practice and using some basic programming terms, e.g. the variable data type, basic control design, analysis, implementation, etc.

2 Theoretical Background

2.1 *Objects-First Method of Learning of Programming*

The basic object-oriented constructions are first explained in the Object-First method of learning of programming. The structured constructions are explained later. The structured constructions are sequences, conditions and cycles. Structured construction are taught based on more complex, object-oriented projects.

The disadvantages of this method of teaching of programming are as follows:

- Abstraction of object structures;
- A large number of new concepts (object-oriented concepts, description of the development environment);
- Low attractiveness of discussed examples;
- Complexity of object-oriented design.

Despite the mentioned disadvantages the method is common method of learning of programming. Structured design can be better understood on more complex and more practical examples.

2.2 *Objects-Later Method of Learning of Programming*

The basic structured constructions (sequence, condition and cycle) are explained in the object-later method of learning of programming first followed by learning of object structures. Structured constructions are explained based on simple examples. The structured examples do not have the practical applications. It may be for some students unattractive and discouraging. The disadvantages of the method of teaching of programming are as follows:

- Small attractiveness of training examples
- Simple artificial training examples;

- Little time for training of object-oriented constructions;
- Misunderstanding of object structures;
- Gaining bad habit of thinking in the design of programs.

Despite the mentioned disadvantages the method is common method of learning of programming.

3 Research of Objects-First and Object-Later Methods in Learning of Programming at University of Hradec Kralove

Many authors deal with the comparison of Objects-First and Objects-Later learning methods of programming [2, 3]. A potential problem of the previous researches, can be e.g. the separation of students into groups as well as the methods of verification of student knowledge. Despite the diversity of above mentioned researches, the authors came to similar conclusions: The learning methods Objects-First resp. Objects-Later show no noticeable differences.

The research of the Objects-First and Objects-Later methods in Learning of Programming was conducted at Faculty of Science University of Hradec Kralove in the academic years 2013/2014 and 2014/2015. The partial results were published in the papers [4–6]. The research was conducted among students of the first grade in the subject Programming 1.

3.1 Comparison of the Learning Methods of Programming

Students were divided into two homogeneous groups in the subject Programming 1 according to the results of the course Algorithms and Data Structures (hereinafter ALGDS). The detailed information can be found in [7, 8]. Students pass Post-test, Re-test 1 and Re-test 2 Post-test is past in the middle of the course. Re-test 1 is past at the end of the course. Re-test 2 can be past only by the student who have succeeded in the Post-test and Re test 1. Post-test and Re-test 1 consist of similar tasks based on the curriculum listed in Table 1. The curriculum is the same in both groups of students after Post-test - see Table 2. The tests consist of a theoretical part as well as practical part. Both parts are divided into structured constructions as well as object-oriented constructions. The object-oriented part of test consists of the following tasks:

1. Definition constructor data items and properties
2. Definition of methods
3. Create an instance method calls and use the program

The groups were taught by different teachers. The results of student's tests can be influenced by the personality of the teacher as well as different teaching methods.

Table 1 Curriculum of the course Programming 1 before Post-test

Objects-Later	Objects-First
Basic commands	Fundamentals of OOP in C #
One-dimensional array	Basic commands
Matrix	One-dimensional array
Square matrix	Matrix
Fundamentals of OOP in C #	Square matrix

Table 2 Curriculum of the course Programming 1 after Post-test

Objects-Later	Objects-First
Sorting algorithms	Sorting algorithms
Working with files	Working with files
Binary files, file system	Binary files, file system
Program parameters	Program parameters

The regular meeting between the teachers were organized to minimized mentioned factors.

The result of the research presented in this paper compare the results of the exam test of students taught by Objects-First method with the results of the exam test of students taught by Objects-Later method of learning of programming. The Objects-First group of student pass the subject Programming 1 in academic year 2013/14 while the Objects-Later group of student pass the subject Programming 1 in academic year 2014/15. Comparing the results of the exam tests passed in different academic years, may involve certain disadvantages:

- Comparability of the groups;
- Other skills of students;
- Various experience of students with subject of Programming 1.

The above mentioned disadvantages are minimized by entrance test students (Pre-test) in the subject ALGDS, based on the students are divided into the groups. Testing of the students is based on a variety of test tasks.

3.2 The Results of Research—Evaluation of Post-test of Object First Gourp and Object Later Groups of Student

The Post test results of students were compared between two groups of students:

1. The first group of students learned by Objects-First method in the academic year 2013/2014 (consists of 14 students);
2. The second group of students learned by Objects-Later method in the academic year 2014/2015 (consists of 18 students).

The Table 3 shows the distribution of Pre-test results of students of both groups.

The Table 3 shows that the better results are achieved by students of Objects-Later group. It can be caused by less number of students in the Objects-First group in the academic year 2013/2014.

To determine whether the median of the Post-test results of student is the same for both group of students the nonparametric Mann-Whitney test was used. Table 4

Table 3 Distribution of Pre-test results of students of Object-First group and Object-Later group

Grade of pre-test	Objects-First (2013/2014)	Objects-Later (2014/2015)
1	5	7
2	1	3
3	5	5
4	3	3
Total	14	18

Table 4 Statistical evaluation of results of Post-test

	Objects-First group	Objects-Later group
<i>Total results</i>		
Value p —Mann—Whitney	1	
Rejection of the null hypothesis	No	
Statistically significant difference	No	
Average test result of the students	46.3%	47.7%
<i>Object part—total results</i>		
Value p —Mann—Whitney	0.425	
Rejection of the null hypothesis	No	
Statistically significant difference	No	
Average test result of the students	44.2%	29.1%
<i>Object part—constructor</i>		
Value p —Mann—Whitney	0.143	
Rejection of the null hypothesis	No	
Statistically significant difference	No	
Average test result of the students	55.4%	30.4%
<i>Object part—methods</i>		
Value p —Mann—Whitney	0.805	
Rejection of the null hypothesis	No	
Statistically significant difference	No	
Average test result of the students	35.9%	31.3%
<i>Object part—instances</i>		
Value p —Mann—Whitney	0.115	
Rejection of the null hypothesis	No	
Statistically significant difference	No	
Average test result of the students	50.9%	25.0%

shows the results of non-parametric test of the total test section as well as object test section. Object test section is divided into three subsections. The Table 4 shows:

- The calculated p -value non-parametric test;
- The evaluation whether the null hypothesis is rejected (based on value of p);
- The decision, whether between both groups of students is statistically significant differences;
- The average test result of the students;

The significance level was set $\alpha = 0.05$.

The results of the Table 4 shows that the first group of student (Object First group) has (as expected) better results in object test section of the Post-test (despite their worse results in the Pre-test). The statistical difference between the groups is not significant. The students of Objects-First group have better results in all three parts of object sub-sections. Both groups have roughly similar results in the definition of methods. On the other hand the students of Object-Later group have better overall results of the Post-test. Unfortunately the statistical results are partly influenced in the Objects-Later group by two students who were unsuccessful in the subject Programming 1 in the previous academic year (they pass the subject Programming 1 for the second time). Research eliminating the effect of the repeated students exceeds the scope of this paper and it will be published later.

4 Conclusion

The paper characterized by two methods of learning of programming Objects-First and Objects-Later. The result of the research conducted at the Faculty of Science, University of Hradec Kralove in the academic years 2013/2014 and 2014/2015 confirm the results of other researches [1–3]—Object First and Object Later learning methods in programming show no noticeable differences. The research presented in the paper minimize the impact of the teacher (both groups were taught by the same teacher) on the other hand the research were influenced by different groups of students as well as by repeated students.

Acknowledgements The paper has been supported by Specific Research Project of Faculty of Science, University of Hradec Kralove, 2016 and by Specific Research Project of Faculty of Education University of Hradec Kralove, 2016.

References

1. Pecinovský, R.: Současné trendy v metodice výuky programování. <http://vyuka.pecinovsky.cz/prispevky/> (2006)
2. Ehlert, A., Schutte, C.: Empirical comparison of Objects-First and Objects-Later. In: Proceedings of the Fifth International Workshop on Computing Education Research

- Workshop, ICER '09, s. 15–26. New York: ACM. <https://home.cc.gatech.edu/csed/uploads/2/ehlert2009.pdf> (2009). ISBN 978-1-60558-615-1
3. Jonson, R.A., Moses, D.R.: Object-first vs. structures-first approaches to OO programming education: an empirical study. In: Allied Academies International Conference, Reno, s. 244–248. <http://www.researchgate.net/publication/> (2008)
 4. Hubálovský, Š., Kořínek, O.: Algorithmic thinking in paradigms of programming. In: Proceedings of the Education and Modern Educational Technologies (EMET 2015). IEEE, Piscataway (2015). ISBN: 978-1-61804-322-1. ISSN: 2227-4618
 5. Hubálovský, Š., Kořínek, O.: Object thinking in paradigms of programming. In: Proceedings of the Education and Modern Educational Technologies (EMET 2015). Piscataway: IEEE (2015). ISBN: 978-1-61804-322-1. ISSN: 2227-4618
 6. Hubálovský, Š., Kořínek, O.: Evaluation of algorithmic thinking of students using control testing environment. Int. J. Educ. Inf. Technol. North Atlantic University Union (2015). ISSN: 2074-1316
 7. Milková, E., Kořínek, O.: Students' programming capabilities evaluation. In: Proceedings of the Efficiency and Responsibility in Education (ERIE 2013), Prague, pp. 434–440 (2013)
 8. Milková, E., Kořínek, O.: Future ICT teachers—programming aptitude. In: Proceedings of the 11th International Conference Efficiency and Responsibility in Education (ERIE 2014), Prague, pp. 456–462 (2014)

Multichannel Queueing Systems and Their Simulation

Miloš Šeda, Jindřiška Šedová and Miroslav Horký

Abstract This paper is concerned with multichannel queueing systems showing how to derive their characteristics if the requirement arrivals correspond to a Poisson process and the service times have the exponential distribution. However, the requirements of stationarity, regularity, and independence of increases needed to model these processes by Markov chains and to define the transition probabilities may not be satisfied, or no information may be available on such parameters. Using randomly generated data, we propose a strategy of processing the requirements in multichannel systems and a way of evaluating the probabilities necessary to express the characteristics of the systems comparing these results with the theoretical ones. It has been discovered that with, as the number of outputs increases, the simulation results converge to the theoretical ones.

Keywords Queueing system • Poisson process • System transition

1 Introduction

The Danish mathematician A.K. Erlang formulated the fundamentals of the queueing theory about hundred years ago, but its current classification was proposed by the English mathematician D.G. Kendall. All details may be found, e.g., in [1–4, 6, 7].

Generally, at random moments, customers (requirements) enter the system and require servicing. Service options may be limited, e.g., the number of service

M. Šeda (✉) · M. Horký

Faculty of Mechanical Engineering, Brno University of Technology,
Technická 2, 616 69 Brno, Czech Republic
e-mail: seda@fme.vutbr.cz

J. Šedová

Faculty of Economics and Administration, Masaryk University, Lipová 41a,
602 00 Brno, Czech Republic
e-mail: jsedova@econ.muni.cz

channels (or service lines). If at least one serving line is empty, the demand entering the system is immediately processed. However, the service time is also random in nature because the performance requirements may vary. If all service lines are busy, then the requirements (customers) must wait for their turn in a queue for the processing of previous requirements, or be rejected.

Here, we restrict our considerations on systems of the form A/B/C/D/E/F, where

- A. characterises the probability distribution of random variable period (interval) between the requirement arrivals to the system,
- B. the probability distribution of random variable *service time of a requirement*,
- C. is the number of parallel service channels, in the case of “unrestricted” (i.e. very large) number of channels is usual to express the parameter C by ∞ ,
- D. integer indicating the maximum number of requirements in the system (i.e. the capacity of the system), unless explicitly restricted, expressed by ∞ ,
- E. integer expressing the maximum number of requirements in the input stream (or in a resource requirements), if it is unlimited, ∞ is used,
- F. queue type (FIFO/LIFO/SIRO/PRI).

Let us first assume that parameters A and B equal to M , i.e. intervals between the arrivals of requirements and requirement-service-time are mutually stochastically independent and have exponential distribution, this means that the input stream represents a Poisson (Markov) process, that satisfies the following properties:

(1) *Stationarity (homogeneity over time)*—the number of events in equally long time intervals is constant; (2) *Regularity*—the probability of more than one event at a sufficiently small interval of length Δt is negligibly small. This means that in, the interval $(t, t + \Delta t)$, there is either exactly one event with probability $\lambda \Delta t$ or no event with probability $1 - \lambda \Delta t$. In other words, in a Poisson process, the only system transition to the next “higher” state is possible or the system remains in the same condition; (3) *Independence of increases*—the number of events that occur in one time interval does not depend on the number of events in other intervals.

2 The M/M/n/n/ ∞ /FIFO System

To derive the characteristics of the system, it is convenient to describe the system activity by a *graph of system transitions*. The nodes of the graph represent the states and the directed edges transitions from one state to another. The evaluation of these edges is described by the probability of transition from one state to another. State S_n or more specifically, $S_n(t)$ for fixed $t \in (0, \infty)$, is a random variable and indicates that, at time t , n requirements are in the system. If m requirements, $m > n > 1$, are in the system M/M/n/n/ ∞ /FIFO, then each requirement is operating in a service channel and the remaining $m-n$ are waiting in the queue. Transitions between states that differ in the number of requirements in a system can be understood as a process of birth and death where the requirement birth represents the requirement entry into

the system and death corresponds to a requirement leaving from the system after being processed.

We assume a Poisson stream of requirements with a parameter λ and an exponential distribution of service time with parameter μ , and the queueing system behaviour described by the *Markov processes*. Due to the regularity, only transition probabilities $P(S_i \rightarrow S_j)$, where either $i = j$ or i and j differ by 1 have sense.

Using the regularity property and the method of calculating the total probability and neglecting the powers of the interval length Δt , from the partial probabilities of conjunction and disjunction of independent events, we get the transition probabilities.

For example, transition probability $P(S_0 \rightarrow S_0)$ corresponds to the probability of the event that, during the time interval of length Δt , no requirement enters the system, transition probability $P(S_k \rightarrow S_{k-1})$, $n > k \geq 1$, is the probability of the event that, during the time interval of length Δt , no requirement enters the system and at the same time one requirement will be served and leaves the system, transition probability $P(S_k \rightarrow S_k)$, $k \geq 1$, is equal to the probability of the event that, during the time interval of length Δt , no requirement enters the system and no requirement leaves the system, or, during this interval, one requirement enters and one requirement will be served, etc. Let us summarise the previous considerations:

$$P(S_{k-1} \rightarrow S_k) = \lambda \Delta t, \quad k = 1, \dots, n \quad (1)$$

$$P(S_k \rightarrow S_k) = (1 - \lambda \Delta t)(1 - k\mu \Delta t) \approx 1 - (\lambda + k\mu)\Delta t, \quad k = 0, \dots \quad (2)$$

$$P(S_{k+1} \rightarrow S_k) = (k+1)\mu \Delta t, \quad k = 0, \dots, n-1 \quad (3)$$

Let $p_k(t)$ denote the probability that, at time t , just k requirements are in the system. Using the previous equations, we can calculate $p_0(t)$, $p_1(t)$, ..., $p_k(t)$, ..., $p_n(t)$.

$$p_0(t + \Delta t) = P(S_0 \rightarrow S_0) + P(S_1 \rightarrow S_0) = p_0(t) \cdot (1 - \lambda \Delta t) + p_1(t) \cdot \mu \Delta t \quad (4)$$

$$\begin{aligned} p_1(t + \Delta t) &= P(S_0 \rightarrow S_1) + P(S_1 \rightarrow S_1) + P(S_2 \rightarrow S_1) \\ &= p_0(t) \cdot \lambda \Delta t + p_1(t) \cdot [1 - (\lambda + \mu) \Delta t] + p_2(t) \cdot 2\mu \Delta t \end{aligned} \quad (5)$$

...

$$\begin{aligned} p_k(t + \Delta t) &= P(S_{k-1} \rightarrow S_k) + P(S_k \rightarrow S_k) + P(S_{k+1} \rightarrow S_k) \\ &= p_{k-1}(t) \cdot \lambda \Delta t + p_k(t) \cdot [1 - (\lambda + k\mu) \Delta t] + p_{k+1}(t) \cdot (k+1)\mu \Delta t, \quad k = 2, \dots, n-1 \end{aligned} \quad (6)$$

However, if all channels are occupied and the queue is nonempty, the last equation changes to (7).

$$p_k(t + \Delta t) = p_{k-1}(t) \cdot \lambda \Delta t + p_k(t) \cdot [1 - (\lambda + n\mu) \Delta t] + p_{k+1}(t) \cdot n\mu \Delta t, \quad k \geq n \quad (7)$$

After easy simplification of Eqs. (4), (6) and (7), a limit transition for $\Delta t \rightarrow 0$ we get a set of first-order ordinary differential equations. Since the initial conditions may also be simply expressed, we can derive that

$$p_0 = \left[\sum_{k=0}^{n-1} \frac{\psi^k}{k!} + \frac{\psi^n}{n!} \frac{1}{1 - \frac{\psi}{n}} \right]^{-1} \quad (8)$$

$$p_k = \frac{\psi^k}{k!} p_0, \quad k = 1, \dots, n-1 \quad (9)$$

$$p_k = \frac{\psi^k}{n!} \frac{n^n}{n^k} p_0, \quad k \geq n \quad (10)$$

These equations may now be used to derive other important characteristics of the M/M/n/n/ ∞ /FIFO system, which include:

1. *Mean number of requirements in the system:*

$$E(N_s) = \overline{n_s} = \sum_{k=0}^{\infty} k p_k \quad (11)$$

2. *Mean number of requirements in the queue (mean queue length):*

$$E(N_f) = \overline{n_f} = \sum_{k=n}^{\infty} (k-n) p_k \quad (12)$$

3. *Mean number of free service channels:*

$$E(N_c) = \overline{n_c} = \sum_{k=0}^{n-1} (n-k) p_k \quad (13)$$

4. *Mean time spent by a requirement in the system:*

$$E(T_s) = \overline{t_s} = \frac{\overline{n_s}}{\lambda} \quad (14)$$

5. Mean waiting time of a requirement in the queue:

$$E(T_f) = \bar{t}_f = \frac{\bar{n}_f}{\lambda} \quad (15)$$

3 Simulation of Queueing Processes

As, in practice, some assumptions may not be satisfied, particularly the Poisson (Markov) process properties of stationarity and the independence of increases, such as the number of clients in shops and railway stations substantially changing during the daytime, the formulas that we have derived, may not be entirely accurate. However, queueing systems can also be studied by Monte Carlo simulations, which generate random numbers representing the moment of the requirements entering into the system and the service time.

In Fig. 1, a queuing system with two service channels, 15 requirements, and the FIFO queue type is considered. We can see that for $2 + 4 = 6$ min from total 70 min there is no requirement in the system, that means

$$p_0 = \frac{\langle 9^{03}, 9^{05} \rangle + \langle 9^{30}, 9^{34} \rangle}{\langle 9^{00}, 10^{10} \rangle} = \frac{2+4}{70} = \frac{6}{70} = 0.086$$

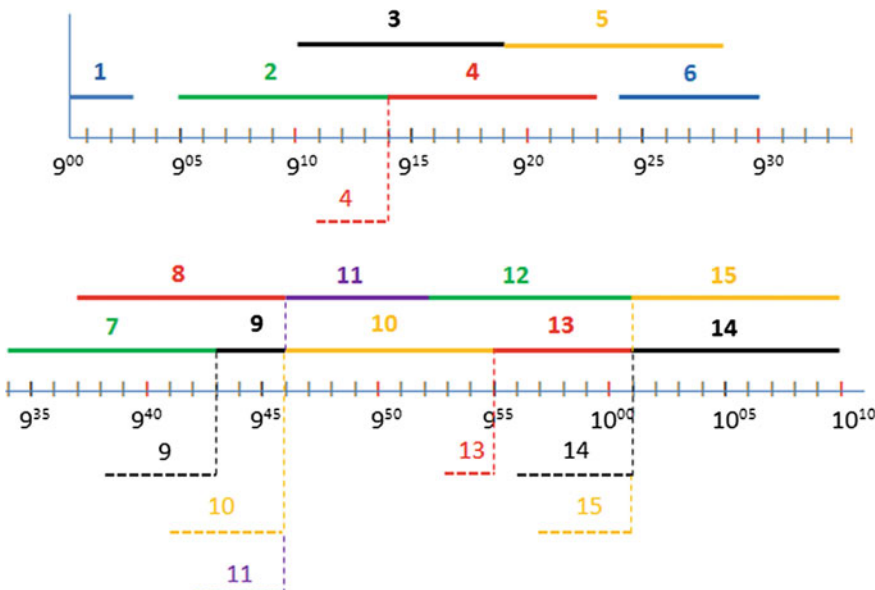


Fig. 1 System with two channels

Similarly, we estimate p_1, \dots, p_5 and compute characteristics (11)–(15).

In [5], the M/M/n/n/ ∞ /FIFO system was implemented in MATLAB using simulation data from a supermarket.

It makes it possible to enter λ (*mean intensity of the input*), μ (*mean service intensity*), the number of service lines n (then it is checked if $\lambda/n\mu < 1$), and the number of requirements. For these data, the probabilities $p_k(t)$ and the above-mentioned characteristics are computed.

To understand the behaviour of the system, the program also offers graphical output of simulations. In Fig. 2, four graphs are shown for a system with three lines, which show requirement arrival times, requirement service times, requirement waiting times for service and finishing times of services for these requirements.

Now we compare the analytical solution with the values obtained by simulation for different numbers of requirements. In the analytical part, we use formulas (8)–(10), and the corresponding characteristics (11), etc. Simulations were run for 50, 200, and 500 requirements (clients). Table 1 sums up the results of the analytical formulas and simulations.

We can see that, if the number of requirements increases, then the difference between the analytical and the simulation results decreases. For 50 requirements, the difference is about 12%, but for 500 requirements, only 5%. Based on these achievements, we can conclude that the computer implementation of the simulation model reasonably approximates the M/M/n/n/ ∞ /FIFO system.

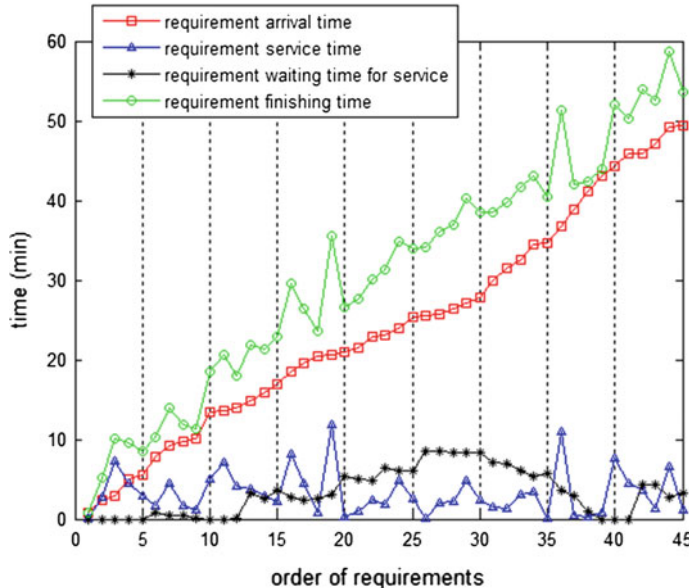


Fig. 2 Simulation of the M/M/n/n/ ∞ system for $\lambda = 45$, $\mu = 18$, $n = 3$, and 45 requirements

Table 1 A comparison of analytical and simulation results

	Analytical evaluation mean values	Simulation results number of requirements		
		50	200	500
$E(T_s)-E(T_f)$	3.33333	3.64353	3.5118	3.45478
$E(T_f)$	4.68165	3.06941	4.17567	5.21177
$E(T_s)$	8.01498	6.71293	7.68747	8.66655
$E(N_s)$	6.01124	5.09125	5.62803	6.23332
$E(N_f)$	3.51124	2.30994	3.05703	3.74851
$E(N_s)-E(T_f)$	2.5	2.78131	2.57101	2.48481

4 Conclusions

This paper describes an approach to modelling a queuing system with the use of Markov process properties and, for an $M/M/n/n/\infty$ /FIFO system, it derives its characteristics in detail. These derivations are based on the assumptions of stationarity, regularity, and independence of Markov processes.

In real situations, some of the assumptions may not be satisfied, particularly the stationarity and the independence of increases, or even the distribution of stochastic variables may not be known at all. For these reasons, the calculations of transition probabilities that do not take this fact into account may give imprecise results. Therefore, we propose a simulation approach, a strategy of requirement processing implemented in MATLAB based on the number of service lines, and a way of computing the characteristics from time intervals with the same number of requirements. However, the approximation of a theoretical model by the simulation model using real or randomly generated data depends on the number of requirements (and, therefore, on the time horizon length of the whole processing). The higher the number of requirements, the more the simulation results match the theoretical ones.

References

1. Bolch, G., Greiner, S., Meer, H., Trivedi, K.S.: *Queueing Networks and Markov Chains*. Wiley, New York (2006)
2. Bose, S.K.: *An Introduction to Queueing Systems*. Springer, Berlin (2001)
3. Cooper, R.B.: *Introduction to Queueing Theory*. North Holland, New York (1981)
4. Gross, D., Shortle, J.F., Thompson, J.M., Harris, C.M.: *Fundamentals of Queueing Theory*. Wiley, New York (2008)
5. Horák, M.: Models of Queueing Systems. Diploma Thesis, Brno University of Technology, Brno (2015)
6. Šeda, M.: Models of Queueing Systems. *Acta Logistica Moravica* **1**, 16–33 (2011)
7. Virtamo, J.: *Queueing Theory*. Lecture Notes. Helsinki University of Technology (2005)

On Computational Evaluation of Stress Concentration Using Micropolar Elasticity

Victor A. Eremeyev, Andrzej Skrzat and Feliks Stachowicz

Abstract We discuss the implementation the finite element approach to the linear micropolar elasticity in order to perform the analysis of the stress concentration near holes and notches. Within the micropolar elasticity we analyze the behaviour of such microstructured solids as foams and bones. With developed new finite element few problems are analyzed where the influence of the microstructure may be important. The provided comparison of solutions obtained within the micropolar and classical elasticity show the influence of micropolar properties on stress concentration near notches and contact areas.

Keywords Cosserat continuum • Micropolar elasticity • FEM • Stress concentration • Porous media

1 Introduction

Nowadays the interest grows to extended models of continuum mechanics in order to model micro- and nanostructured materials which demonstrate complex inner structure. Among these generalized models there are the surface elasticity, micropolar or Cosserat continua, microstretched and micromomorphic media, surface elasticity, media with internal variables, gradient elasticity, etc. In particular, the micropolar model [6, 7] proposed by Cosserat brothers more than hundred years ago found applications for modeling such materials as porous solids, bones, masonries, composites, see [3, 8, 10, 12, 13] and reference therein.

V.A. Eremeyev (✉) · A. Skrzat · F. Stachowicz

Faculty of Mechanical Engineering and Aeronautics, Rzeszow University of Technology,

al. Powstańców Warszawy 8, 35959 Rzeszów, Poland

e-mail: veremeyev@prz.edu.pl

A. Skrzat

e-mail: askrzat@prz.edu.pl

F. Stachowicz

e-mail: stafel@prz.edu.pl

Within the Cosserat continuum model the translations and rotations determine the kinematics of the medium and the stress and couple stress tensors are introduced. The micropolar properties of material may be important near singularities or to describe observed experimentally size-effect [1, 9, 11]. Let us also note that for such complex media even more general models of continuum mechanics may be useful, see for example [2]. Effective solution of boundary value problems requires advanced numerical code such as the finite element method. For the moment commercial FEM software gives the possibility to use user defined elements and user defined procedure for implementation of nonstandard material models. Here we developed new finite element and implement it in ABAQUS.

The paper is organized as follows. In Sect. 2 we present the basic equations of the linear micropolar elasticity. The equilibrium equations, static and kinematic boundary conditions and constitutive equations are given. In Sect. 3 we discuss the finite element modelling for the micropolar solids.

2 Basic Governing Equations of the Micropolar Elasticity

Following [6, 7] we recall here the basic equations of the linear micropolar elasticity of isotropic solids. The kinematic of a micropolar solid is described by two fields that the field of translations u_i and the field of rotations θ_i . The latter is responsible for the description of moment interactions of the material particles. Hereinafter the Latin indices take on values 1, 2, or 3 and we use the Einstein summation rule over repeating indices. The equilibrium equations take the form

$$t_{ji,j} + f_i = 0, \quad m_{ji,j} + e_{imn} t_{mn} + c_i = 0, \quad (1)$$

where t_{ij} and m_{ij} are the stress and couple stress tensors, respectively, e_{ijk} is the Levi-Civita third-order tensor, and f_i and c_i are external forces and couples. Unlike the linear elasticity tensors t_{ij} and m_{ij} are not symmetric. Equations (1) constitute the local balance of momentum and moment of momentum, respectively.

The static and kinematic boundary conditions have the following form

$$n_i t_{ij} \Big|_{A_t} = \phi_j, \quad n_i m_{ij} \Big|_{A_t} = \eta_j, \quad u_i \Big|_{A_u} = u_i^0, \quad \theta_i \Big|_{A_u} = \theta_i^0, \quad (2)$$

where n_i is the unit vector of external normal to the boundary $A = A_t \cup A_u$, ϕ_j and η_j are external forces and couples given on A_t , and u_i^0 and θ_i^0 are given on A_u surface fields of translations and rotations, respectively.

In what follows we are restricting ourselves by isotropic case. Using the Voigt notation modified for the micropolar elasticity and introducing the stress and moment stress vectors with stretch and wryness vectors by the formulae

$$\{\mathbf{T}\} = \{t_{11}, t_{22}, t_{33}, t_{12}, t_{21}, t_{23}, t_{32}, t_{13}, t_{31}\}^T, \quad (3)$$

$$\{\mathbf{M}\} = \{m_{11}, m_{22}, m_{33}, m_{12}, m_{21}, m_{23}, m_{32}, m_{13}, m_{31}\}^T, \quad (4)$$

$$\{\mathbf{E}\} = \{\varepsilon_{11}, \varepsilon_{22}, \varepsilon_{33}, \varepsilon_{12}, \varepsilon_{21}, \varepsilon_{23}, \varepsilon_{32}, \varepsilon_{13}, \varepsilon_{31}\}^T, \quad (5)$$

$$\{\mathbf{K}\} = \{\kappa_{11}, \kappa_{22}, \kappa_{33}, \kappa_{12}, \kappa_{21}, \kappa_{23}, \kappa_{32}, \kappa_{13}, \kappa_{31}\}^T, \quad (6)$$

we represent the constitutive equations in the following unified form

$$\{\sigma_M\} = [\mathbf{C}]\{\varepsilon_M\}, \quad [\mathbf{C}] = \begin{bmatrix} \mathbf{A} & \mathbf{0} \\ \mathbf{0} & \mathbf{B} \end{bmatrix}, \quad \{\sigma_M\} = \begin{bmatrix} \mathbf{T} \\ \mathbf{M} \end{bmatrix}, \quad \{\varepsilon_M\} = \begin{bmatrix} \mathbf{E} \\ \mathbf{K} \end{bmatrix}, \quad (7)$$

with 18×18 stiffness matrix $[\mathbf{C}]$, where \mathbf{A} and \mathbf{B} are three-diagonal 9×9 matrices which is not shown here. The values of used micropolar elastic moduli can be found from direct experiments provided in [10, 13] or using homogenization [3, 8, 12]. Analysis of general constitutive equations of anisotropic micropolar solids is performed in [4, 5, 7].

3 Implementation of Micropolar Elasticity into Commercial Code

In order to solve various boundary value problems a special 8-node micropolar isoparametric finite element has been developed in the form of UEL (user element) procedure for commercial ABAQUS program. Requirements considering the UEL procedure in ABAQUS program are very restricted. UEL procedure is called twice for each finite element and for each Gaussian point. In the first call the element stiffness is welcomed. Very often UEL procedure calls UELMAT (user material procedure) necessary to obtain the relation between stress and strain tensors (or between stress and strain increments). Another call of UEL procedure is necessary to compute residual forces—element nodal forces resulting from element stresses—which essential in the monitoring of convergence in nonlinear problems. This second call may also require another call of UELMAT procedure. The typical call of UEL procedure is presented below

```

subroutine uelmat(rhs,amatr,svars,energy,ndofel,nrhs,
1 nsvars,props, nprops, coords, mcrd, nnodes, u, du, v, a,
2 jtype, time, dtime, kstep, kinc, jelem, params, ndload,
3 jdltyp, adlmag,predf, npredf, lflags, mlvarx, ddlmag,
4 mdload, pnewdt,jprops, njpro, period, materiallib)

```

The most important parameters are `amatr` (element stiffness matrix) and `rhs` (right-hand side vector of residuals necessary to check the convergence of computation). In the most simple case of static linear analysis the `rhs` parameter can be omitted because the convergence (equilibrium equations at nodes) is achieved in the first iteration. The meaning of other parameters is described in ABAQUS documentation. UEL procedure can be slightly simplified if contains constitutive properties—the call of UELMAT procedure is not necessary, therefore. Short description of micropolar elasticity 8-node isoparametric element implementation consists of several steps

- In the loop over the Gaussian points ($2 \times 2 \times 2$ Gaussian procedure is used)
 1. Find the shape functions at each Gaussian point and their derivatives with respect to natural coordinates
 2. Find the Jacobian matrix, numerically compute its inverse and determinant
 3. Find the shape functions derivatives with respect to Cartesian coordinates x , y , z
 4. Find the matrix of shape functions derivatives \mathbf{D} (the relation between strain components and nodal displacements and microrotations)
 5. Find the constitutive matrix \mathbf{C} (the relation between stress and strain tensors)
 6. Compute $\mathbf{D}^T \mathbf{C} \mathbf{D}$ (for the 2 point Gaussian quadrature all weights are equal to ones) and add it as the contribution to the stiffness matrix which uses the determinant of Jacobian matrix as the multiplier
- Find the element nodal forces resulting from element stresses and subtract them from the external nodal forces in order to compute residuals (necessary to check the rate of the solution convergence)
- Make other computations e.g. update the strain energy

The whole procedure is typical for the isoparametric finite element formulation in 3D problems with the exception of considered degrees of freedom (in micropolar elasticity there are three displacement components and additionally three micro-rotations) and strain and stress measures (strain and stress tensors contain more components and are not symmetric). In UEL implementation of micropolar elasticity the same shape functions are used for displacement and microrotations

$$N_i(\xi, \eta, \mu) = \frac{1}{8}(1 + \xi\xi_i)(1 + \eta\eta_i)(1 + \mu\mu_i),$$

where ξ_i , η_i and μ_i are the nodal coordinates in the local coordinate system. For the Eringen strain measure the matrix of the shape functions derivatives is:

$$\left\{ \begin{array}{l} \boldsymbol{\varepsilon}_{xx} \\ \boldsymbol{\varepsilon}_{yy} \\ \boldsymbol{\varepsilon}_{zz} \\ \boldsymbol{\varepsilon}_{xy} \\ \boldsymbol{\varepsilon}_{yx} \\ \boldsymbol{\varepsilon}_{yz} \\ \boldsymbol{\varepsilon}_{zy} \\ \boldsymbol{\varepsilon}_{xz} \\ \boldsymbol{\varepsilon}_{zx} \\ \boldsymbol{\kappa}_{xx} \\ \boldsymbol{\kappa}_{yy} \\ \boldsymbol{\kappa}_{zz} \\ \boldsymbol{\kappa}_{xy} \\ \boldsymbol{\kappa}_{yx} \\ \boldsymbol{\kappa}_{yz} \\ \boldsymbol{\kappa}_{zy} \\ \boldsymbol{\kappa}_{xz} \\ \boldsymbol{\kappa}_{zx} \end{array} \right\} = \left[\begin{array}{ccccccccccccc} f_{1,x} & 0 & 0 & 0 & 0 & 0 & \dots & f_{8,x} & 0 & 0 & 0 & 0 & 0 & 0 & 0 \\ 0 & f_{1,y} & 0 & 0 & 0 & 0 & \dots & 0 & f_{8,y} & 0 & 0 & 0 & 0 & 0 & 0 \\ 0 & 0 & f_{1,z} & 0 & 0 & 0 & \dots & 0 & 0 & f_{8,z} & 0 & 0 & 0 & 0 & 0 \\ 0 & f_{1,x} & 0 & 0 & 0 & f_1 & \dots & 0 & f_{8,x} & 0 & 0 & 0 & 0 & f_8 & \\ 0 & f_{1,y} & 0 & 0 & 0 & -f_1 & \dots & f_{8,y} & 0 & 0 & 0 & 0 & 0 & -f_8 & \\ 0 & 0 & f_{1,y} & f_1 & 0 & 0 & \dots & 0 & 0 & f_{8,y} & f_8 & 0 & 0 & 0 & \\ 0 & f_{1,z} & 0 & -f_1 & 0 & 0 & \dots & 0 & f_{8,z} & 0 & -f_8 & 0 & 0 & 0 & \\ 0 & 0 & f_{1,x} & 0 & -f_1 & 0 & \dots & 0 & 0 & f_{8,x} & 0 & -f_8 & 0 & 0 & \\ f_{1,z} & 0 & 0 & 0 & f_1 & 0 & \dots & f_{8,z} & 0 & 0 & 0 & f_8 & 0 & \\ 0 & 0 & 0 & f_{1,x} & 0 & 0 & \dots & 0 & 0 & 0 & f_{8,x} & 0 & 0 & \\ 0 & 0 & 0 & 0 & f_{1,y} & 0 & \dots & 0 & 0 & 0 & 0 & f_{8,y} & 0 & \\ 0 & 0 & 0 & 0 & 0 & f_{1,z} & \dots & 0 & 0 & 0 & 0 & 0 & f_{8,z} & \\ 0 & 0 & 0 & f_{1,y} & 0 & 0 & \dots & 0 & 0 & 0 & f_{8,y} & 0 & 0 & \\ 0 & 0 & 0 & 0 & f_{1,x} & 0 & \dots & 0 & 0 & 0 & 0 & f_{8,x} & 0 & \\ 0 & 0 & 0 & 0 & f_{1,z} & 0 & \dots & 0 & 0 & 0 & 0 & f_{8,z} & 0 & \\ 0 & 0 & 0 & 0 & 0 & f_{1,y} & \dots & 0 & 0 & 0 & 0 & 0 & f_{8,y} & \\ 0 & 0 & 0 & f_{1,z} & 0 & 0 & \dots & 0 & 0 & 0 & f_{8,z} & 0 & 0 & \\ 0 & 0 & 0 & 0 & 0 & f_{1,x} & \dots & 0 & 0 & 0 & 0 & 0 & f_{8,x} & \end{array} \right] \left\{ \begin{array}{l} u_x^1 \\ u_y^1 \\ u_z^1 \\ \theta_x^1 \\ \theta_y^1 \\ \theta_z^1 \\ \dots \\ u_x^8 \\ u_y^8 \\ u_z^8 \\ \theta_x^8 \\ \theta_y^8 \\ \theta_z^8 \end{array} \right\},$$

where u_i^j and θ_i^j are the i -th displacement or microrotation components in the j -th node, respectively.

4 Examples

Using the presented above finite element we analyzed few 3D static problems for solids with certain singularities such as notch or small contact area. For comparison with the linear elasticity let us note that the micropolar elasticity provides the same solutions if all microrotations are fixed, or if only two material data are used (shear or Young's modulus and Poisson ratio) while the other material data are assumed to be zeros.

In Fig. 1 the stressed state in the rectangular plate with two notches under tension is presented with comparison with commercial software for classic elasticity. One can see that excellent convergence of the distribution of stress and stress magnitudes (not shown for micropolar software) is achieved. It proves that the results obtained by the UEL procedure are reliable.

Another benchmark test considers the Hertzian contact between the cylinder and the flat plate which is an example of the nonlinear problem. The main problem arising in this type of analysis is that ABAQUS program does not recognize the volumes and faces of user elements—user element is represented by the set of nodes. The only possible contact formulation is the contact between the surface (ordinary finite elements implemented in ABAQUS) and the set of nodes

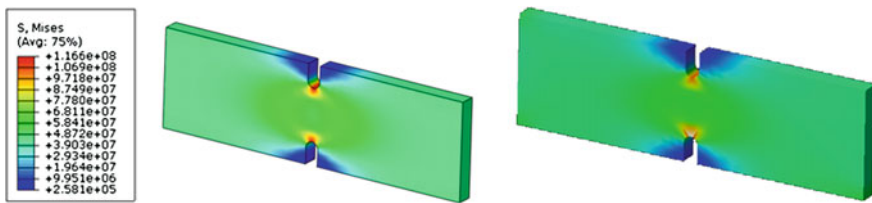
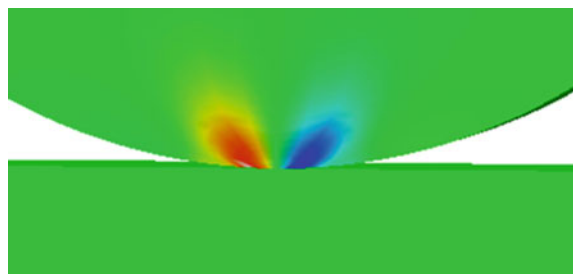


Fig. 1 Comparison of von Mises stress (Pa) obtained by use of commercial software (*left*) and micropolar user procedure (*right*)

Fig. 2 The distribution of couple stress m_{yy} near the contact zone



(UEL elements), therefore. In this benchmark test the cylinder is modelled with the micropolar user elements, while the plate is made of ordinary 3D finite elements. Surface-nodes contact formulation is less precise than the contact between two surfaces, but reasonable results can be achieved for sufficiently dense meshes. Obtained results confirmed well known Hertz formulas. In Fig. 2 the distribution of couple stress m_{yy} (y is the vertical axis) in the vicinity of the contact zone is shown.

5 Conclusions

The new 8-node hybrid micropolar isoparametric element and its implementation in ABAQUS is discussed. We analyzed few 3D benchmark problems of the micropolar elasticity. Comparison of classical and micropolar solutions is carefully discussed. Numerical tests have shown that couple stress appears almost in the vicinity of singularities that is near notches and contact area. In other words the influence of the micropolar properties is almost related to singularities of size of the same order as length-scale parameters of the micropolar elasticity.

Acknowledgements Authors acknowledge the support by the People Program (Marie Curie ITN transfer) of the European Union's Seventh Framework Programme for research, technological development and demonstration under grant agreement No PITN-GA-2013-606878.

References

1. Ariman, T.: On the stresses around a circular hole in micropolar elasticity. *Acta Mech.* **4**(3), 216–229 (1967)
2. dell'Isola, F., Giorgio, I., Pawlikowski, M., Rizzi, N.: Large deformations of planar extensible beams and pantographic lattices: heuristic homogenization, experimental and numerical examples of equilibrium. *Proc. R. Soc. A* **472**(2185), 20150790 (2016)
3. Dos Reis, F., Ganghoffer, J.: Construction of micropolar continua from the asymptotic homogenization of beam lattices. *Comput. Struct.* **112**, 354–363 (2012)
4. Eremeyev, V.A., Pietraszkiewicz, W.: Material symmetry group of the non-linear polar-elastic continuum. *Int. J. Solids Struct.* **49**(14), 1993–2005 (2012)
5. Eremeyev, V.A., Pietraszkiewicz, W.: Material symmetry group and constitutive equations of micropolar anisotropic elastic solids. *Math. Mech. Solids* **21**(2), 210–221 (2016)
6. Eremeyev, V.A., Lebedev, L.P., Altenbach, H.: Foundations of Micropolar Mechanics. Springer, Heidelberg (2013)
7. Eringen, A.C.: Microcontinuum Field Theory. I. Foundations and Solids. Springer, New York (1999)
8. Goda, I., Ganghoffer, J.F.: Identification of couple-stress moduli of vertebral trabecular bone based on the 3d internal architectures. *J. Mech. Behav. Biomed. Mater.* **51**, 99–118 (2015)
9. Kaloni, P.N., Ariman, T.: Stress concentration effects in micropolar elasticity. *ZAMP* **18**(1), 136–141 (1967)
10. Lakes, R.: Experimental microelasticity of two porous solids. *Int. J. Solids Struct.* **22**(1), 55–63 (1986)
11. Salehi, S.H., Salehi, M.: Numerical investigation of nanoindentation size effect using micropolar theory. *Acta Mech.* **225**(12), 3365–3376 (2014)
12. Trovalusci, P., Ostoja-Starzewski, M., De Bellis, M.L., Murali, A.: Scale-dependent homogenization of random composites as micropolar continua. *Eur. J. Mech. A/Solids* **49**, 396–407 (2015)
13. Yang, J., Lakes, R.S.: Experimental study of micropolar and couple stress elasticity in compact bone in bending. *J. Biomechanics* **15**(2), 91–98 (1982)

An Algorithm for Edge Detection of the Image for Application in WSN

Adrian Shehu, Astrit Hulaj and Xhevahir Bajrami

Abstract The conversion of the image in black and white image is a very important factor in the case of WSNs. This conversion affects the image size reduction. In other words, it affects energy saving and bandwidth transmission of sensor nodes. However, in this case, we can have a loss of details of image characteristics. With purpose of preserving the image characteristics, the edge detection as accurately as possible is a key factor. So, in this paper, we will present a new algorithm which enables the efficient realization of pixels detection that corresponds to the edges of the image captured by the sensor nodes. The results obtained with the application of this algorithm will be compared with results obtained from the application of traditional Filters.

Keywords Edge detection • Sensor • Image • Filter • Algorithm

1 Introduction

Edge Detection is the process of locating the pixels that correspond to the edge of the image. Edge detection affects the image size reduction and filters out information that can be considered as less important, but maintaining important struc-

A. Shehu

Telecommunication Department Faculty of Information Technology,
Polytechnic University of Tirana, Square “Mother Teresa”, 4, Tirana, Albania
e-mail: adshehu@tcn.al

A. Hulaj (✉)

Telecommunication Department Faculty of Information Technology,
Polytechnic University of Tirana, Mati 1, Fitorja 2/13, Prishtina, Kosova
e-mail: astrithulaj@hotmail.com

X. Bajrami

Vienna University of Technology, IHRT, Favoritenstrasse 9/E325A6,
Vienna, Austria
e-mail: xhevahirbajrami@gmail.com

tural properties of the image. Reducing the size of the image is directly related to the reduction of the transmission power of a sensor node. This reduction affects the saving of energy in WSN. This is directly related to the lifetime of WSN.

Since edges in most cases represent the object boundaries, edge detection is widely used in image segmentation, where in this case the images are divided into zones, which correspond to different objects.

2 The Problem Description

The application of WSN along the state borderline is characterized by many challenges [1]. One of these challenges is the power supply. Power supply of sensor nodes is vital to the operation of WSNs. In other words, energy is WSN lifetime itself.

The task of a sensor node is the capture, processing and routing of images thought the network to the nearest Border Police Station. However, it is required to be realized with minimum energy consumption. One of the methods to realize an energy saving is conversion images captured by WSN in black and white images. Conversion to black and white image affects the image size reduces. Reducing the image size impact the reduction of the transmission power of sensor node. By reducing transmission power, energy consumption is reduced. This directly affects the lifetime of the sensor node. A black and white image with 128×128 pixels has a size of 2 kB. The same image with greyscale has a size of 16 kB. The formula for the file size in kBytes is:

$$\text{Size of an image} = \frac{(\text{rows}) * (\text{columns}) * \text{bit depth}}{8 (\text{convert to bytes}) * 1024} \quad (1)$$

However, it should be noted that through the black and white images it can't be seen all specific details of the objects. Today, with purpose of the detection these details of images some algorithms are presented. With details, we will understand detection pixels that represent edges of the image. In this paper, a new algorithm for edges detection in the framework of an image is presented.

3 Existing Filters for Edge Detection

With edge detection, we understand each mathematical method which is used for identification of points in a digital image in which the brightness of the image rapidly changes or more formally, where are discontinuities. To realize the detection of edges in an image, the main purpose is to capture important events that occur within the image. Usually, the edges are presented at the boundary between the two different regions in an image. Points at which the intensity varies rapidly are

organized by lines that represent the image edges. Today there are some types of filters that enable the edges detection in a digital image, as: Sobel, Prewitt, Roberts, Laplacian, Canny, etc.

3.1 Sobel Filter

Sobel filter is a filter that is used for edges detection. Edges Detection is realized through calculating the intensity gradient of the image at each pixel inside the image. This filter finds the direction of increasing the intensity from brighter to darker part, and the ratio of change in this direction. The Sobel Filter consists of a pair of 3×3 convolution kernels. One kernel matrix is simply the other rotated by 90° . These kernel matrices are shown in [2, 3].

3.2 Prewitt Filter

The working principle of the Prewitt filter is similar to Sobel filter. Mathematically, Prewitt filter also consists of a pair of 3×3 convolution kernels. One kernel matrix is simply the other rotated by 90° . However, Prewitt Filter, unlike the Sobel Filter, uses other kernel matrices. These kernel matrices are shown in [2]. This filter uses first order derivative for calculate the difference of intensity of pixels in an edge region.

3.3 Robert Filter

Robert Filter, as Sobel and Prewitt filter uses first order derivative for the edges detection. Also, the application logic is similar to that of the Sobel and Prewitt filter. Robert filter uses a pair 2×2 convolution masks. These masks are designed to respond maximally to edges running at 45° to the pixel grid, one mask for each of the two perpendicular orientations [3]. These matrices are rotated with each other for 90° . These kernel matrices are shown in [3].

3.4 Laplacian Filter

The Laplacian Filter of an image highlights regions of rapid intensity change and is therefore often used for edge detection [4]. The Laplacian is often applied to an image that has first been smoothed with something approximating a Gaussian Smoothing

filter in order to reduce its sensitivity to noise [5]. The Laplacian filter is an operator of the second order derivative. More about Laplacian Filter you can read in [4].

3.5 Canny Filter

Canny Edge Detector technique is very important for detecting edges in an image. This operator isolates noise from an image before finding, edges of an image without affecting the features of the image, and then applying the tendency to find the edges and the critical value for threshold [3].

4 The Proposed Algorithm

So far, many methods have been applied for image edges detection. However, we will present a new algorithm. This algorithm can be summarized as follows.

Let's take an image $A(i,j)$ as input image with dimensions $m \times n$. Where i take values $i \in (1, \dots, m)$ and j take values $j \in (1, \dots, n)$.

The algorithm goes through these steps:

Step 1. Read input colors image;

Step 2. Give value for Thresh;

Step 3. Convert read image to grayscale image, $A(i,j)$;

Step 4. Return the size of matrix $A(i,j)$ in separate variables m and n ;

Step 5. Create the output using zeros with the data type for image $A(i,j)$;

Step 6. Implementation using loops for rows and columns;

Step 7. Application 3×3 filter within loops;

Step 8. Gradient magnitude calculation;

Step 9. Apply condition for finding edges in the image;

Step 10. Give value for Factor;

Step 11. Find edges including Thresh and Factor values;

Step 12. Display image after edges detection.

5 Results and Discussions

In this section we will present and discussions the results obtained with the application of existing filters for edges detection within an image, and these results will be compared with results obtained with the application of the new algorithm.

Results were derived by using MATLAB 2014 and an image with 153×329 pixels. In Fig. 1 are presented the results obtained with the application of Roberts Filter. In Fig. 2, are presented the results obtained with the application of Prewitt Filter. In Fig. 3 are presented the results obtained with the application of Sobel Filter. In Fig. 4 are presented the results obtained with the application of Laplace Filter. In Fig. 5 are presented the results obtained with the application of Canny Filter. While in Fig. 6 are presented the results obtained as a result of applying the proposed algorithm in this paper.



Fig. 1 Roberts Filter



Fig. 2 Prewitt Filter



Fig. 3 Sobel Filter



Fig. 4 Laplace Filter



Fig. 5 Canny Filter



Fig. 6 New algorithm

From the results shown in Fig. 1, we can see that Roberts Filter does not provide the desired results. Comparing the results shown in Fig. 1 with the results presented in Fig. 6, we can see that in the case of Roberts Filter, we have lost many pixels along the edges.

From the results shown in Fig. 2, we can see that Prwitt Filter, same as the Roberts Filter doesn't provide the desired results. Comparing the results shown in Fig. 1 with the presented results in Fig. 6, we can see that also in the case of Roberts Filter, we have lost many pixels along the edges.

From the results shown in Fig. 3, we can see that Sobel Filter, same as the Roberts and Prwitt Filter doesn't provide good results for edges detection. If the results obtained with the application of Sobel Filter compared with the presented results in Fig. 6 we can see that in the case of Sobel Filter we have a lot of pixels no detected along the edges.

From the results shown in Fig. 4, we can see that Laplace Filter, provide better results than Robert, Prwitt and Sobel Filter. However, if the results obtained with the application of Laplace Filter compared with the presented results in Fig. 6 we can see that in the case of Laplace Filter we have least pixels the detected along the edges. Especially, we can see changes in the tail, fingers and wings of the eagle.

From the results shown in Fig. 5, we can see that Canny Filter, provide best results than Laplace, Robert, Prwitt and Sobel Filter. However, if the results obtained with the application of Canny Filter compared with the presented results in Fig. 6 we can see that in the case of application of Canny Filter isn't reached to edges detection in the tail of the eagle.

Another difference we can see at the bottom of the left wing of the eagle (Right in the Fig. 5). From Figs. 5 and 6 we can see that in the case of application of Canny Filter detected edges are less highlighted than in the case of the results

obtained by our proposed algorithm. The same changes we can see also to the toes of the Eagle. However, despite this, the application of Canny Filter, as shown in Fig. 5 offers a better correlation of pixels, especially those pixels that are detected within the Eagle.

From the results shown in Fig. 2, it can be seen that with the application of our proposed algorithm, we can obtain very good results in the detection of edges within the image captured by the sensor nodes or any other electronic device. If the results presented in Fig. 6 are compared with the results presented in Figs. 1, 2, 3, 4 and 5 it can be seen that the proposed algorithm enables a very good detection of pixels that represent the edges of the image.

6 Conclusions

In this paper we presented an algorithm which is very efficient in the detection of pixels that correspond to the edges of the image. From comparing the results obtained with the application of traditional filters with those obtained with the application of the proposed algorithm, it can be seen that the proposed algorithm provides very good results and concrete. Therefore, based on the results presented and analyzed we can conclude that the proposed algorithm is very suitable to be applied for edges detection of the image.

In the future, this algorithm should be applied to the image in which noise has been present, and practically in the sensor, as and other electronic devices, as to look at the results of practical application of this algorithm.

References

1. Hulaj, A., Shehu, A., Bajrami, X.: Application of wireless multimedia sensor networks for green borderline surveillance, *Annals of DAAAM & Proceedings*, **27**, (2016)
2. Sharma, P., Singh, G., Kaur, A.: Different techniques of edge detection in digital image processing. *Int. J. Eng. Res. Appl.* **3**(3), 458–461 (2013)
3. Igbinosa, I.E.: Comparison of edge detection technique in image processing techniques. *Int. J. Inf. Technol. Electr. Eng.* **2**(1), 25–29 (2013)
4. Maini, R., Aggarwal, H.: Study and comparison of various image edge detection techniques. *Int. J. Image Process. (IJIP)* **3**(1), 1–11 (2009)
5. Huertas, A., Medioni, G.: Detection of intensity changes with subpixel accuracy using Laplacian-Gaussian masks. *IEEE Trans. Pattern Anal. Mach. Intell.* **5**, 651–664 (1986)

A Mathematical Model of the Behavior of SIP Signaling and Media Messages

Naser K.A. Alajmi, Hadeel Saleh Haj Aliwi, Kamal Alieyan
and Muhammad-Imran Sarwar

Abstract Over the last few years, many multimedia conferencing and Voice over Internet Protocol (VoIP) applications have been developed due to the use of signaling protocols in providing video, audio and text chatting services between at least two participants. This paper studies the behavior of the widely common signaling protocol; Session Initiation Protocol (SIP) in terms of the behavior of the signaling and media messages, as well as the delay time during call setup, call teardown, and media sessions.

Keywords Signaling protocol • Media conferencing • VoIP • SIP

1 Introduction

With the appearance of numerous multimedia conferencing and Voice over Internet protocols [1, 2], the decision to choose the appropriate protocol to be utilized in such a service has become very difficult since each protocol has its own privileges which differ from the corresponding privileges of the other protocols.

Choosing SIP protocol [3] to be discussed is due to many reasons; SIP is an interesting alternative compared to the conventional VoIP protocols. Nowadays, SIP is being deployed by service providers for their VoIP service offerings. SIP protocol offers significant features that are not provided by other existent VoIP

N.K.A. Alajmi
Saad Al-Abdullah Academy for Security Sciences, Al Asimah, Kuwait

H.S.H. Aliwi (✉)
School of Computer Sciences, Universiti Sains Malaysia, 11800 Gelugor,
Pulau Penang, Malaysia
e-mail: Hha11_com030@student.usm.my; hadeelsaleh12@yahoo.com

K. Alieyan • M.-I. Sarwar
National Advanced IPv6 Centre, Universiti Sains Malaysia, 11800 Gelugor,
Pulau Penang, Malaysia

signaling protocols. Furthermore, many researchers have shown that SIP is slightly better than H.323 [4], MGCP [5] and RSW [6, 7] in terms of quality of services.

2 SIP Protocol

SIP is an application-layer control protocol [8, 9] that can establish, modify, and terminate multimedia sessions (conferences) such as Internet telephony calls [10]. SIP can also invite participants to already existing sessions, such as multicast conferences. Media can be added to (and removed from) an existing session. SIP transparently supports name mapping and redirection services, which supports personal mobility-users can maintain a single externally visible identifier regardless of their network location [11, 12].

SIP protocol enables Internet endpoints (called user agents) to discover one another and to agree on a characterization of a session they would like to share. For locating prospective session participants, and for other functions, SIP enables the creation of an infrastructure of network hosts (called proxy servers) to which user agents can send registrations, invitations to sessions, and other requests. SIP is an agile, general-purpose tool for creating, modifying, and terminating sessions that works independently of underlying transport protocols and without dependency on the type of session that is being established [13]. SIP does not carry any voice or video data itself. It merely allows two endpoints to set up connection to transfer that traffic between each other via Real-time Transport Protocol (RTP) [14].

User Datagram Protocol (UDP) and Transport Control Protocol (TCP) [14] are transport protocols used to transfer audio and video data. SIP protocol has many features such as the service of text-based which allows easy implementation in object oriented programming languages, flexibility, extensibility, less signaling, transport layer-protocol neutral and parallel search. SIP uses many signaling messages in order to handle the communication between two nodes or more. SIP makes use of the request methods: INVITE, ACK, OPTIONS, BYE, CANCEL, etc. in order to control the call setup and call teardown [15].

3 SIP Messages Analysis

Each control protocol has three types of sessions; registration session, call setup and teardown sessions, and media data session. In this section each protocol session type is presented by number I varies from 1 to 3 as number as the session types, so when $i = 1$ means the current message is related to the registration session, and same when $i = 2$ and 3 . In this paper, only the behavior of the signaling and media data messages will be discussed.

$$I = \begin{cases} 1 \rightarrow \text{Registration Message} \\ 2 \rightarrow \text{Signaling Message} \\ 3 \rightarrow \text{Media data Message} \end{cases}$$

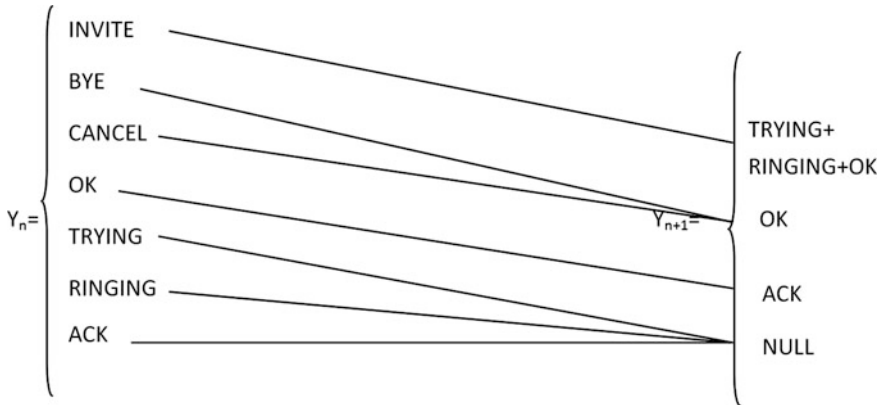
Each one of the aforementioned messages has lists of messages type related to a certain session. For example, the signaling messages can be either initiate message or ringing message or accept message or terminate message. SIP signaling message type is presented by number j varies from 1 to 7 as number as the signaling messages.

$$J = \begin{cases} 1 \rightarrow \text{INVITE} \\ 2 \rightarrow \text{TRYING} \\ 3 \rightarrow \text{RINGING} \\ 4 \rightarrow \text{OK} \\ 5 \rightarrow \text{BYE} \\ 6 \rightarrow \text{CANCEL} \\ 7 \rightarrow \text{ACK} \end{cases}$$

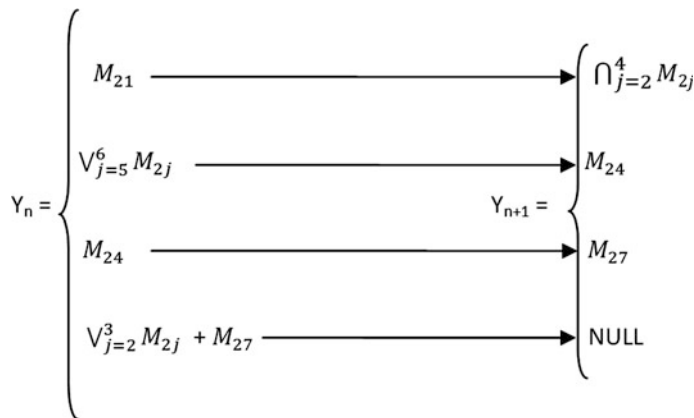
As the protocol message type is presented by I , so as an example when $i = 2$ and $j = 5$ means the message is related to the SIP signaling session which is BYE. As a result, to identify exactly each protocol message belongs to which session and what is the message type during that session, each SIP message can be presented by I which is the number of the session and J which is the number of the message inside the session i .

$$\text{SIP Message Type} = M_{ij} \quad (1)$$

During the SIP signaling session, if client 1 sends message to client 2 (except OK message), the latest should notify client 1 of receiving the message successfully before receiving the next message. Otherwise, no message has to be sent back to client 1. If the SIP message sent from client 1 to client 2 is presented by the function Y_n , so the notification message sent back to client 1 is presented by the function Y_{n+1} . With more details:



As each SIP message is defined by the number of session and the number of the message inside the session, therefore:



In media session, j represents the order of a certain media message. J varies from 1 to r where 1 represents the order of the first SIP message, r is an integer positive number represents the order of the last SIP message respectively. Assuming that N is the number of messages, so number of SIP media messages = (the order of the last media message – the order of the first media message) + 1. Thus,

$$N_{M_{3j}} = (r - 1) + 1 = r \quad (2)$$

Since the payload of SIP client carried by RTP header in the media session, by assuming that payload is presented by PL, so

$$RTP_{PL} = M_{3j} \quad (3)$$

4 SIP Session Time Analyses

In SIP Environment, two main sessions has to be considered which are signaling session and media session. Signaling session is divided into two sessions; setup session and teardown session. The delay time of each message is the difference between the message sending time from client 1 and the message's receiving time by client 2. In order to calculate the time spent to complete the call setup session, the time difference between the first SIP message sent by client 1 and the last SIP message received by client 2 during the setup session should be measured. Assuming that T presents the message time, T_s presents the sent time of the message, and T_r presents the received time of the message.

$$T_{M_{2j}} = T_{R_M_{2j}} - T_{S_M_{2j}} \quad (4)$$

$$T_{Setup_{SIP}} = T_{R_ACK} - T_{S_INVITE} \quad (5)$$

Hence,

$$T_{Setup_{SIP}} = T_{R_M_{27}} - T_{S_M_{21}} \quad (6)$$

In order to calculate the time spent to complete the call teardown session, the time difference between BYE message sending time and OK message arrival time should be calculated.

$$T_{Teardown_{SIP}} = T_{R_OK} - T_{S_BYE} \quad (7)$$

Hence,

$$T_{Teardown_{SIP}} = T_{R_M_{24}} - T_{S_M_{25}} \quad (8)$$

Similar to the signaling message sending/receiving status, the delay time of each media message is the difference between its sent and arrival times.

$$T_{M_{3j}} = T_{R_M_{3j}} - T_{S_M_{3j}} \quad (9)$$

In order to calculate the time spent to complete the media session, the time difference between BYE message sending time and ACK message arrival time (once the call answered) has to be calculated.

$$T_{Media_{SIP}} = T_{S_BYE} - T_{R_ACK} \quad (10)$$

$$T_{Media_{SIP}} = T_{S_M_{25}} - T_{R_M_{27}} \quad (11)$$

5 Conclusion

This paper provided a mathematical analysis of the behavior of the SIP protocol in terms of the signaling and media messages, and the time of each call setup, call teardown, and media sessions.

References

1. Goode, B.: Voice over internet protocol (VoIP). Proc. IEEE 1495–1517 (2002)
2. Haj Aliwi, H.S., Sumari, P.: A comparative study of VoIP protocols. (*IJCSIS*) Int. J. Comput. Sci. Inf. Secur. **11**, 97–101 (2013)
3. Haj Aliwi, H.S., Sumari, P.: A comparative study of VoIP, MCS, instant messaging protocol and multimedia applications. (*IJCNS*) Int. J. Adv. Comput. Netw. Secur. **4**, 67–70 (2014)
4. Basicevic, I., Popovic, M., Kukolj, D.: Comparison of SIP and h.323 protocols. In: The Third International Conference on Digital Telecommunications ICDT '08, pp. 162–167 (2008)
5. Dagiuklas, T., Ioannou, K., Garmpis, A.: A lightweight and scalable VoIP platform based on MGCP/H.323 interworking and QOS management capabilities. In: Proceedings of the 4th WSEAS International Conference on Information Security, Communications and Computers, Tenerife, Spain, pp. 548–553 (2005)
6. Haj Aliwi, H.S., Alomari, S.A., Sumari, P.: An efficient audio translation approach between SIP and RSW protocols. In: Proceedings of 3rd World Conference on Information Technology (WCIT-2012), University of Barcelon, Barcelona, Spain, vol. 3, pp. 31–37 (2013)
7. Ramadass, S., Subramanian, R.K., Guyennet, H., Trebel, M.: Using RSW control criteria to create a distributed environment for multimedia conferencing. In: Proceedings on Research and Development in Computer Science and its Applications, Penang, Malaysia, pp. 27–29 (1997)
8. Montoro, P., Casilar, E.: A comparative study of VoIP standards with asterisk. In: Fourth International Conference on Digital Telecommunications (ICDT), France (2009) 1–6
9. Abbasi, T., Prasad, S., Seddigh, N., Lambadaris, I.: A comparative study of the SIP and IAX. In: Canadian Conference on Electrical and Computer Engineering (CCECE), Saskatoon, Canada, pp. 179–183 (2005)
10. Papageorgiou P.: A comparison of H.323 vs SIP. Master thesis, University of Maryland at College Park, USA (2001)
11. Schulzrinne, H., Rosenberg, J.: A comparison of SIP and H.323 for internet telephony. In: Proceedings of the 8th International Workshop on Network and Operating Systems Support for Digital Audio and Video (NOSSDAV'98), Cambridge, UK, pp. 83–86 (1998)
12. Geneiatakis, D., Dagiuklas, T., Kambourakis, G., Lambrinoudakis, C., Gritzalis, S.: Survey of security vulnerabilities in session initial protocol. *IEEE Commun. Surv. Tutor.* **8**, 68–81 (2006)
13. Glasmann, J., Kellerer, W., Muller, H.: Service architectures in H.323 and SIP: a comparison. *IEEE Commun. Surv. Tutor.* **5**, 32–47 (2003)
14. Forouzan, B.: Data Communications and Networking, 4th edn. McGrawHill, New York, USA (2007)
15. Abouabdalla, O., Ramadass, S.: Enable communication between the RSW control criteria and SIP using R2SP. In: The 2nd International Conference on Distributed Frameworks for Multimedia Applications (DFmA), Penang, Malaysia, pp. 1–7 (2006)

Blood Vessel Segmentation from Color Retinal Images Using K-Means Clustering and 2D Gabor Wavelet

Aziah Ali, Wan Mimi Diyana Wan Zaki and Aini Hussain

Abstract This paper presents a new unsupervised method for segmenting blood vessels in digital retinal images. The proposed method uses K-means clustering to binarize grayscale vessel-enhanced images derived from green channel image and Gabor wavelet feature image. The binary images are then combined using logical OR to produce segmented vessels. The method was evaluated on the publicly available DRIVE database and the results compared to published literature. The method proved to have comparable performance to other published unsupervised methods while being simple and fast to implement. In the future, the proposed method can be further improved to be applied in real clinical setting to assist the physicians in diagnosing ocular diseases through an automated screening system.

Keywords Retinal image • Blood vessel segmentation • K-means clustering • Gabor wavelet

1 Introduction

Accurate detection and measurement of retinal blood vessels from digital retinal image is very important for early screening of disease onset and also in quantifying the severity of ocular diseases. A reliable method of segmenting the retinal blood vessels is necessary towards the development of automated diagnosis system for retinal images. While manual segmentation is possible, the amount of effort and time needed for even a small set of images could eventually become prohibitive.

A. Ali (✉) · W.M.D. Wan Zaki · A. Hussain
Faculty of Engineering and Built Environment, Universiti Kebangsaan Malaysia,
Bangi, Selangor, Malaysia
e-mail: aziah.ali@mmu.edu.my; aziah@siswa.ukm.edu.my

A. Ali
Faculty of Computing and Informatics, Multimedia University,
Cyberjaya, Selangor, Malaysia

This is one of the reasons a large number of researchers have been investigating the topic of automatic segmentation of retinal blood vessels in the recent years.

An extensive summary of previous works on blood vessel segmentation methodologies was presented in [1], where the methods of segmenting retinal blood vessels were divided into five main approaches namely pattern classification, matched filtering, morphological processing, vessel tracking and multi-scale approaches.

Pattern recognition approach with supervised classification method have been employed in [2–4], and in [5] Soares et al. proposed the use of Gaussian Mixture Models classifier to classify Gabor wavelet features extracted from retinal images. Matched filtering method was initially proposed by Chauduri in [6] which inspired more extended work by Hoover [7] and Zhang [8]. Zana and Klein [9] adopted morphological processing method to segment retinal blood vessels while Mendonca et al. [10] combined it with centerline detection. In [11], Strisciuglio employed a set of trainable B-COSFIRE filters to better capture the elongated structure of retinal blood vessels.

This paper proposes an unsupervised method to perform automated segmentation of blood vessels on retinal images that is inspired by the use of Gabor wavelet filter in a number of previous studies, for example in [5, 12]. As opposed to the use of supervised classification methods to binarize the Gabor feature in previous studies, we propose the use of K-means clustering to binarize the Gabor wavelet feature, which is simpler to implement and more efficient for processing a huge number of retinal images.

2 Proposed Method

The proposed method of automatic retinal vessel segmentation is divided into four main parts. In Part 1, pre-processing is performed on the green channel image obtained from the original color retinal and then enhanced to highlight blood vessels. In Part 2, the green channel image is inverted and Gabor wavelet feature is extracted. The Gabor feature then undergoes vessel-enhancement process. In Part 3 of the proposed method, K-means clustering are performed on the two vessel-enhanced images from the previous part separately, resulting in binary images that later go through post-processing. The final segmentation output is then produced in Part 4 by combining the two binary images using logical OR operation after which a final post-processing step is performed.

Pre-processing. Since green channel of the color retinal image provides highest contrast between retinal background and blood vessels, it will be used as the initial input in the proposed method. The Field-of-View (FOV) region in the green channel image is expanded according to Soares's recommendation in order to minimize effects from the high contrast between FOV and black background [5].

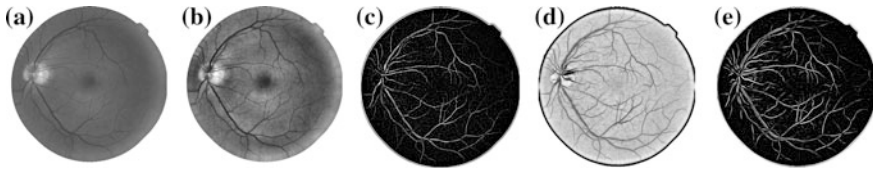


Fig. 1 Sample green channel image and its corresponding pre-processing output: **a** Green channel image with padded FOV, **b** contrast-adjusted green channel image, **c** vessel-enhanced green channel image, **d** contrast-adjusted Gabor feature image, and **e** vessel-enhanced Gabor feature image

Blood vessels on the padded green channel image are then first enhanced using contrast-limited adaptive histogram equalization (CLAHE) method. After the contrast is adjusted, the mean image is obtained by convolving the contrast-adjusted image with a mean arithmetic kernel. The mean image is later subtracted from the contrast-adjusted image and the resulting image is contrast-adjusted again to further enhance the vessels resulting in a vessel-enhanced image.

Gabor Wavelet. We used the same parameters as proposed by Soares in [5] in our method to derive Gabor wavelet response of inverted green channel image obtained from the previous step. The Gabor wavelet response is further processed to produce a vessel-enhanced Gabor wavelet feature image. Figure 1 shows a sample of green channel image with its corresponding contrast-adjusted and vessel-enhanced images for both green channel and Gabor feature.

Binary Thresholding. After obtaining both vessel-enhanced images from green channel and Gabor wavelet feature, K-means clustering is performed on both grayscale images to produce binary vessel images. The number of cluster for K-means clustering is set to two clusters, one for a vessel pixel (value 1) and another for background pixel (value 0). The output of this step normally contains noisy pixels which are mostly background pixels detected as disconnected vessel pixels. The objective of the next step is to remove as much of these noisy pixels as possible, without removing actual vessel pixels.

Image Post-processing. In this step, noisy pixels and small regions that mostly do not represent blood vessels are removed. This is achieved by adopting a morphological operation called opening to remove any connected vessel pixels containing less than a threshold value, which has been empirically determined to be 50 pixels for green channel binary image and 25 pixels for Gabor feature binary image.

Binary Image Combination. After the images have been individually post-processed, they are then combined using the logical OR operation to produce a single binary image. A final post-processing step using morphological opening is performed on the combination output. The result is a binary image representing the vessels from both green channel and Gabor feature binary images, as illustrated in Fig. 2.

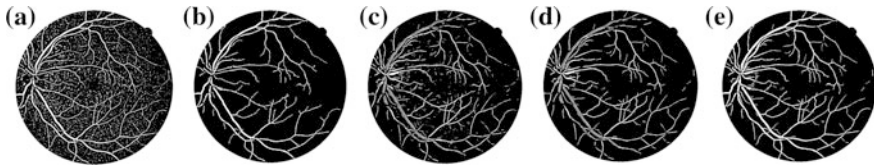


Fig. 2 Clustering, post-processing and binary image combination outputs: **a** Binary image from green channel, **b** post-processed green channel image, **c** binary image from Gabor feature, **d** post-processed Gabor feature image, and **e** result of OR operation on images 2(b) and 2(d)

3 Results and Discussion

3.1 Image Database

Our proposed method was evaluated using retinal images from the publicly available DRIVE database [7]. The database contains 40 color retinal images which are divided into two sets, namely training set and test set. The image size is 565 by 584 pixels with 8 bits per color channel and they were captured using a Canon CR5 non-mydiatic camera with a field of view of 45°. For each image in the database, the authors also provide its corresponding mask image and a manual segmentation image. For the test set, a second set of manually segmented images are also included. In our evaluation, we used the test set for testing with the first set of manual segmentation (1st human observer) as ground truth. We use the second manual segmentation (2nd human observer) set as the target benchmark for our method.

3.2 Performance Metric

A number of different performance measure have been described in the literature to evaluate vessel segmentation algorithm. For performance measure assessment in this study, only pixels within the FOV are considered. A true positive (TP) is defined as a pixel identified as vessel by the algorithm and is also specified as vessel in ground truth image. A false positive (FP) is a vessel identified as vessel by the algorithm but specified as non-vessel in ground truth image. Any vessel identified as non-vessels by the algorithm but marked as vessel in ground truth is a false negative (FN) and true negatives (TN) are pixels identified as non-vessels by both algorithm and ground truth image. The counted values for all TP, FP, TN and FN can be used to calculate the performance measure of a vessel segmentation algorithm. We have selected a number of usual measures used in previous literature which includes Accuracy rate (ACC), Sensitivity (SN), Specificity (SP) and Matthews Correlation Coefficient (MCC) in order to quantify the performance of our

proposed method. We used the same formulas specified in [11] to calculate the performance metric for our results.

3.3 Experimental Results

Before the binary images were combined, performance measures were calculated for binary images from green channel and binary images from Gabor feature image individually. 2nd human observer's performance was obtained by comparing the 2nd observer's segmentation to the 1st observer's segmentation outputs which were used as the ground truth in this study. From the results in Table 1, segmentation outputs using only green channel image performs better than the outputs using only Gabor feature image on all metrics considered except sensitivity. However sample binary images from both feature in Fig. 2 indicates that Gabor feature (Fig. 2d) is better in capturing finer vessels compared to green channel image. This could be due to the chosen value of 2 pixels for Gaussian envelope scale parameter, σ that highlights fine vessels well. While this is true, some of the larger vessels appear hollow due to the central vessel reflex on Gabor binary image. This can be complemented by the binary image from green channel that preserves most of the large vessels well, contributing to a much improved results when the two binary images combined as shown in the last row of Table 1.

Results for Zana, Chaudhuri and Jiang are calculated using the output images provided on DRIVE database website, while other results are obtained from the published literature. The proposed method has an average accuracy of 0.9425

Table 1 Performance of proposed method compared to other published methods

Methods	SN	SP	ACC	MCC
2nd human observer	0.7763	0.9723	0.9470	0.7660
Green channel image	0.5987	0.9884	0.9378	0.7021
Gabor feature image	0.6062	0.9787	0.9306	0.6716
Zana ^a [9]	0.6697	0.9830	0.9429	0.7315
Chaudhuri ^a [6]	0.2706	0.9887	0.8969	0.4236
Jiang ^a [13]	0.6480	0.9623	0.9218	0.6509
Strisciuglio [11]	0.7655	0.9704	0.9442	0.7475
Mendonca [10]	0.7344	0.9764	0.9452	–
Proposed method	0.7206	0.9757	0.9425	0.7400

^aResults calculated from provided binary images on DRIVE website

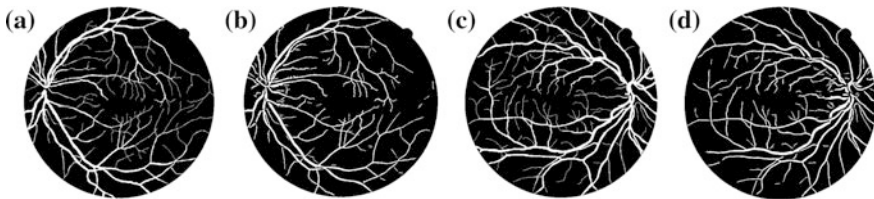


Fig. 3 Sample vessel segmentation outputs of Image 12 and 2 from DRIVE database. **a** Ground truth Image 12 from DRIVE database, **b** final segmented vessels of Image 12, **c** Ground truth Image 2 from DRIVE database, and **d** final segmented vessels of Image 2

which are comparable to other methods' results with highest accuracy of 0.9452 by Mendonca. The proposed method's sensitivity value of 0.7206 is higher than Zana, Chauduri, and Jiang but slightly lower than Strisciuglio and Mendonca. In terms of specificity, the proposed method has the value of 0.9757 which is comparable to other published methods. Strisciuglio's method recorded highest MCC value of 0.7475 while the proposed method has the second highest MCC value of 0.7400. Specificity value of our method also exceeds those of second observer's manual segmentation results. Figure 3 compares 2 sample outputs with their corresponding manual segmentation outputs, i.e. the ground truth.

4 Conclusion

We proposed a novel retinal blood vessel segmentation method that combines binary images obtained from the vessel-enhanced green channel image and vessel-enhanced Gabor feature image. The binary images are produced using unsupervised K-means clustering and combined using logical OR operation. The combination of binary images increased the performance of individual features by complementing each other well. The results achieved ($SN = 0.7206$, $SP = 0.9757$, $ACC = 0.9425$ and $MCC = 0.7400$) are comparable to published unsupervised methods. The proposed method is efficient since it does not involve sophisticated calculations nor prior training of labeled images. In future work, other methods of image combination will be investigated to improve the overall performance of the segmentation method.

Acknowledgements This research is supported by MOHE Malaysia (FRGS/1/2015/TK04/UKM/01/3) and UKM (DIP-2015-012). We thank Assoc. Prof. Dr. Jemaima Che Hamzah from Dept. of Ophthalmology PPUKM who provided insight and expertise that greatly assisted the research and also MMU for the funding.

References

1. Fraz, M.M., Remagnino, P., Hoppe, A., Uyyanonvara, B., Rudnicka, A.R., Owen, C.G., Barman, S.A.: Blood vessel segmentation methodologies in retinal images—a survey. *Comput. Methods Programs Biomed.* **108**, 407–433 (2012)
2. Manoj, S., Sandeep, P.M.: Neural network based classifier for retinal blood vessel segmentation. *Int. J. Recent Trends Electr. Electron. Eng.* **3**, 44–53 (2013)
3. Osareh, A., Shadgar, B.: An automated tracking approach for extraction of retinal vasculature in fundus images. *J. Ophthalmic Vis. Res.* **5**, 20–26 (2010)
4. Staal, J.J., Abramoff, M.D., Niemeijer, M., Viergever, M.A., Van Ginneken, B.: Ridge-based vessel segmentation in images of the retina. *IEEE Trans. Med. Imaging* **23**, 501–509 (2005)
5. Soares, J.V.B., Leandro, J.J.G., Cesar Jr, R.M., Jelinek, H.F., Cree, M.J.: Retinal vessel segmentation using the 2-D Gabor wavelet and supervised classification. *IEEE Trans. Med. Imaging* **25**, 1214–1222 (2006)
6. Chaudhuri, S., Chatterjee, S., Katz, N., Nelson, M., Goldbaum, M.: Detection of blood vessels in retinal images using 2D matched filters. *IEEE Trans. Med. Imaging* **8**, 263–269 (1989)
7. Hoover, A.: Locating blood vessels in retinal images by piecewise threshold probing of a matched filter response. *IEEE Trans. Med. Imaging* **19**, 203–210 (2000)
8. Zhang, B., Zhang, L., Zhang, L., Karray, F.: Retinal vessel extraction by matched filter with first-order derivative of Gaussian. *Comput. Biol. Med.* **40**, 438–445 (2010)
9. Zana, F., Klein, J.C.: A multimodal registration algorithm of eye fundus images using vessels detection and Hough transform. *IEEE Trans. Med. Imaging* **18**, 419–428 (1999)
10. Mendonça, A.M., Campilho, A.: Segmentation of retinal blood vessels by combining the detection of centerlines and morphological reconstruction. *IEEE Trans. Med. Imaging* **25**, 1200–1213 (2006)
11. Strisciuglio, N., Azzopardi, G., Vento, M., Petkov, N.: Supervised vessel delineation in retinal fundus images with the auto selection of B-COSFIRE filters. *Mach. Vis. Appl.* 1–13 (2016)
12. Li, Q., You, J., Zhang, L., Bhattacharya, P.: A multiscale approach to retinal vessel segmentation using Gabor filters and scale multiplication. In: *IEEE International Conference on Systems, Man and Cybernetics 2006. SMC '06*, vol. 4, pp. 3521–3527 (2006)
13. Jiang, Y.: Blood vessel tracking in retinal images. In: *Proceedings of Image and Vision Computing New Zealand 2007*, pp. 126–131, Hamilton, New Zealand (2007)

Training Samples Construction for Energy Utilities Operational Assets Management

Alexandra Khalyasmaa and Stanislav Eroshenko

Abstract The paper is concerned with the training sets formation problems in the intelligent information analytical systems for electrical grid equipment technical state assessment and repair programs formation with the purpose of the power grid companies' plant assets management. The basic principles of the developed intelligent information analytical system are presented in the paper. The problems associated with the training sets formation for electrical grid equipment are also described and the basic requirements to them are defined. Within the framework of the presented paper the analysis of the training set size impact on the equipment state identification accuracy in the context of 110 kV power transformers state identification was performed.

Keywords Plant assets • Training set • Analytical system • Electrical equipment

1 Introduction

Nowadays different information analytical systems intended to electrical grid equipment technical state assessment at substations, equipment residual life analysis and power grid companies (utilities) plant assets management have become popular. It comes from the fact that under the modern conditions the hardware and software are sufficiently developed which allows for the large data volumes

A. Khalyasmaa (✉) · S. Eroshenko

Ural Federal University named after the first President of Russia B. N. Yeltsin,
Mira st. 19, 620002 Ekaterinburg, Russia
e-mail: lkhalysmaa@mail.ru

S. Eroshenko
e-mail: stas_ersh@mail.ru

accumulation [1]. The large data volume in its turn gives the opportunity to receive the useful analytical information on the basis of which the new knowledge can be obtained and possible correlations and interrelations can be found. Different artificial intelligence methods such as the neural networks, the fuzzy inference, the genetic algorithms, the machine learning [2] etc. are used for operational efficiency improvement in the modern information analytical systems. Each method has its advantages and disadvantages, but the system training principle is used in practically all the methods as far as the new system knowledge is obtained just by means of training. Nowadays there exist a great number of the networks learning methods, for instance: the supervised learning, the unsupervised learning, the statistical learning, the self-organization etc. [3].

It is unlikely that the unsupervised learning can be used during the equipment technical state and residual life assessment as far as the problem is finally reduced to the analysis of equipment state and defects specified by the governing documents. In other words the present system has always both input and output vector. The electrical grid equipment diagnostics and tests results are used as the training set. It is the parameters set (inputs) which characterizes the equipment state as far as diagnoses and defects (outputs) corresponding to the present parameters sets. It is obvious that the efficiency of the information analytical system with the supervised learning depends heavily on the training set quality.

Not so much the high percentage of erroneous diagnoses (defects) as the possibility of the information analytical system further training is the major problem of the defective training set. In this case the latter is of particular importance as far as it is too difficult to find the equipment failures and defects statistics sufficient for the high-quality training set formation. Firstly, the problem is in that the total damage rate of equipment is not so high, for instance according to [4] it is 0.5–2.5% per a year for power transformers (the average value is ~1%). It means that for the middle-size grid company with seventy 110 kV substations on the balance sheet with consideration of reserve facilities etc., the total number of 110 kV transformers will be approximately 150, and, consequently, the transformers damage rate will be approximately 2 transformers per a year.

In this case it will take approximately 50 years for the required representative sample formation at least by the sufficient minimum quantity condition. It is not necessarily that over this period we will obtain any and all equipment defects types, specified by the governing documents, moreover, the equipment fleet even the fleet of the same type equipment comprises different modifications and in this case the defects parameters of one modification can differ markedly from another one. In other words, the training set formation is one of the key problems during the intelligent information analytical systems implementation, that is why the paper is concerned with the presented problem solving.

2 The Intelligent Information Analytical System Description

The intelligent information analytical system (IIA) developed by the authors is designed for the electrical equipment state identification, maintenance and repair cycles optimization. IIA is based on the Takagi-Sugeno fuzzy knowledge base (neuro fuzzy inference), which is described in detail in [5]. Actually the neuro fuzzy inference structure and adjustment optimization are reduced to the iterative determination problem of the membership functions optimal number and type as far as the production rules and training sets etc. The Takagi-Sugeno algorithm was taken as the fuzzy inference algorithm because of the fact that the present algorithm is the universal approximator of functions, which in case of the large number of the input parameters has the advantage over the other neuro fuzzy inference algorithms. According to [6] when modeling the multifactorial problems, for instance the equipment technical state assessment problem, it is appropriate to use the Takagi-Sugeno algorithm. The network in the Takagi-Sugeno algorithm comprises 5 layers and the linear function of the input variables is used as the conclusive rule

$$y_1(x) = p_{i0} + \sum_{j=1}^N p_{ij}x_j \quad (1)$$

where N is the number of the X set parameters; $p_{i0}, p_{i1}, \dots, p_{iN}$ are the Takagi-Sugeno polynomial parameters.

2.1 The Fuzzy Parameters Identification Problems

The fuzzy knowledge base was used due to the fact that the equipment parameters analyzed during the system operation can indicate the different equipment states (defects types) at the same time with different degrees of membership to these states. The state analysis of two TRDN-25000/110/10 type transformers (T1 and T2) was performed for illustrative purposes. The results of chromatographic analysis of dissolved in oil gases (DGA) over the period of 2005–2015 were taken as initial data. The concentrations of the following gases were analyzed: methane (CH_4), acetylene (C_2H_2), ethylene (C_2H_4), ethane (C_2H_6), hydrogen (H_2), carbon oxide (CO), and carbon dioxide CO_2 by six different methods: Rodgers method, Dornenburg method, IEC standard, nomograms method, ETRA method, Duval's triangle, and also experts estimates method. The detailed analysis is presented in [7].

Among all the measurements the gases boundary concentrations exceedance was observed only in two cases: in case of oil sampling from T1 transformer ($T1^1$) and in case of oil sampling from T2 transformer ($T2^1$). In other cases all concentrations values of the dissolved in oil gases are within the boundary values range. In spite of

this fact many DGA methods allow the defect identification without gases concentrations exceedance criterion. The results of DGA data analysis by different methods are presented in Table 1. As it is seen from Table 1 each method identifies the transformer state in its own way and the methods results are not always the same. In this case the unique identification of the transformer state is difficult, moreover the degree of membership to a particular state is also various due to the differences in the boundary concentrations values for each method. It should be mentioned that for each method the particular state possibility will also differ as well as in the previous case due to the differences in the boundary concentrations values and also due to the differences in the states gradation in each particular method.

All the above mentioned shows that the use of the fuzzy knowledge base is well-founded, moreover the necessity of the training sets formation by state (defects) on the basis of the precedent information is obvious. In other words, in different cases for the same transformer type, but, for instance, being operated in different climatic conditions, the same gases concentrations values in one case show that there is an incipient defect, in other case—that there is the outlier. Therefore special attention should be given to the training sets creation for quality improvement of the technical state assessment results and decisions concerning its further operation.

2.2 *Equipment Types Structure in the Training Set*

On the first step the initial training set is formed for each equipment type (transformer, circuit breaker, disconnector etc.) with consideration of each type division into the main subtypes. For instance, the “power transformer” type comprises the following subtypes: autotransformers; 110–220 kV transformers; 35 kV transformers; 6–20 kV oil transformers; 6–35 kV dry-type transformers. The present grading is based on the equipment design features, equipment operation mode parameters as far as the techniques of diagnostics and tests during which the present parameters are defined. For each subtype the training set is initial, as far as the uplearning is a cyclic process in the developed system. Only new precedents (inputs and the corresponding outputs) are included in the holdout training set. In case of the precedents repetition the network will not be uplearned, the training set will remain constant from the last uplearning stage. As it was mentioned above, the present decision is caused by the problems of equipment defects statistics accumulation, and training without the training set completion leads to the increase in the errors probability during the equipment state identification.

Table 1 The transformers state identification results

Method	T1 ¹	T1 ²	T2 ¹	T2 ²	T2 ³
Rodgers method	High-temperature defect	Insignificant overheating (200–300 °C)	Undiagnosed state	High-temperature defect	High-temperature defect
Dornenburg method	Thermal impact	–	–	–	–
60599 IEC method	Overheating at a temperature more than 700 °C	–	–	–	–
Nomograms method	Thermal defect at high temperatures	–	Defects caused by arc	–	–
ETRA	–	–	High power electrical discharges	–	–
Duval's triangle	Thermal defect at temperature more than 700 °C	–	High power electrical discharges	–	–
Expert estimates method	–	–	–	–	–

2.3 The Training Set Size

The training set size has a significant impact and it should be sufficient for correct and certain equipment state identification. It is generally accepted that if the dependency between the analyzed variables is heavy it can be identified even in case of small set. If the training set size is insufficient it means that there are few possible combinations of the present variables values and consequently the possibility of the values combination identification which show the heavy dependence is relatively high. In the technical assessment problem the dependence between the analyzed variables is weak therefore the present dependence can be identified only for sufficiently large set.

At the same time the smaller size of the required training set as compared to the traditional multilayer neural network [8] is the neuro fuzzy inference advantage which makes possible the sufficient training set formation even under the condition of the limited data. Analysis of the training set size impact on the equipment state identification accuracy in the context of 110 kV power transformers state identification was performed in the paper. For each element of 110 kV power transformer its own neuro fuzzy inference structure was developed. The developed system adjustment accuracy was evaluated on the basis of the training and test sets of different size for 110 kV power oil transformers of the similar power and the same type structure. The sets mentioned above are presented in Table 2. Due to the high dimension of the current problem its verification was performed on the basis of the diagnostic data of the following elements: transformer oil (in the transformer tank) —on the basis of the chromatographic analysis data of the dissolved in oil gases;

Table 2 Basic network parameters for the transformers state assessment

The pairs number in the training set	30	40	50	60	70	80	90	100
The pairs number in the test set	74	74	74	74	74	74	74	74
Number of nodes	524	524	524	524	524	524	524	524
Number of linear parameters	243	243	243	243	243	243	243	243
Number of nonlinear parameters	45	45	45	45	45	45	45	45
Total number of parameters	288	288	288	288	288	288	288	288
The fuzzy rules number	243	243	243	243	243	243	243	243
Average training error (%)	10.2	9.4	8.5	7.8	6.8	6.7	6.5	6.3
Average testing error (%)	0.1081	0.0682	0.0594	0.0524	0.0495	0.0489	0.0488	0.0486

magnetic core—on the basis of no load measurements data; solid insulation—on the basis of the measurements data of the winding insulation resistance; general state of windings—on the basis of the windings' ohmic resistances and also on the basis of the transformer production and overhaul year (the operational lifetime data).

The training set size impact on the equipment state identification accuracy was verified during the obtained data analysis. It is seen from Table 2 that the more the training set size the less the average training and testing errors, that is the more the equipment state identification accuracy. Consequently, the sufficient amount of statistical data should be accumulated during the training set formation, in this case more than 70 pairs are required for the presented problem solving. As it is seen from Table 2 when using 70 and more pairs there is a slight reduction in the prediction error. In this case the set structure, information value and completeness in addition to the training set size have an impact on the identification results accuracy. It is described in detail by the authors in [9, 10].

3 Conclusions

Determination of the minimum required training set size is one of the basic problems during the transformer equipment technical state assessment and reliable identification of the equipment state on the basis of neuro fuzzy inference. In order to exclude the system model overfitting it is also required to use the independent data for training and test sets, in this case the test and training sets should meet the same requirements concerning the set structure, completeness etc. The requirements mentioned above are explained by the fact that the system model further operation and the equipment state identification accuracy depend on the system model adjustment. And on the real objects the defective training and test sets can lead to the incorrectly identified equipment state and consequently to the false staff operation.

Acknowledgements The reported study was supported by Russian Foundation for Basic Research, research project No. 16-38-00310 (mol_a).

References

1. Shevelev L.V. Methods of analytical data to support decision making. DBMS 4–5 (1998) (in Russian). <http://infovisor.ivanovo.ru/press/paper04.html>
2. Hastie T., Friedman, J.: The Elements of Statistical Learning: Data Mining, Inference, and Prediction R. Tibshirani, 745 pp.. Springer (2009)
3. Zhou, Z., Wang, H., Lou, P.: Manufacturing Intelligence for Industrial Engineering: Methods for System Self-Organization, Learning, and Adaptation, p. 407 (2010)
4. Lohanin, A.K.: Questions transformer production of 43 the session CIGRE. Electricity 1, 58–64 (2011) (in Russian)

5. Jang, J.-S.R.: ANFIS: adaptive-network-based fuzzy inference system. *IEEE Trans. Syst. Cybern.* **23**, 665–685 (1993)
6. Nguyen, Hung T., Prasad, Nadipuram R.: *Fuzzy Modeling and Control: Selected Works of Sugeno*, p. 429. CRC Press, Boca Raton (1999)
7. Khalyasmaa, A.I., Bliznyuk, D.I., Verkhozin, A.A., Ovchinnikov, K.Y.: The problems of dissolved in oil gases analysis results' interpretation in information analytical systems. In: Conference and Exposition on Electrical and Power Engineering (EPE) (in press)
8. Galushka, V.V., Fathi, V.A.: Formation of the training sample by using artificial neural networks in search problems database errors. *Inženernyj vestnik Dona* (Rus) 2 (2013) (in Russian). <http://ivdon.ru/magazine/archive/n2y2013/1597>
9. Khalyasmaa, A.I., Dmitriev, S.A., Verxozin, A.A., Sarapulov, S.F.: Hybrid neural network and fuzzy logic methods for implementation of equipment actual state assessment of power stations and substations. In: Proceedings of Modelling, Identification and Control (MIC 2015), Innsbruck, Austria, pp. 167–170 (2015)
10. Khalyasmaa, A.I., Dmitriev, S.A.: Expert system for engineering assets' management of utility companies. In: Proceedings 10th edition of the IEEE International Symposium on Diagnostics for Electric Machines, Power Electronics and Drives (SDEMPED 2015), pp. 421–427 (2015)

A Host Program Implementation for Linux File System Tracing Method Using the Kprobes Linux Dynamic Instrumentation System

Sang-Young Cho

Abstract A storage performance analysis tool is crucial to finding performance bottlenecks in I/O storage systems and developing efficient storage system architectures or algorithms. This work is based on an integrated performance analysis tool for Linux file systems. The tool provides actual time information for Linux file system functions. In contrast to other existing tools, the tool provides a filtering mechanism, a graphical interface, and system-level analysis information without a heavy load of measurement. This paper describes a host program implementation for the performance analysis tool. It may be used by Linux developers or end-users for analyzing file system layers or measuring software performance to find bottlenecks in Linux file systems.

Keywords Linux filesystem • Performance analysis • EXT4 • Kernel trace

1 Introduction

Though the application performance of an Android-based device can be affected by many factors, the most influential factor is the performance of the underlying I/O storage system [1]. The storage system is a collection of software layers such as SQLite, EXT4, a block device driver, and a storage media driver. Each software module of the I/O storage system has been utilized for hard-disk storage media. Several performance issues began to occur when the integrated I/O storage system is applied to battery-powered mobile devices that are using NAND-based media. Therefore, many studies have been devoted to improving the performance of I/O storage systems.

S.-Y. Cho (✉)

Division of Computer & Electronic Systems Engineering,
Hankuk University of Foreign Studies, 81 Oedae-ro, Mohyeon-myeon,
Cheoin-gu, Yongin-si, Gyeonggi-do 17035, Korea
e-mail: sycho@hufs.ac.kr

Existing benchmarking tools measure storage system performance in various ways. The most well-known tool is IOzone [2], which provides numerous testing environments and data views with read/write speed and I/O turnaround time. IOzone shows performance results in statistical values, but it is difficult to use in Android-based systems. AndroBench [3] was developed to benchmark the storage performance of Android-based mobile devices at the application layer. These tools can give the overall performance behavior at the system level, but they lack the ability to report detailed inter- or intra-function behaviors that are useful for analyzing exact timing behaviors.

There are many function-level performance analysis tools, also known as function tracers [4–8], such as ftrace, perf, strace, dtrace, and blktrace. These tools allow users to trace almost all function-level events within the Linux kernel including file system domain functions. However, the tools do not provide any convenient interfaces to interpret or to filter the trace results, so users find it difficult to translate the trace results into useful information for analysis. To get system-level performance information, several tools should be used at the same time and each tool's trace information should be integrated to generate a wholistic view of system-level performance data.

In this paper, we describe a host program implementation for the performance analysis tool. It may be used by Linux developers or end-users for analyzing file system layers or measuring software performance to find bottlenecks in Linux file systems.

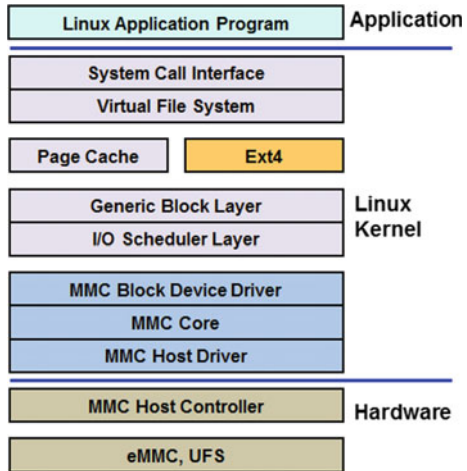
This paper is organized as follows. In Sect. 2, we introduce the Linux file system layers as well as the Kprobes Linux dynamic instrumentation system. Section 3 elaborates on the design of the Linux tracing tool and its host program implementation issues are discussed. The paper is concluded in Sect. 4.

2 Related Studies

2.1 *Linux Filesystem Layer and Write System Call Operation*

The Linux file system can be analyzed by investigating the function call sequence of the kernel when a read or write system call has been invoked by a user process. All of the performance analysis information is acquired by collecting the timing data of every invoked function's call and return, which is then processed in order to draw a complete picture of the read/write process. Though read and write system calls are all frequently invoked file-related functions in the Linux file system, write is the most influential system call on the entire storage system's performance if the file system is constructed on NAND-based storage media. This is because the write operation of NAND-based media is more time-consuming than the read operation

Fig. 1 An example of the Linux file system's layers



and the journaling operation is performed during the write operations. Therefore, we focus on analyzing the Linux file system's write operation.

Figure 1 shows an example of the Linux file system's layers. The Linux file system has a layered structure that is divided into layers of VFS (Virtual File System), EXT4 (for example), a generic block layer, the I/O scheduler layer and block device driver, and physical storage media. Various file systems can co-exist in a Linux system through the VFS interface. The generic block layer supports the block-based device I/O. Each block device has its own queue and I/O requests are inserted at the I/O scheduler layer. When storage media are eMMC or UFS devices, the MMC block device driver, MMC core, and MMC host driver are in charge of media accesses for storage I/O.

2.2 *The Kprobes Linux Dynamic Instrumentation System*

A static or dynamic Linux kernel tracepoint is a kind of breakpoint that provides a hook to call a function (probe) to extract kernel behavior information [9]. Static tracepoints cannot be inserted at run-time but they can be located at any points throughout the program. Dynamic tracepoints can be easily inserted or enabled during run-time, but they incur some overhead and are usually placed at function entry and exit points. Kprobes enables us to dynamically break into any kernel routine and collect debugging and performance information non-disruptively. The Kprobes instrumentation is built as a kernel module. Thus, rather than having to recompile and reboot the system with an instrumented kernel, a kprobe instrumentation module can be written, compiled, and loaded on the system. There is no need to reboot the system. Once the instrumentation module has served its purpose, it can be unloaded, and the kernel returned to its normal operation.

There are currently three types of probes: kprobes, jprobes, and kretprobes (also called return probes). A kprobe can be inserted on virtually any instruction in the kernel. A jprobe is inserted at the entry point of a kernel function, and provides convenient access to the function's arguments. A return probe fires when a specified function returns. Kretprobes also provides an optional user-specified handler which runs on function entry. The performance analysis tool of this paper was aimed at dynamic focusing. Probing overhead may not be significant because our main concern lies not on debugging information such as local variable investigation, but on the functions' timing information. The main focus of this work is the execution time of each function in relation to file-related operations. Therefore, we modify "kretprobe" to invoke entry and exit handlers for each kernel function.

Kretprobe can be applied within a kernel module using the following function calls: int register_kretprobes(struct kretprobe *p) and void unregister_kretprobes (struct kretprobe *p).

3 Software Structure and Operation Scenario

Figure 2 shows the software structure and the operating scenario of the storage performance analysis tool.

A kernel module has been implemented under Fedora 3.13 using the kretprobe interface to store the tracing data of the Linux filesystem on main memory. The collected data is written on a text file after executing a test application that has file access operations. To do this, user sets up the testing environment including writing a test program and choosing functions to trace. The testing environment setting is written as a text file and transmitted through Xshell via serial communication. The target Linux system receives the text file and configures a corresponding test environment based on the information of the file. The kernel module that controls the whole trace operation starts gathering tracing data with kretprobe interface. The result file is transferred to a Windows host PC through Xshell and analyzed by a viewer program that is developed under .NET framework 4 in C# language.

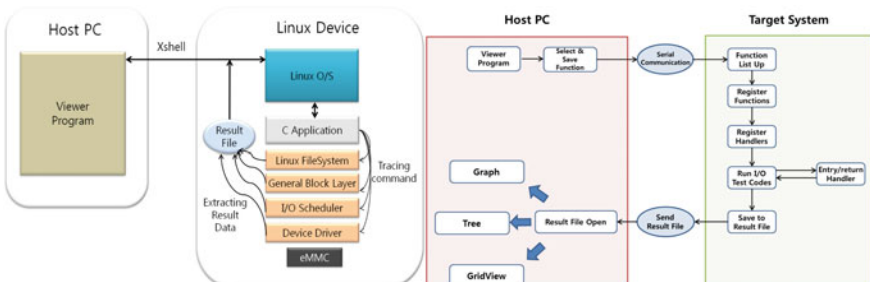


Fig. 2 The structure and operating scenario of the storage performance analysis tool

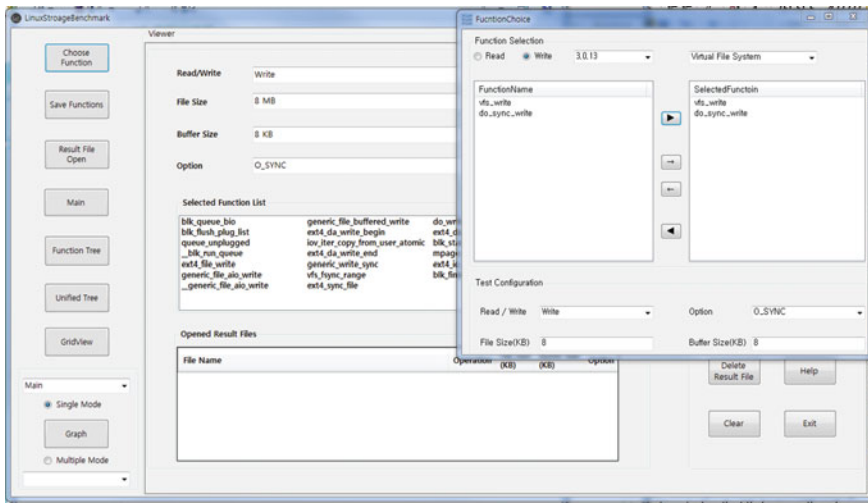


Fig. 3 The main window and a pop-up function selection window of the host program

The viewer program provides the storage performance analysis information using visualized interface such as graph, grid view and trees.

The host control program initiates filesystem tracing and shows tracing results in graphical views. Figure 3 shows the main window and a pop-up function selection window of the host control program. The Kprobes mechanism requires function names to call an entry and the return handler. These names must be registered using the Kprobes API. This means the user must know the exact names of the functions he/she wishes to trace. It is not easy to remember all of the function names. Furthermore, function names may change from version to version in Linux kernels. The host control program provides function names in four versions of Linux kernels. The names are classified according to the file system layers. Therefore the user can select a Linux version and a specific layer. The program lists the function names for the chosen layer so that the user can select the functions that the user wants to trace. The selected function names and trace environment setting information are written to an input file and transferred to the trace control program of a target system.

It is very important for a tracing tool to provide an intuitive and informative interface. The tool presented here supports three types of viewing interfaces. The graph view interface as shown in Fig. 4a displays the cumulative time of each function of a result file in single mode view. The view enables the user to find time-consuming functions at a glance. It also supports a multiple mode view where several test results can be compared to verify algorithmic performance enhancements or the differences in performance of various file access modes. The grid view interface of Fig. 4b shows the map data of a result file analysis. A file access system call in the Linux Ext4 file system is performed by three threads: the main thread that makes system calls, the jdb2 thread for journalling, and the mmcqd thread for

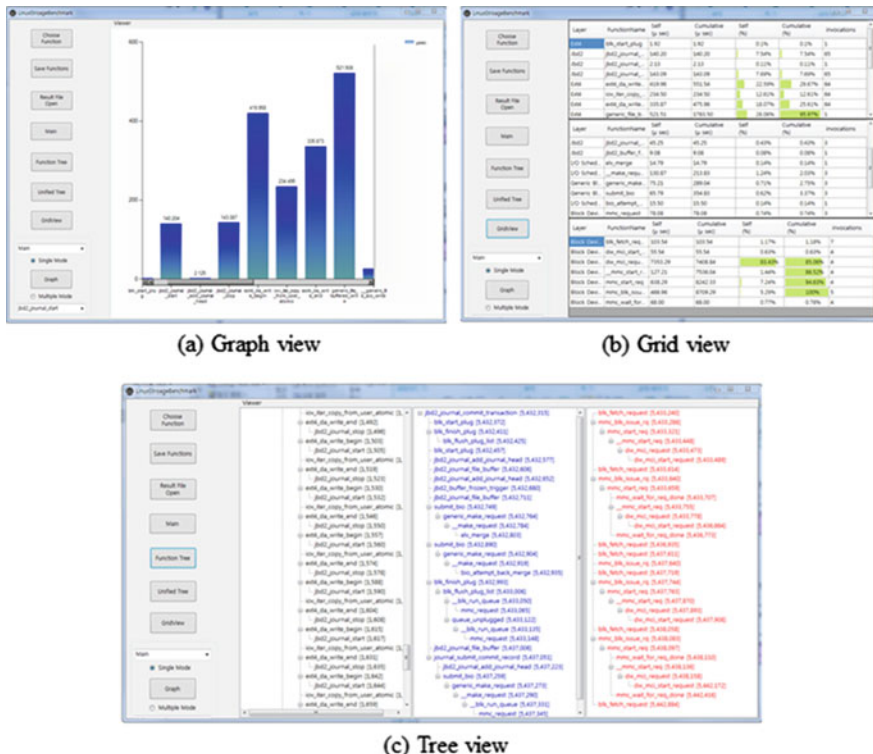


Fig. 4 User interface of the host viewer program

low-level I/O. The tool in this paper can trace all the functions called by the three threads and the traced data is displayed in three different grids. By providing the layer information of each function, the user can easily recognize the overhead of layers during file system access. The tree view interface in Fig. 4c displays the whole call graph of all the individual function calls using the tree data structure of a result file. The call graph display can be merged or expanded at a function so as to hide all functions called by a specific function. This helps the user see only the part of the call graph that is of interest. A pop-up window is used to show node time information when the mouse is located at a specific function name.

4 Conclusion

In this paper, we describe the design and implementation of a powerful Linux file system analysis tool that provides filtering services, a graphical interface, and system-level analysis information without incurring heavy penalties. The tool mainly consists of an in-kernel tracing module and a host control program that runs

on a host PC. The host control program is developed on .NET framework 4 in C#. The kernel module has low probing overhead compared to other existing tools. The host control program sets up a performance tracing environment and provides three types of performance viewers after analyzing a result file generated by the kernel trace module.

Acknowledgements This research was supported by Basic Science Research Program through the National Research Foundation of Korea (NRF) funded by the Ministry of Science, ICT & Future Planning (2015R1A5A7036384). This work was supported by Hankuk University of Foreign Studies Research Fund of 2017.

References

1. Jeong, S., Lee, K., Lee, S., Son, S., Won, Y.: I/O stack optimization for smartphones. In: Proceedings of the 2013 USENIX Annual Technical Conference, San Jose, USA, pp. 309–320 (2013)
2. IOzone. <http://www.iozone.org/>
3. Kim, J.-M., Kim, J.-S.: AndroBench: benchmarking the storage performance of android-based mobile devices. In: Proceedings of the Frontiers in Computer Education, vol. 133, pp. 667–674. Springer, Heidelberg (2012)
4. Spear, A., Levy, M., Desnoyers, M.: Using tracing to solve the multicore system debug problem. *IEEE Comput.* 60–64 (2012)
5. de Oliveria, D.B., de Oliveria, R.S.: Comparative analysis of trace tools for real-time Linux. *IEEE Latin America Trans.* **12**(6), 1134–1140 (2014)
6. Kernel Trace System. http://elinux.org/Kernel_Trace_Systems/
7. Bird, T.: Measuring function duration with Ftrace. In: Proceedings of the Linux Symposium, Ottawa, Canada, pp. 47–54 (2009)
8. LTTng Documentation. <http://lttng.org/docs/>
9. Mavinakayanahalli, A., Panchamukhi, P., Keniston, J.: Probing the guts of Kprobes. In: Proceedings of the Linux Symposium, Ottawa, Canada, vol. 2, pp. 109–123 (2006)

Simulation VANET Networks on a Random and Realistic Spatial Scenario

Suad Kasapovic and Lejla Banjanovic-Mehmedovic

Abstract The paper describes the use of VANET simulator to demonstrate the potential and importance of their application in a network of vehicles, as well as some of the network performance that can be predicted in this way. Using VANET simulator is shown scenario analysis of selected traffic parameters and network performance, based on the coupling traffic simulator VanetMobiSim and network simulator ns2. Vanet simulator using OpenStreetMap for the insertion of real map of the city.

Keywords VANET · Networks · Simulation · ITS · VanetMobiSim · ns2

1 Introduction

VANET (Vehicular Ad hoc NETwork) network play a key role in ITS (Intelligent Transport Systems). VANET comprises a number of technologies and active areas of research, standardization and development. Therefore, issues of stability, scalability, reliability, and network security vehicles is a challenge [1]. In VANET network, mobile nodes are vehicles. Network topology changes often and very quickly because of their high mobility and speed. For test purpose of VANET networks, software simulations can play a major role in imitating real world scenarios because it simple, easy and cheap [2]. Comparative survey of several publicly available mobility generators, network simulators, and VANET simulators are presented in [3, 4]. This paper presents a one of available VANET simulation software and their components and characteristics with simulation environment.

S. Kasapovic (✉) · L. Banjanovic-Mehmedovic
Faculty of Electrical Engineering, University of Tuzla, Franjevacka 2,
75000 Tuzla, Bosnia and Herzegovina
e-mail: suad.kasapovic@untz.ba

L. Banjanovic-Mehmedovic
e-mail: lejla.mehmedovic@untz.ba

2 Vehicular Mobility Simulation for VANET

This article presents the simulation of network traffic vehicles using two modules of VANET simulator. In one case, VanetMobiSim is used as a traffic simulator, and in the second case, ns2 is used as a network simulator [5].

Traffic simulator VanetMobiSim includes a number of models of mobility, and parsers for geographic data sources in different formats and modules for data visualization (Fig. 1).

It is based on the concept of switching modules, so that this software tool easily expandable. Its main drawback is that it offers a poor documentation. A set of extensions that contain VanetMobiSim, divided into spatial model and a set-oriented model of mobility vehicles [6, 7]. The spatial model of the vehicle is made up of spatial elements such as traffic lights or multi-lane road, their attributes and ways of linking these spatial elements. The spatial model is made up of topological data obtained (user-defined, random, geographic data files). Within it, there is a set of models of mobility vehicles such as: Intelligent Driving Model with Intersection Management (IDS_IM)—a model that perfectly describes the relationship vehicle-to-vehicle and managed intersections and Intelligent Driving Model with Lane Changing (IDM_LC)—model that includes overtaking other vehicles, communicate with IDM_IM management changes lane and accelerate or slow the vehicle. VanetMobiSim provides many opportunities to create a realistic scenario. The simulation scenario for VanetMobiSim defined in XML format. VanetMobiSim simulator requires a Java Development Kit (JDK) and Apache Ant, tasked with developing Java applications. For the first scenario analyzed in this

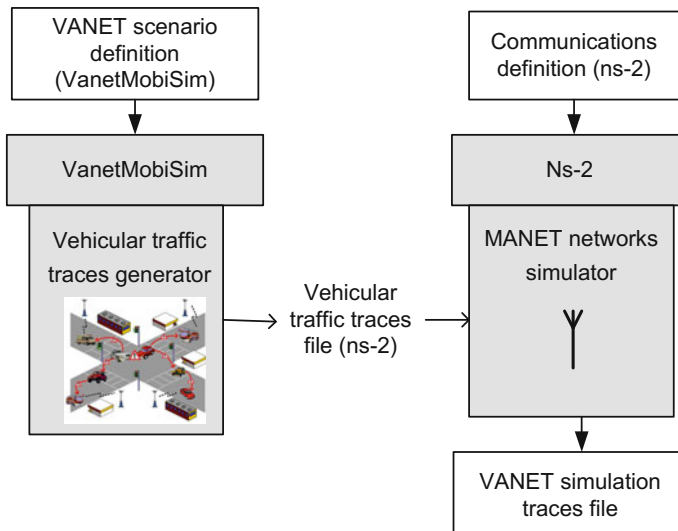


Fig. 1 VANET simulator based on coupling VanetMobiSim and ns-2

article is used Random Spatial Model. With `<seed>` tag specifies the random numbers of vehicles VanetMobiSim. With an instance of the class `x.mobisim.extensions.NSOutput` defined file format and with ns2 simulation selected time of 400 s, which is defined by instance: `x.mobisim.simulations.TimeSimulation`. Spatial environment is added with the help of instance `x.spatialmodel.core.SpatialModel`. Spatial environment provides support for different types of roads and leaves the possibility of the existence of the traffic lights at intersections. Support for traffic lights added by instance `x.spatialmodel.extensions.TrafficLight`. It is possible to define the time interval between changes color traffic lights, expressed in ms. The XML file is implemented with random option, known as *SpaceGraph* using instances `x.spacegraph.SpaceGraph`. It creates random graph constructed using the Voronoi tessellation method to set random points. Characteristics of clusters (areas) are given using the `<cluster>` tag. In the analyzed a random scenario density cluster has a value of 0.000001 clusters/m², which means that the surface area of 4,000,000 m² divided into 400 clusters. The `<ratio>` determines the percentage of certain types of cluster on the simulation area, `<speed>` tag specifies the maximum permissible speed in m/s on the segment path created with this kind of cluster. Group nodes are added to the simulation using `<nodegroup>` tag. The presented scenario includes only some of the possible specifications, such as maximum and minimum speed, although VanetMobiSim includes many more features that can be configured. During simulation, GUI environment shows the spatial model and its constituent elements such as roads and facilities. Figure 2 shows random scenario spatial model.

When the simulation is complete, a file named `ns_trace` is created. `Ns_trace` file contains traces of mobility necessary for ns2 simulation. At the start of the simulation are given x, y and z coordinates of each of the 10 monitored nodes. The first two coordinates describe the position of the nodes in the simulation area. The third coordinate describes time observation of the vehicle in the area of simulation, in seconds. Any change time of 0.1 s, gets the current position of the nodes. After some time, some of the nodes disappear, because the duration of each node substantially less than 400 s. After losing a node, occurs another node with the same label and the new duration. On the other hand, the ns2 network simulation and provides simulation-level package through many different protocols in wired or wireless network (the ability to use mobile nodes) [8]. The mobility of the nodes can be specified either directly in the simulation file, or by using the mobility trace files. To run the simulation, it is necessary to define the script by using the TCL programming language. General simulation specifications, such as the duration of the simulation, the simulation space, as well as some characteristics of networks and channels are defined. After completing the simulation, ns2 stops communication and closes `out.tr` file containing information of the routing during simulation, as well as `scenario.nam` file. From `out.tr` files can know more about the simulation. On the output file `out.tr` can apply a filter to the selected part of the simulation. For these purposes can be used awk scripts. Example start awk filter is `awk -f filter.awk out.tr`. After completion of the awk scripts `output.txt` file contains traces such as the number of sent and received packets or bits.

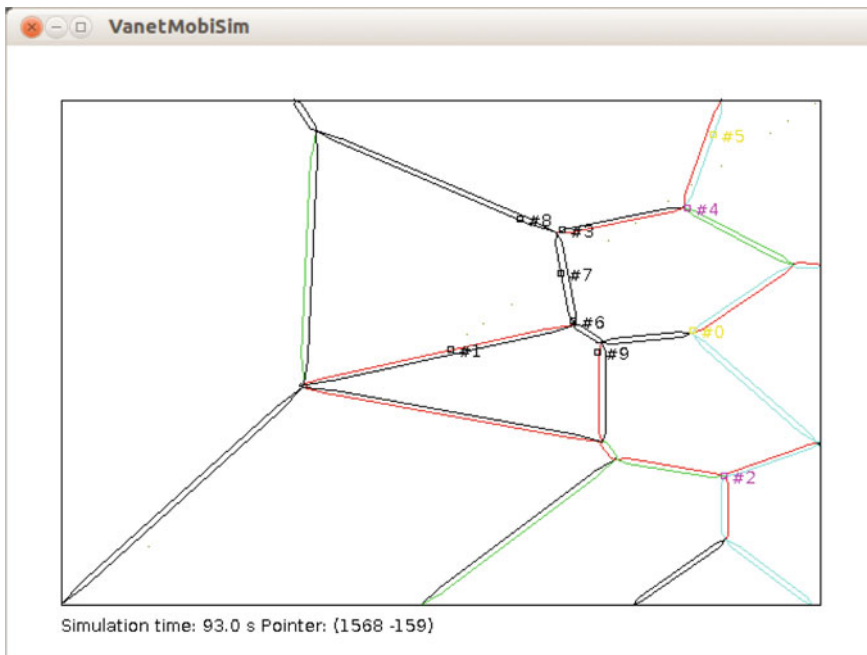


Fig. 2 Illustration of the selected scenarios

3 Simulation Using a Map Part of the City of Sarajevo

For the simulation can be used and a real map part of the city. In the real case, in this paper is used map of Sarajevo along with tools Openstreetmaps [9]. After using Openstreetmap find specific area to perform simulations (in this example the core of the city of Sarajevo) takes on the desired map. The already initiated the simulator, choose the folder *sarajevo.osm* and imported into the simulator. When taking a map, we will choose XML as the desired file format. The simulator is tested by opening the folder *sarajevo.xml* and loading the script file *sarajevo_scenarij.xml*. The urban part of the script, configured the way with two different directions. As for the attributes of the vehicle, there are different speeds, as well as the level of traffic congestion. For vehicles has set the maximum speed and acceleration of the vehicle that can be achieved. During the simulation you can display and some additional information about the scenario, such as the communication distance, vehicle ID etc. The movement of nodes and data transmission starts at $t = 0$ s. Simulation is used with quite a large number of vehicles and wireless communication includes all active vehicles. Figure 3 shows a transport map of the selected area of Sarajevo by VANET simulator.

The blue arrow represents the area of observation related to transport and communication. It analyzes the traffic in the street Hamdije Čemerlića in Sarajevo,

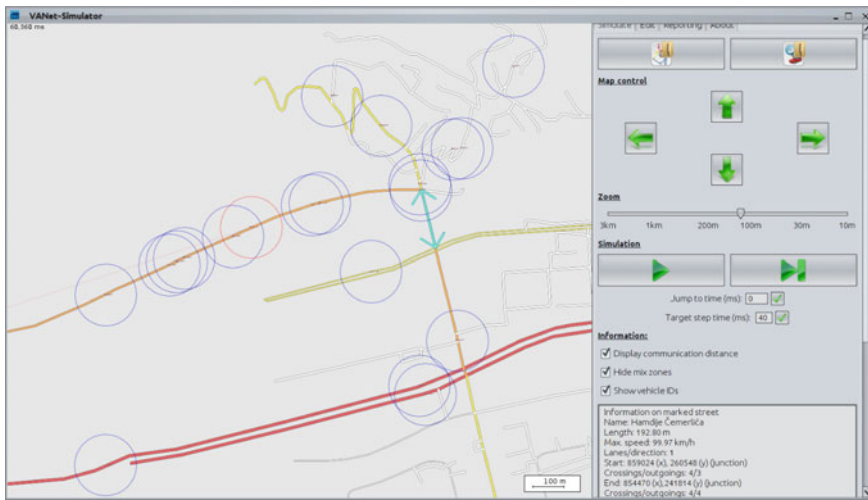


Fig. 3 Simulation VANET communication on a map of Sarajevo

at a distance of 192.8 m. For all vehicles that are observed, showing the communication distance as well as their ID code. Traces of simulations show that the total number of active vehicles during the simulation is 20, and all the vehicles are covered by wireless communication. The value of the mean velocity of the vehicle is 49.43 km/h. The mean distance that vehicles crossing for a period of 60 s is 700.22 m.

4 Algorithmic Flow and Simulation Results

In terms of implementation of the simulator, it is first necessary to install the simulator ad hoc network VanetMobiSim then define spatial scenario parameters. After starting the.xml script creates the output file with the extension.txt. Then, after the installation of a network simulator ns2 and start.tcl script, it create at the output file with extension.tr and.nam. Tcl script takes as input a vehicular traffic traces file. Thereafter, using filters such as awk script performs simulation analysis. As a result of the examples presented here are given the ratio of the received packet (PDR—Packet Delivery Ratio) and the ratio of lost packets (PLR—Packet Loss Ratio). PDR is the ratio between the number of packets received at the destination node and the number of packets transmitted from the source node and indicates the success of the delivery of packages from source to destination. In order to calculate these data, should be defined by two counters, one that should increase for each successfully received packet to the destination node, and another that would increase each time you send a package. Figure 4 graphically shows the dependence of the number of packages of the duration of the simulation.

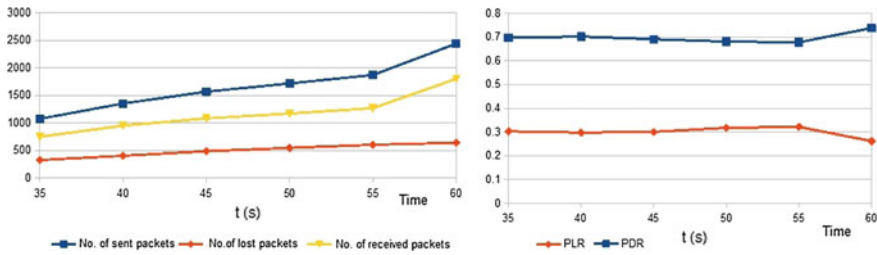


Fig. 4 Number of sent, received and lost packets, depending on the time and their changes during the simulation

After completing simulations and the obtained values, as an example shown by the ratio of received and lost packets, i.e., PDR and PLR value: 73.8% and 26.2% respectively. Figure 4 shows the change in the value of the PDR and PLR during the simulation time and where you see that at the end of the simulation the biggest success of transmitted packets.

5 Conclusion

The vehicular safety application should be thoroughly tested before it is deployed in a real world to use. Due to the high mobility of nodes and high speed of the vehicle, routing data packets through VANET network is a very complex process. Disentangling herself density traffic, which affects the reliability of delivery of the package. Before you embark on the implementation of projects with VANET networks, is of great importance to make high-quality simulation as similar real scenario, in order to reduce costs in the implementation of the project. The simulation should be “closer to the” real scenario, traffic and network performance. Network simulators are used to evaluate network performances and the traffic simulators are used for traffic engineering in a variety of conditions. Required solution is to use traffic and network simulator together, with proper coordination. Such attempts are given in [10, 11].

References

1. Olariu, S., Weigle, M.C.: Vehicular Networks: From Theory to Practice. Chapman and Hall/CRC Press (2012)
2. Guo, H.: Automotive informatics and communicative systems: principles in vehicular networks and data exchange. Information Science Reference, Chapter XIV, pp. 264–282 (2009)
3. Mittal, N.M., Choudhary, S.: Comparative study of simulators for vehicular ad-hoc networks. Int. J. Emerg. Technol. Adv. Eng. **4**, 528–537 (2014)

4. Martinez, F.J., Toh, C.K., Cano, J.-C., Calafate, C.T., Manzon, P.: A survey and comparative study of simulators for vehicular ad hoc networks. *Wirel. Commun. Mobile Comput.* **11**(7), 813–828 (2011)
5. Härrí, J., Fiore, M., Fethi, F., Bonnet, C.: VanetMobiSim: generating realistic mobility patterns for VANETs. In: Proceedings of the 3rd ACM International Workshop on Vehicular Ad Hoc Networks (VANET'06), Los Angeles, pp. 96–97 (2006)
6. University of Malaga, E.T.S.I. Informática, Dept. Lenguajes y Ciencias de la Computación. <http://neo.lcc.uma.esv>
7. Fiore, M., Härrí, J., Fethi, F., Bonnet, C.: Vehicular mobility simulation for VANETs. In: Proceedings of the 40th IEEE Annual Simulation Symposium (ANSS'07), Norfolk (2007)
8. Boston University, Department of Computer Science. <http://www.cs.bu.edu>
9. Ramm, F., Topf, J., Chilton, S.: OpenStreetMap: Using and Enhancing the Free Map of the World. UIT Cambridge (2011)
10. Su, Y., Cai, H., Shi, J.: An improved realistic mobility model and mechanism for VANET based on SUMO and NS3 collaborative simulations. In: 20th IEEE International Conference on Parallel and Distributed Systems (ICPADS), pp. 900–905 (2014)
11. Sanjay Kumar, A.K.A.: Traffic simulation of vehicular cloud network using sumo. *Int. J. Adv. Res. Comput. Sci. Softw. Eng.* **6**(1), 379–383 (2016)

Sensor Module for Monitoring Wine Fermentation Process

Dimitrija Angelkov and Cveta Martinovska Bande

Abstract This paper presents a module for monitoring the grape fermentation process constructed of low cost sensors for temperature, wine acidity (pH), alcohol and carbon dioxide released gases. Sensor values are recorded over the wine fermentation process and are sent through wireless modules in real time to a server. Constituent part of the module is a microcontroller PIC16F877A. It processes data received from sensors and sends them to the server through Ethernet controller ENC28J60. The main advantage of this low cost prototype is the possibility to be used by small winemakers for control and monitoring of a grape fermentation process. The proposed system has been tested in a winery in the Tikves region and it fulfilled the initial expectations.

Keywords Sensor network • Wine fermentation • Temperature sensor

1 Introduction

Over the past decade sensor networks have gained increased attention due to the applications in different areas, such as agriculture [1], environment monitoring [2], air pollution [3], health care [4–7], positioning and tracking [8], localizations, traffic detection and avoiding road congestion [9], etc. Recent applications of wireless sensor networks are systems for recognition of human activity and behavior which enables ambient assisted living and home automated systems [10]. There are many systems that use sensor networks based on different technologies, applications and standards [11, 12].

This paper describes implementation of a system for remote monitoring and control of sensor module installed in a winery. The aim is to monitor the conditions

D. Angelkov · C. Martinovska Bande (✉)
Computer Science Faculty, University Goce Delcev, Shtip, Macedonia
e-mail: cveta.martinovska@ugd.edu.mk

D. Angelkov
e-mail: dimitrija.21098@student.ugd.edu.mk

in the winery as well as weather conditions for growing grapes. Sensors located in the vineyard are used to gain knowledge about relations between soil and air conditions and interventions like fertilization, treatment with chemicals and irrigation. Parameters relevant for these systems are: solar irradiation and temperature which affect the sugar level and the ripeness of grapes, and air humidity which stimulates the development of some fungi and could lead to spread of infections.

The temperature in the fermentation process has impact on wine characteristics and quality. In the process of wine fermentation microorganisms transform must into wine. Microorganisms use grape's sugar to produce alcohol and CO₂. As a result of the fermentation process the heat of the must increases. In order to preserve the microorganisms alive and for proper fermentation the temperature has to be maintained at about 30 °C. The designed sensor prototype enables efficient monitoring of the parameters important for wine fermentation and production using low cost equipment.

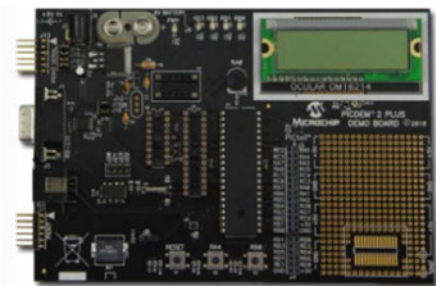
There are many studies that report on developed sensor systems for monitoring and control of wine production process [13] including temperature [14] sensing phenolic components [15] or sulfites in wines [16]. Several systems are proposed for classification of wines according to grape types and geographic origin [17–21]. For wine quality during winemaking process is important to measure some grape quality parameters, including pH-value, tartaric acid and malic acid. To assess these quality parameters of wine grapes during ripening different methods are developed [22, 23].

2 Structure of the Portable Sensor Module

The microcontroller PIC16F877A is the main component of the system. This component processes sensors data, transforms them from analog to digital and sends the data to the server through Ethernet module ENC28J60. Our aim was to develop small, portable device that can be inserted in the wine barrels, therefore the size of the board was important for preparing the sensor module. Other reasons for selection of this device were its high performance and low power consumption which have influence over the system autonomy. The proposed sensor module is applicable for small wineries. The owners of these wineries are not ready to invest in technology so we searched for the cheap components that we can easily integrate and program.

Among the many producers that offer commercial solutions we have chosen PIC family of microcontrollers developed by Microchip Technology Inc. Important properties of the PIC microcontrollers are wide availability, low cost, ease of reprogramming with built-in EEPROM and many development tools. Microchip Technology offers simple and economic development board PICDEM 2 Plus (Fig. 1), software MPLAB ICD 3, low price microcontroller, with low consumption and many applications and examples available on Internet. These reasons made this company the best option for development of our prototype.

Fig. 1 PICDEM 2 Plus development board



PICDEM 2 Plus includes port for communication with the computer, in-circuit programmer/debugger module for testing of the programs, access to the input/output ports of the microcontroller and the necessary software and drivers for the computer.

2.1 Description of the Microcontroller PIC16F877A

The microcontroller PIC16F877A is selected from the set of microcontrollers developed by Microchip Technology due to the compatibility with PICDEM 2 Plus development board. This microcontroller includes internal temperature sensor and integrated analog-to-digital convertor, programmable in C, and has small price and low power consumption.

The module for ADC conversion supports fast, 10 bits analog-to-digital conversions. It is configured with two control registers: control register ADCON0 and control register ADCON1. The module is powered up with ADCON0 bit 0. ADCON0 register controls the operation of the A/D module, while the ADCON1 register configures the functions of the port pins. The port pins can be configured as analog inputs (RA3 can also be the voltage reference) or as digital I/O. Every time the ADC module prepares and stores the conversion result in the register pair ADRESH:ADRESL the data transfer controller is triggered without any software intervention. The central processing unit is stopped to avoid any connection over the data bus during the data transfer. When data transfer operation is finished then CPU continues its work. In order to activate the integrated temperature sensor in the microcontroller analog input has to be selected. With this sensor the microcontroller uses the internal voltage reference. The way of accessing the ADC registers is the same when external temperature sensor is used. As an external temperature sensor is used LM35 precision integrated-circuit.

2.2 Connecting the Microcontroller with the Network Controller

The communication between the microcontroller PIC16F877A and the network controller ENC28J60 is established through 5 pins: RC0, RC1, RC3, RC4 and RC5. Except RC4 the other pins are directly connected with the network module ENC28J60 (Fig. 2).

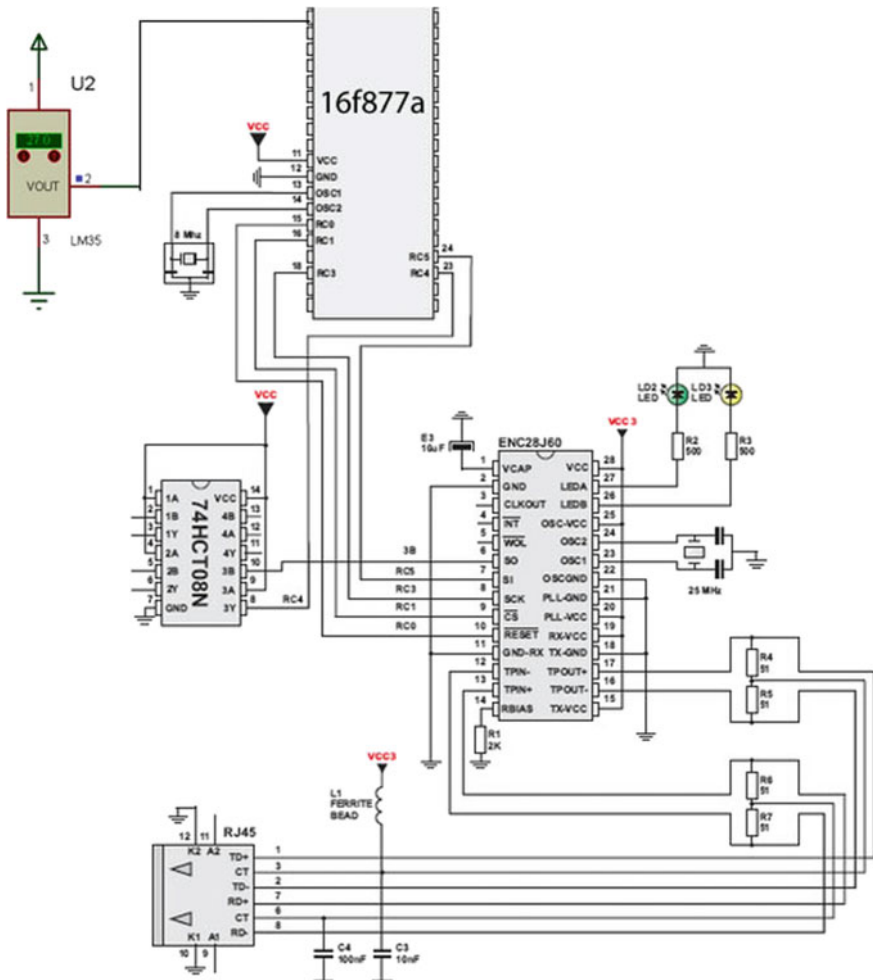


Fig. 2 Electric scheme for data transmission from temperature sensor to the server through the network module ENC28J60

The microcontroller PIC16F877A and the Ethernet controller ENC28J60 operate on different voltages. While the microcontroller operating voltage is 5 V the network module has operating voltage range of 3.14–3.45 V. For that reason the integrated circuit 74HCT08N is used as a logic multiplier which in this combination acts as amplifier for the logic signal that comes from the network controller.

3 Design and Development of the Prototype

To create the prototype we used advanced integrated development environment FLOWCODE, developed by Matrix Technology Solutions, which includes templates for popular development boards such as Microchip devices. It enables debugging during the development of the program after installing the drivers on the computer (Fig. 3). The program developed in C language was embedded into the microcontroller. After that the microcontroller without the computer can be used.

Using the design suite Proteus (Fig. 4) which is a product of Labcenter Electronics we designed a scheme to test the connections. Figure 4 shows schematic design of the components. Using this software tool we designed the prototype, first with internal temperature sensor and then with external temperature sensor LM35DZ.

Figure 5 shows the box with sensors fixed on the wine reservoir. The sensor module for monitoring and recording sensor data which is shown on Fig. 6 sends values over Internet in real time.

4 Sensor Network

The next step of our project was to create a sensor network where one computer will store the data from sensors installed on each of the reservoirs in the winery. To connect the server which stores the data and each of the sensor modules installed in the reservoirs we used the integrated circuit FT232BM (Fig. 7). The FT232BM circuit was connected with the computer using USB port and served as a USB to serial UART interface with data transfer rates from 300 baud to 3 Mbaud.

In the process of communication each of the reservoirs has a dedicated port, such as COM3, COM4, etc. USB Hub device is used to solve the problem with the small number of USB ports. The values from the sensors installed in the reservoirs are read with time sharing. Each of the reservoirs has sets of sensors with microcontroller. The microcontroller through the UART protocol communicates with the

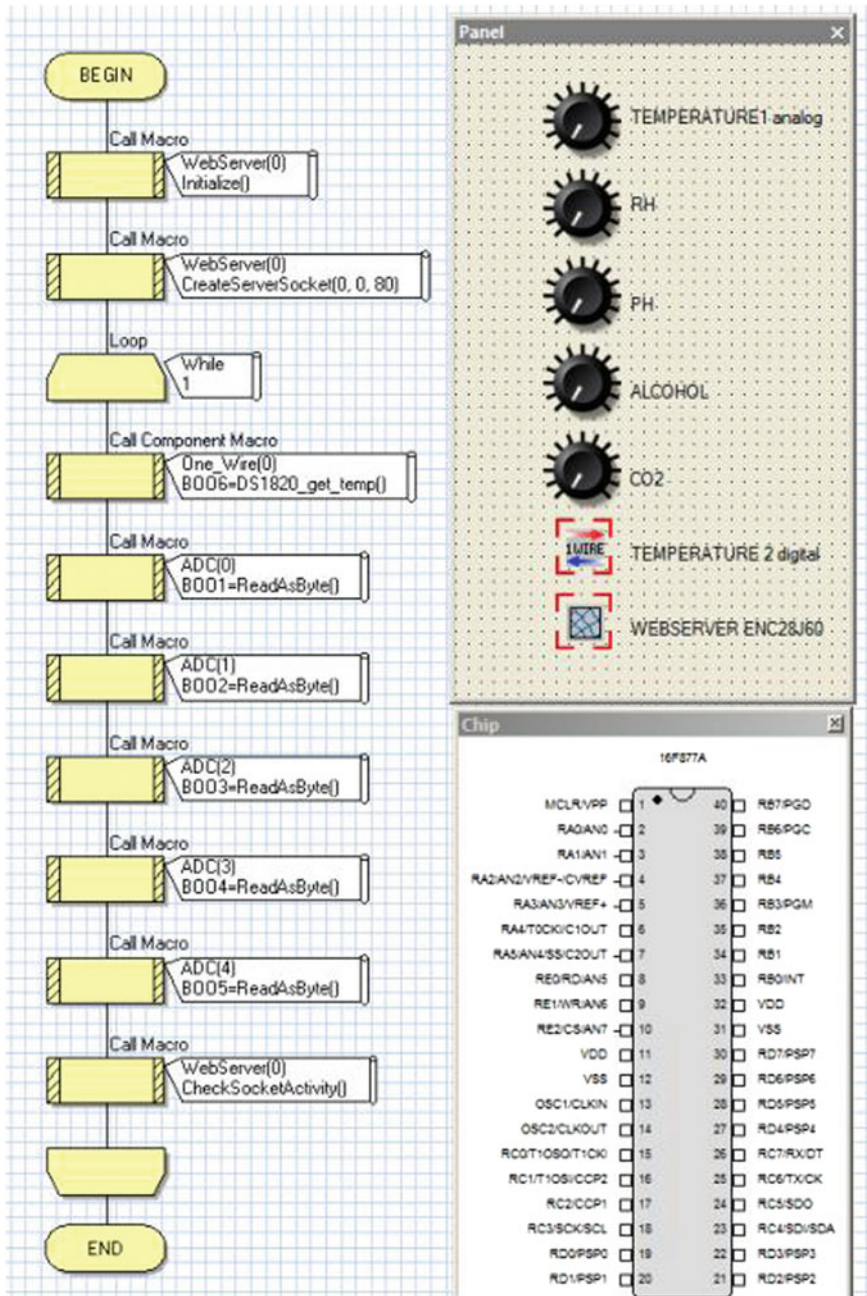


Fig. 3 Block diagram and panel of the simulation

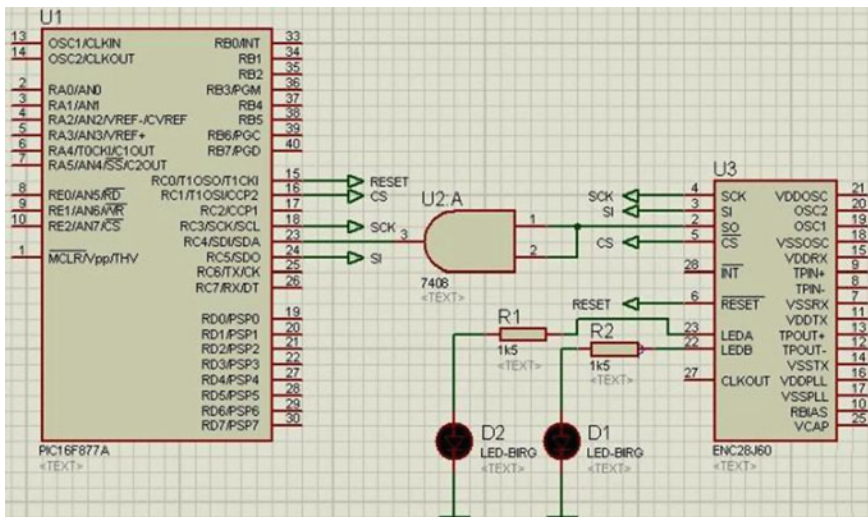


Fig. 4 Design and simulation of the electric circuit in PROTEUS

Fig. 5 Module for monitoring and recording sensor data



integrated circuit FT232BM. Communication is performed using pin 25 for TXD and 24 for RXD of the FT232BM with RS-232 transceiver MAX232ECWE which transforms the voltage of the logic signals using specified UART protocol.



Fig. 6 Box with sensors fixed on a reservoir

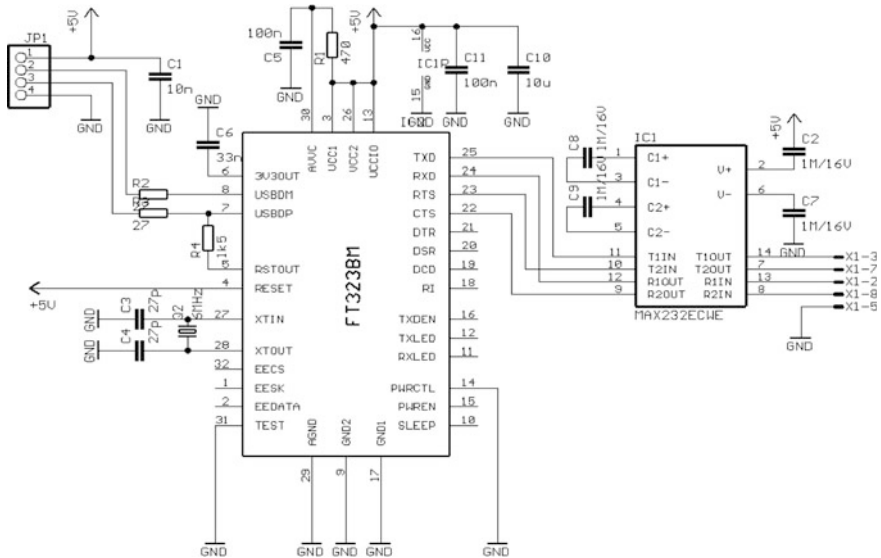


Fig. 7 Electric circuit USB2COM for the connection between the computer and reservoirs with installed communication and sensor modules

5 Conclusion

This paper describes application of Internet based control of sensor network for monitoring the fermentation process in a winery. The design of such a control system includes requirements specifications, architecture design, algorithm design and control interface for data access.

Specifically the paper presents design of sensor network for monitoring the conditions like temperature and humidity in the winery and monitoring the fermentation of wine by controlling the level of CO₂, alcohol and temperature in the barrels. Data from sensors are processed with PIC16F877A microcontroller and sent to the server via Ethernet controller ENC28J60.

We expect that the data collected while using the system will be useful for wine producers and will contribute to better quality of wines. The stored data can be analyzed in order to reveal correlations between environmental parameters and the resulting quality of the wine.

References

1. Ruiz-Garcia, L., Lunadei, L., Barreiro, P., Robla, J. I.: A review of wireless sensor technologies and applications in agriculture and food industry: state of the art and current trends. *Sensors* **9**, 4728–4750 (2009)
2. Ong, J., You, Y.Z., Mills-Beale, J., Tan, E.L., Pereles, B., Ghee, K.: A wireless, passive embedded sensor for real-time monitoring of water content in civil engineering materials. *IEEE Sensors J.* **8**, 2053–2058 (2008)
3. Yi, W.Y., Lo, K.M., Mak, T., Leung, K.S., Leung, Y., Meng, M.L.: A survey of wireless sensor network based air pollution monitoring systems. *Sensors* **15**(12), 31392–31427 (2015)
4. Lorincz, K., et al.: Sensor networks for emergency response: challenges and opportunities. *IEEE Pervasive Comput.* 16–23 (2004)
5. Alemdar, H., Ersoy, C.: Wireless sensor networks for healthcare: a survey. *Comput. Netw.* **54** (15), 2688–2710 (2010)
6. Shnayder, V., Chen, B., Lorincz, K., Fulford, T., Jones, F., Welsh, M.: Sensor networks for medical care. Technical Report TR-08-05, Division of Engineering and Applied Sciences, Harvard University (2005)
7. Ghamari, M., Janko, B., Sherratt, R. S., Harwin, W., Piechockic, R., Soltanpur, C.A.: Survey on wireless body area networks for eHealthcare systems in residential environments. *Sensors* **16**(6), 831–864 (2016)
8. Hao, J., Brady, J., Guenther, B., Burchett, J., Shankar, M., Feller, S.: Human tracking with wireless distributed pyroelectric sensors. *IEEE Sensors J.* **6**, 1683–1696 (2006)
9. Nellore, K., Hancke, G.P.: A survey on urban traffic management system using wireless sensor networks. *Sensors* **16**(2), 157–182 (2016)
10. Tunca, C., Alemdar, H., Ertan, H., Incel, O.D., Ersoy, C.: Multimodal wireless sensor network-based ambient assisted living in real homes with multiple residents. *Sensors* **14**(6), 9692–9719 (2014)
11. Akyildiz, I.F., Su, W., Sankarasubramaniam, Y., Cayirci, E.: A survey on sensor networks. *IEEE Commun. Mag.* **40**(8), 102–114 (2002)
12. Buratti, C., Conti, A., Dardari, D., Verdone, R.: An overview on wireless sensor networks technology and evolution. *Sensors* **9**(9), 6869–6896 (2009)
13. Anastasi, G., Farruggia, O., Lo Re, G., Ortolani, M.: Monitoring high-quality wine production using wireless sensor networks. In: Proceedings of 42st Hawaii International Conference on Systems Science (HICSS-42 2009): Waikoloa, Big Island, HI, USA (2009)
14. Sainz, B., Antolín, J., López-Coronado, M., Castro, C.D.: A novel low-cost sensor prototype for monitoring temperature during wine fermentation in tanks. *Sensors* **13**(3), 2848–2861 (2013)

15. Kim, S.K., Kwen, H.D., Choi, S.H.: Fabrication of a microbial biosensor based on QD-MWNT supports by a one-step radiation reaction and detection of phenolic compounds in red wines. *Sensors* **11**, 2001–2012 (2011)
16. Chinvongamorn, C., Pinwattana, K., Praphairaksit, N., Imato, T., Chailapakul, O.: Amperometric determination of sulfite by gas diffusion-sequential injection with boron-doped diamond electrode. *Sensors* **8**, 1846–1857 (2008)
17. Aguilera, T., Lozano, J., Paredes, J.A., Álvarez, F.J., Suárez, J.I.: Electronic nose based on independent component analysis combined with partial least squares and artificial neural networks for wine prediction. *Sensors* **12**, 8055–8072 (2012)
18. Fu, J., Huang, C., Xing, J., Zheng, J.: Pattern classification using an olfactory model with PCA feature selection in electronic noses: study and application. *Sensors* **12**, 2818–2830 (2012)
19. Gutiérrez, M., Llobera, A., Ipatov, A., Vila-Planas, J., Mínguez, S., Demming, S., Büttgenbach, S., Capdevila, F., Domingo, C., Jiménez-Jorquerá, C.: Application of an E-tongue to the analysis of monovarietal and blends of white wines. *Sensors* **11**, 4840–4857 (2011)
20. Verrelli, G., Lvova, L., Paolesse, R., Di Natale, C., Damico, A.: Metalloporphyrin-based electronic tongue: an application for the analysis of Italian white wines. *Sensors* **7**, 2750–2762 (2007)
21. Twomey, K., Truemper, A., Murphy, K.: A portable sensing system for electronic tongue operations. *Sensors* **6**, 1679–1696 (2006)
22. González-Caballero, V., Pérez-Marín, D., López, M.I., Sánchez, M.T.: Optimization of NIR spectral data management for quality control of grape bunches during on-vine ripening. *Sensors* **11**, 6109–6124 (2011)
23. Ghozlen, N.B., Cerovic, Z.G., Germain, C., Toutain, S., Latouche, G.: Non-destructive optical monitoring of grape maturation by proximal sensing. *Sensors* **10**, 10040–10068 (2010)

Study the Transmittance Properties of Light Sources Under Simulated Hazy Condition

Haibo Yuan, Xiaoli Zhou, Zheqian Zhang and Fanghui Xu

Abstract With the rapid development of industrialization, pollutant from industry and automobile has a big influence on the air quality of cities. With the high humidity caused by the urban microclimate, the visibility is greatly reduced due to the hazy weather formed by the accumulation of pollutant and vapor. In this paper, a hazy simulation environment is established to measure the transmittance of LED lamps, metal halide lamps and sodium lamps. First, we studied their transmittance under the fog condition (liquid) as well as the haze condition (solid). Then, the comparison among transmittance of light sources under different hazy environment is shown. The results are useful to the road lighting design.

Keywords Hazy weather · LED lamp · Halide lamp · Sodium lamp · Atmospheric aerosol

1 Introduction

All the studies of visibility of the target is under ideal conditions for road lighting or other visual environment, that is the gaseous medium (air) is dry, clean, and attenuation of light energy can be neglected. But in actually, all kinds of outdoor lighting in different weather conditions, especially for bad weather such as hazy condition, actual illumination value may be far lower than the theoretical calculation value. It is necessary to carry out the related research on the performance of light sources in bad weather conditions to ensure that the actual lighting effect can meet the requirements of relevant standards.

H. Yuan

School of Automotive Engineering, Wuhan University of Technology,
Wuhan 430070, China

X. Zhou (✉) · Z. Zhang · F. Xu

Institute for Electric Light Sources, Fudan University, Shanghai 200433, China
e-mail: zhoulx@fudan.edu.cn

Hazy weather, regarded as atmospheric aerosol, appear frequently in recent years [1–3]. The light from light sources reduced rapidly in severe weathers due to atmospheric aerosols' extinction for light. The present studies are concentrated on optical engineer and meteorology, the former aims to interpret the adsorption of monochromatic light (e.g. laser) because of the atmospheric aerosols, the latter tends to uncover the adsorption of natural light (e.g. sunlight) and the influence of scattering or determination of visibility owing to atmospheric aerosols [4, 5]. Lots of literatures mentioned how to measure the optical adsorption behaviors of aerosols quantitatively, however experimental data were rarely referred to and the previous researches were not systematically. In the lighting field, it's more realistic to understand the transmission properties of lamps under the condition of atmospheric aerosol. Most of the studies were focused on the special light sources such as laser, which can't be used in road lighting. The studies are meaningless for electronic light sources, especially for HID or LED lamps which have a compound spectrum. Reference [6] accomplished the experiment with only several different low-power LEDs to study the transmittance in fog conditions, Ref. [7] investigated the optimal transmittance wavelength in fog weather, they compared the transmission of light at a certain distance under different thickness of the fog. The results showed the best wavelength is 578 nm. Whereas this study is useless for outdoor lighting since the light sources for outdoor lighting are mostly compound light. In this paper, LEDs with various wavelengths and color temperatures, metal halide lamps and sodium lamps are used to study the transmittance in fog and haze conditions.

2 Set-Up of the Experimental Device

2.1 *Simulation of the Uniform Hazy Condition*

The formation of fog requires plenty of water vapor in air and thermal cools sharply or flows past a cold surface, i.e. rather high humidity, or proper temperature and suitable wind. The fog must be uniform, stable and controllable in the experiments. In this paper an ultrasonic humidifier is used to produce fog, minute droplets of water is formed by making the atomization piece remain in high frequent resonance with ultrasonic wave (1.7 MHz), the diameters of the water droplets is 5 μm which are in agreement with the diameter of fog in nature, which is from 4 to 10 μm . The uniformity of fog is guaranteed by a fan attached to the humidifier, and different thickness of fog is obtained through changing the gears of humidifier. Haze is aerosol system composed of non-aqueous materials, such as dirt, sulfuric acid, nitric acid and hydrocarbon. The diameters of particles of haze mainly range from 0.001 to 10 μm . The relative humidity is small when haze happens, while the relative humidity in fog is saturated. In this paper, we simulate haze by using air blower to

blow plant ashes into a box, through changing the quantity of plant ashes into the box, we can achieve different densities of simulative haze.

The schematic diagram of hazy simulation device is shown in Fig. 1. This experiment is to be completed under the dark environment to exclude the external interference. This paper uses a large dark box of $4.2\text{ m} \times 1.2\text{ m} \times 1.2\text{ m}$ (length \times width \times height). The floor of the box is spliced by two pieces of wood, bracket is made of wood, and its surface is covered by a black plastic. The light sources is installed at the end of the box, blow head of the humidifier and power supply is fixed on both sides of the box by opening holes. There are slots at 1, 2, and 3 m away from the light sources. Each slot is equipped with a long board and a short one. Inserting the short board can only close slots, however, insert the long one can separate the box into two independent space. We can test illumination value of the different distance by changing the position of the long board. Make a hole at the center of the long board to insert the detector of photometer. There is a guide in the corresponding location in the box to ensure that the detector is fixed.

2.2 Determination the Thickness of Haze

The air conditioner is used to keep room temperature stable to achieve the same initial humidity. After setting the thickness of fog or haze, illumination values are detected when the light source is stable. The data is recorded when haze inside the box reaches uniform state, in which the illumination value is stable. The humidifier or blower is turned off before recording data in order to avoid the influence of air

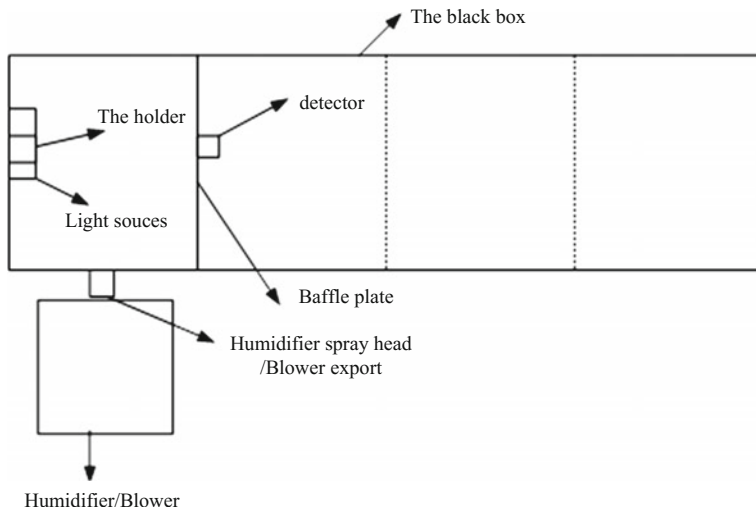


Fig. 1 Schematic diagram of hazy simulation device

flow on the results. For example, in the fog condition, when adjusting the humidifier knob in the same position, blowing fog into the dark box and conducting a number of tests for 40 W incandescent lamp, the illumination values detected at 1 m away is shown in Table 1.

From Table 1, the average value of illumination is 280.2 lx, the standard deviation S is 1.54 lx, $S/E_{avg} \approx 0.5\%$ through calculation. That is a relatively uniform fog field can be obtained after fixing the humidifier gear for a period of time. On this basis, fog thickness is divided into 1–3 three levels, and draw a tick at the corresponding position of the knob to mark. The state that humidifier is not open is defined as 0 gear. The fog thickness increases from 1 to 3 gear. The amount of blown dust is changed to get different thickness of haze. Two different haze thickness is tested in this paper, 0 gear presents no haze and haze thickness increases from 1 to 2 gear.

2.3 Light Sources for the Experiment

LED lamps of different colors and different color temperature, incandescent lamps, metal halide lamps and high pressure sodium lamps are chosen to do the experiment; relevant information of lamps is shown in Table 2.

Table 1 Results for incandescent lamp

The number of experiments	1	2	3	4	5	6
E (lx)	282	278	279	282	281	279

Table 2 Parameters of the experiment lamps

No	Type of the lamps	Power (W)	Remarks
1	Incandescent lamp	40	40 W
2	Metal halide lamp	400	PHILIPS HPI-T400
3	High pressure sodium lamp	150	150 W
4	Red LED	48	Main wavelength of 625 nm
5	Green LED	48	Main wavelength of 660 nm
6	Blue LED	48	Main wavelength of 470 nm
7	Yellow LED	48	Main wavelength of 575 nm
8	White LED	48	Color temperature of 3200 K
9	White LED	48	Color temperature of 4500 K
10	White LED	48	Color temperature of 6500 K

3 Transmittance of Light Sources Through Different Thickness of Fog

The dark box is set in a ventilated state, and air conditioner is turned on (20°C , 1 gear wind velocity). Twenty minutes later, put the light source into the dark box and connect the power. In this paper, the illumination is detected at a distance of 2 m from the light source. Long board is inserted in the slot at 2 m; other slots are closed with short board. Insert the detector of photometer into the hole at the center of the long board, and the blow head of the humidifier nozzle aim at the vent hole. Turn on the power; record the illumination value 30 min later when the system is stable. Open the humidifier and raise to the first gear, record the illumination value until the data does not change. Change humidifier gears and repeat the above steps. Remove the lamps and dry water within the box when complete the test, measure another lamps after 20 min of ventilation. All the results for tested light sources are shown in Table 3. Gear 0 is the illumination value without fog, gear 1, 2, 3 are the measured illumination value for the fog thickness gradually increasing, transmittance of different fog thickness is the illumination values under that thickness divide with the value without fog, that is

$$T = E/E_0 \quad (1)$$

T is transmittance, E is illumination value in the fog, and E_0 is illumination value without fog.

Figure 2 is the illumination of a variety of light sources at different thickness of fog. It shows that the transmittance of all the light sources significantly decreased with the thickness of fog increasing.

Table 3 Transmittance of light sources under different thickness of fog

	Illumination				Transmittance		
	Gear 0	Gear 1	Gear 2	Gear 3	Gear 1	Gear 2	Gear 3
Red LED	169	151.8	30.3	16.9	0.898	0.179	0.10
Green LED	297	270	50.5	31.9	0.909	0.170	0.107
Blue LED	63.9	54	14.3	6.8	0.845	0.224	0.106
Yellow LED	167.4	171	43	21.1	1.022	0.257	0.126
White LED (3200 K)	320	321	95	42.5	1.003	0.297	0.132
White LED (4500 K)	356	315	60.6	32	0.884	0.170	0.090
White LED (6500 K)	400	340	65.9	36	0.850	0.165	0.09
High pressure sodium lamp	1140	1130	220	160	0.991	0.193	0.1409
Metal halide lamp	3340	3300	1180	530	0.988	0.353	0.159
Incandescent lamp	24.1	23.6	7	4	0.979	0.290	0.166

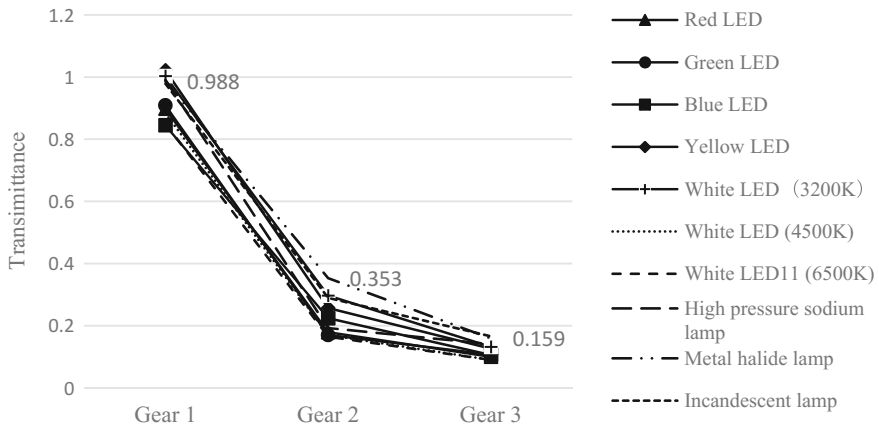


Fig. 2 Transmittance of different light sources

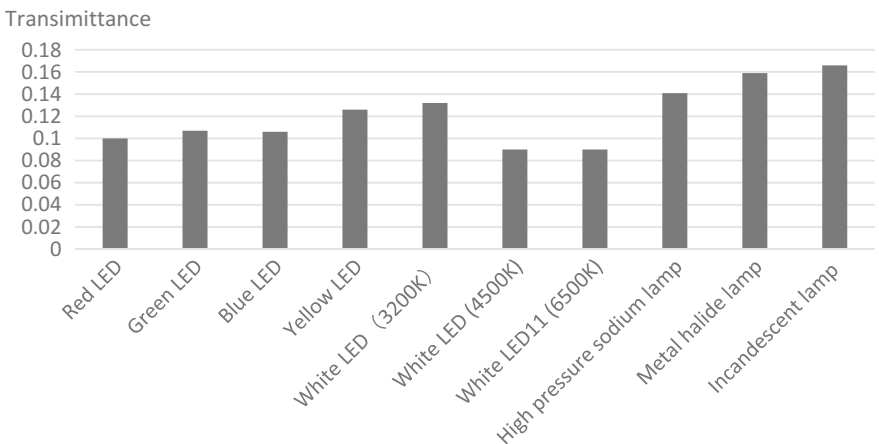
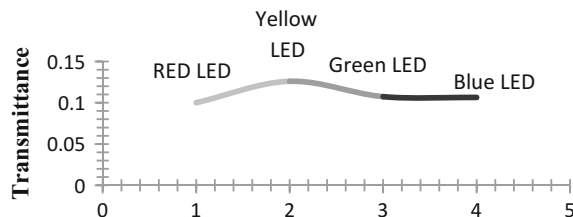


Fig. 3 Transmittance of different lamps in the same thickness of fog

Figure 3 shows the transmittance of different light sources in the maximum thickness of the fog (humidity is more than 90%).

The incandescent lamp has the best performance through the fog in all the types of lamps. For different color LEDs, the order of performance through fog is yellow, green, blue and red. The 3200 K White LED has best performance in white LEDs with different color temperature. Further analysis of LEDs' performance through fog is shown in Fig. 4. The performance through fog first increase and then decrease with wavelength increasing, that is to say there is an optimal wavelength, yellow due to the study, for using in the fog condition. This is consistent with prior research. Transmittance of monochromatic radiation in atmosphere depends on two factors: the absorption and scattering of the atmosphere. Therefore, the

Fig. 4 Transmittance of LEDs



transmittance of monochromatic light in the fog also depends on absorption and scattering of fog.

The absorption of different medium to different wavelengths of light are not the same, when use a humidifier to produce fog, the main Component is water vapor. There is such a law of the moisture absorption of light of different colors: the longer the wavelength, the more absorbent. And Light is scattered mainly by Mie scattering and Rayleigh scattering. Rayleigh scattering study the scattering phenomenon of particles that the particle diameter is much smaller than the wavelength. Mie scattering mainly study the scattering phenomenon that particle diameter is greater than 10. The scattered light intensity is inversely proportional to the fourth power of the incident wavelength in Rayleigh scattering. Namely, the shorter the wavelength, the greater the scattering coefficient. That is to say, the greater the attenuation coefficient, The lower transmittance. Scattered light intensity is almost independent of the wavelength in Mie scattering. Therefore, considered the absorption and scattering two factors, there is such a wavelength that the sum of absorption and scattering is the minimum, so that transmittance is the maximum. And the results obtained in our experiments is that the transmittance of yellow band is the best, which agrees with the literature [7].

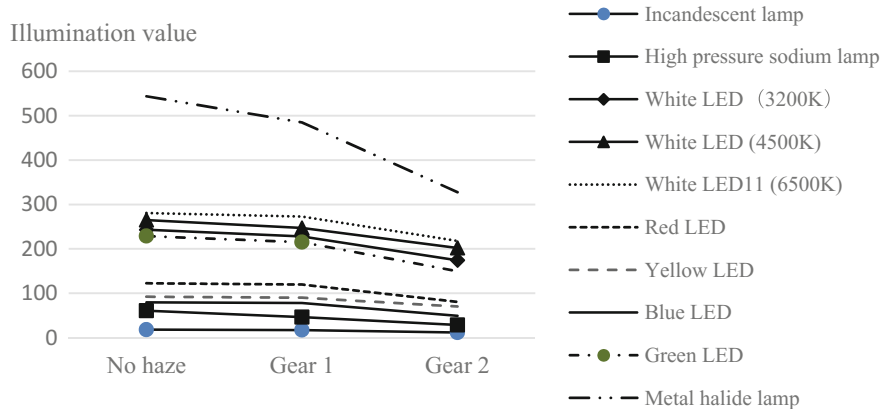
4 Transmittance of Light Sources Through Different Thickness of Haze

The Measurement methods in the haze is similar to in the fog, the blower hole is aligned with vent, measure dust with dosage cup in the box outlet, change the amount of blown dust to adjust different haze thickness. Two different thickness are measured in this paper, the experimental data is shown in Table 4. Gear 0 is data without haze, Gear 1, 2 are data with haze. Transmittance of different haze thickness is defined the illumination values under that thickness divide with the value without haze.

The transmittance of various lamps in haze at different thickness is shown in Fig. 5, the comparison of transmittance of lamps in haze at the same thickness is shown in Fig. 6.

Table 4 Illumination values in different thickness of haze

Type of lamp	Illumination values			Transmittance	
	No haze	Gear 1	Gear 2	Gear 1	Gear 2
Incandescent lamp	17.9	17.1	11.5	0.956	0.642
High pressure sodium lamp	60.6	46.2	28.5	0.762	0.470
White LED (3500 K)	243	228	174.3	0.938	0.717
White LED (4500 K)	265	247	202	0.932	0.762
White LED (6500 K)	281	273	218	0.972	0.776
Red LED	122.5	119.7	80.9	0.977	0.660
Yellow LED	92.2	90.1	70.4	0.977	0.764
Blue LED	79.4	78.1	49.2	0.984	0.620
Green LED	229	215	149.9	0.939	0.655
Metal halide lamp	544	485	328	0.892	0.603

**Fig. 5** Illumination value of light sources in different thickness of haze

It can be conclude from Figs. 5 and 6 that:

- (1) The transmittance of all light sources decrease with the thickness of haze increasing.
- (2) Different lamps has different performance through haze, the order of the transmittance is LED, Metal Halide lamp, Incandescent lamp and sodium lamp. LED has best performance among all the light sources.
- (3) For white LED, the higher the color temperature, the better performance through haze.
- (4) For LEDs with different color, the order of the performance through haze is yellow, red, green and blue in higher thickness of haze.

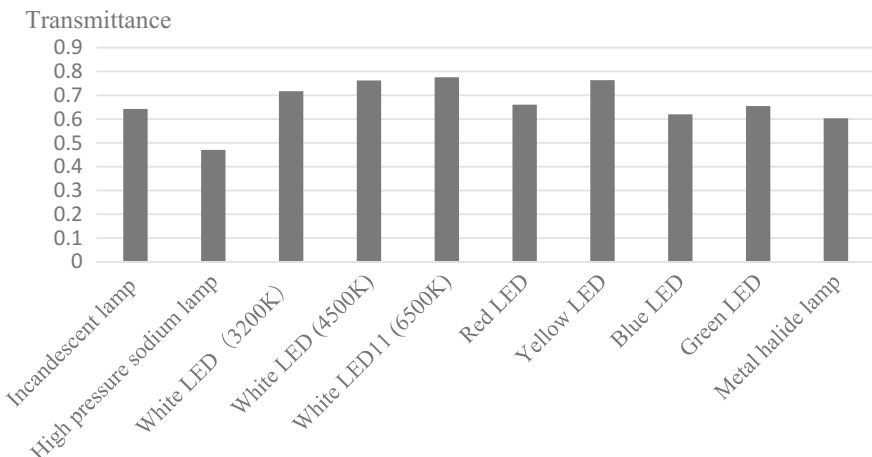


Fig. 6 Transmittance of various lamps in the same thickness of haze

5 Conclusion

A uniform hazy simulated environment is produced in this paper, and experiment is carried out to study the performance of different light sources, such as LEDs with different color and color temperature, incandescent lamp, metal halide lamp and sodium lamp, through fog and haze respectively. The results show that light sources of different types and different colors through fog and haze have different performance.

References

1. Jue, D., Liying, L.: An analysis on characteristics of particulate pollutants and the process of absorbing gaseous pollutants in hazy weather. *Shanghai Environ. Sci.* **28**(1), 11–14 (2009)
2. Huang, S., Li, Z., Yang, J.: Light absorbing properties of aerosols in the atmospheric boundary layer over China. *Plateau Meteorol.* **19**(4), 487–494 (2000)
3. Yang, X., Luo, J., Wang, J., et al.: Measurement of the absorption coefficient of light by aerosol particles in atmosphere. *High Power Laser Part. Beams* **15**(6), 543–546 (2003)
4. Li, X., Hu, S., Xu, Q., et al.: Characteristics measurement of extinction and refractive index of aerosol particles. *High Power Laser Part. Beams* **19**(2), 207–210 (2007)
5. Li, X., Li, W., Zhou, X.: Analysis of the solar radiation variation of China in recent 30 years. *Q. J. Appl. Meteorol.* **9**(1), 25–31 (1998)
6. Kurniawan, B.A., Nakashima, Y., Takamatsu, M., et al.: Visual perception of color LED light in dense fog. *J. Light Vis. Environ.* **31**(3), 152–154 (2007)
7. Lv, Z., Xu, T.: Determination of optimum penetration wavelength for fog lights. *J. Appl. Opt.* **29**(4), 530–532, 547 (2008)

Numerical Study on the Thermal Fatigue of Cryogenic Vacuum Insulated Pipe

Jae-Hoon Lee, Si-Pom Kim, Rock-Won Jeon and Geun-Ho Lee

Abstract A vacuum insulated pipe used to transport LNG was exposed to repeated thermal loads at an extremely low temperature in order to study its thermal-fatigue lifetime. To prevent fatigue failure, the lifetime of vulnerable parts needs to be estimated beforehand; therefore, thermal stress and thermal deformation were first observed using thermal-structural coupling analysis. Based on the results, the structural safety of the vacuum insulated pipe was evaluated. Furthermore, fatigue life was evaluated according to the design parameters by applying the boundary condition of thermal fatigue analysis based on the results from the thermal-structural coupling analysis.

Keywords Vacuum insulated pipe • Bellows type • Joint type • Thermal-structural analysis • Thermal fatigue analysis

1 Introduction

Natural gas is one of the world's three major energy resources including petroleum and coal, and its production and demand rate are increasing [1]. As a result, the development of natural gas transport and storage technology is accelerating. The use of natural gas as fuel is also increasing; however, the pipe used for LNG transport is exposed to various environments, and approximately 0.15% of the LNG

J.-H. Lee (✉) · S.-P. Kim (✉) · R.-W. Jeon · G.-H. Lee

Department of Mechanical Engineering, Dong-a University, Busan City,
Republic of Korea

e-mail: dhxowkd31019@naver.com

S.-P. Kim

e-mail: spkim@dau.ac.kr

R.-W. Jeon

e-mail: rockwoni@naver.com

G.-H. Lee

e-mail: lgh6072@gmail.com

evaporate sowing to temperature differences. This evaporation, known as boil-off gas (BOG), has an adverse effect on the transport and storage of LNG [2, 3]. To prevent BOG, a vacuum insulated pipe was introduced to cut off the flow of external heat. A vacuum insulated pipe is a double-structure pipe with a vacuum layer that helps to minimize heat conduction/convection [4]. The disadvantage of vacuum insulated pipe is that it is affected by the adverse thermal load generated by the low-temperature LNG owing to structural problems. The continuous and repeated thermal load of the LNG flowing in the pipe causes thermal fatigue in the pipe [5]. Research on the durability of vacuum insulated pipe and fatigue problems is sparse, and the fatigue fracture mechanism needs to be studied. When the vacuum of a vacuum insulated pipe is lost, the insulation performance drops abruptly as the convective heat transfer increases through the insulating material; the pipe breaks as a result of the sudden pressure change, and subsequently, other equipment may be damaged [6]. Therefore, fatigue fracture needs to be prevented by predicting the vulnerable areas in the vacuum insulated pipe using thermal fatigue analysis [7, 8].

In this study, a thermal fatigue analysis was performed for the cryogenic vacuum insulated pipe according to pipe type and diameter. Thermal stress and thermal deformation were observed by thermal structural coupling analysis, and the structural stability of the vacuum insulated pipe was evaluated. Moreover, based on the temperature distribution, stress distribution, and strain changes obtained from the thermal structural coupling analysis and applying them as the boundary conditions in the thermal fatigue analysis, the fatigue life was evaluated according to the design factors of the vacuum insulated pipe. The results are provided as basic data for the thermal fatigue study.

2 Numerical Analysis

2.1 Finite Element Method Model

The vacuum insulated pipe used as the model in the numerical analysis was a circular pipe, and its model was reduced in size by applying the symmetry condition for modeling. The model used in the actual numerical analysis was 1/16 the size of the vacuum insulated pipe. The types of pipe and parameters used in the numerical calculation are shown in Fig. 1 and Table 1, respectively.

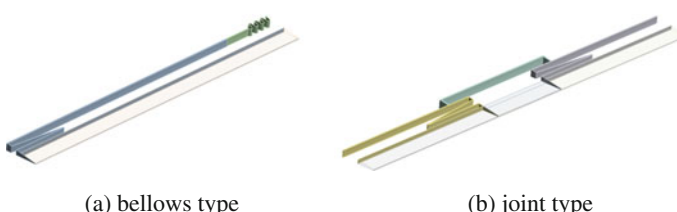


Fig. 1 Types of vacuum insulated pipe

The pipe length in Table 1 is the total length of the numerical model applied in the calculation, and the materials commonly used for the insulation and pipe were selected for the numerical analysis also.

2.2 Thermal Structural Coupling Analysis

A transient thermal analysis suitable for the time-dependent transient analysis was completed before the thermal structural coupling analysis. The total calculation time was set to 30 min, and the transient thermal analysis was carried out at 1-s intervals to increase precision.

The temperature distribution acquired by the transient thermal analysis was applied in the thermal structural coupling analysis, while forced deformation was applied as the boundary condition at both ends of the pipe. The conditions for thermal and thermal structural coupling analysis are summarized in Table 2. The thermal stress and thermal deformation data were obtained for the thermal fatigue analysis.

2.3 Thermal Fatigue Analysis

The thermal fatigue analysis was performed based on the stress distribution obtained from the thermal structural coupling analysis. The parameters used in the numerical calculation are shown in Table 3.

Table 1 Design parameters of vacuum insulated pipe

Vacuum insulated pipe type	Bellows, joint
Pipe length (mm)	2000
Pipe radius (mm)	15, 50, 100, 150
Insulation material radius (mm)	15
Insulation material	Polyurethane
Pipe material	SUS304

Table 2 Boundary condition for thermal structural coupling analysis

Inner tube temperature	-179 °C
Outer tube temperature	22 °C
Convective heat transfer coefficient	6.5 W/m ² K
Radiation rate of pipe	0.1
Radiation rate of insulation material	0.2
Internal pressure condition	320 bar
Vacuum pressure	10 ⁻³ Torr (-6.6661e-7 MPa)

The surface roughness weakens the fatigue behavior. In this study, the surface was treated to enhance the fatigue strength. In addition, the structure analysis result in terms of multi-axis load was converted to a single-axis load for depiction on the S-N diagram.

3 Results and Discussions

3.1 Thermal Structural Coupling Analysis

The thermal stress and thermal deformation according to the diameter and type of vacuum insulated pipe results of the thermal structural coupling analysis are shown in Fig. 2.

Based on the result of the thermal structural coupling analysis, the maximum thermal stress and thermal deformation occurred at both ends and the middle of the pipe for both the joint type and the bellows type. Changes in thermal stress and thermal deformation increased as the pipe diameter increased, and the maximum joint-pipe thermal stress and thermal deformation at the largest diameter of 150 A were 228.34 MPa and 0.1 mm, respectively. However, the maximum thermal stress was much less than the allowable stress of SUS304, and the thermal deformation was negligible, making it structurally stable.

Table 3 Parameter for thermal fatigue analysis

Surface roughness factor	Polished
Short-axis stress condition	Von-Mises stress
Stress life estimation	Goodman corrected equation
Load type	Ratio

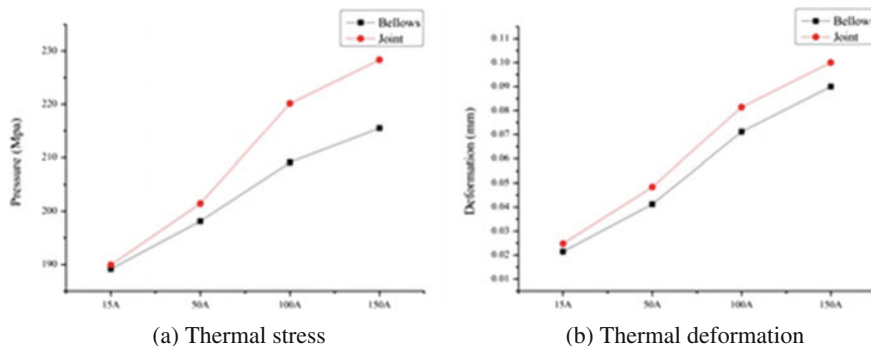


Fig. 2 Thermal structural coupling analysis result for vacuum insulated pipe

3.2 Thermal Fatigue

The results of thermal fatigue analysis using the thermal stress data of thermal structural coupling analysis for different sizes and types of pipe are shown in Figs. 3 and 4.

Based on the thermal fatigue analysis results, the 150A case showed the lowest fatigue lifetime. The fatigue lifetimes of the bellows-type and join-type pipes were 3.572E6 and 1.744E6, respectively, proving that the bellow-type pipe structure is more stable. The fatigue lifetime decreases at the curved surface for both pipe types due to the stress distribution obtained from the thermal-structural coupling analysis. This result demonstrates that pipe fatigue lifetime is inversely proportional to its stress level. The thermal fatigue results according to fatigue lifetime, type, and pipe size are shown in Fig. 5.

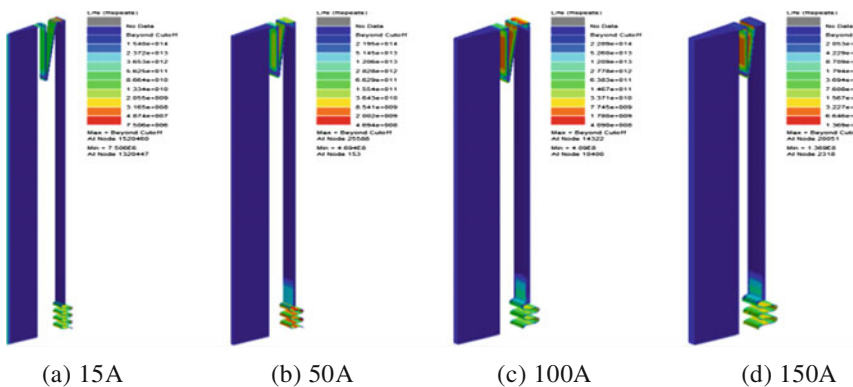


Fig. 3 Thermal fatigue analysis of bellows-type pipe

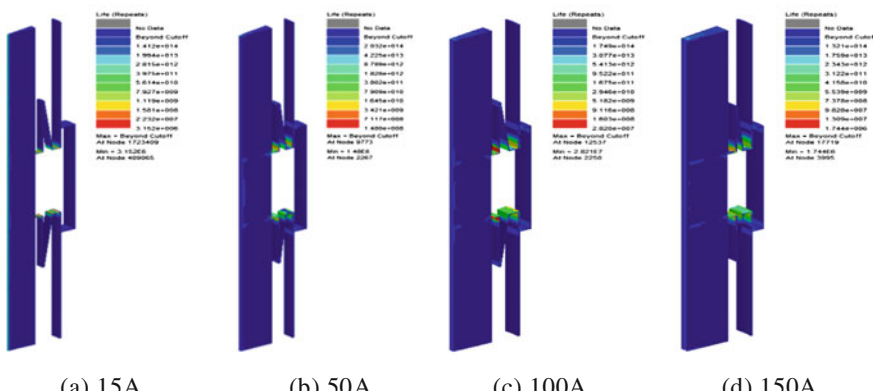


Fig. 4 Thermal fatigue analysis of joint-type pipe

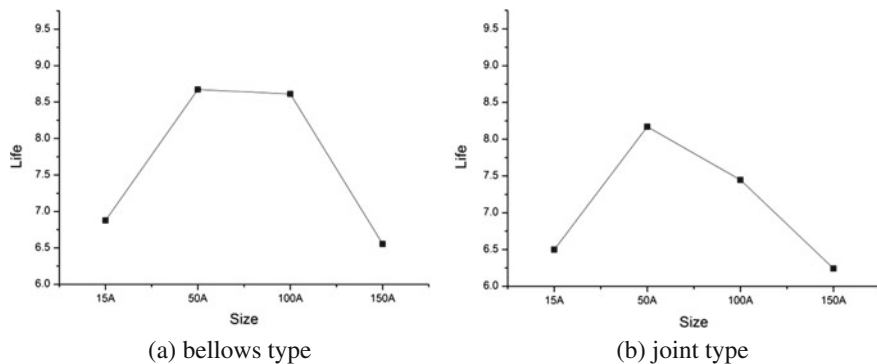


Fig. 5 Thermal fatigue according to type and size of pipe

Of the four pipe sizes, the bellows type was found to be the safest considering the fatigue lifetime, but since the fatigue lifetime varied with the size of the pipe, additional studies using a variation of pipe diameters are needed.

4 Conclusions

In this study, the structural safety of vacuum insulated pipe was evaluated by thermal and thermal structural coupling analysis. Based on the results of these analyses, a thermal fatigue analysis was carried out, and the conclusions are as follows.

1. We found a lack of examples of fatigue lifetime calculated by thermal fatigue analysis for vacuum insulated pipe. The results of this study can be used as basic data for estimating the lifetime of a vacuum insulated pipe.
2. The thermal structural coupling analysis showed that the thermal stress and thermal deformation were higher for the joint-type pipe (228.34 MPa and 0.1 mm, respectively) than the bellows-type pipe, but the thermal stress was still lower than the SUS304 allowable stress, and thus, the joint-type pipe is considered structurally stable.
3. The thermal fatigue analysis showed that the minimum fatigue lifetime of the bellows-type pipe (3.572E6) was higher than that of the joint-type (1.744E6) for a pipe size of 150A; therefore, the bellows-type is recommended for a 150A pipe.
4. The effect of pipe size on fatigue lifetime needs to be further investigated.

Acknowledgements This work was supported by the Materials and Components Technology Development Program of MOTIE/KEIT. [10046500/Development of Cryogenic (-196°C), high pressure (320 bar) welded insulation piping and valve jacket.]

References

1. Lee, D.-S.: A developing tendency of liquefied natural gas carriers. *J. Korean Soc. Marin Environ. Saf.* **15**(3), 269–274 (2009)
2. Lee, D.H., Jang, C.B., Jung, S.Y., Kim, J.H., Lee, H.S., Kim, B.S., Ko, J.W.: Study on the comparison of new and used reliquefaction system of boil-off-gas by LNG cold energy. *J. Korean Inst. Gas* **14**(1), 42–46 (2010)
3. Lee, Y.P., Shin, Y.H., Lee, S.H., Kim, K.H.: Boil-off gas reliquefaction system for LNG carriers with BOG-BOG heat exchange. *J. Soc. Nav. Arch. Korea* **46**(4), 444–451 (2009)
4. Kim, H.-Y., Kang, B.H.: Thermal Insulation technology for cryogenic cooling devices. *J. Korean Soc. Precis. Eng.* **19**(11), 24–30 (2002)
5. Hong, S.W., Seok, C.S., Koo, J.M.: Study on the fatigue life of spiral welded waterworks pipe material. *Korea Soc. Mech. Eng.* 2395–2398 (2015)
6. Lee, H.-Y., Kim, Y.: A Study on thermal performance for damaged vacuum insulation. *Arch. Inst. Korea* **34**(2), 319–320 (2014)
7. Lee, J.-H., Lee, J.-S.: On the Fatigue Analysis of Large Crane Pedestal in Drillship. *J. Soc. Nav. Arch. Korea* **48**(4), 342–345 (2011)
8. Choi, B.L., Chang, H.: Prediction of thermal fatigue life of engine exhaust manifold under thermo-mechanical cyclic loading. *Trans. Korean Soc. Mech. Eng. A* **34**(7), 911–917 (2010)

Unconventional Usage of Entropy in the Field of Web Usage Data Preprocessing and Machine Translation Evaluation

Michal Munk and Lubomír Benko

Abstract This paper focuses on an unconventional usage of entropy. On one side it deals with preprocessing phase, especially the session identification using the Reference Length method. Entropy, in this case, offers an alternative to determining the ratio of auxiliary pages that is important for this method. With the approach introduced in this paper, the need of a sitemap becomes void. On the other hand, the paper looks at entropy in the case of reliability analysis of Machine Translation metrics. In this case, entropy offers also an alternative mean to validate the metrics.

Keywords Entropy • Data preprocessing • Reference length • Machine translation

1 Introduction

Entropy offers a lot of possibilities to many fields of study. This paper focuses on Information Entropy introduced by Shannon and its unorthodox usage in two fields—Web Usage Mining and Machine Translation evaluation. Entropy can be used as a measure of disorder, where lower entropy means order and higher entropy on the contrary disorder. Following the definitions by Shannon [1], entropy can be used as a measure of uncertainty in a data set.

The rest of the paper is structured as follows: in Sect. 2 is summarized the related work of other authors about entropy and maximum entropy. In the field of

M. Munk (✉) · L. Benko
Faculty of Natural Sciences, Department of Informatics,
Constantine the Philosopher University, Nitra, Slovakia
e-mail: mmunk@ukf.sk

L. Benko
e-mail: lubomir.benko@gmail.com

L. Benko
Institute of System Engineering and Informatics,
University of Pardubice, Pardubice, Czech Republic

Web Usage Mining was the aim of the paper to create an alternative way to calculate the ratio of auxiliary pages for the session identification method Reference Length. This is dealt with in Sect. 3. To validate Machine Translation metrics were usually used Cronbach's alpha or Standardized alpha. Section 4 deals with another aim of the paper, to analyze entropy as an alternative mean to evaluate the metrics. Subsequently, the discussion and future work are offered in the last section.

2 Related Work

The first concept of entropy originates from thermodynamics [2], where it was used to provide a statement of the second law of thermodynamics on the irreversibility of the evolution, i.e. an isolated system cannot pass from a state of higher entropy to a state of lower entropy [3]. Shannon (1948) was the first to re-define entropy and mutual information, for this purpose he used a thought experiment to propose a measure of uncertainty in a discrete distribution based on the Boltzmann entropy of classical statistical mechanics [3]. Entropy can be described as a measure of the expected content of the information or uncertainty probability distribution. It is also described as the degree of disorder or randomness in a system. Based on Shannon's definition [1, 4], given a class random variable C with a discrete probability distribution $\{p_i = Pr[C=c_i]\}_{i=1}^k$, $\sum_{i=1}^k p_i = 1$ where c_i is the i th class. Then the entropy $H(C)$ is defined as $H(C) = - \sum_{i=1}^k p_i \log p_i$, while the function decreases from infinity to zero and p_i takes values from interval 0–1 [1, 4].

E.T. Jaynes formulated [5] the principle of Maximum Entropy and transformed that way entropy to a modeling tool. Maximum Entropy is used to estimate unknown parameters of a multinomial discrete choice problem, whereas the Generalized Maximum Entropy includes noise terms in the multinomial information constraints [3].

3 Entropy in the Field of Web Usage Data Preprocessing

Data preprocessing is a crucial part of Web Usage Mining and based on another experiment [6] especially session identification can prove important. Authors in [7] combine the maximum entropy model for the recommendation system. Their results showed that the recommendation system can achieve better accuracy than standard Markov model for page recommendation. It also provided a better interpretation of web users' navigational behavior. Authors in [8] focused on comparing the performance of maximum entropy with Naïve Bayes and Support Vector Machine, where the entropy outperformed both of them.

In the experiment [6] was the assumption about the ratio of auxiliary pages estimated for the session identification method Reference Length based on the sitemap. Based on the ratio can be determined the cutoff time $C = \frac{-\ln(1-p)}{\lambda}$ [6]. The

sitemap can offer an accurate estimate of the ratio but can be problematic if the examined web portal was changed in the meantime. In that case is the log file the only possible option to get the necessary data. One option would be to extract the sitemap from the log file using a complicated algorithm.

The experiment was conducted on a log file of a course of virtual learning environment (VLE) portal. The log file was prepared using standard data mining techniques same as in [9]. The final log file was imported to a database where were conducted several experiments involving the entropy, on the basis of which could be distinguished navigation pages from the content pages from one another. The aim was to create an algorithm that would be able to calculate entropy for a specific page on the basis of a random variable Length that represents the length of the time spent on each web page of the portal. With the use of the algorithm was created the variable Relative Time, which represented the relative time spent on the page by the user. From this variable was derived MaxEnt for each page and created a new data matrix (Table 1) that contained MaxEnt of each page. Subsequently was calculated the average length of all accesses on the web portal and served as the cutoff time that divides the pages to auxiliary and content pages. Pages with smaller MaxEnt than the MaxEnt of the average length of time spent across the whole portal will be classified as auxiliary pages. On the opposite pages with higher MaxEnt will be content pages.

In the log file of the course of VLE portal were identified 58 pages. Using the algorithm were 10 pages classified as auxiliary and the rest (48 pages) was classified as content pages (Table 2). Therefore the ratio of auxiliary pages of the web portal is 17.24%. Another option for specifying the time threshold of time spent on the web portal were quartiles. The time was calculated by $Q_{STT} = Q_{III} + 1.5Q$, where Q_{III} represents the upper quartile and Q represents the quartile range. Using the quartiles were 9 pages classified as auxiliary and 49 pages were identified as content pages. Compared to the calculation of the ratio of auxiliary pages based on the sitemap (15.34%) that was based on previous research [6], is the ratio calculated based on MaxEnt average time spent on the whole portal higher by almost 2%. But the ratio calculated based on MaxEnt quartiles of the time spent on the whole portal was almost similar (15.51%) to the sitemap calculation. In comparison to the subjective estimate of the ratio (25%), that was determined by the administrator of the web portal, the estimates calculated from the sitemap or MaxEnt offer more accurate results. The influence of more accurately calculated ratio of auxiliary pages in the session identification phase was described in more detail by authors in [6].

Table 1 Data matrix extended by maximum entropy

URL ID	Length	Relative Time	MaxEnt
58450	24	0.0039636	7.9789487
661	138	0.0001486	12.7156915
69022	48	0.0008319	10.5307314
69022	6	0.0001039	13.2311711
:	:	:	:

Table 2 Ratio of auxiliary pages based on different calculations

	Auxiliary pages	Content pages	Ratio (%)
Subjective estimate	–	–	25
Sitemap calculation	29	189	15.34
MaxEnt of average	10	48	17.24
MaxEnt of quartiles	9	49	15.51

Table 3 Statistics of automatic metrics of error rate

	Metrics-total correlation	Alpha if deleted	Metrics-total accuracy entropy
PER	0.878	0.934	0.934
WER	0.845	0.964	0.852
CDER	0.958	0.869	0.895

4 Entropy in the Field of Machine Translation Evaluation

Entropy can be used not only in the phase of preprocessing but also for analysis of reliability. Authors experiment with entropy also in the field of Machine Translation. Authors in [10] offer a complex survey of data selection methods in Machine Translation. They also describe articles that focused on cross-entropy which has become the most commonly used approach in data selection. Authors in [11] introduce a novel framework based on maximum entropy for word alignment. Based on the experiment the authors improved the alignment quality and translation quality as measured by standard reliability metrics.

PER, *WER*, and *CDER* metrics are called metrics of error rate, i.e. the higher values of these metrics, the lower the translation quality. On the other hand, metrics *Precision*, *Recall*, *F-measure*, and *BLEUs* are called metrics of accuracy, i.e. the higher values of these metrics, the better the translation quality. The automatic metrics defining Machine Translation error rate and representing the automatic evaluation of Machine Translation are considered highly reliable based on the direct estimation of reliability. The aim of this experiment was to assess the reliability of the automatic evaluation of machine translation for inflectional languages using traditional methods and entropy; in this case on-line statistical machine translation system was used.

All items (Table 3) correlate (*Avg inter-metrics correlation*: 0.885) with the total score of evaluation and after their eliminating the coefficient of reliability has not increased except the *WER* metric (*Cronbach's alpha*: 0.947; *Standardized alpha*: 0.950). After elimination of the metric *WER*, the coefficient of reliability—*Cronbach's alpha* increased from 0.947 to 0.964, but that it is negligible.

For the *entropy* calculation (Table 3), in the case of analysis of automatic metrics characterizing the error rate of Machine Translation evaluation, individual metrics in comparison over accuracy metrics were used. *Entropy* was calculated for each sentence analyzed using the specific metrics and for the comparison was used the

average entropy of all sentences. From the Shannon definition of entropy [1], if the *entropy* is closer to 1, then the system is more irregular. The results of the *entropy* for each of the error rate metric relate with the coefficient of reliability—*Cronbach's alpha*.

Even though the reliability analysis of automatic metrics characterizing the error rate of Machine Translation evaluation showed that the *WER* metric is the most deviated from the other automatic metrics of automatic Machine Translation evaluation (PER or CDER) in translation quality assessment. It is understandable seeing that, the *WER* metric is very strict to syntax errors (word order).

The estimations of the entropy of automatic metrics of accuracy were similarly calculated as in the case of metrics of error rate. Also, in this case, was used the average entropy of all sentences for each metric and the results relate with the coefficient of reliability—*Cronbach's alpha* with negligible variations. In the case of *entropy*, it also showed that the metric *BLEU-4* deviates the most from the other metrics.

We explain this by the fact that *BLEU-4* metric measures a score of a sequence of four words (including articles and prepositions) and sometimes it is very complicated to achieve an output with such a sequence by systems of machine translation.

5 Discussion and Future Work

As has been shown in this paper it is possible with the use of Maximum Entropy to divide the pages of the web portal to auxiliary and content pages. This can be used in the method Reference Length of session identification of data preprocessing of log files. The ratio of auxiliary pages for the Reference Length method can be then calculated with similar accuracy as if calculated from the sitemap. Since it is possible to work also with historical data, there could not be available an appropriate sitemap of the web portal of that time. Therefore the possibility to estimate the ratio of the auxiliary pages without the sitemap of the web portal is beneficial. An important role plays also a thoroughly made log file cleaning from unnecessary data because poorly cleaned log may generate an inaccurate ratio of auxiliary pages. The experiment was realized only on log file of a course of VLE portal, the future work could be focused also on web portals with anonymous accesses because of a bigger variance of the structure of such portals. Also these kind of portals (for example e-shops) contain bigger log files that could prove more difficult to analyze for the algorithm. Future work could be also focused on determining the size of the page content. It would be assumed that the high entropy would suggest the high proportion of the content of a particular page. That would inform the web portal administrator of content-rich pages. On basis of such information, the page could be divided into more pages with less content and thus improve browsing of the web portal for users. The principle could be based on research [12] which calculated page rank for each page of the web portal.

The next aim of the paper was focused on verifying the reliability of the automatic metrics for Machine Translation evaluation. Three different measures of reliability were used—*Cronbach's alpha*, *Standardized alpha*, and *entropy*—to estimate reliability. *Cronbach's alpha* and *Standardized alpha* were very similar, i.e. individual automatic metrics for Machine Translation evaluation have the same variability. The use of *entropy* provided alternative means to validate the reliability of metrics and the results relate to results of *Cronbach's alpha* and *Standardized alpha*.

Acknowledgements This work was supported by the Slovak Research and Development Agency under the contract No. APVV-14-0336 and Scientific Grant Agency of the Ministry of Education of the Slovak Republic (ME SR) and of Slovak Academy of Sciences (SAS) under the contracts No. VEGA-1/0559/14 and by the project No. UGA VII/3/2015 Modelling the behavior of web users depending on time.

References

- Shannon, C.E.: A mathematical theory of communication. ACM SIGMOBILE Mob. Comput. Commun. Rev. **5**, 3 (2001)
- Clausius, R.: On the Motive Power of Heat, and on the Laws which Can Be Deduced from It for the Theory of Heat. Dover (1960)
- Holzinger, A., Hörtenhuber, M., Mayer, C., Bachler, M., Wassertheurer, S., Pinho, A.J., Koslicki, D.: On entropy-based data mining. In: Holzinger, A., Jurisica, I. (eds.) Interactive Knowledge Discovery and Data Mining in Biomedical Informatics: State-of-the-Art and Future Challenges, pp. 209–226. Springer, Berlin (2014)
- Lima, C.F.L., de Assis, F.M., de Souza, C.P.: A Comparative Study of Use of Shannon, Rényi and Tsallis Entropy for Attribute Selecting in Network Intrusion Detection (2012)
- Jaynes, E.T.: Information theory and statistical mechanics. Phys. Rev. **106**, 620 (1957)
- Munk, M., Benko, L., Gangur, M., Turčáni, M.: Influence of ratio of auxiliary pages on the pre-processing phase of Web Usage Mining. E+M Ekon. a Manag. **3**, 144–159 (2015)
- Jin, X., Zhou, Y., Mobasher, B.: A maximum entropy web recommendation system. In: Proceeding of the eleventh ACM SIGKDD International Conference on Knowledge Discovery in Data Mining—KDD'05, p. 612. ACM Press, New York (2005)
- Wang, H., Wang, L., Yi, L.: Maximum entropy framework used in text classification. In: 2010 IEEE International Conference on Intelligent Computing and Intelligent Systems, pp. 828–833. IEEE (2010)
- Benko, L., Reichel, J., Munk, M.: Analysis of student behavior in virtual learning environment depending on student assessments. In: ICETA 2015: 13th International Conference on Emerging eLearning Technologies and Applications, Stary Smokovec, November 26–27, 2015, pp. 33–38. IEEE, Stary Smokovec, Danvers (2015)
- Etemadi, S., Lewis, W., Toutanova, K., Radha, H.: Survey of data-selection methods in statistical machine translation. Mach. Transl. **29**, 189–223 (2015)
- Tomeh, N., Allauzen, A., Yvon, F.: Maximum-entropy word alignment and posterior-based phrase extraction for machine translation. Mach. Transl. **28**, 19–56 (2014)
- Kapusta, J., Munk, M., Drlik, M.: Analysis of differences between expected and observed probability of accesses to web pages. In: Hwang, D., Jung, J., and Nguyen, N.-T. (eds.) Computational Collective Intelligence. Technologies and Applications SE-68, pp. 673–683. Springer International Publishing (2014)

Advantages of Intelligent Multimedia Application

Eva Milkova and Abdel-Badeeh M. Salem

Abstract The aim of subjects dealing with graph theory and combinatorial optimization is above all to develop and deepen students' capacity for logical and algorithmic thinking. It should also support the ability to form images in mind. Students should be able to describe various situations with the aid of graphs, solve the given problem expressed by the graph, and translate the solution back into the initial situation. As a lot of our students are visual learners it is useful to complete teaching and learning using various multimedia applications. One of the programs enabling visual representation of basic graph-concepts and graph-algorithms is introduced in the paper, as well as relevant educational principles, which have been applied in the course of many years. The paper can serve to the teachers and instructors as an inspirational material when dealing with graph theory and combinatorial optimization.

1 Introduction

Information and communication technology has changed many things in the world and has substantially influenced also education. Demonstration and visualization using suitable multimedia applications make the subject much clearer and comprehensible. *Students need images and visualization in addition to words. Science learning is about creating images in mind, and teaching should support such image formation [1].*

E. Milkova (✉)

University of Hradec Králové, Rokitanskeho 62,
50002 Hradec Kralove, Czech Republic
e-mail: eva.milkova@uhk.cz

A.-B.M. Salem

Faculty of Computer and Information Sciences,
Ain Shams University, Abbassia, Cairo, Egypt
e-mail: abmsalem@yahoo.com

Intelligent learning system has been focusing on acquiring and building the student's knowledge, experience, to minimize their weaknesses and boost their strengths. It allows flexibility in teaching methods, achieving many of the same benefits as one-on-one instruction (cf. [2]).

Graph theory and combinatorial optimization, the areas located at the intersection of applied mathematics and operations research, belong to fundamental parts of computer science. For the reasons that students could get a deeper insight into a problem and were able to solve it using a suitable algorithm, it is necessary to ensure especially in the instruction of subjects dealing with these areas that the students are first informed about the necessary graph-concepts and they thoroughly understand their properties (corresponding theorems and their proofs). There are various pedagogical ways to achieve this.

Our approach is based on the following basic teaching principles that we have been applying in our teaching for many years.

When starting an explanation of new subject matter, we introduce a particular problem with a real life example, logical task or puzzle as a prototype of the explained concept or algorithm and properly discuss suitable graph-representation of a problem. *Student engagement is crucial for successful education. Practical tasks attract students to know more about the explained subject matter and to apply gained knowledge* (cf. [3]). *If an interesting enjoyable task is assessed to each topic, students recall the explained subject matter much better and their engagement progresses when looking for similar examples.*

We examine each problem from more than one point of view and discuss various approaches to the given problem solution with respect to the already explained subject matter. Using the constructed knowledge and suitable modification of the problem solution we proceed to new subject matter. In this way students get deeper insight into each problem and entirely understand it.

In addition to words we visualize the particular issue as well as it is possible. For the subjects dealing with the graph theory and combinatorial optimization was created GrAlg program that is closer presented in Sect. 2. *Visual attributes of a problem or situation are the primary, and most influential, connection to meaning and understanding. Visualization used before symbolic development increases the likelihood that students will remember the mathematical concept being taught. Mathematics reasoning both takes from and gives the other parts of the mind. Thanks to graphs, we primates grasp mathematics with our eyes and our mind's eye* [4].

We thoroughly practice the explained topic on various examples, discuss students' own examples describing the topic and encourage them to solve similar examples. *Practical and enjoyable examples serve very well as good tool for finding out if students are able to describe a given task with the aid of graphs, i.e. find a graph-representation of the task, solve it and translate the solution back into the initial situation. When solving tasks using graph theory knowledge, it isn't always easy to find immediately the needed graph-representation.*

The aim of the paper is to introduce the multimedia program GrAlg enabling visual representation of basic graph-concepts and graph-algorithms with respect to above mentioned principles.

2 Multimedia Support—GrAlg Program

In the introductory course dealing with graph theory and graph algorithms we explain and discuss only the algorithms on simple undirected graphs (cf. [5–8]). In Fig. 1 the graph whose edges illustrate the interactions between these algorithms is presented. Numbers of vertices indicate the order in which the algorithms are gradually discussed in the lectures.

Technology and social media have not only become a part of school life, but have also begun to have a significant effect on the forms and methods of teaching and learning [10]. Along with large software products dealing with a wide spectrum of objects developed by a team of professionals there are also various smaller programs dealing with objects appropriate to course subject matter created by a student on a script given by the teacher with regard to student's needs. In this way the students receive study material closely corresponding with their reasoning. Student-author forms the content of the application, according to teacher's documents and guidelines, but on the other hand he/she formally captures the visual sensibilities of their fellow-students (cf. [11]).

One of the most important applications among programs created within students' theses for the subjects dealing with the graph theory and combinatorial optimization is the GrAlg program [12].

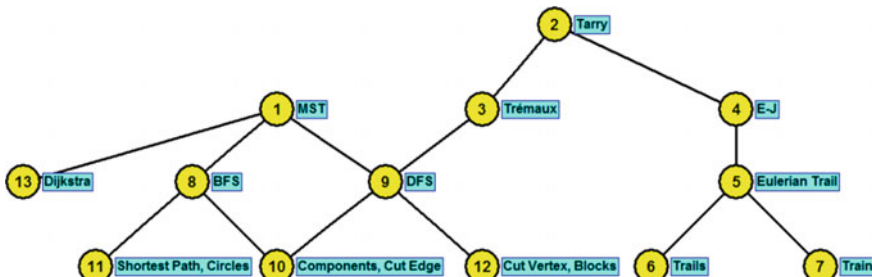


Fig. 1 Mutual relation among given graph algorithms. 1. MST = Minimum spanning tree problem, 2. Tarry = Tarry's approach to maze problem, 3. Trémaux = Trémaux's approach to maze problem, 4. E-J = Edmonds-Johnson's approach to maze problem, 5. Eulerian Trail = algorithm determining an Eulerian trail, 6. Trails = algorithm determining a minimum trail cover, 7. Train = algorithm solving the Chinese Postman Problem, 8. BFS = Breadth-First-Search, 9. DFS = Depth-First-Search, 10. Components = algorithm determining components, Cut Edge = algorithm determining if an edge is/isn't cut edge, 11. Shortest Path = algorithm determining the length (according number of edges) of the shortest path between two vertices, Circles = algorithms determining circles with given properties (in more detail—see [9]), 12. Cut Vertex = algorithm determining if a vertex is/isn't cut vertex, Blocks = algorithm determining blocks, 13. Dijkstra = Dijkstra's algorithm

2.1 GrAlg Program—Brief Description

The program is created in the Delphi environment and its main purpose is the easy creation and modification of graphs and the possibility to emphasize with colours basic graph-concepts and graph algorithms on graphs created within the program.

There are the following main possibilities of the program:

The program enables the creation of a new graph represented by figure, editing it, saving graph in the program, in its matrix representation and also saving graph in bmp format.

It also makes it possible to display some graph properties of the given graph.

The program enables to add colour to vertices and edges, to add text next vertices, and to change positions of vertices and edges by “drop and draw a vertex (an edge respectively)”.

The program allows the user to open more than one window so that two (or more) objects or algorithms can be compared at once. Window size can be adjusted as needed (see Fig. 2).

In the GrAlg program there is the option to run programs visualizing all of the subjects explained algorithms in a way from which the whole process and used data structures can clearly be seen (see Fig. 2).

The program is available on http://lide.uhk.cz/prf/ucitel/milkoev1/en_index.htm, the page GRAFALG/Lectures.

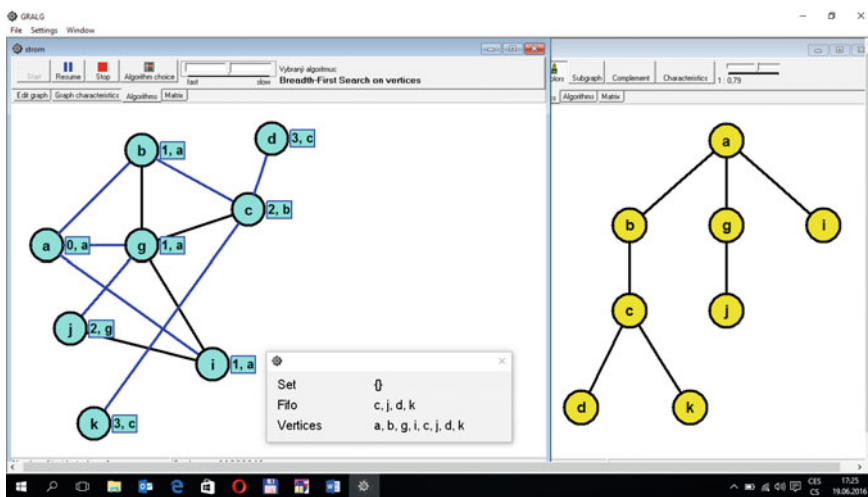


Fig. 2 Two open windows of the GrAlg program with BFS algorithm visualization (left window) and found appropriate BFS tree (in the window)

2.2 *GrAlg Program—Advantages from Teacher Point of View*

The GrAlg program enables the teacher to complete his/her explanation within lectures in such a way that the topic is more comprehensible; the possibility to use colours allows the teacher to emphasize needed objects and relations, the option to open more than one window enables him/her to explain the problem from more points of view and show mutual relations among used concepts and algorithms. The possibility to save each created graph in bmt format allows him/her easy insertion of needed graphs into the study material (all graphs in this paper were prepared with the program) and thus saves his/her time when preparing text material and presentations.

2.3 *GrAlg Program—Advantages from Student Point of View*

Using the GrAlg program students can revise subject-matter within the area of graph theory and more deeply understand it. They can use not only graphs prepared by the teacher but also graphs created by themselves, explore the properties of these graphs and monitor the behaviour of algorithms. The possibility to open more than one window enables them to follow mutual relations among used concepts and algorithms. The option “Save Graph in bmp format” enables them easy creation needed graphs for their tasks (texts and/or presentations) where they describe various practical situations with the aid of graphs and solve the given problem.

3 Conclusion and Future Work

Mathematics is one of the oldest sciences however the area known as Combinatorial Optimization close connected with Graph Theory and Computer Science is quite young. Modern technology provides access to education and learning in the areas (and not only in them) in a modern way attractive for students.

We agree with the authors of [13], who underpin that the core of enhancing mathematical thinking is conscious questioning (discussion) where the numbers do not have to be used. Students need to apprehend vocabulary, definitions and implement/shift aspects of a problem situation into understanding, solving and then connecting new knowledge into their mental concepts. Deeper questioning is the means for students to make sense of mathematics and digital tools should be effectively used to promote student questioning.

Intended learning may fail to be achieved for many reasons and if the purpose of the mathematical tasks is confined or limited to ‘solving’, rather than ‘learning from solving’, it is likely that learners may neither learn nor enjoy engaging with the problem [13].

In the paper we have presented our teaching principles together with intelligent multimedia application GrAlg, a useful complement of the subjects dealing with the graph theory and combinatorial optimization. This program which visualises the discussed concepts and graph algorithms, and which enables their comparison, gives students the opportunity to get deeper insight into the subject matter and to enhance their facility to solve everyday life practical situations. Students gain many useful ideas and inspiration for their own solutions to tasks within various research areas.

At present we are dealing with a research concerning visualization of theorems and their proofs explained within the above mentioned courses.

Acknowledgements This research has been supported by specific research project of the Faculty of Science, University of Hradec Králové in 2016.

References

1. Williams, R.: e-Learning strategy: what's in the blend? In: Proceedings of the 4th European Conference on e-Learning, Amsterdam, Nederland, ACL, UK, pp. 245–251 (2005)
2. Salem, A.-B.M.: Intelligent methodologies and technologies for e-Learning. In: IEEE 10th International Conference on Emerging eLearning Technologies and Applications, pp. 331–337 (2012)
3. Prazak, P.: Teaching simulation for management students in LMS. In: Advances in Web-Based Learning—ICWL 2015, vol. 9412 of the series Lecture Notes in Computer Science, pp. 121–130 (2015)
4. Pinker, S.: How the Mind Works, Norton (1997)
5. Biggs, N.L., Lloyd, K.E., Wilson, R.J.: Graph Theory 1736–1936. Clarendon Press, Oxford (1976)
6. Graham, R.L., Hell, P.: On the history of the minimum spanning tree problem. *Ann. Hist. Comput.* **7**(1), 43–57 (1985)
7. Tarjan, R.E.: Data structures and network algorithms, Chap. 6. In: CBMS Regional Conference, SIAM, Philadelphia (1983)
8. Dijkstra, E.W.: A note on two problems in connection with graphs. *Numer. Math.* **1**, 269–271 (1959)
9. Milková, E.: Breadth-first-search tree—levels and subtrees. *Int. J. Math. Comput. Simul.* **9**, 206–212 (2015)
10. Kurvits, M., Laanpere, M., Väljataga, T.: Analysis of tools and methods for describing and sharing reusable pedagogical scenarios. In: Advances in Web-Based Learning—ICWL 2015, vol. 9412 of the series Lecture Notes in Computer Science, pp. 251–257 (2015)
11. Valjataga, T., Fiedler, S., Laanpere, M.: Re-thinking digital textbooks: students as co-authors. In: Advances in Web-Based Learning—ICWL 2015, vol. 9412 of the series Lecture Notes in Computer Science, pp. 143–151 (2015)
12. Šitina, J.: Grafové algoritmy a jejich vizualizace. Thesis, University of Hradec Králové, Czech Republic (June 2010)
13. Khan, K., Mason, J.: Non numerical aspects of school mathematics. In: Proceedings of the 23rd International Conference on Computers in Education (ICCE 2015), Hangzhou, China, pp. 477–482 (2015)

FFLD-Based Modeling of Fractional-Order State Space LTI MIMO Systems

Krzysztof J. Latawiec, Rafał Stanisławski, Marian Łukaniszyn,
Marek Rydel and Bogusław R. Szkuta

Abstract This paper introduces a multivariable version of the Grünwald-Letnikov fractional-order difference (FD) and approximates it with a powerful combination of finite fractional difference (FFD) and finite Laguerre-based difference (FLD) to yield finite fractional/Laguerre-based difference (FFLD). The multivariable FFLD is effectively used to model fractional-order state-space LTI MIMO systems.

Keywords Grünwald-Letnikov fractional difference · Laguerre-based difference · Multivariable fractional difference · Fractional order systems · State space systems

Nomenclature

CFLD	Combined fractional/Laguerre-based difference
FD	Grünwald-Letnikov fractional-order difference
FFD	Finite fractional difference
FFLD	Finite fractional/Laguerre-based difference
FLD	Finite Laguerre-based difference
GL	Grünwald-Letnikov
LD	Laguerre-based difference
OBF	Orthonormal basis functions

K.J. Latawiec (✉) · R. Stanisławski · M. Łukaniszyn · M. Rydel · B.R. Szkuta
Department of Electrical, Control and Computer Engineering, Opole University
of Technology, ul. Prószkowska 76, 45-758 Opole, Poland
e-mail: k.latawiec@po.opole.pl

R. Stanisławski
e-mail: r.stanislawska@po.opole.pl

M. Łukaniszyn
e-mail: m.lukaniszyn@po.opole.pl

M. Rydel
e-mail: m.rydel@po.opole.pl

B.R. Szkuta
e-mail: b.szkuta@po.opole.pl

1 Introduction

Various approximations to the Grünwald-Letnikov fractional difference (FD) have been pursued in order to prevent its computational explosion problem [1–11]. Our main reservation against a plethora of approximation approaches results from the fact that the proposed approximating IIR/FIR/OBF filters are quite arbitrary in that they do not use any a priori knowledge about the mathematical (not to say physical) structure of the Grünwald-Letnikov FD. Therefore, an alternative approach relying on the approximation of the FD filter with its truncated, finite-length versions is advocated here [1, 2]. In analogy to finite impulse response (FIR) the term finite FD, or FFD, has been coined [12, 13]. New, effective combinations of FFD with Laguerre filters have led to the introduction of Finite Laguerre-based difference (or FLD) [14, 15] and Finite Fractional/Laguerre-based difference (or FFLD) [14, 15]. In the FFLD, the FFD contribution covers the high-frequency properties of FD, while its medium/low-frequency range is modeled by the FLD share. The FFLD provides excellent performance, both in terms of high approximation accuracy and low computational load [15]. Up to date, FFLD has been employed in the single-input/single-output (SISO) environment [16, 17]. Here we extend the applicability of the FFLD to modeling of multivariable state-space systems.

This paper is organized as follows. Having introduced the approximation problem for the Grünwald-Letnikov difference in Sect. 1, the FD modeling task by means of FFD is recalled and extended to the multivariable case in Sect. 2. In a similar way, Laguerre-based fractional differences LD and CFLD together with their approximations FLD and FFLD, are resumed in Sect. 3. A unified multivariable framework for FD/LD/CFLD and their approximators FFD/FLD/FFLD is presented in Sect. 4. An FFLD-based application to fractional-order state space modeling is given in two implementation schemes in Sect. 5. Conclusions of Sect. 6 complete the paper.

2 Fractional Difference and Finite Fractional Difference

It is well known that the Grünwald-Letnikov fractional order difference (FD)

$$\Delta_{FD}^\alpha x(t) = x(t) + \sum_{j=1}^t P_j(\alpha)x(t-j) \quad t = 0, 1, \dots \quad (1)$$

can be described as [12]

$$\begin{aligned} \Delta_{FD}^\alpha x(t) &= x(t) + \sum_{j=1}^{\infty} P_j(\alpha)x(t-j) \\ &= x(t) + X_{FD}(t) \quad t = 0, 1, \dots \end{aligned} \quad (2)$$

with $x(l) = 0 \forall l < 0$, $P_j(\alpha) = (-1)^j \binom{\alpha}{j}$ and $\alpha \in (0, 2)$ is the fractional order. Here we admit the signal $x(t)$ to be an n_x -vector, thus introducing the multivariable FD.

The simplest time-domain approximation to FD, avoiding its possible computational explosion, is the finite fractional difference (FFD) defined as [12]

$$\Delta_{FFD}^{\alpha} x(t) = x(t) + \sum_{j=1}^J P_j(\alpha) x(t) q^{-j} \quad (3)$$

where $J = \min(t, \bar{J})$ and \bar{J} is the upper bound for j when $t > \bar{J}$. It is well known that the FFD suffers from the steady-state error problem.

2.1 Multivariable FFD

In the multivariable FD case, the signal $x(t)$ is assumed to be an n_x -vector. For the multivariable FFD case, we discriminate between various bounds $J = J_r$, $r = 1, \dots, n_x$, with $J_r = \min(t, \bar{J}_r)$, thus accounting for various dynamics in the x_i -to- $(\Delta^{\alpha} x)_i$ channels, $i = 1, \dots, n_x$. This way we introduce the multivariable version of FFD.

3 Laguerre-Based Fractional Differences and Their Approximators

Firstly, the Laguerre-based (fractional) difference (LD) is recalled [14], which, like the FD, is valid for both scalar and multivariable cases

$$\begin{aligned} \Delta_{LD}^{\alpha} x(t) &= x(t) + \sum_{j=1}^{\infty} c_j L_j(q^{-1}) x(t) \\ &= x(t) + X_{LD}(t) \quad t = 0, 1, \dots \end{aligned} \quad (4)$$

with $x(l) = 0 \forall l < 0$, $L_j(q^{-1})$ and c_j , $j = 1, 2, \dots$, are the Laguerre filters and weighting parameters, respectively. Interestingly, in the scalar case, values of c_j have been derived that provided the equivalence of LD and FD in the sense that $X_{LD} \equiv X_{FD}$ [14].

Again, to cope with the computational explosion problem, a finite approximation to LD, called FLD, has been defined [14] for the scalar case

$$\begin{aligned}\Delta_{FLD}^\alpha x(t) &= x(t) + \sum_{j=1}^M c_j L_j(q^{-1}) x(t) \\ &= x(t) + X_{FLD}(t) \quad t = 0, 1, \dots\end{aligned}\tag{5}$$

where M is the number of the Laguerre filters used do calculate the difference FLD and $c_j, j = 1, 2, \dots, M$, are computed as for LD in Eq. (4). For the multivariable case, the signal $x(t)$ is an n_x -vector and $M_s, s = 1, \dots, n_x$, is substituted for M .

Also, another Laguerre-based (fractional) difference, being a combination of the FFD and LD, called CFLD, has been defined for the scalar case as [14]

$$\Delta_{CFLD}^\alpha x(t) = x(t) + X_{CFLD}(t) \quad t = 0, 1, \dots\tag{6}$$

where

$$X_{CFLD}(t) = \sum_{i=1}^J P_i(\alpha) x(t) q^{-i} + \sum_{j=1}^{\infty} c_j L_j(q^{-1}) q^{-\bar{J}} x(t)\tag{7}$$

and the first component at the right-hand side of Eq. (7) constituting the FFD contribution into the CFLD, while the second one being the (\bar{J} -delayed) LD share, with $P_j(\alpha), j = 1, \dots, J$, as in Eqs. (2) and (3), and $L_j(q^{-1})$ and $c_j, j = 1, 2, \dots$, as in Eqs. (4) and (5), respectively.

Again, conditions for equivalence of CFLD and FD have been established in the scalar case [14].

Finally, a finite approximation to CFLD/FD, called FFLD, has been presented for the scalar case [14, 15]

$$\begin{aligned}\Delta_{FFLD}^\alpha x(t) &= x(t) + \sum_{i=1}^J P_i(\alpha) x(t) q^{-i} + \sum_{j=1}^M c_j L_j(q^{-1}) q^{-\bar{J}} x(t) \\ &= x(t) + X_{FFLD}(t) \quad t = 0, 1, \dots\end{aligned}\tag{8}$$

where J is as before and M is a number of Laguerre filters used in the model.

In the scalar case, the Laguerre-based approximators to FD, in particular FFLD, have been shown to provide excellent modeling performance [14], outperforming the recognized FD approximators [15].

In the multivariable FFLD case, the signal $x(t)$ is an n_x -vector and $J_r, r = 1, \dots, n_x$ and $M_s, s = 1, \dots, n_x$, are substituted for J and M , respectively, just like in case of the multivariable FFD and FLD.

4 FFLD-Based Approximators to Multivariable FD—A Unified Framework

Now, a unified framework is offered for both multivariable FD/LD/CFLD and their FFLD-based approximators FFD/FLD/FFLD

$$\Delta_{FFLD}^\alpha x(t) = x(t) + X_{FFLD}(t) \quad t = 0, 1, \dots \quad (9)$$

where

$$X_{FFLD}(t) = \sum_{j=1}^{J_r} P_j(\alpha)x(t)q^{-j} + \sum_{j=1}^{M_s} c_j L_j(q^{-1})x(t - \bar{J}_r) \quad (10)$$

with J_r and M_s defined as before, which is specified to

- (i) FD for $\bar{J}_r \rightarrow \infty$, $r = 1, \dots, n_x$ and $M_s = 0$, $s = 1, \dots, n_x$,
- (ii) FFD for $\bar{J}_r < \infty$ and $M_s = 0$,
- (iii) LD for $\bar{J}_r = 0$, $M_s \rightarrow \infty$ and c_j calculated as in Theorem 1 of [14],
- (iv) FLD for $\bar{J}_r = 0$, $M_s < \infty$ and c_j calculated as in Theorem 1 of [14],
- (v) CFLD for $0 < \bar{J}_r < \infty$, $M_s \rightarrow \infty$ and c_j calculated as in Theorem 2 of [14],
- (vi) FFLD for $0 < \bar{J}_r M_s < \infty$, $r = 1, \dots, n_x$, $s = 1, \dots, n_x$, and c_j calculated as in Theorem 2 of [14].

It should be emphasized that Eqs. (9) and (10) constitute a generalization of the FD/FFD/LD/FLD/CFLD/FFLD models, thus presenting a unified framework for the three fractional differences and their three approximators considered. Now, depending on a specific application, or a specific context, we can pick up one (or more) of the specific items (i) to (vi) in order to analyze/synthesize a specific model.

5 Application to Fractional State Space System

Consider a discrete-time state space LTI MIMO system governed by the (commensurate-order) fractional equations

$$\Delta^\alpha x(t+1) = A_f x(t) + Bu(t), \quad x_0 \quad (11)$$

$$y(t) = Cx(t) + Du(t) \quad (12)$$

where $x(t) \in \Re^{n_x}$, $u(t) \in \Re^{n_u}$ and $y(t) \in \Re^{n_y}$ are the state, input and output vectors, respectively, $A_f \in \Re^{n_x \times n_x}$, $B \in \Re^{n_x \times n_u}$, $C \in \Re^{n_y \times n_x}$ and $D \in \Re^{n_y \times n_u}$. Without loss of generality we will assume in the sequel that the initial vector x_0 is zero, especially that we will operate on finite-length FD approximators that do not trace back to x_0 . Note that $A_f = A - I$, with $A \in \Re^{n_x \times n_x}$ representing a discrete-time state space system in a ‘regular’ form (with $\alpha = 1$) and $I \in \Re^{n_x \times n_x}$ is the identity matrix.

Accounting that the FD is described by formula (2), Eq. (11) can be modeled in the following form [2, 18, 19]

$$x(t+1) = (A_f + \alpha I)x(t) - \sum_{j=2}^{t+1} P_j(\alpha)x(t-j+1) + Bu(t) \quad (13)$$

Using the approximations to FD presented in Sect. 4, the corresponding state space models can be specified.

The stability analysis for discrete-time state space systems has been given in Refs. [18, 19].

5.1 Unified Framework for State Space Models

Using the unified framework for all the approximations to multivariable FD presented in Sect. 4, the FD/FFD/LD/FLD/CFLD/FFLD-based discrete-time state equation can be unified as

$$\begin{aligned} x(t+1) &= A_f x(t) + Bu(t) - X_{FFLD}(t+1) \quad t = 0, 1, \dots \\ &= A_f x(t) + Bu(t) - \sum_{j=1}^{J_r} P_j(\alpha)x(t-j+1) - \sum_{j=1}^{M_s} c_j L_j(q^{-1})x(t-\bar{J}_r+1) \end{aligned} \quad (14)$$

with the specifications (i) to (vi) of Sect. 4 still valid here.

Note that, in fact, the FFLD description (14) is the most general one for all the FD/FFD/LD/FLD/CFLD/FFLD-based LTI state space systems, as can be seen from the unified framework of Sect. 4.

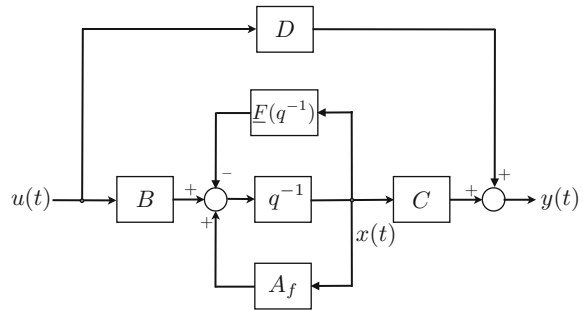
Remark 1 Possible accounting for the sampling period T (when transferring from a continuous-time derivative to the discrete-time difference) results in the substitutions $A_f \rightarrow A_f T^\alpha$ and $B \rightarrow BT^\alpha$ in Eqs. (13) and (14) [2, 18, 19].

5.2 Implementation of State Space Models

Implementation of the fractional order state space system reduces to determining the function $X_{FFLD}(t)$ in the state Eq. (14).

Implementation scheme 1 (general). Since the summation bounds J_r and M_s , $r, s = 1, \dots, n_x$, are varying with entries of the vector $x(t)$, the particular entries $x_i(t)$, $i = 1, \dots, n_x$, have to be calculated separately, which is rather burdensome.

Fig. 1 Block diagram of regular/fractional-order state space system



Implementation scheme 2 (simplified). We can simplify the calculations assuming that $J_1 = J_2 = \dots = J_{n_x} = J$ and $M_1 = M_2 = \dots = M_{n_x} = M$. This enables to calculate the whole vector $x(t)$ as in the quite familiar block diagram of Fig. 1. Accounting for the response of the “fractionalizing” filter $\underline{F}(q^{-1})$ to the signal $x(t)$, the block diagram of the fractional-order state space models of Fig. 1 is similar to the regular one. For fractional-order systems the filter $\underline{F}(q^{-1})$ represents the particular approximation to FD/LD/CFLD and can be specified as follows:

- (a) $\underline{F}(q^{-1}) = \sum_{j=1}^J P_j(\alpha)q^{-j+1}$ for FFD-based state space system,
- (b) $\underline{F}(q^{-1}) = \sum_{j=1}^M c_j L_j(q^{-1})q$ with c_j calculated as in Theorem 1 of [14] for FLD-based system,
- (c) $\underline{F}(q^{-1}) = \sum_{j=1}^J P_j(\alpha)q^{-j+1} + \sum_{j=1}^M c_j L_j(q^{-1})q^{-\bar{j}+1}$ with c_j calculated as in Theorem 2 of [14] for FFLD-based system.

Remark 2 Note that for the ideal case of FD/LD/CFLD we have $\underline{F}(q^{-1}) = q[(1 - q^{-1})^\alpha - 1]$ (compare [18, 19]). Also note that for the regular state space system ($\alpha = 1$), we have $\underline{F}(q^{-1}) = -1$.

6 Simulation Example

Example 1 Out of a plethora of simulation runs we select a simple two-input/two-output discrete-time fractional-order (commensurate) state space system A_f, B, C as in Eqs. (11) and (12) with $D = 0$, $n_x = 2$, $\alpha = 0.5$ and

$$A_f = \begin{bmatrix} -0.1 & 0.1 \\ 0.15 & -0.6 \end{bmatrix}, \quad B = \begin{bmatrix} 0 & 0.85 \\ 0.3 & 0.1 \end{bmatrix}, \quad C = I_2$$

thus providing different dynamics in the dynamical channels. The multivariable FD is approximated with the (multivariable) FFLD as in Eq. (10), specification (vi), and implemented using the general scheme 1. In order to limit the computational load of the modeling algorithm we introduce the constraint on the maximum number of

Table 1 Modeling accuracy for fractional state space system; Ex. 1

\bar{J}_1, M_1	15, 15	15, 20	15, 20	20, 20	25, 25	25, 20	25, 25
J_2, M_2	15, 15	15, 15	15, 20	15, 15	15, 15	20, 25	15, 25
$N \times \text{MSPE}(\epsilon_1)$	8.137	0.64	0.79	0.1025	0.02	0.039	0.0045
$N \times \text{MSPE}(\epsilon_2)$	0.64	0.031	0.061	0.027	0.042	0.0017	0.0012

parameters $\bar{J}_i + M_i \leq 90$, $i = 1, \dots, n_x = 2$. (Note that the constraint is only loosely related with the computational complexity of the algorithm due to the presence of the Laguerre filters in the FLD part of the FFLD.) Table 1 presents selected results of computation of modeling accuracy in terms of MSPEs for $\epsilon_i(t) = x_i(t) - \hat{x}_i(t)$, $i = 1, 2$, where $x_i(t)$ and $\hat{x}_i(t)$ are the system state and its FFLD-based estimates at time $t = 1, \dots, N = 3000$, respectively. We do not provide plots of exemplary x_i s and \hat{x}_i s, $i = 1, 2$ as these are hardly distinguishable, especially for higher \bar{J}_i and M_i , $i = 1, 2$. For the same ‘distinguishability’ reason, in Table 1 we show the values of $N \times \text{MSPE}(\epsilon_i)$ instead of $\text{MSPE}(\epsilon_i)$, $i = 1, 2$.

The heuristically driven results in Table 1 are self-explanatory. Clearly, higher \bar{J}_i and M_i , $i = 1, 2$ produce lower modeling errors, with diversified values of \bar{J}_i and M_i , $i = 1, 2$ in various dynamical channels also justified. We have additionally confirmed those results arranging for the optimization task

$$[\hat{\bar{J}}_1, \hat{M}_1, \hat{\bar{J}}_2, \hat{M}_2] = \arg \min_{\bar{J}_1, M_1, \bar{J}_2, M_2} \sum_{t=1}^N [\epsilon_1^2(t) + \epsilon_2^2(t)]$$

subject to the aforementioned constraint $\bar{J}_i + M_i \leq 90$, $i = 1, 2$. The solution yields the optimal least-squares estimates

$$\hat{\bar{J}}_1 = 24, \hat{M}_1 = 27, \hat{\bar{J}}_2 = 14, \hat{M}_2 = 25$$

with the sum of error squares equal to 0.00179. The outcome supports the results of Table 1.

Remark 3 It is interesting to compare the above modeling results for the FFLD-based state space system of Example 1 with those for ‘classical’ FFD-based ones ($M_1 = M_2 = 0$). Not surprisingly, the comparable modeling accuracy in the latter case can be obtained for as high $\bar{J}_1 = \bar{J}_2 = \bar{J}$ as 2865 that is at the (very) high computational cost. The FLD-based modeling is more effective than that for FFD but still remarkably inferior to FFLD (compare [15]).

Remark 4 It is worth mentioning that the introduced methodology for approximation of multivariable GL fractional-order differences would most likely be more effective in modelling of noncommensurate-order fractional state space LTI MIMO

systems. In fact, various fractional orders in the channels x_i -to- $(\Delta^\alpha x)_i$, $i = 1, \dots, n_x$, can incur (much) more diversified dynamics in the particular channels than for commensurate-order systems. This will be a subject of our future research.

7 Conclusion

This paper has presented a unified framework for various time-domain approximations to a multivariable version of the Grünwald-Letnikov fractional-order difference (FD) and its Laguerre-based equivalents (LD, CFLD), namely FFD, FLD and FFLD. The approximators have been employed to model fractional-order state space LTI MIMO systems, with the multivariable FFLD model clearly outperforming the two other ones. A simulation example confirms the quality of the new FFLD-based methodology for modeling of fractional-order commensurate state space LTI MIMO systems. Extension to noncommensurate systems is a subject of our future research work.

References

- Podlubny, I.: *Fractional Differential Equations*. Academic Press, Orlando, FL (1999)
- Monje, C., Chen, Y., Vinagre, B., Xue, D., Feliu, V.: *Fractional-Order Systems and Controls: Fundamentals and Applications*. Series on Advances in Industrial Control. Springer, London, UK (2010)
- Chen, Y., Vinagre, B., Podlubny, I.: A new discretization method for fractional order differentiators via continued fraction expansion. In: Proceedings of DETC'2003, ASME Design Engineering Technical Conferences. vol. 340, pp. 349–362, Chicago, IL (2003)
- Maione, G.: On the Laguerre rational approximation to fractional discrete derivative and integral operators. *IEEE Trans. Autom. Control* **58**(6), 1579–1585 (2013)
- Baeumer, B., Kovacs, M., Sankaranarayanan, H.: Higher order Grünwald approximations of fractional derivatives and fractional powers of operators. *Trans. Am. Math. Soc.* **367**(2), 813–834 (2015)
- Gao, Z.: Improved Oustaloup approximation of fractional-order operators using adaptive chaotic particle swarm optimization. *J. Sys. Eng. Electron.* **23**(1), 145–153 (2012)
- Gao, Z., Liao, X.: Rational approximation for fractional-order system by particle swarm optimization. *Nonlinear Dyn.* **67**(2), 1387–1395 (2012)
- Khanra, M.: Rational approximation of fractional operator—a comparative study. In: International Conference on Power, Control and Embedded Systems (ICPCES), Allahabad, India, pp. 1–5 (2010)
- Lin, Y., Xu, C.: Finite difference/spectral approximations for the time-fractional diffusion equation. *J. Comput. Phys.* **225**, 1533–1552 (2007)
- Ditzian, Z.: Fractional derivatives and best approximation. *Acta Math. Hung.* **81**(4), 323–348 (1998)
- Tseng, C.C.: Design of variable and adaptive fractional order FIR differentiators. *Signal Process.* **86**(10), 2554–2566 (2006)
- Stanisławski, R., Latawiec, K.J.: Normalized finite fractional differences—the computational and accuracy breakthroughs. *Int. J. Appl. Math. Comput. Sci.* **22**(4), 907–919 (2012)

13. Stanisławski, R., Latawiec, K.J.: Modeling of open-loop stable linear systems using a combination of a finite fractional derivative and orthonormal basis functions. In: Proceedings of the 15th International Conference on Methods and Models in Automation and Robotics, Miedzyzdroje, Poland, pp. 411–414 (2010)
14. Stanisławski, R.: New Laguerre filter approximators to the Grünwald-Letnikov fractional difference. *Math. Probl. Eng.* **2012**, 1–21 (2012) Article ID: 732917
15. Stanisławski, R., Latawiec, K.J., Łukaniszyn, M.: A comparative analysis of Laguerre-based approximators to the Grünwald-Letnikov fractional-order difference. *Math. Probl. Eng.* **2015**, 1–10, Article ID: 512104 (2015)
16. Stanisławski, R., Latawiec, K.J., Łukaniszyn, M., Gałek, M.: Time-domain approximations to the Grünwald-Letnikov difference with application to modeling of fractional-order state space systems. In: 20th International Conference on Methods and Models in Automation and Robotics (MMAR), Miedzyzdroje, Poland, pp. 579–584, Aug 2015
17. Stanisławski, R., Latawiec, K.J.: Fractional-order discrete-time Laguerre filters—a new tool for modeling and stability analysis of fractional-order LTI SISO systems. *Discret. Dyn. Nat. Soc.* **2016**, 1–9, Article ID: 9590687 (2016)
18. Stanisławski, R., Latawiec, K.J.: Stability analysis for discrete-time fractional-order LTI state-space systems. Part I: New necessary and sufficient conditions for asymptotic stability. *Bull. Pol. Acad. Sci. Tech. Sci.* **61**(2), 353–361 (2013)
19. Stanisławski, R., Latawiec, K.J.: Stability analysis for discrete-time fractional-order LTI state-space systems. Part II: New stability criterion for FD-based systems. *Bull. Pol. Acad. Sci. Tech. Sci.* **61**(2), 362–370 (2013)

A Dispatching Policy for the Dynamic and Stochastic Pickup and Delivery Problem

Gianpaolo Ghiani, Emanuele Manni and Alessandro Romano

Abstract Real-time vehicle routing problems arise in a number of applications spanning from couriers to emergency services. In this article, we present a new dispatching policy for the dynamic and stochastic pickup and delivery problem, in which a fleet of vehicles must service a set of dynamically occurring customers requests that are partitioned in several classes (according to their priority). The basic idea of our policy is to reserve a fraction of the fleet capacity to the top prior classes that deserve to be serviced as soon as possible. Moreover, our dispatching policy is parameterized and the optimal parameter setting is determined by solving an off-line training problem on a sample of the instance population. To asses the quality of our approach, we compare it with two policies already proposed in the literature, namely a reactive and an anticipatory procedure. Computational results on randomly-generated instances indicate that our procedure can often match the quality of an anticipatory algorithm with a computational effort comparable to that of a reactive approach.

Keywords Real-time vehicle routing · Dispatching policies · Pickup and delivery · Optimization

G. Ghiani · E. Manni (✉) · A. Romano
Dipartimento di Ingegneria dell’Innovazione, Università del Salento,
via per Monteroni, 73100 Lecce, Italy
e-mail: emanuele.manni@unisalento.it

G. Ghiani
e-mail: gianpaolo.ghiani@unisalento.it

A. Romano
e-mail: alessandro.romano@unisalento.it

1 Introduction

In this paper, we deal with the dynamic and stochastic Pickup and Delivery Problem (PDP) in which a fleet of vehicles must service a set of customers requests characterized by a pickup and a delivery location, as well as by a class according to their priority. The goal is to maximize the overall customer service level (which is equivalent to minimize customer inconvenience). The problem is dynamic in that customers requests are disclosed during the planning horizon, whereas it is stochastic because we assume that the requests arrive according to known stochastic processes. This type of problem occurs in several sectors (e.g., the couriers industry and emergency systems). Nowadays, the recent advances in communication and information technologies allow to obtain in real-time—among others—data on vehicles locations and customers requests. This continuous flow of data forces the dispatcher to modify the vehicle routes in real time. Moreover, at each stage it is important to make accurate decisions, since a bad choice in the present might affect the ability to make good decisions in the future. A detailed survey can be found in [5]. For this class of problems two kinds of policies are common in the literature: (i) reactive policies which manage new requests only once they have occurred, neglecting any available stochastic information; (ii) anticipatory algorithms which exploit the stochastic characterization of future demand, in an attempt of anticipating it, to provide the highest possible quality of service. Reactive policies [2] are characterized by extremely fast running times, which are obtained at the expenses of solution quality, mainly because of the myopic choices made at each stage. On the other hand, anticipatory procedures [1, 3, 4] typically achieve better results than reactive algorithms, but with longer running times mainly due to the computational effort of simulating future demand. In this paper we aim to devise a dispatching policy that, trading off between these two extremes, is able to match the quality of anticipatory algorithms with a computational effort comparable to that of reactive approaches. The work by Ghiani et al. [3] is particularly relevant to our paper, because we consider a problem with similar characteristics. Moreover, we use their anticipatory algorithm as a benchmark for our approach, as will be described in Sect. 3.

2 A Dispatching Policy

In our formulation of the dynamic and stochastic PDP, we assume that the entire territory is represented by a rectangular area with given dimensions h and w , so that a generic point a (pickup, delivery, depots and vehicles' positions) is identified by means of its Cartesian coordinates (x_a, y_a) . The time t_{ab} needed to go from an origin a to a destination b is obtained by using the Euclidean distance between the two points and considering a given fixed speed. We assume there is a fleet of m vehicles at disposal, each of which is located at a depot at the beginning of the planning horizon. In addition, each vehicle route must meet the following constraints: (i) each

route starts and ends at a depot; (ii) the pickup and the delivery points of a request must be visited by the same vehicle; (iii) a pickup point must precede its associated delivery point; (iv) a vehicle cannot be diverted from its next destination to service a new request. The customers (and therefore their service requests) are classified into a number C of classes, according to their “importance”. Without any loss of generality, we assume that class $c = 1$ represents the most important requests, whereas class $c = C$ represents the requests of customers whose service can be delayed without incurring in high penalties. In general, the k -th request ($k = 1, 2, \dots$) is characterized by $(\mathbf{i}_k^+, \mathbf{i}_k^-, c_k, T_k)$, where $\mathbf{i}_k^+ = (x_k^+, y_k^+)$ are the coordinates of the pickup point, $\mathbf{i}_k^- = (x_k^-, y_k^-)$ are the coordinates of the delivery point, $c_k \in \{1, \dots, C\}$ is the class of the request, $T_k \geq 0$ is the occurrence time of the request. We assume that the requests are independent and uniformly distributed over the service territory and arrive according to a known stochastic process.

Our goal is to maximize the customer satisfaction by minimizing the sum of the inconveniences of the requests, that are calculated differently according to the class the request belongs to. More specifically, we denote by $f(\tau_k, \mathbf{w}_k)$ the penalty function measuring the inconvenience associated with the k -th request, defined as:

$$f(\tau_k, \mathbf{w}_k) = \begin{cases} 0 & T_k \leq \tau_k < D_k \\ p_{c_k}(\tau_k - D_k) & \tau_k \geq D_k. \end{cases}$$

Here, τ_k is the time instant when the delivery is performed and $\mathbf{w}_k = (l_{c_k}, p_{c_k})$. In particular, $l_{c_k} \geq 0$ is the amount of time (after the instant T_k) after which the penalty starts to be counted, determining a *soft deadline* $D_k = T_k + l_{c_k}$. Finally, $p_{c_k} \geq 0$ is the slope of the penalty function. Thus, the objective function is: $\min z = \sum_k f(\tau_k, \mathbf{w}_k)$.

The policy we propose in this paper aims to achieve performance that are comparable to those of a reactive approach in terms of reduced computing times and to those of an anticipatory algorithm in terms of solution quality. For the former purpose, we avoid using complex rules for assigning the requests to the vehicles and for managing the multiple classes of requests. Rather, we choose to reserve a fraction α_c of the fleet of m vehicles to service the requests belonging to class $c = 1, \dots, C$. Thus, α_c denotes the fraction of the fleet that can be used to service the requests belonging to class c and to the more prioritized classes. In this way, when taking the dispatching decision we employ a cheapest-insertion approach, but the number of alternatives is limited by the fact that not all the vehicles can service all the requests. As an additional dispatching rule, when evaluating the different alternatives we allow an insertion if the delivery instants of the requests of each class c ($c = 1, \dots, C$) that are already allocated on a route are not delayed more than a given value $\epsilon_c \geq 0$. As pointed out before, we also want to get advantage of the available stochastic knowledge of the problem. As a consequence, the values of the vector $\boldsymbol{\alpha} = (\alpha_1, \dots, \alpha_C)$ are determined by solving off-line a training problem on a sample that is representative of the instances to be solved. Of course, the solution must be such that $\sum_{i=1}^C \alpha_i = 1$. The procedure starts with a given value for $\boldsymbol{\alpha}$. Then, we try to repeatedly modify each component α_c by adding or subtracting a value δ and evaluating the (possible)

objective function improvement. In case of an improvement, the value of α_c is updated and the procedure is iterated. The procedure terminates when no further improvements are possible.

3 Experimental Results

To asses the effectiveness of our dispatching policy, we compare it with two different approaches: (a) a purely reactive procedure that for each new request chooses the vehicle with the cheapest insertion cost, neglecting all the available stochastic information; (b) the anticipatory procedure proposed in [3], suitably modified to manage different classes of requests. All the heuristics are implemented in C++ and run on a Linux machine clocked at 2.67 GHz and equipped with 27 GB of RAM. We perform a number of computational experiments on randomly generated instances. All the datasets are characterized by several experimental factors, some of which have the same value across all the datasets, whereas the others have different values. In particular, in the former set of experimental factors we consider: $C = 2$, a planning horizon of 480 min, an average speed of the vehicles of 40 km/h, $h = 20$ km, $w = 20$ km, $p_1 = 10$ and $p_2 = 1$. Then, the experimental factors having different values depending on the specific dataset are:

- expected number of requests per class N_c ($c = 1, \dots, C$): we have tested various values for N_1 and N_2 , such that the overall expected number of requests is 200 or 1500;
- number m of vehicles at disposal: $m = 20, 40, 60, 80, 100, 120, 140$;
- parameters l_c and ϵ_c ($c = 1, \dots, C$): we have tested various combinations, generating four different datasets.

We evaluate the performance of the different dispatching policies by using two indicators. First, we consider the average time T_s (in seconds) needed by the procedure to allocate a single request. We observe that, to allow a particular heuristic to be useful in the real world, the value of T_s must be lower then the inter-arrival time between two consecutive requests. Second, we compute the average percentage objective function deviation of the anticipatory algorithm (ANT, in the following) and of our policy reserving a fraction of the vehicles for the most prioritized classes (RES, in the following) with respect to the reactive procedure. These deviations are obtained as $100 * (\text{obj}_H - \text{obj}_R)/\text{obj}_R$, where obj_R represents the objective function value of the reactive procedure, whereas obj_H is the objective function value of the heuristic we want to evaluate. Thus, a negative value indicates that the considered heuristic achieves an improvement over the reactive procedure. Tables 1 and 2 contain the results of our experiments, differentiated according to the average number of overall daily requests per class. For all the datasets, we have first determined the best values for α by employing the procedure illustrated in the previous section with $\delta = 0.1$. Such values are reported in the tables under the column α^* . The results contained in Table 1 show that the RES policy obtains a maximum improvement of about 3%,

Table 1 Results for $N_1 = 40$ and $N_2 = 160$

Dataset ($l_1, l_2, \epsilon_1, \epsilon_2$)	m	α^*	RES		ANT	
			DEV (%)	T_s	DEV (%)	T_s
(0, 0, 0, 0)	20	(0.1, 0.9)	-0.39	0.01	4.92	29.36
	40	(0.2, 0.8)	-1.09	0.01	-4.43	76.97
	60	(0.2, 0.8)	-1.12	0.01	-4.84	144.205
	80	(0.2, 0.8)	-1.12	0.01	-5.21	243.92
	100	(0.2, 0.8)	-1.12	0.01	-4.87	383.23
(15, 15, 0, 0)	20	(0.1, 0.9)	-0.46	0.01	10.24	28.145
	40	(0.2, 0.8)	-2.78	0.01	-8.03	71.005
	60	(0.2, 0.8)	-2.9	0.01	-10.57	134.68
	80	(0.2, 0.8)	-2.9	0.01	-10.19	229.54
	100	(0.1, 0.9)	-2.9	0.01	-9.76	361.67
(15, 15, 15, 15)	20	(0.1, 0.9)	-0.35	0.01	13.32	24.445
	40	(0.2, 0.8)	-2.1	0.01	-7.36	70.405
	60	(0.1, 0.9)	-2.16	0.01	-7.91	133.395
	80	(0.1, 0.9)	-2.11	0.01	-8.64	229.63
	100	(0.1, 0.9)	-1.97	0.01	-8.81	359.105
(15, 15, 0, 15)	20	(0.1, 0.9)	-0.46	0.01	13.74	30.74
	40	(0.2, 0.8)	-2.06	0.01	-6.87	72.66
	60	(0.1, 0.9)	-2.11	0.01	-7.56	131.995
	80	(0.1, 0.9)	-2.07	0.01	-8.1	226.97
	100	(0.1, 0.9)	-1.92	0.01	-9.01	363.075

whereas the maximum improvement of the anticipatory procedure is about 10%. On the other hand, we observe that the RES policy is extremely fast, with an average time to allocate a single request that is consistently equal to 0.01 s. As expected, the ANT procedure is much slower, taking up to 383 s to take a dispatching decision. This is obviously in contrast with the requirement that the value of T_s must be lower than the inter-arrival time between two consecutive requests (about 144 s in this case). Table 2 contains the results for the case with an overall number of requests equal to 1500. For this table, we report only the results for RES because the ANT procedure has always obtained a value for T_s consistently higher than the inter-arrival time between two consecutive requests (about 20 s in this case). The results show that the RES policy obtains a maximum improvement of about 33%. As far as the values of T_s are concerned, the procedure is a little slower than the previous case, even if still feasible for a real-world application. Indeed, the values are always 0.02 s, with the only exceptions of 0.03 s in one case and 0.30 s in two cases.

Table 2 Results for $N_1 = 750$ and $N_2 = 750$

Dataset ($l_1, l_2, \epsilon_1, \epsilon_2$)	m	α^*	RES	
			DEV (%)	T_s
(0, 0, 0, 0)	60	(0.6, 0.4)	-23.86	0.30
	80	(0.2, 0.8)	-0.27	0.02
	100	(0.3, 0.7)	-1.46	0.02
	120	(0.4, 0.6)	-2.11	0.02
	140	(0.4, 0.6)	-2.19	0.02
(15, 15, 0, 0)	60	(0.6, 0.4)	-32.72	0.30
	80	(0.2, 0.8)	-1.13	0.02
	100	(0.4, 0.6)	-3.86	0.02
	120	(0.4, 0.6)	-5.36	0.02
	140	(0.4, 0.6)	-5.48	0.02
(15, 15, 15, 15)	60	(0.1, 0.9)	0.08	0.02
	80	(0.2, 0.8)	-1.59	0.02
	100	(0.3, 0.7)	-4.34	0.02
	120	(0.3, 0.7)	-5.12	0.02
	140	(0.3, 0.7)	-5.05	0.02
(15, 15, 0, 15)	60	(0.6, 0.4)	-2.23	0.03
	80	(0.3, 0.7)	-1.8	0.02
	100	(0.3, 0.7)	-4.18	0.02
	120	(0.4, 0.6)	-4.98	0.02
	140	(0.3, 0.7)	-5.04	0.02

4 Conclusions

In this paper, we have studied the dynamic and stochastic pickup and delivery problem, in which a fleet of vehicles must service a set of customers requests that arise dynamically and are partitioned in several classes. We have proposed a simple but effective dispatching policy that, every time a new request occurs, allocates it with the goal of minimizing the overall customers inconvenience. The basic idea is to reserve a fraction of the vehicles to service the requests qualified for being satisfied as soon as possible. In addition, our policy is parameterized and the optimal parameter setting is determined by solving off-line a training problem. The goal of our computational results was to show that our policy can achieve results comparable to those of an anticipatory procedure in terms of solution quality and to those of a simple reactive approach in terms of running times. The results of the experimentation on randomly-generated instances have confirmed this intuition, especially when the number of overall daily requests grew up to 1500.

Acknowledgements This work was partly supported by the Ministero dell’Istruzione, dell’Università e della Ricerca (MIUR) of Italy (PRIN project “Transportation and Logistics Optimization in the Era of Big and Open Data”). This support is gratefully acknowledged.

References

1. Ferrucci, F., Bock, S., Gendreau, M.: A pro-active real-time control approach for dynamic vehicle routing problems dealing with the delivery of urgent goods. *Eur. J. Oper. Res.* **225**(1), 130–141 (2013)
2. Gendreau, M., Guertin, F., Potvin, J.Y., Sguin, R.: Neighborhood search heuristics for a dynamic vehicle dispatching problem with pick-ups and deliveries. *Transp. Res. Part C: Emerg. Technol.* **14**(3), 157–174 (2006)
3. Ghiani, G., Manni, E., Quaranta, A., Triki, C.: Anticipatory algorithms for same-day courier dispatching. *Transp. Res. Part E: Logist. Transp. Rev.* **45**(1), 96–106 (2009)
4. Ghiani, G., Manni, E., Thomas, B.W.: A comparison of anticipatory algorithms for the dynamic and stochastic traveling salesman problem. *Transp. Sci.* **46**(3), 374–387 (2012)
5. Ritzinger, U., Puchinger, J., Hartl, R.F.: A survey on dynamic and stochastic vehicle routing problems. *Int. J. Prod. Res.* **54**(1), 215–231 (2016)